EXPERIMENTAL AND ANALYTICAL EVALUATION OF FRP-RETROFITTED REINFORCED CONCRETE DIAPHRAGMS FOR IN-PLANE SHEAR STRENGTHENING

Henry W. McKlin

Thesis submitted to the faculty of the Virginia Polytechnic Institute and State University
in partial fulfillment of the requirements for the degree of

Master of Science
In
Civil Engineering

Eric J. Jacques, Chair
Matthew R. Eatherton, Co-Chair
Carin L. Roberts-Wollmann
David W. Mokarem

5/2/2025
Blacksburg, VA

Keywords: reinforced concrete diaphragm, retrofit, FRP

EXPERIMENTAL AND ANALYTICAL EVALUATION OF FRP-RETROFITTED REINFORCED CONCRETE DIAPHRAGMS FOR IN-PLANE SHEAR STRENGTHENING

Henry W. McKlin

ABSTRACT

Diaphragms are a key component of the horizontal lateral force resisting system (hLFRS) in a reinforced concrete (RC) structure and are crucial for providing sufficient load path to the vertical lateral force resisting system (vLFRS). Diaphragms may require retrofit due to the relocation of vLFRS elements during renovation, penetrations cut into the slab, or in older RC structures that were designed according to outdated design codes. Multiple methods exist for retrofitting diaphragms, including a concrete overlay, infilling of penetrations, and the application of externally bonded fiber reinforced polymer (FRP). FRP is an attractive option because it is quick to install, non-corrosive, and increases the mass of the structure far less than other methods. Although FRP is commonly used to strengthen the in-plane shear capacity of reinforced concrete diaphragms, there is no guidance for this specific application in the current ACI PRC-440.2R-23 (2023) *Guide for the Design and Construction of Externally Bonded FRP Systems for Strengthening Concrete Structures*. A design methodology was developed by Hutton et al. (2023) along with design recommendations based on a smaller dataset, but there is a need for a broader dataset to validate and modify existing guidance.

One part of this thesis describes an experimental program intended to broaden the depth of experimental data relevant to in-plane shear strengthening of RC diaphragms with FRP. The program contained eight cantilever RC diaphragm specimens subject to a displacement controlled reversed cyclic loading protocol at the free end. The diaphragm specimens were designed to represent the diaphragm shear zone adjacent to a shear wall, a typical location of high in-plane shear demand. Seven specimens were strengthened with FRP, while one served to establish a baseline. FRP performance was examined as a function of ply configuration, ply orientation, anchorage type, and anchorage scheme.

A diaphragm specimen database was assembled, including the eight specimens described in this thesis, five specimens from Aryan et al. (2022), and six specimens from Hutton

et al. (2023). It was shown that FRP strengthening was effective in increasing in-plane shear capacity of all 16 strengthened specimens. The typical failure mode of the strengthened specimens was FRP debonding followed by diagonal shear failure in the concrete, although anchorage failures, FRP rupture, and crushing of the compression strut also occurred. As FRP surface coverage increased, diaphragm ductility reduced while the shear strength contribution of the FRP increased. Configuring FRP in an orthogonal grid was more effective in increasing diaphragm shear strength relative to the same total quantity of FRP oriented parallel to applied shear. Variations in anchorage were also investigated and found to have little effect on diaphragm strength.

The database was used to refine and expand design recommendations for shear strengthening of reinforced concrete diaphragms with externally bonded FRP. Recommendations relevant to the shear strength contribution for varying orientations of FRP, reinforcement limits, and anchorage schemes were proposed. Existing recommendations from Hutton et al. (2023) relevant to FRP effective design strains and anchorage design were corroborated.

Additionally, the stringer-panel model (SPM) was investigated as an analytical technique for determining diaphragm demands. Direct comparisons between chord, collector, and diaphragm shear demands were made between the SPM and the equivalent beam model (EBM). In the one design example, the SPM demonstrated higher fidelity, capturing indirect load paths and more distributed demands in the diaphragm. Furthermore, the SPM offers a practical advantage as a single model can accommodate multiple load combinations while producing interpretable design demands for detailing steel reinforcement or externally bonded FRP retrofits.

EXPERIMENTAL AND ANALYTICAL EVALUATION OF FRP-RETROFITTED REINFORCED CONCRETE DIAPHRAGMS FOR IN-PLANE SHEAR STRENGTHENING

Henry W. McKlin

GENERAL AUDIENCE ABSTRACT

Reinforced concrete diaphragms are essential in ensuring the stability of buildings during earthquakes and other lateral load events. Diaphragms are the floors and roof of a building that act to transfer lateral loads and provide bracing to the walls and columns. However, many existing buildings were designed before modern seismic codes were developed, and renovations can compromise their structural integrity, both of which make strengthening necessary. Traditional methods, such as adding a concrete overlay, can be labor intensive and increase the weight of the structure. Externally bonded fiber reinforced polymer (FRP) is a promising alternative due to its high strength, low weight, and ease of installation. While FRP has been studied extensively for use in other structural applications, there is limited research and no formal design guidance for its use in diaphragm strengthening. This study aims to both contribute to the range of available experimental data and assemble a database to evaluate the effectiveness of FRP in enhancing diaphragm shear capacity.

An experimental program was conducted to assess how different FRP configurations influence diaphragm performance. Eight diaphragm specimens were tested under cyclic loading, simulating earthquake-induced forces. A database of 19 diaphragm specimens was assembled and FRP orientation, configuration, and anchorage techniques were examined for their effect on shear strength in addition to other parameters that quantify seismic performance. The database confirmed that FRP strengthening is effective in increasing shear strength, though variations in FRP configuration, orientation, and anchorage influenced overall performance. Findings from this research contributed to the development of design recommendations for diaphragm shear strengthening with FRP, providing engineers with necessary tools for improving the safety and reliability of existing structures.

Dedication

To my grandfather, Elmer George Kuhlman, who always encouraged my curiosity.

Acknowledgments

Diaphragm Specimen CD7, CD8, CD9, CD10, CD11, and CD12 described in this thesis were supported by Simpson Strong-Tie. Specimen CD13 and CD14 described in this thesis were supported by Fyfe. The experimental test setup was made possible through the support of a consortium led by the Concrete Research Council of the American Concrete Institute Foundation, along with contributions from Simpson Strong-Tie, Structural Technologies, Fyfe, and GeoTree Solutions. Simpson Strong-Tie, Structural Technologies, Fyfe, and Banker Steel also provided in-kind funding. Additionally, this work was supported by the National Science Foundation (NSF) under Grant No. CMMI-2050030. Any opinions, findings, conclusions, or recommendations presented in this thesis are those of the author and do not necessarily represent the views of the NSF or any other sponsoring organization.

I am very grateful for the guidance and support of Dr. Matthew Eatherton and Dr. Eric Jacques throughout the duration of this research, in addition to Dr. Carin Roberts-Wollmann and Dr. David Mokarem who served on my advisory committee. Hunter Hutton and Ryan Stevens played a pivotal role in the development of the test setup described in this thesis. I would also like to acknowledge the contributions of my colleagues Pratiksha Dhakal, Ann Albright, Thomas Carnes, Avinash Jadhav, Omar Almasarani, and Jack Cross, whose insights and collaboration were invaluable. This research would not have been possible without the dedication of undergraduate research assistants Chloe Green, Raymond Bodnar, Jackson Keating, Joe Tramontano, and Celia McDermott. The expertise of Brett Farmer and Garrett Blankenship was instrumental during specimen construction. Finally, I am profoundly grateful for the unwavering support of my friends and family whose encouragement and companionship have kept me grounded throughout this journey.

I am thankful to have been awarded the Charles Via M.S. Fellowship from Virginia Polytechnic Institute and State University which provided financial support throughout my graduate studies.

Table of Contents

Chapter 1. Introduction

1.1. General

Diaphragms are a key component of the horizontal lateral force resisting system (hLFRS) in a reinforced concrete structure. When a structure is subjected to lateral loads, diaphragms transfer in-plane forces to the vertical lateral force resisting system (vLFRS). In addition to externally applied lateral loads, diaphragms may resist transfer forces due to varying vLFRS layouts over the height of the structure, column bracing forces, and lateral loads due to inclined columns (Moehle 2015). Typical diaphragm actions are shown in Figure 1-1(a). A diaphragm may include chords, which create a force couple to resist in-plane moment, as shown in Figure 1-1(b). A diaphragm also may include collectors, which collect in-plane diaphragm shear and transfer it to the vLFRS, as shown in Figure 1-1(c).

The deep beam analogy is a simple and commonly used analytical technique for establishing diaphragm demands, especially in buildings without transfer forces or major irregularities (CRSI 2019). The flow of internal stresses in the diaphragm is assumed to be analogous to a beam, where in-plane flexural resistance is provided by bundled reinforcement at the extreme tension fibers, as depicted by the chords in Figure 1-1(b). In-plane diaphragm shear is assumed to be constant along the diaphragm depth, and collector reinforcement is provided parallel to vLFRS elements that do not extend the full diaphragm depth to collect shear forces and transfer them to the vLFRS, as depicted in Figure 1-1(c). For a reinforced concrete diaphragm, the diaphragm is typically assumed to be rigid relative to the vLFRS elements, and seismic forces are established by applying lateral loads at the locations of mass (typically distributed throughout the diaphragm) and allowing rigid body rotation around the center of rigidity (CRSI 2019). Finally, the deep beam analogy can be applied to diaphragms with openings through the use of subdiaphragms located adjacent to the opening, where each subdiaphragm contains its own chords and collectors to provide sufficient load path around the opening (CRSI 2019).

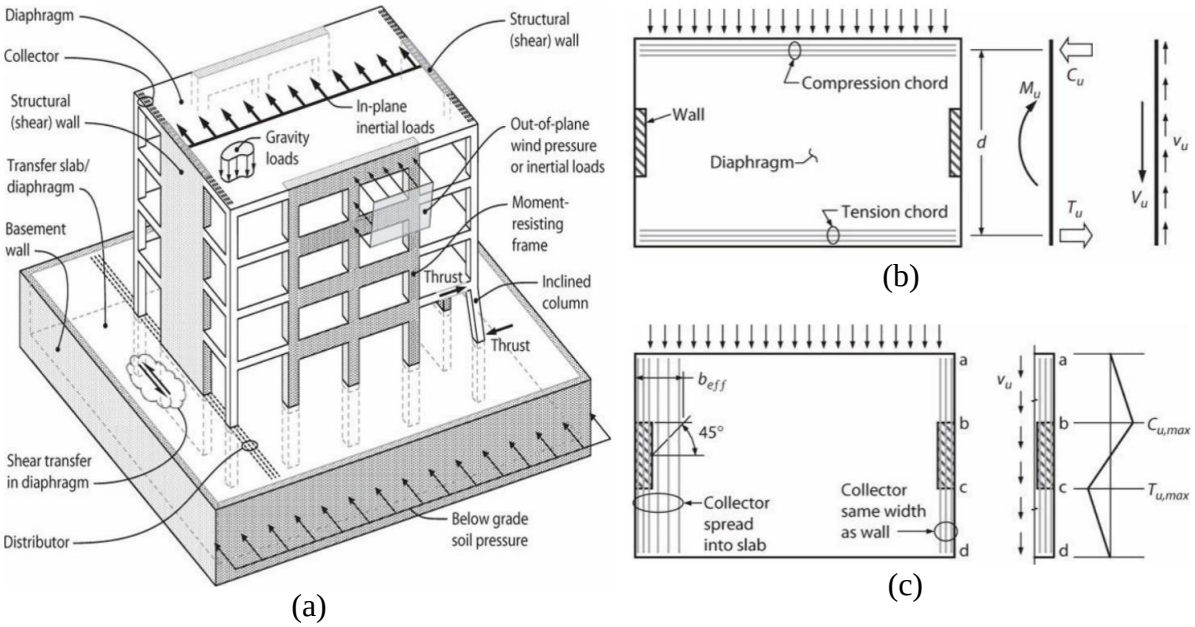

Figure 1-1. (a) Typical Diaphragm Actions in a Reinforced Concrete Structure; (b) Simplified Diaphragm Model Including Chords; (c) Simplified Collector Model [from (Moehle 2015)].

1.2. Motivation

Diaphragms may require retrofit due to many reasons, including the relocation of vLFRS elements during renovation, holes cut into the slab, or in older reinforced concrete structures that were designed according to outdated design codes (Hutton et al. 2023). Typical properties of older reinforced concrete structures include low strength concrete (less than 3000 psi compressive strength), thin slabs, Grade 40 steel reinforcement, and reinforcement detailing that does not meet current code specifications (Hutton et al. 2023). Some of the existing methods to strengthen reinforced concrete diaphragms include a concrete or shotcrete overlay system, or the concrete infilling of openings cut in the slab (FEMA 2006). These methods can increase the mass of the structure to the point where additional strengthening of the vLFRS or gravity system is necessary.

An alternative diaphragm retrofitting technique involves the application of externally bonded fiber reinforced polymer (FRP) to the diaphragm surface. This technique has several advantages over other diaphragm retrofitting techniques, as it is relatively quick to install, adds minimal weight to the structure, is noncorroding, and only increases the thickness of the diaphragm by the thickness of the laminate, typically less than 0.1 in. Over recent years, research

has been conducted to investigate the effectiveness of diaphragm strengthening with FRP, most notably the experimental programs described in Aryan et al. (2022) and Hutton et al. (2023). Although some design recommendations have emerged from these studies based on their individual sets of experiments, no prior study evaluated all the data together and the American Concrete Institute (ACI) is still working toward providing guidance on the application of FRP strengthening in diaphragms.

ACI PRC-440.2R-23 (2023) is the American Concrete Institute's *Guide for the Design and Construction of Externally Bonded FRP Systems for Strengthening Concrete Structures*. Because the research was not available at the time of its writing, no guidance on diaphragm shear strengthening was provided in the document. Therefore, engineers typically adopt equations for shear strengthening of reinforced concrete beams for diaphragm strengthening (Ormeno et al. 2019). This approach may be insufficient, as stress states, geometry, steel reinforcement configurations, and failure modes can differ between beams and diaphragms. Additionally, internal shear stresses in a beam are typically in one direction, while internal shear stresses in a diaphragm must be considered in a minimum of two directions. Consequently, some FRP strengthening schemes involve the application of two orthogonal layers of FRP sheets (Ormeno et al. 2019), which is a configuration that was not considered in the fundamental study (Khalifa et al. 1998) that the guidance in ACI PRC-440.2R-23 (2023) was developed from.

Research gaps were identified and discussed in a workshop described in Dhakal et al. (2022). Industry experts confirmed that design expressions for beams, walls, and slabs are often used for diaphragm strengthening although they do not accurately represent diaphragm behavior. Carbon FRP (CFRP) was identified as the most commonly used material for diaphragm strengthening, and that the utilized fabric is typically unidirectional. FRP anchorage was identified as highly proprietary, with some industry professionals determining anchorage spacing using a strut-and-tie approach. Discussion regarding the design effective FRP strain indicated that it is typically limited to 0.0015 to maintain aggregate interlock in the concrete. A research gap was identified regarding the use of orthogonal FRP sheets or inclined FRP sheets relative to the building axis, and some industry professionals indicated the steel

contribution is ignored if the steel and FRP are not oriented in the same direction (Dhakal et al. 2022).

The work described in this thesis is part of a broader reinforced concrete diaphragm initiative at Virginia Polytechnic Institute and State University. The first phase of experimental testing (see Hutton et al. 2023) involved the development of a novel experimental program that demonstrated the effectiveness of FRP strengthening to increase shear strength. Design recommendations were proposed after the first phase of experimental testing and are summarized in Section 2.3.2. Additionally, the experimental results from the first phase were used by Dhakal (2025) to validate a finite element model. The motivation behind the development of this finite element model was to better understand the interaction between reinforcing steel, FRP, and concrete in addition to topology optimization and the ability to model larger, more complex diaphragms. Although the tests described in the experimental program of this thesis were not used to validate the finite element model, they served to help understand the effectiveness and failure modes of heavily strengthened specimens with and without lightweight concrete (LWC), varying anchor types, and fiber orientations that were not parallel to internal steel reinforcement. The six specimens from the first phase featured comparatively less FRP relative to the experimental program described in this thesis, and did not include specimens strengthened with an orthogonal grid of FRP. Finally, the results of this experimental program were used to inform the team in developing a larger, 3-bay, simply supported specimen (Dhakal 2025), validating a stringer-panel model (SPM) for predicting specimen capacity, and improving upon the design recommendations presented in Hutton et al. (2023).

Whether designing new construction or retrofitting an existing structure, it is crucial to have sufficient methods for determining diaphragm demands. ACI 318 (2019) R12.1.1 states "When subject to lateral loads … a diaphragm acts essentially as a beam spanning horizontally between elements of the lateral-force-resisting system". However, synonymizing beams to diaphragms requires a stark oversimplification of diaphragm behavior. While beams typically have a consistent cross section across their length, diaphragms can be irregularly shaped with re-entrant corners and openings, potentially leading to stress concentrations not usually seen in beams. ACI 318 (2019) allows the use of a strut-and-tie model (STM) and a finite element model (FEM) for determining diaphragm demands. However, using a STM to design a

diaphragm can be a cumbersome procedure as a separate STM must be created for each load combination and direction. While the use of a FEM in diaphragm design is the most commonly used method in practice, it can be computationally expensive and difficult to interpret the results into diaphragm demands (Godínez et al. 2023, Godínez et al. 2024).

The SPM is an alternative analytical method for determining diaphragm demands. The linear SPM discretizes a reinforced concrete planar element (such as a diaphragm) into stringers that experience pure axial stress and panels that experience pure shear stress. The SPM could be an attractive alternative to the STM and the FEM as it is computationally efficient (only a linear analysis is necessary for determining demands), well discretized, and the output is clearly interpretable design demands that can be used to detail reinforcement.

1.3. Objectives

The objectives of this research involved investigating the performance of FRP strengthening of reinforced concrete diaphragms and exploring the application of the SPM for determining reinforced concrete diaphragm demands. To investigate the performance of FRP diaphragm strengthening, an experimental program consisting of eight specimens was conducted and then an experimental data base of nineteen diaphragm specimens was assembled. Debonding strains and FRP shear capacity contributions were investigated as a function of FRP material, orientation, and configuration. The effectiveness of two layers of orthogonal FRP sheets was also explored. Additionally, the effectiveness of fiber splay anchors and anchor plate systems were compared, in addition to the effectiveness of end and intermediate anchorage. Finally, the application of existing limits on shear reinforcement was explored. The overall objective of assembling this database was to improve design recommendations for reinforced concrete diaphragm FRP shear strengthening. In addition to developing design recommendations, the SPM was investigated as an alternative analytical method for determining diaphragm demands with the objective of proposing an analytical method that, compared to a typical beam model, better captures the internal stress states in a reinforced concrete diaphragm.

1.4. Scope

The scope of this research program was as follows:

1. Conducted experimental testing of six reinforced concrete cantilever diaphragm specimens and documented another two specimens, for a total of eight specimens. One specimen served to establish a baseline for LWC, while the remaining seven specimens were strengthened with varying configurations of FRP and mechanical anchorage.

2. Assembled a database of 19 diaphragm specimens and investigated how variations in FRP material, width, spacing, orientation, anchorage, and orthogonal layering effected stiffness, strength, FRP debonding strains, ductility, and limits on shear reinforcement. The analysis of this data base was used to develop design recommendations and propose revisions to ACI PRC-440.2R-23 (2023).

3. Analyzed a reinforced concrete diaphragm design example presented in the Concrete Reinforcing Steel Institute's (CRSI) *Design Guide for Reinforced Concrete Diaphragms* using the SPM. Comparisons between design demands were made between the SPM and the equivalent beam model (EBM) used in the design guide to highlight key differences between the two analytical methods.

1.5. Thesis Organization

Chapter 1 presents the primary motivation and objectives of the research project. Chapter 2 provides a review of relevant experimental programs and analytical methods for determining demands. Chapter 3 presents the FRP strengthening test matrix in addition to specimen details, instrumentation schemes, and construction and testing processes. Chapter 4 presents experimental results of the eight cantilever diaphragm specimens included in the experimental program. Chapter 5 presents the analysis of a data base of nineteen diaphragm specimens, which is discussed in Chapter 6. Chapter 7 presents an overview of the SPM using a side-by-side example from the CSRI (2019) design guide. Chapter 8 summarizes key findings and design recommendations.

Chapter 2. Literature Review

2.1. Overview

This chapter contains a review of literature relevant to reinforced concrete diaphragm strengthening with externally bonded FRP. To effectively strengthen reinforced concrete diaphragms, it is imperative to have confidence in predicting both their capacity and demands. Current guidelines for predicting capacity in ACI PRC-440.2R-23 (2023) and ACI 318 (2019) are reviewed in Section 2.2. Literature on experimental programs exploring the efficacy of reinforced concrete diaphragm strengthening with externally bonded FRP is reviewed in Section 2.3. Typical methods for quantifying diaphragm design demands are reviewed in Section 2.3.2. An alternative method for predicting both demand and capacity, the SPM, is also reviewed in Section 2.3.2.

2.2. Current Guidelines for Shear Strengthening

ACI PRC-440.2R-23 (2023) is the American Concrete Institute's *Guide for the Design and Construction of Externally Bonded FRP Systems for Strengthening Concrete Structures*. The guide discusses the advantages of FRP systems, including their ease of installation, light weight, and noncorroding properties, in addition to specific guidance on the use of these systems in various applications (ACI PRC-440.2R-23 2023). Chapter 11 of ACI PRC-440.2R-23 (2023) provides guidance on shear strengthening of reinforced concrete beams and columns but provides no guidance on diaphragm shear strengthening. A paper presented at the 2019 Pacific Conference on Earthquake Engineering, Ormeno et al. (2019), noted that despite the lack of diaphragm-specific guidance, Chapter 11 of ACI PRC-440.2R-23 (2023) is still used in the design of retrofit schemes for reinforced concrete diaphragms. Eq. (1) can be used to calculate the shear capacity of a reinforced concrete member strengthened with externally bonded FRP.

$$V_n = V_c + V_s + \psi_f V_f \tag{1}$$

where: V_n is the nominal shear capacity (lbs); V_c is the concrete contribution to shear capacity (lbs); V_s is the internal reinforcing steel contribution to shear capacity (lbs); ψ_f is a reduction

factor based on the wrapping scheme; and V_f is the FRP contribution to shear capacity (lbs). This equation implies the debonding or rupture of the FRP occurs while the internal steel reinforcement is yielding.

ACI PRC-440.2R-23 (2023) references ACI 318 (2019) to determine the concrete contribution to shear capacity. Eq. (2) can be used.

$$V_c = A_{cv} 2\lambda \sqrt{f_c'} \tag{2}$$

where: V_c is the concrete contribution to shear capacity (lbs); A_{cv} is the gross concrete section (in.^{2}); λ is the LWC reduction factor; and f_c' is the concrete compressive strength (psi).

ACI PRC-440.2R-23 (2023) also references ACI 318 (2019) to determine the internal steel reinforcement contribution to shear capacity. Eq. (3) can be used.

$$V_s = A_{cv} \rho_t f_y \tag{3}$$

where: V_s is the internal reinforcing steel contribution to shear capacity (lbs); A_{cv} is the gross concrete section (in.^{2}); ρ_t is the area ratio of internal steel reinforcement parallel to the direction of in-plane shear; and f_y is the yield stress of the internal steel reinforcement (psi). Additionally, steel oriented perpendicular to in-plane shear is not considered to have an effect on shear capacity.

The FRP contribution to shear capacity can be calculated using Eq. (4), originally presented in Triantafillou (1998) and adjusted to fit ACI code format in Khalifa et al. (1998).

$$V_f = \frac{A_{fv} f_{fe} (\sin\alpha + \cos\alpha) d_{fv}}{s_f} \tag{4}$$

where: V_f is the FRP contribution to shear capacity (lbs); A_{fv} is the area of effective FRP (in.^{2}); f_{fe} is the effective stress in the FRP (psi); α is the orientation of FRP reinforcement relative to the longitudinal axis of the member (degrees); d_{fv} is the effective depth of the diaphragm (in.); and s_f is the center-to-center spacing of FRP sheets (in.). Unlike for steel, the equation for shear capacity contribution from FRP provides the same contribution for FRP strips oriented perpendicular and parallel to in-plane shear.

To determine the shear capacity contribution of FRP, an effective stress must be calculated. Because FRP is typically linear elastic, the effective stress is directly proportional to the effective strain in the FRP. Eq. (5) can be used.

$$f_{fe} = E_f \varepsilon_{fe} \tag{5}$$

where: f_{fe} is the effective stress in the FRP (psi); E_f is the elastic modulus of the FRP (psi); and ε_{fe} is the effective strain in the FRP.

ACI PRC-440.2R-23 (2023) provides two equations for the effective strain in the FRP: one associated with FRP rupture and one associated with debonding of the FRP. Because diaphragm retrofits do not typically enclose the entire section, ACI PRC-440.2R-23 (2023) indicates that Eq. (6) should be used as FRP in unenclosed retrofits typically debonds prior to the loss of aggregate interlock in the concrete.

$$\varepsilon_{fe} = \kappa_t \varepsilon_{fu} \leq 0.004 \tag{6}$$

where: ε_{fe} is the effective strain in the FRP; κ_t is the bond-reduction coefficient for shear; and ε_{fu} is the ultimate fiber strain in the FRP.

The calculation procedure for the bond-reduction coefficient is adopted from bond mechanism equations presented in Khalifa et. al (1998), where researchers applied experimental data on direct tension tests of concrete-bonded FRP (Maeda et al. 1997) to calibrate an equation for the reduction in effective stress associated with the debonding failure mode. According to Khalifa et al. (1998), the bond-reduction coefficient is affected by the concrete strength, the FRP configuration and the stiffness of the FRP laminate. The bond-reduction coefficient can be calculated using Eq. (7).

$$\kappa_t = \frac{k_1 k_2 L_e}{468 \varepsilon_{fu}} \leq 0.75 \tag{7}$$

where: κ_t is the bond-reduction coefficient for shear; k_1 is the concrete strength modification factor; k_2 is the wrapping scheme modification factor; L_e is the active bond length (in.); and ε_{fu} is the ultimate fiber strain in the FRP.

The active bond length refers to the length over which bond stresses are maintained (ACI 2019). An active bond length, as opposed to the total bonded length, is used because FRP debonding typically propagates progressively from the loading point. For an idealized FRP strip in pure tension, debonding first occurs due to concrete cracking near the loading point. As debonding occurs, the active bond length shifts down the total bonded length of the FRP sheet until the entire sheet debonds (Khalifa et al. 1998). The active bond length can be calculated using Eq. (8).

$$L_e = \frac{2500}{\left(nt_f E_f\right)^{0.58}} \tag{8}$$

where: L_e is the active bond length (in.); n is the number of layers of FRP sheets; t_f is the thickness of the FRP laminate (in.); and E_f is the tensile modulus of the FRP (psi).

The concrete strength modification factor can be calculated using Eq. (9).

$$k_1 = \left(\frac{f_c'}{4000}\right)^{\frac{2}{3}} \tag{9}$$

where: k_1 is the concrete strength modification factor; and f_c' is the compressive strength of the concrete (psi).

The wrapping scheme modification factor can be calculated using Eq. (10).

$$k_2 = \begin{cases} \dfrac{d_{fv} - L_e}{d_{fv}} \; for\; U-wraps \\ \dfrac{d_{fv} - 2L_e}{d_{fv}} \; for\; two\; sides\; bonded \end{cases} \tag{10}$$

where: k_2 is the wrapping scheme modification factor; L_e is the active bond length (in.); and d_{fv} is the effective depth of FRP shear reinforcement (in.). As diaphragm retrofits are typically one-sided, the equation for U-wraps is typically used for diaphragm retrofits. Additionally, Hutton et al. (2023) recommended that the k_2 term should be equal to 1.0 for diaphragm retrofits as the bonded length, L_e, is typically much smaller than the effective depth of the FRP shear reinforcement, d_{fv}.

In addition to guidance on the FRP contribution to shear strength, ACI PRC-440.2R-23 (2023) also provides guidance on spacing of FRP strips. ACI PRC-440.2R-23 (2023) references ACI 318 (2019) by stating that the limits prescribed therein for internal steel reinforcement spacing should be adopted for FRP strip spacing. The maximum spacing is given in ACI 318 (2019) section 12.7.2.2 and summarized in Eq. (11).

$$s_{max} = min\begin{cases}5t_{dia}\\ 18"\end{cases} \tag{11}$$

where: s_{max} is the maximum center-to-center spacing of internal steel reinforcement (in.); and t_{dia} is the diaphragm slab thickness (in.).

ACI PRC-440.2R-23 (2023) also provides a limit on the shear strength provided by steel reinforcement and FRP, shown in Eq. (12).

$$V_s + V_f \leq 8\sqrt{f_c'}b_w d \tag{12}$$

where: V_s is the internal reinforcing steel contribution to shear capacity (lbs); V_f is the FRP contribution to shear capacity (lbs); f_c' is the compressive strength of the concrete (psi); b_w is the minimum width of cross section over the effective depth (in.); and d is the effective depth of the cross section (in.).

A limit on the nominal shear strength of a diaphragm is presented in ACI 318 (2019) Clause 12.5.3.4, as shown in Eq. (13).

$$V_n \leq 8\sqrt{f_c'}A_{cv} \tag{13}$$

where: V_n is the nominal shear capacity (lbs); f_c' is the concrete compressive strength (psi); and A_{cv} is the gross area of the concrete bounded by the diaphragm wed thickness and depth, reduced by void areas if present (in.^{2}).

Chapter 13 of ACI PRC-440.2R-23 (2023) provides guidance on seismic strengthening with externally bonded FRP. Although diaphragms are not explicitly mentioned, Ormeno et al. (2019) stated that provisions for other structural elements, such as shear walls, are often adopted for diaphragms. Section 13.7.3 of ACI PRC-440.2R-23 (2023) provides guidance on shear wall strengthening with FRP, summarized in Eq. (14).

$$V_f = \begin{cases} 2t_f \varepsilon_{fe} E_f d_{fv} \; for\; a\; two - sided\; retrofit \\ 0.75 t_f \varepsilon_{fe} E_f d_{fv} \; for\; a\; one - sided\; retrofit \end{cases} \quad (14)$$

where: V_f is the FRP contribution to shear capacity (lbs); t_f is the thickness of the FRP laminate (in.); ε_{fe} is the effective strain in the FRP; E_f is the tensile elastic modulus of the FRP (psi); and d_{fv} is the effective depth of the diaphragm (in.).

Additionally, Chapter 13 of ACI PRC-440.2R-23 (2023) provides a limit on the maximum nominal shear strength of a wall segment, as shown in Eq. (15).

$$V_n \leq 10\sqrt{f_c'} A_{cw} \quad (15)$$

where: V_n is the nominal shear capacity including the contribution of shear strength from the FRP (lbs); f_c' is the concrete compressive strength (psi); and A_{cw} is concrete section area of an individual vertical wall (in.^{2}).

2.3. Relevant Experimental Programs

There is limited literature on experimental programs containing reinforced concrete diaphragm specimens strengthened with externally bonded FRP. This section reviews two experimental programs: Aryan et al. (2022) and Hutton et al. (2023). The experimental program described in Chapter 3 of this thesis is a continuation of the experiments described in Hutton et al. (2023).

2.3.1 Aryan et al. (2022)

The experimental program described in Aryan et al. (2023) contained four diaphragm specimens strengthened with FRP and one control specimen. Of the four strengthened specimens, two were strengthened with glass fiber reinforced polymer (GFRP) and two were strengthened with carbon fiber reinforced polymer (CFRP). One of the specimens strengthened with GFRP was strengthened on both sides of the diaphragm slab, while the remaining strengthened specimens had FRP on one side only. All FRP plies were oriented parallel to the direction of applied shear, and the ply coverage was relatively low, ranging from 12.5% coverage for the CFRP strengthened specimens to 25% for the GFRP specimens. Anchorage of

the FRP sheets was provided by wrapping the ends of the sheets around the edges of the slab, providing excellent anchorage, though this is often not feasible in the field (Aryan et al. 2022).

The test setup used by Aryan et al. (2022) is shown in Figure 2-1. Each specimen was subject to cyclic, in-plane, three-point bending. As opposed to the test setup described in Hutton et al. (2023) and this thesis, the specimens in Aryan et al. (2022) were oriented vertically (perpendicular to a typical diaphragm plane).

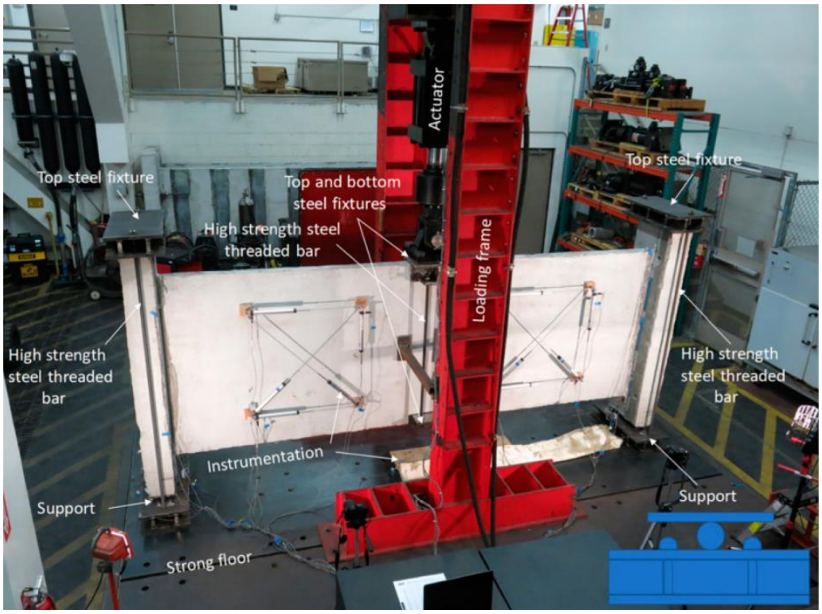

Figure 2-1. Test Setup Designed by Aryan et al. [From (Aryan et al. 2022)].

All strengthened specimens withstood higher loads in both push and pull directions, in addition to greater energy dissipation. The application of FRP strengthening was shown to increase the peak applied load between 25% and 40% and shown to increase energy dissipation between 59% and 132%, relative to the control specimen. The control, Specimen 3-0, failed through diagonal shear cracking in the concrete, while all retrofitted specimens except for Specimen 3-G-2 failed through FRP debonding followed by concrete diagonal shear. Specimen 3-G-2 failed through concrete crushing under the loading point. Aryan et al. (2022) refers to this type of failure as a local failure mode which prevented the specimen from reaching its peak shear capacity. Additionally, Aryan et al. (2022) suggested that the enhanced energy dissipation in GFRP-strengthened specimens was due to the greater width of the GFRP sheets compared to CFRP sheets. However, they also noted that the increased width decreased ductility.

Envelope curves for the experiments described in Aryan et al. (2022) are presented in Figure 2-2. All strengthened specimens experienced an increase in initial stiffness, while all specimens except Specimen 3-G-2 experienced an increase in ductility in both push and pull directions. It was hypothesized that the reduced ductility in Specimen 3-G-2 compared to other strengthened specimens was due to the higher yield point of GFRP specimens (Aryan et al. 2022).

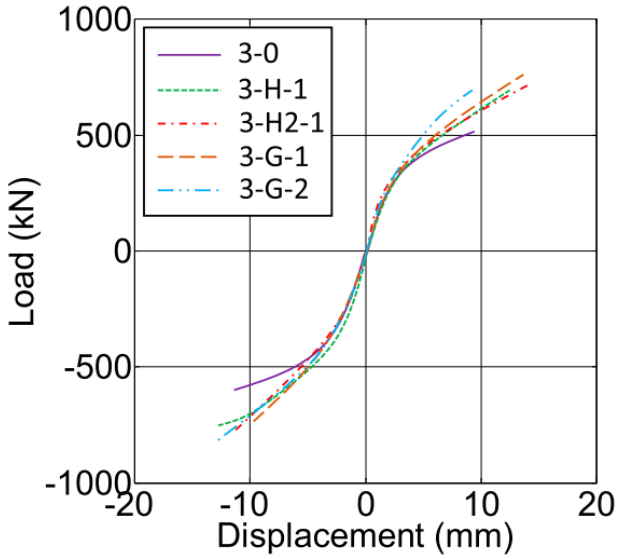

Figure 2-2. Load Versus Mid-Span Displacement Envelope Curves [From (Aryan et al. 2022)].

The experiments described in Aryan et al. (2022) also included strain gages on the reinforcing steel and FRP. All strengthened specimens experienced reduced strains (50% to 75% reduction) in the reinforcing steel relative to the control specimen due to the contribution of FRP to shear reinforcement. FRP strains in the CFRP-strengthened specimens were limited to 0.5%, while FRP strains in the GFRP-strengthened specimens were limited to 0.75%. Higher strains in the GFRP-strengthened specimens were attributed to the lower modulus of elasticity of GFRP compared to CFRP (Aryan et al. 2022).

Additionally, Aryan et al. (2022) compared their experimental results to the shear wall strength calculations in ACI PRC-440.2R-23 (2023) displayed in Eq. (14). They found the strength calculations to be conservative by 14% to 33% relative to their experimental results, with a higher level of conservatism in strengthened specimens relative to the control specimen (Aryan et al. 2022).

2.3.2 Hutton et al. (2023)

The experimental program described in Hutton et al. (2023) contained five diaphragm specimens strengthened with FRP and one control specimen. The test matrix is shown in Table 2-1. Of the five strengthened specimens, four were strengthened with CFRP while one was strengthened with GFRP. All strengthened specimens were strengthened on one side only, and mechanical anchorage was provided by fiber splay anchors. The experimental program studied variations in FRP type and configuration, FRP sheet orientation, and splay anchor layout, while maintaining an FRP axial stiffness near 4000 kips/in/in for all strengthened specimens. Concrete compressive strength varied between 3600 psi and 4800 psi, while the internal steel reinforcement, two layers of Grade 75 D5 deformed wire at 12 in. on center (O.C.), remained constant for all specimens (Hutton et al. 2023).

Table 2-1. FRP Strengthening Test Matrix [From (Hutton et al. 2023)].

Specimen ID	FRP Material	FRP Ply Configuration					FRP Anchor Configuration			Design
		Composite Modulus, E_f (ksi)	Thickness, t_f (in.)	Width, w_f (in.)	Spacing, s_f (in.)	Orientation, α (deg.)	Layout	Diameter (in.)	Anchors Per Sheet	Axial Stiffness, K_f (kip/in./in.)
CD1	N/A	N/A	N/A	N/A	N/A	N/A	N/A	N/A	N/A	N/A
CD2	VWrap C100HM, CFRP	16700	0.02	12.0	24	90	End only	0.5	2	4008
CD3	Tyfo SCH-11UP, CFRP	13900	0.02	14.5	23.2	90	Int. + End	0.75	4	4031
CD4	Tyfo SEH-51A, GFRP	3730	0.05	21.0	21	90	End only	0.5	4	3917
CD5	VWrap C200HM, CFRP	14240	0.04	7.0	25.7	90	End only	0.75	2	3987
CD6	VWrap C100HM, CFRP	16700	0.02	12.0	24	0	Int. + End	0.75	4	4008

The test setup is shown in Figure 2-3 and was developed based on the experimental program described in Nakashima et al. (1981). Each specimen was subject to cyclic loading at the free end following the quasi-static guidelines in FEMA 461 (2007) (Hutton et al. 2023).

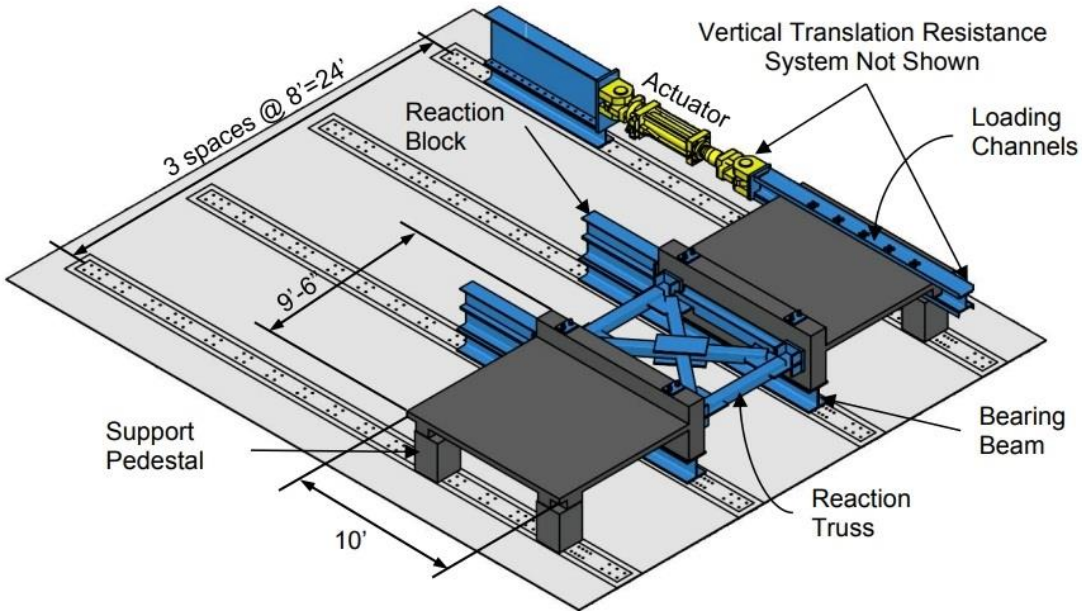

Figure 2-3. Test Setup Used by Hutton et al. [From (Hutton et al. 2023)].

Envelope curves for the six specimens are presented in Figure 2-4. The control specimen (Specimen CD1) failed due to diagonal tension cracking, while all strengthened specimens failed due to FRP debonding caused by diagonal tension cracking. All strengthened specimens experienced an increase in shear strength and post-cracking stiffness. The average increase in shear strength amongst the strengthened specimens was 27% relative to Specimen CD1. Although the pre-cracking stiffness was similar between all specimens, the cracking strength was on average 85% higher in strengthened specimens relative to Specimen CD1 (Hutton et al. 2023).

Additionally, the effect of FRP strengthening on diaphragm ductility was investigated. It was found that FRP strengthening parallel to applied shear has little effect on diaphragm ductility. Although the yielding shear angle and critical shear angle were reduced due to additional stiffness from FRP strengthening, the ductility ratios were similar between all specimens except for Specimen CD6, which had FRP sheets installed perpendicular to applied shear. Specimens CD3 and CD6 were compared to investigate the effect of orientation on strength and ductility. Experimental results from Specimen CD6 suggest that FRP strengthening perpendicular to applied shear increases strength by approximately 75% relative to the same retrofit oriented parallel to applied shear. The increase in ductility for Specimen CD6 was

attributed to improved flexural behavior of the diaphragm specimen due to FRP sheets oriented in the same direction as longitudinal internal steel reinforcement (Hutton et al. 2023).

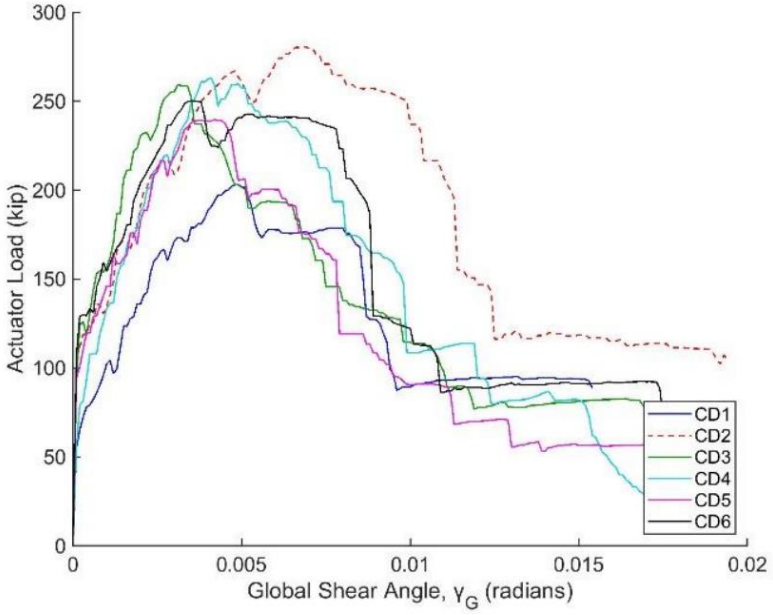

Figure 2-4. Load Versus Global Shear Angle Envelope Curves [From (Hutton et al. 2023)].

Hutton et al. (2023) also investigated the debonding strains of the FRP sheets used on the strengthened specimens. Six strain gages were placed on the FRP for each specimen, typically towards the center of the two interior FRP sheets. The experimental debonding strains recorded by the strain gages were compared against strains back calculated by removing steel, concrete, and frame action contributions to find the experimental FRP shear contribution and solving for ε_{fe} using Eq. (4) and Eq. (5). These back calculated strains are referred to as the estimated FRP debonding strain. Additionally, estimated and experimental debonding strains were compared against the design strain following the methodology in ACI PRC-440.2R-23 (2023) presented in Section 2.2. A summary of the FRP strain analysis is presented in Table 2-2. The design strain was found to underpredict the experimental debonding strain by an average of 18% (Hutton et al. 2023).

Table 2-2. Summary of FRP Strain Analysis [From (Hutton et al. 2023)].

Specimen ID	Estimated FRP Debonding Strain, $\varepsilon_{f,exp}$ (%)	Experimental FRP Debonding Strain, $\varepsilon_{f,SG}$ (%)	Design Strain, $\kappa_v \varepsilon_{fu}$ (%)	$\frac{\kappa_v \varepsilon_{fu}}{\varepsilon_{f,SG}}$
CD2	0.48	0.37	0.35	0.95
CD3	0.47	0.45	0.34	0.75
CD4	0.44	0.47	0.42	0.90
CD5	0.32	0.36	0.24	0.66
CD6	0.42	0.42	0.35	0.83
			Average	0.82
			COV	0.14

Additionally, Hutton et al. (2023) investigated the effects of FRP surface coverage and anchorage scheme. Increasing surface coverage from 33% to 100% was found to increase the shear strength provided by FRP by a factor of 1.625, with negligible effect on ductility. This increase was attributed to enhanced crack restraint associated with higher surface coverage, reducing the loss of aggregate interlock and delaying FRP debonding. End FRP anchors were found to prevent debonding at the end of the FRP sheets prior to intermediate crack debonding. Intermediate FRP anchors were found to have a negligible effect on the FRP shear strength contribution, and in some cases lead to stress concentrations in the diaphragm field causing the underlying structure to become the limiting factor (Hutton et al. 2023).

Finally, Hutton et al. (2023) provided several design recommendations based on the results of their experimental program. The design recommendations are summarized as follows:

1. The FRP strength reduction factor, Ψ_f, was recommended to be taken as 0.75 for one-sided diaphragm strengthening.

2. FRP sheets placed perpendicular to applied shear were recommended to be conservatively ignored, adopting ACI 318 (2019) provisions for reinforcing steel perpendicular to applied shear.

3. The effective design strain was recommended to be calculated following Eq. (6) through (10), with the exception that $k_2 = 1.0$ for one-sided diaphragm strengthening.

4. Mechanical anchorage was recommended at the ends of the FRP sheets or at the effective depth of the FRP sheets, whichever is less. FRP anchors were recommended to be designed to develop 1.5 times the tensile capacity of the FRP sheet being anchored.

5. Mechanical anchorage was recommended intermediately in the field of the diaphragm to mitigate debonding but should be designed to fail before the end anchors and after debonding of the FRP laminate. It was recommended that intermediate anchors be designed to develop 0.5 times the tensile capacity of the FRP sheet being anchored, and that intermediate FRP anchors be spaced no more than 9 feet apart.

6. The limit on total steel and FRP reinforcement presented in Eq. (12) was recommended to be sufficient for one-sided diaphragm retrofits.

7. The clear spacing between strips was recommended to not exceed three times the diaphragm thickness to limit crack widths and delay debonding.

2.4. Analytical Methods for Determining Demand

To sufficiently design a diaphragm, it is imperative to have robust methods not only for determining capacity, but also in determining axial, moment, and shear demands. Section 12.4.2.4 of ACI 318 (2019) provides five methods for determining required moment, shear, and axial forces:

1. A rigid diaphragm model if the diaphragm can be idealized as rigid.

2. A flexible diaphragm model if the diaphragm can be idealized as flexible.

3. A bounding analysis in which both rigid and flexible diaphragm idealizations are considered.

4. Finite element modeling.

5. Strut-and-tie modeling.

Methods 1 through 3 are typically used in conjunction with an EBM and are commonly used analytical methods for determining diaphragm demands in buildings without major

irregularities or transfer forces (CRSI 2019). In the case of reinforced concrete diaphragms, rigid diaphragm analysis and the EBM are commonly used and assume a constant in-plane shear demand along the depth of the diaphragm (Fanella 2018). However, irregularities such as re-entrant corners and openings in the slab can often justify more advanced analytical techniques, such as methods 4 and 5 (CSRI 2019).

Godínez et al. (2023) noted that the strut-and-tie model (STM) is generally not used for diaphragms in design practice due to difficulties in considering various load combinations, each of which requires its own STM, in addition to difficulties detailing nodal zones for each load combination and direction. Furthermore, standards for the discretization of a STM often lack robustness, leaving the design engineer responsible with determining a sufficient layout of struts, ties, and nodes.

Conversely, Godínez et al. (2023) noted that the finite element model (FEM) is the most widely used analytical method in current practice. As diaphragms are typically designed to remain linear (ACI 2019), a diaphragm modeled with linear finite elements is generally sufficient for inclusion in a structural model. FEM for reinforced concrete diaphragms typically consist of linear shell elements (Godínez et al. 2024). Key challenges with FEM are that it is computationally expensive, and the output is difficult to interpret into clear design demands (Godínez et al. 2023).

The need for a computationally efficient and well discretized analytical method with clearly interpretable design demands is met with the SPM. Originally developed to aid aeronautical engineers in analyzing large aircrafts constructed with metal sheets separated by ribs, the SPM has been adapted for use in analyzing planar concrete elements where Bernoulli beam theory does not apply (Godínez et al. 2023). For a detailed review of literature regarding the history of the SPM, see Godínez et al. 2023.

J. Blauuwendraad's *Stringer-Panel Models in Structural Concrete* (Blauuwendraad 2018) provides an excellent overview on the degrees of freedom, equilibrium equations, and solution techniques for the SPM in the context of reinforced concrete design. As the name suggests, a SPM consists of two types of structural members: one-dimensional members, *stringers*, that transfer normal stresses and two-dimensional members, *panels*, that transfer

shear stresses (Blauuwendraad 2018). A notable exception is in the case of a non-linear analysis, where normal forces are included in the panels to account for concrete dilation after cracking and the distributed panel steel reinforcement contributing to the axial strength of the panel (Hoogenboom 1998). As only the linear SPM is utilized in this thesis, panels are only considered to transfer shear stresses. A schematic of forces in stringers and panels is presented in Figure 2-5.

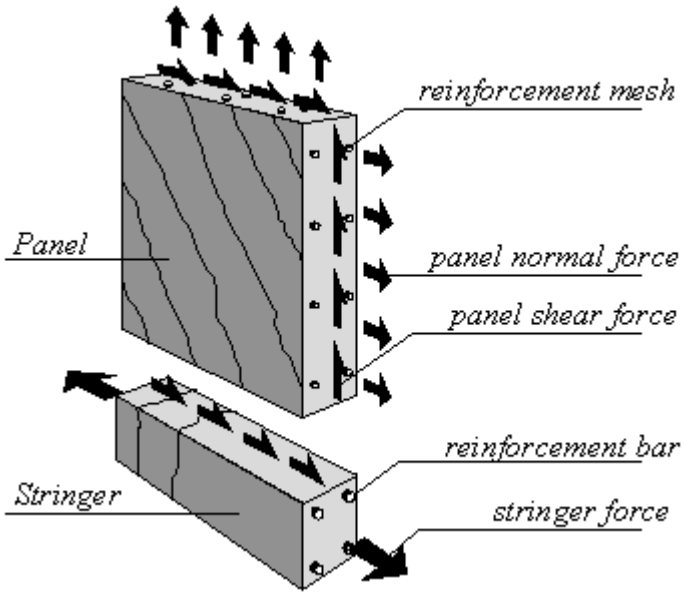

Figure 2-5. Schematic of Forces in Stringers and Panels [From (Hoogenboom 1998)].

The degrees of freedom associated with stringers and panels is presented in Figure 2-6. A stringer always has three degrees of freedom, one at each of the ends and one at the middle, which represents the average displacement along the length of the stringer. A panel has four degrees of freedom, one along each of its edges representing the average displacement along that panel edge. The degree of freedom at the middle of the stringer corresponds with the degree of freedom along its respective panel edge, ensuring compatibility between the two elements. The end degrees of freedom on the stringers ensure compatibility between connected stringers (Blauuwendraad 2018).

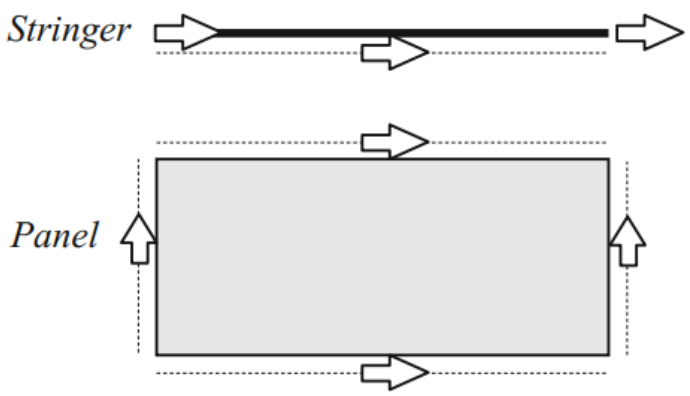

Figure 2-6. Degrees of Freedom for Stringers and Panels [From (Blauuwendraad 2018)].

Discretization of a structure into an SPM is well defined in Hoogenboom 1998. He writes "Stringers are drawn along edges, around holes, at supports and at concentrated loads. Panels are simply drawn in between the stringers." The design engineer does not need to make any assumptions about the flow of internal stresses in the structure to arrive at a sufficient model. This provides a clear advantage over STM, where the design engineer would have to anticipate areas of internal tension and compression in the structure for numerous load combinations and directions (Hoogenboom 1998).

In addition to a general overview of the SPM, J. Blauuwendraad's *Stringer-Panel Models in Structural Concrete* provides several design examples utilizing linear SPM analyses. Chapter 10 provides an example on the analysis of a diaphragm floor slab, the plan view of which is shown in Figure 2-7. The structure is discretized into a SPM as shown in Figure 2-8, where stringers are drawn along edges, around holes, and at supports. The seismic force distribution is shown in Figure 2-9. Seismic forces are applied at the stringers' middle degree of freedom, and are proportioned based on tributary area. The core walls and columns are idealized as springs. The extensional stiffness of the stringers and the shear stiffness of the panels is determined based on material properties of the concrete (Blaauwendraad 2018).

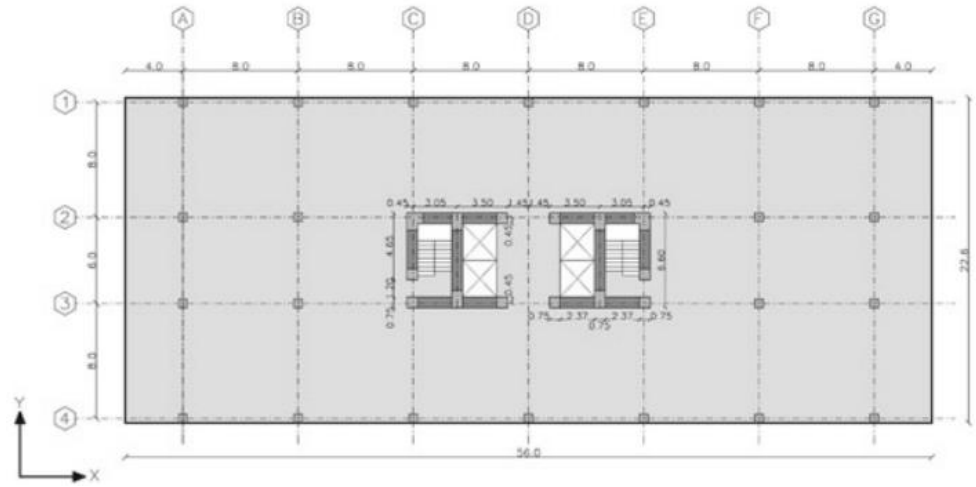

Figure 2-7. Plan View of Diaphragm Floor Slab [From (Blaauwendraad 2018)].

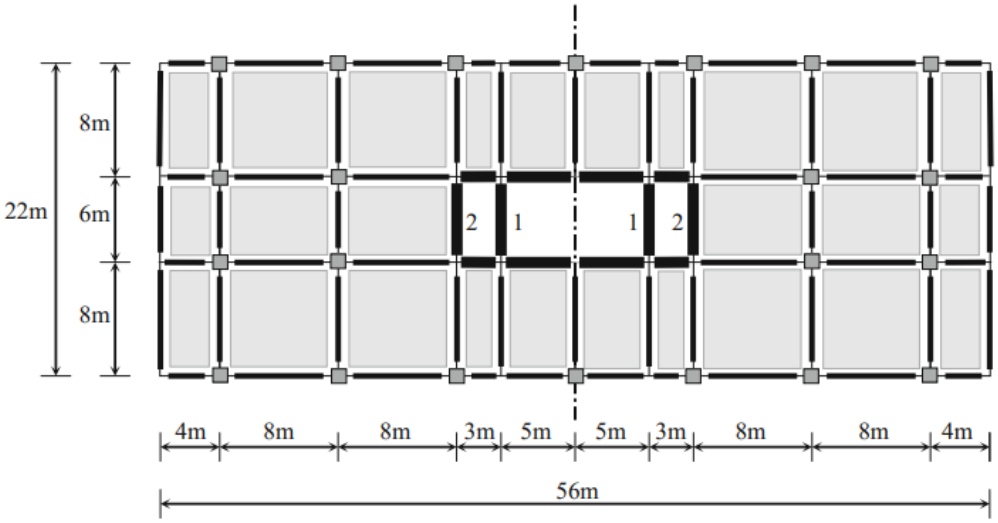

Figure 2-8. Schematic of Stringers and Panels in the Model [From (Blaauwendraad 2018)].

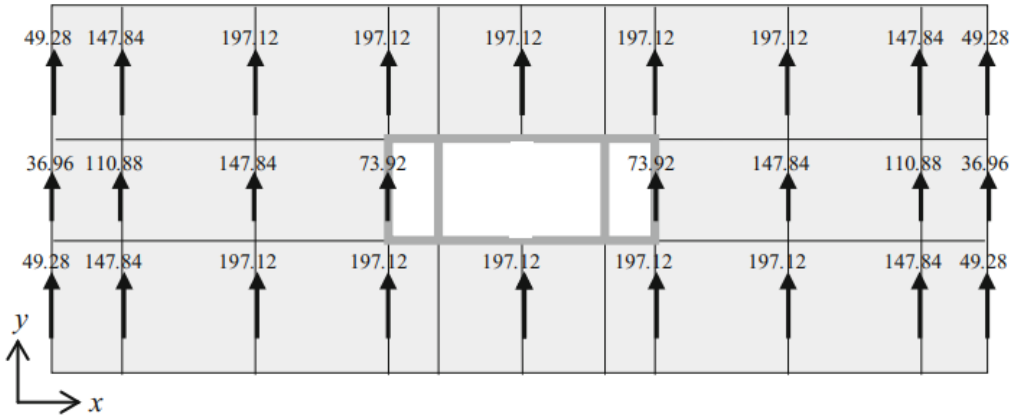

Figure 2-9. Seismic Forces in the Positive y-direction [From (Blaauwendraad 2018)].

Stringer forces from the linear SPM analysis are presented in Figure 2-10. Forces along stringers in the x-direction could be used to design chords in the diaphragm, while forces along the stringers in the y-direction could be used to design collectors to sufficiently transfer load to the core walls. Panel forces from the linear SPM analysis are presented in Figure 2-11. These panel demands could be directly used to detail internal steel reinforcement. The advantage over the deep beam analogy is that the SPM provides a more accurate representation of the flow of stresses in the diaphragm. Where the deep beam analogy assumes constant shear across the depth of the diaphragm, the SPM provides varying demand which may lead to a more efficient reinforcement configuration.

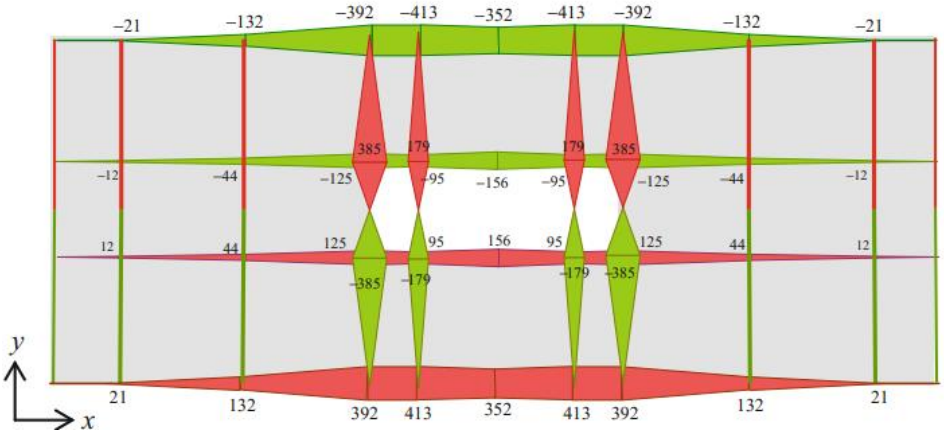

Figure 2-10. Stringer Forces (in kN) for Seismic Load in the Positive y-direction [From (Blaauwendraad 2018)].

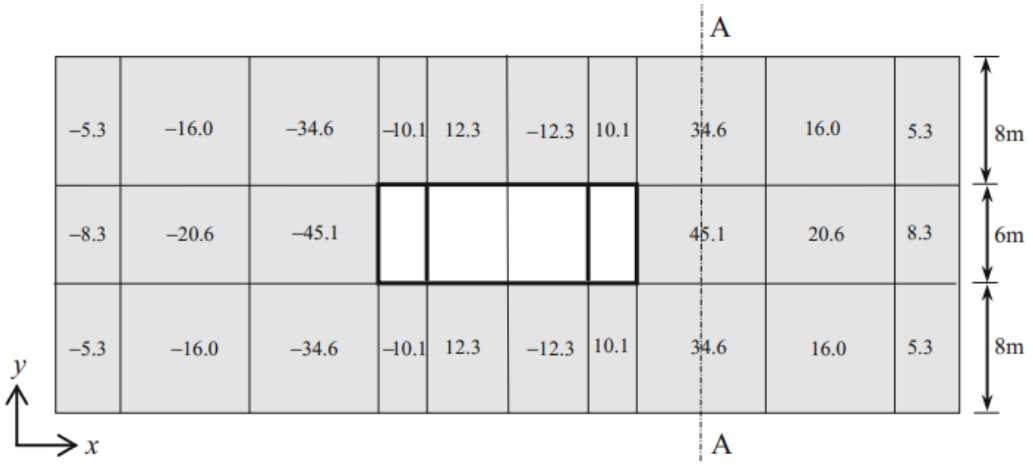

Figure 2-11. Panel Forces (in kN/m) for Seismic Load in the Positive y-direction [From (Blaauwendraad 2018)].

In addition to the SPM, other alternative analytical methods have been proposed for use in determining diaphragm demands. Notably, the truss method (also referred to as the grillage method) was proposed by Gardiner et al. (2011) and Scarry (2014). In the truss method, a planar concrete element (such as a diaphragm) is discretized into a lattice of axial only elements, as shown in Figure 2-12. The diagonal elements are limited to axial compression only, forcing tensile demands into the orthogonal members, allowing the tension to coincide with the typical directions of internal steel reinforcement. The truss model is a type of STM, but poses the advantage of not requiring multiple models for various load combinations and directions. However, the truss model is not as well discretized as the SPM, as the size of the grillage is a matter of engineering judgement.

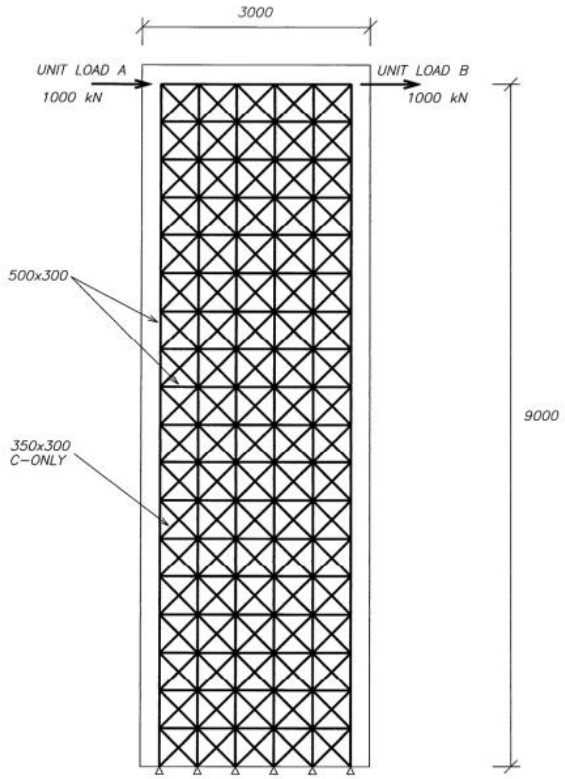

Figure 2-12. Truss Model for a Shear Wall (units in mm) [From (Scarry 2014)].

Chapter 3. Experimental Program

3.1. Overview

This experimental program consisted of eight cantilever reinforced concrete diaphragm tests. Two specimens, Specimen CD11 and CD12, were constructed with LWC, while the remaining six specimens were constructed with normal weight concrete (NWC). One of the specimens, Specimen CD11, was not strengthened with FRP to establish a baseline for LWC. All other tests described in this chapter were strengthened with varying arrangements of CFRP. A baseline NWC specimen was not included in this experimental program, because a similar specimen has already been tested and reported in Hutton et al. (2023). This chapter provides information on concrete, reinforcing steel, and FRP properties and arrangements for each specimen, in addition to loading protocols, specimen construction details, and instrumentation schemes.

3.2. Test Matrix

Isometric views from both the top and bottom of the diaphragm specimen are shown in Figure 3-1. Each specimen consisted of a 4 in. thick diaphragm slab measuring 10 ft in depth and 8 ft 6 in. in length. Each specimen was supported by two 10 in. by 10 in. chord beams and one 12 in. by 10 in. edge beam to facilitate load transfer into the specimen. Both the chord beams and the edge beam were cast integrally with the 4 in. slab.

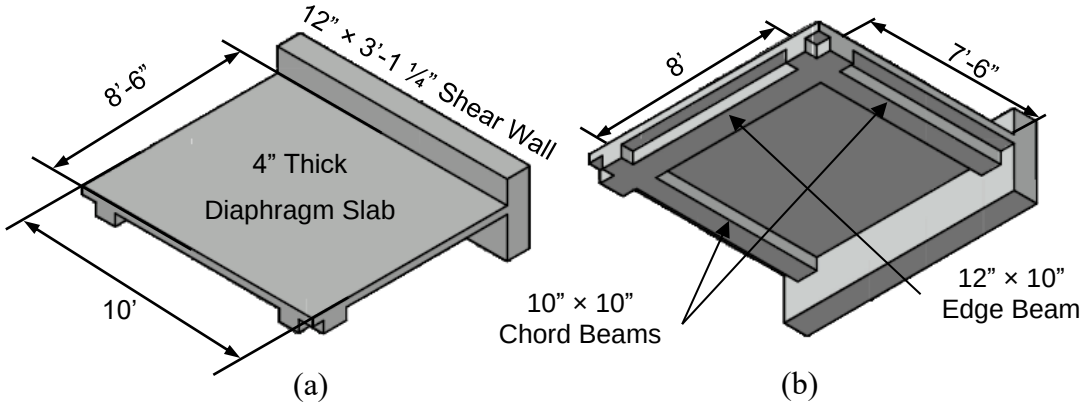

Figure 3-1. Isometric Views of the Diaphragm Specimen: (a) Top View; (b) Bottom View.

The FRP strengthening testing matrix is presented in Table 3-1. All FRP strengthened specimens contained two layers of CFRP applied on one side only, in varying orientations. Specimen CD7, CD8, CD13, and CD14 contained two unidirectional layers of CFRP, while Specimen CD9, CD10, and CD12 contained two orthogonal layers of CFRP, to create pseudoisotropic reinforcement as mentioned in Khalifa et al. (1998). The FRP ply orientation, α, is referenced to the longitudinal axis of the specimens, where $\alpha = 0°$ refers to FRP plies oriented perpendicular to applied shear, and $\alpha = 90°$ refers to FRP plies oriented parallel to applied shear. It should be noted that this sign convention differs from the convention used in Hutton et al. (2023) but is consistent with the convention used in ACI PRC-440.2R-23 (2023). Although the orientation sometimes varied between layers, the FRP material, width, and spacing was always consistent between two layers applied to the same specimen.

Table 3-1. FRP Strengthening Testing Matrix.

Specimen ID	FRP Material	FRP Ply Configuration						FRP Anchor Configuration	
		Number of Layers	Composite Modulus, E_f (ksi)	Thickness per ply, t_f (in.)	Width, w_f (in.)	Spacing, s_f (in.)	Orientation, α (deg.)	Anchor type	Layout
CD7	VWrap C220HM, CFRP	2	14700	0.04	12.0	12.0	90	5/8 in. CSS-HMPCA Carbon Anchors	Two Rows at Ends
CD8	VWrap C220HM, CFRP	2	14700	0.04	12.0	12.0	90	N/A	N/A
CD9	VWrap C220HM, CFRP	2	14700	0.04	12.0	12.0	0 and 90	5/8 in. CSS-HMPCA Carbon Anchors	Perimeter Between Layers
CD10	VWrap C100HM, CFRP	2	16700	0.02	12.0	24.0	47 and 133	5/8 in. and 3/4 in. CSS-HMPCA Carbon Anchors	Ends only
CD11	N/A	N/A	N/A	N/A	N/A	N/A	N/A	N/A	N/A
CD12	VWrap C220HM, CFRP	2	14700	0.04	12.0	12.0	0 and 90	5/8 in. CSS-HMPCA Carbon Anchors	Perimeter Between Layers
CD13	Tyfo SCH 41, CFRP	2	14600	0.04	6.0	10.0	90	Duktil D8.25 FRP Anchor System	Ends and Intermediate
CD14	Tyfo SCH 41, CFRP	2	14600	0.04	12.0	22.0	90	Duktil D8.25 FRP Anchor System	Ends and Intermediate

In addition to variations in FRP material and ply configuration, mechanical anchorage was provided by various types, sizes, and layouts of anchorage systems. Specimen CD7, CD9, CD10, and CD12 were anchored with CSS-HMPCA Carbon Anchors, which are a type of fiber splay anchor that anchors into the concrete through dowel action with splays that are bonded to the FRP with a thermosetting resin. Furthermore, the location of the fiber splays varied between specimens, where the anchors in Specimen CD9 and CD12 were splayed between layers and the anchors in Specimen CD7 and CD10 were splayed on top of both layers.

Specimen CD13 and CD14 were anchored with Duktil D8.25 FRP Anchors, which are a type of anchor plate that is bonded to the top of the FRP plies with a thermosetting resin. After the resin hardened, ¼ in. concrete screws were driven through at least six of the eight holes in the plate to provide anchorage into the concrete. An additional 10 in. long strip of FRP was placed directly beneath FRP anchor plate to reinforce the FRP plies at all anchor locations.

Finally, some of the strengthened specimens intentionally exceeded the limit on steel and FRP shear strength contribution described in Eq. (12). As this limit was adopted from the maximum shear strength contribution for steel reinforcement in ACI 318 (2019), the purpose of exceeding this limit was to investigate its applicability in diaphragms strengthened with FRP.

Schematics of FRP ply configurations, anchor layout, anchor type, and anchor size are provided in the following sections, in addition to discussion regarding the intention of each experimental test.

3.2.1 CD7: 2 Full Coverage Layers CFRP With End Anchors

FRP strengthening applied to Specimen CD7 is presented in Figure 3-2. Specimen CD7 was strengthened with two layers of 12 in. wide sheets of V-wrap C220HM spaced at 12 in. O.C. to achieve two layers of full FRP coverage. Both layers were oriented parallel to applied shear. Mechanical anchorage was provided with two rows of 5/8 in. V-Wrap CSS-HMPCA Carbon Anchors at each end of the FRP sheets. The anchors were splayed above both layers of CFRP and bonded using a thermosetting resin. The anchors were spaced at 6 in. O.C. for a total of four anchors at both ends of each anchored FRP sheet. The anchors were set at a 90-degree angle into predrilled holes in the slab. The holes were drilled entirely through the slab

at a 3/4 in. diameter and rounded at the top of the slab to a 3/4 in. radius. The FRP sheets located beneath the loading beam and on the free end of the specimen were unanchored.

The strengthening of Specimen CD7 was selected to investigate the limit on maximum nominal shear strength presented in ACI 318 (2019) Clause 12.5.3.4 and summarized in Eq. (13) in addition to the effect of mechanical anchorage, which is explained later in Section 3.2.2. Following the shear capacity equations presented in Section 2.2, the nominal shear capacity is approximately $10.9\sqrt{f_c'}A_{cv}$ exceeding the $8\sqrt{f_c'}A_{cv}$ limit prescribed in ACI 318 (2019).

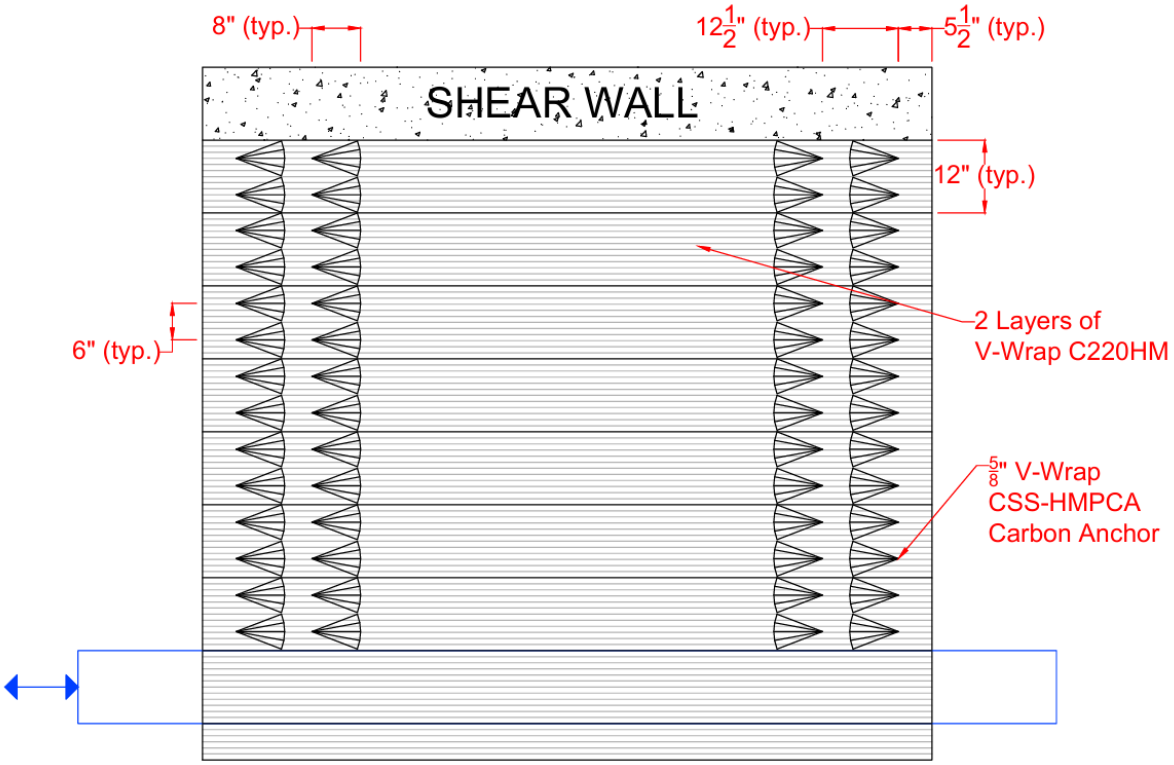

Figure 3-2. FRP Strengthening Applied to Specimen CD7.

3.2.2 CD8: 2 Full Coverage Layers CFRP Without Anchors

FRP strengthening applied to Specimen CD8 is presented in Figure 3-3. The FRP strengthening applied to Specimen CD8 is identical to Specimen CD7, except that Specimen CD8 does not include mechanical anchors. Specimen CD8 contained two full-coverage layers of 12 in. wide sheets V-Wrap C220HM spaced at 12 in. O.C. Anchors were chosen not to be included in Specimen CD8 to allow for sufficient comparison between strengthening schemes

detailed with and without anchorage when the total quantity of FRP increases the nominal shear strength near or above the prescribed limit presented in ACI 318 (2019) Clause 12.5.3.4 and summarized in Eq. (13). Following the shear capacity equations presented in Section 2.2, the nominal shear capacity is approximately $10.8\sqrt{f_c'}A_{cv}$, exceeding the $8\sqrt{f_c'}A_{cv}$ limit prescribed in ACI 318 (2019).

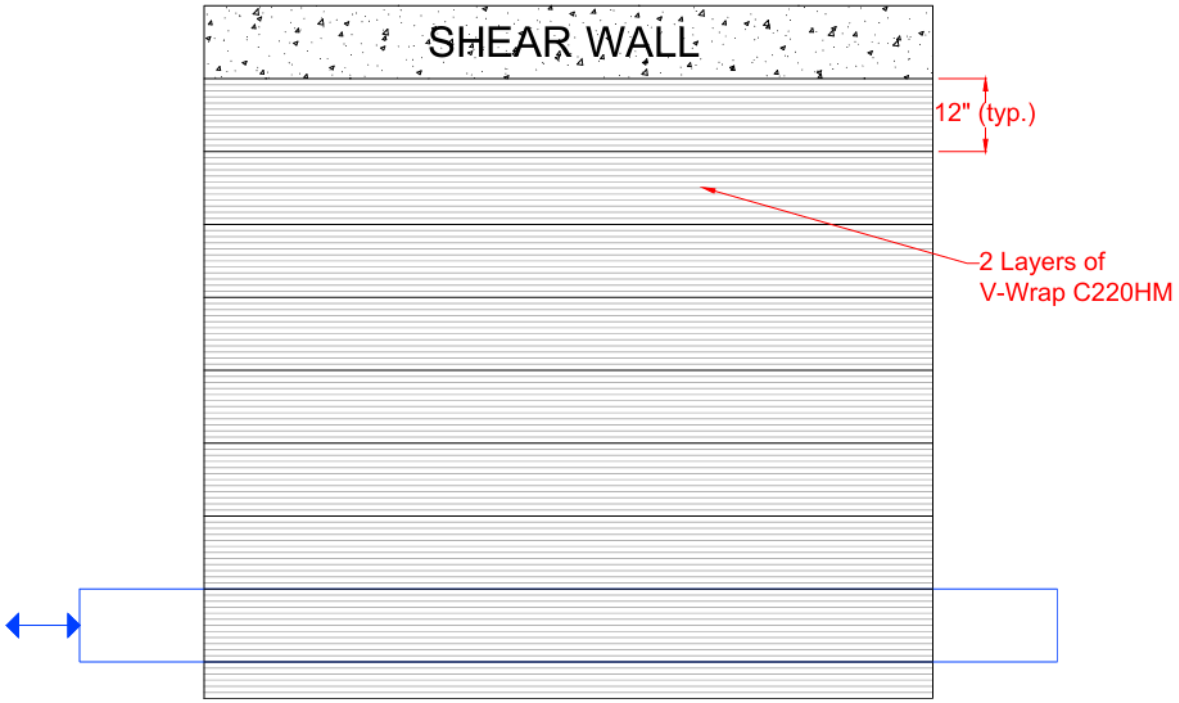

Figure 3-3. FRP Strengthening Applied to Specimen CD8.

3.2.3 CD9: 2 Orthogonal Full Coverage Layers CFRP with Perimeter Anchorage

FRP strengthening applied to Specimen CD9 is presented in Figure 3-4 and Figure 3-5. Similar to Specimen CD7 and CD8, Specimen CD9 contained two full-coverage layers of 12 in. wide sheets of V-Wrap C220HM spaced at 12 in. O.C. Unlike Specimen CD7 and CD8, the two layers in Specimen CD9 were placed orthogonal to each other. The first layer was oriented parallel to applied shear, while the second layer was oriented perpendicular to applied shear. Specimen CD9 utilized 5/8 in. CSS-HMPCA Carbon Anchors that were splayed above the first layer, but beneath the second layer around the perimeter of the shear span. The anchors were spaced at 6 in. O.C. and were set at a 90-degree angle into predrilled holes in the slab. The holes were drilled entirely through the slab at a 3/4 in diameter and rounded at the top of

the slab to a 3/4 in. radius. The anchors were installed through the slab depth but not into the perimeter beams surrounding the diaphragm specimen.

The strengthening of Specimen CD9 was selected to study the effectiveness of two layers of orthogonal FRP in addition to the effectiveness of FRP strengthening when the nominal shear strength approaches the code prescribed limit of $8\sqrt{f_c'}A_{cv}$ presented in ACI 318 (2019) Clause 12.5.3.4.

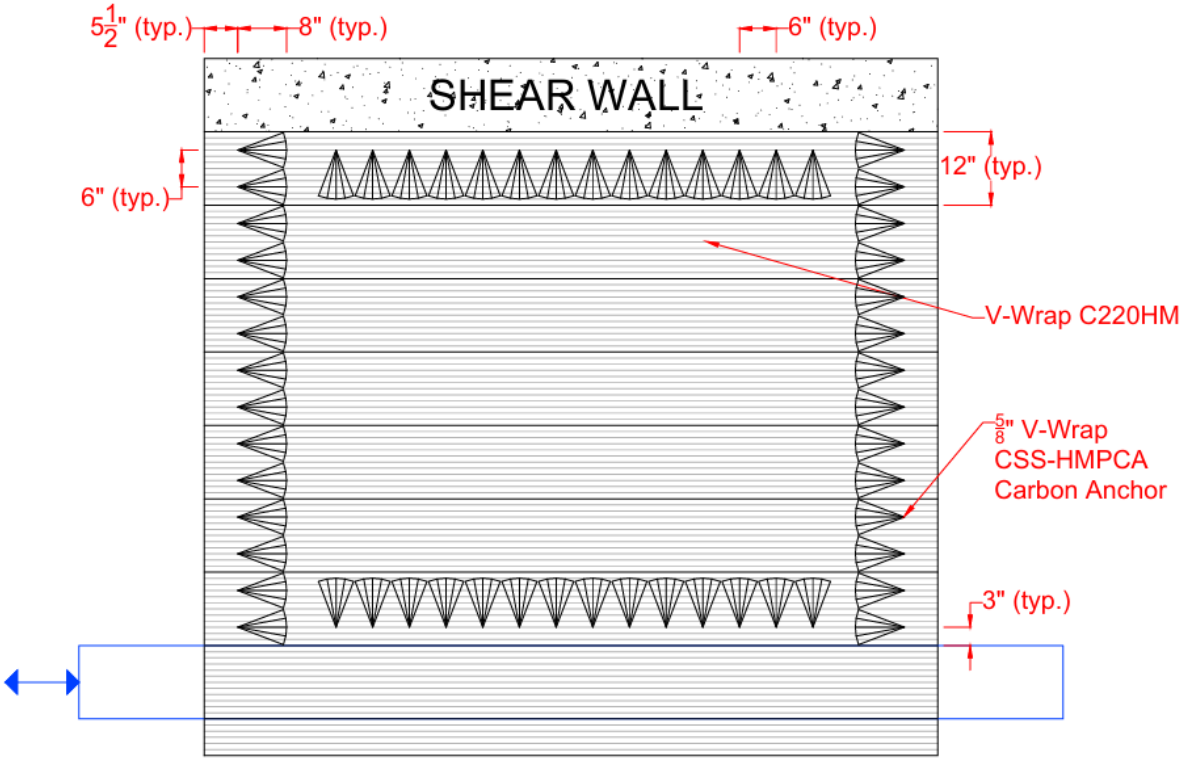

Figure 3-4. First Layer of FRP Strengthening Applied to Specimen CD9.

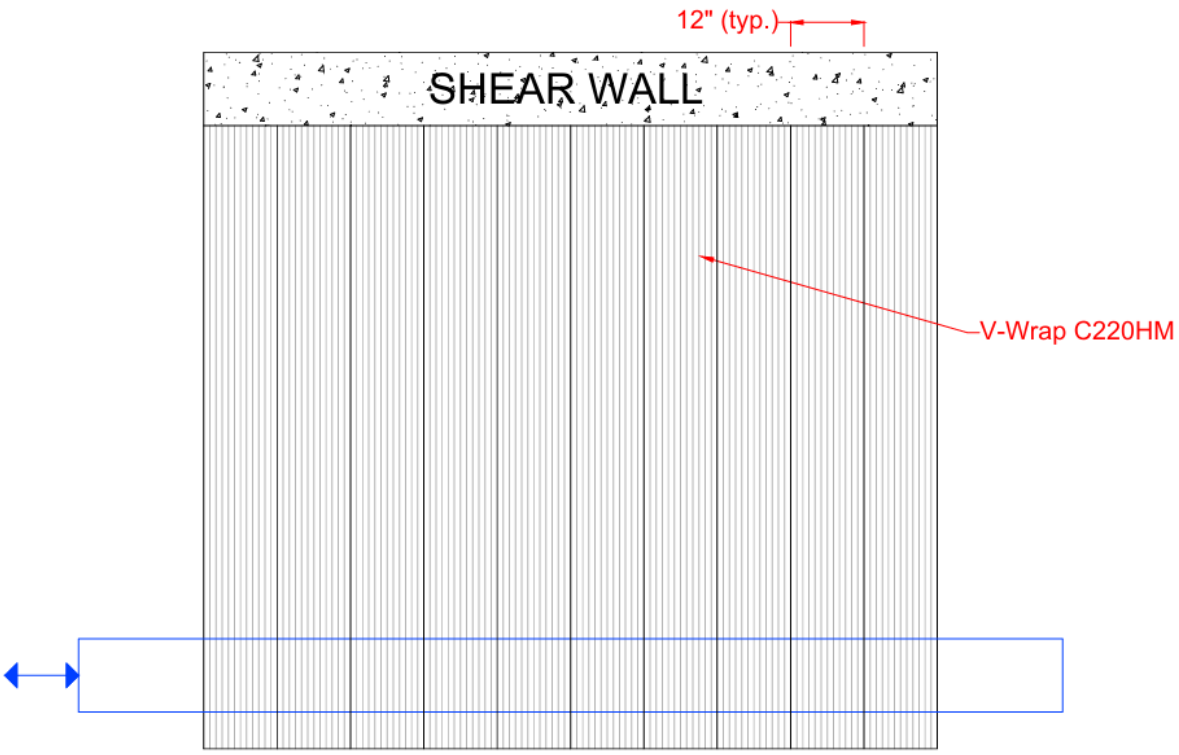

Figure 3-5. Second Layer of FRP Strengthening Applied to Specimen CD9.

3.2.4 CD10: 2 Orthogonal Full Coverage Layers CFRP with Perimeter Anchorage

FRP strengthening applied to Specimen CD10 is presented in Figure 3-6. Specimen CD10 was strengthened with two layers 12 in. wide sheets of V-Wrap C100HM spaced at 24 in. O.C. Each layer was placed at approximately 45 degrees relative to the direction of applied shear. Specimen CD10 contained perimeter anchorage of two sizes. Six 5/8 in. CSS-HMPCA Carbon Anchors were used near the shear wall, while 14 3/4 in. CSS-HMPCA Carbon Anchors were used along the rest of the shear span perimeter. The anchors were set at a 90-degree angle into predrilled holes in the slab. For the 5/8 in. CSS-HMPCA Carbon Anchors, holes were drilled to 3/4 in. diameter through the entire depth of the slab. For the 3/4 in. CSS-HMPCA Carbon Anchors, holes were drilled to 7/8 in. diameter through the entire depth of the slab. All of the anchor holes were rounded to a 3/4 in. radius at the top of the slab.

The strengthening of Specimen CD10 was selected to investigate the effectiveness of orienting FRP sheets perpendicular to the direction of expected diagonal shear cracks. It was anticipated that orienting the sheets in this direction would allow for more effective engagement of the FRP.

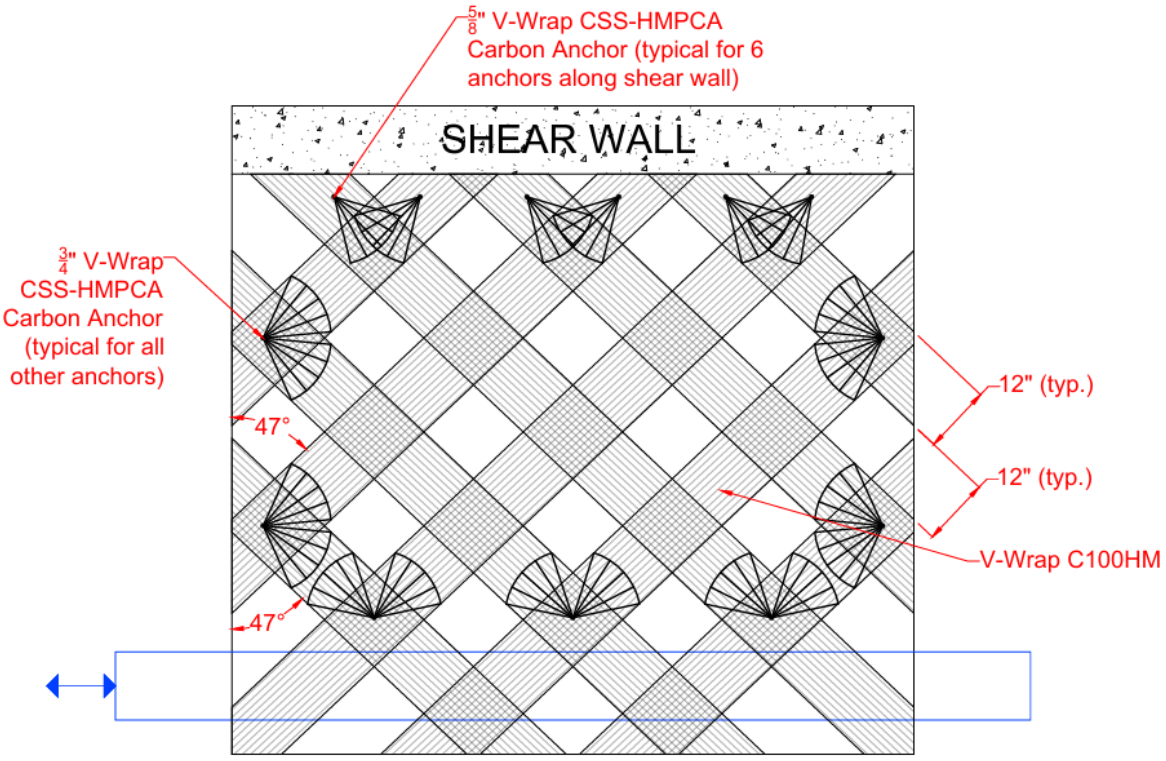

Figure 3-6. FRP Strengthening Applied to Specimen CD10.

3.2.5 CD11: Baseline LWC Specimen without FRP

Specimen CD11 was not strengthened with FRP. Specimen CD11 was constructed with LWC and served as a baseline specimen for Specimen CD12. It was believed that a baseline specimen was necessary for LWC as its material properties differ from that of NWC, for which a baseline specimen has already been presented in Hutton et al. (2023). Notably, it was observed through splitting tensile tests of the LWC used in Specimen CD11 and CD12 that cracks formed through the expanded shale aggregate, as opposed to around the aggregate. It was believed that this might lead to reduced biaxial concrete behavior and a weaker compression strut, thus necessitating a baseline specimen for LWC to study this effect.

3.2.6 CD12: LWC with 2 Orthogonal Layers CFRP and Perimeter Anchorage

Specimen CD12 was constructed with LWC and strengthened with FRP. The FRP strengthening applied to Specimen CD12 is presented in Figure 3-7 and Figure 3-8. Similar to Specimen CD9, Specimen CD12 contained two full-coverage layers of 12 in. wide sheets of V-Wrap C220HM spaced at 12 in. O.C. The two layers in were placed orthogonal to each

other. The first layer was oriented parallel to applied shear, while the second layer was oriented perpendicular to applied shear. Also similar to Specimen CD9, Specimen CD12 utilized 5/8 in. CSS-HMPCA Carbon Anchors that were splayed above the first layer, but beneath the second layer around the perimeter of the shear span. The anchors were spaced at 6 in. O.C. and were set at a 90-degree angle into predrilled holes in the slab. The holes were drilled entirely through the slab at a 3/4 in. diameter and rounded at the top of the slab to a 3/4 in. radius. The anchors were installed through the slab depth but not into the perimeter beams surrounding the diaphragm specimen. The FRP configuration and anchor layout is identical to Specimen CD9, except for Specimen CD12 containing four additional 5/8 in. CSS-HMPCA Carbon Anchors.

The strengthening of Specimen CD12 was selected to study the effectiveness of two layers of orthogonal FRP in addition to the effectiveness of FRP strengthening when the nominal shear strength approaches the code prescribed limit of $8\sqrt{f_c'}A_{cv}$ presented in ACI 318 (2019) Clause 12.5.3.4. Furthermore, the FRP configuration and anchor layout was nearly identical to Specimen CD9 to facilitate an effective comparison between NWC and LWC in FRP shear strengthening applications.

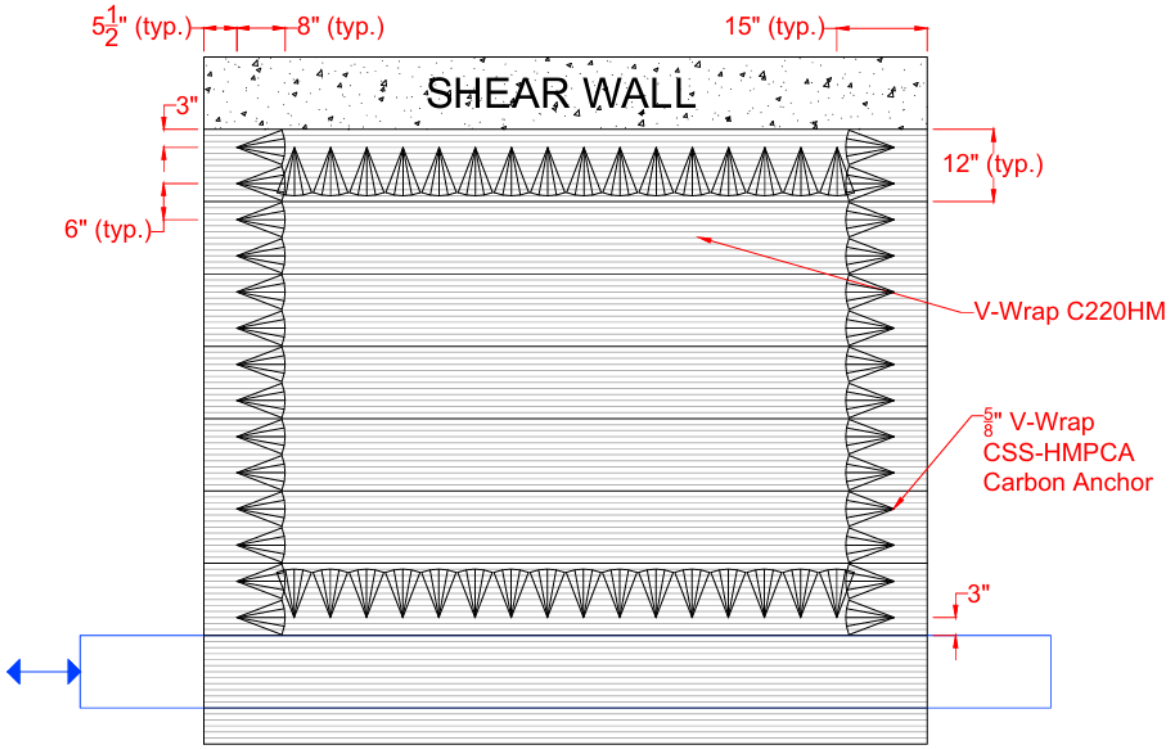

Figure 3-7. First Layer of FRP Strengthening Applied to Specimen CD12.

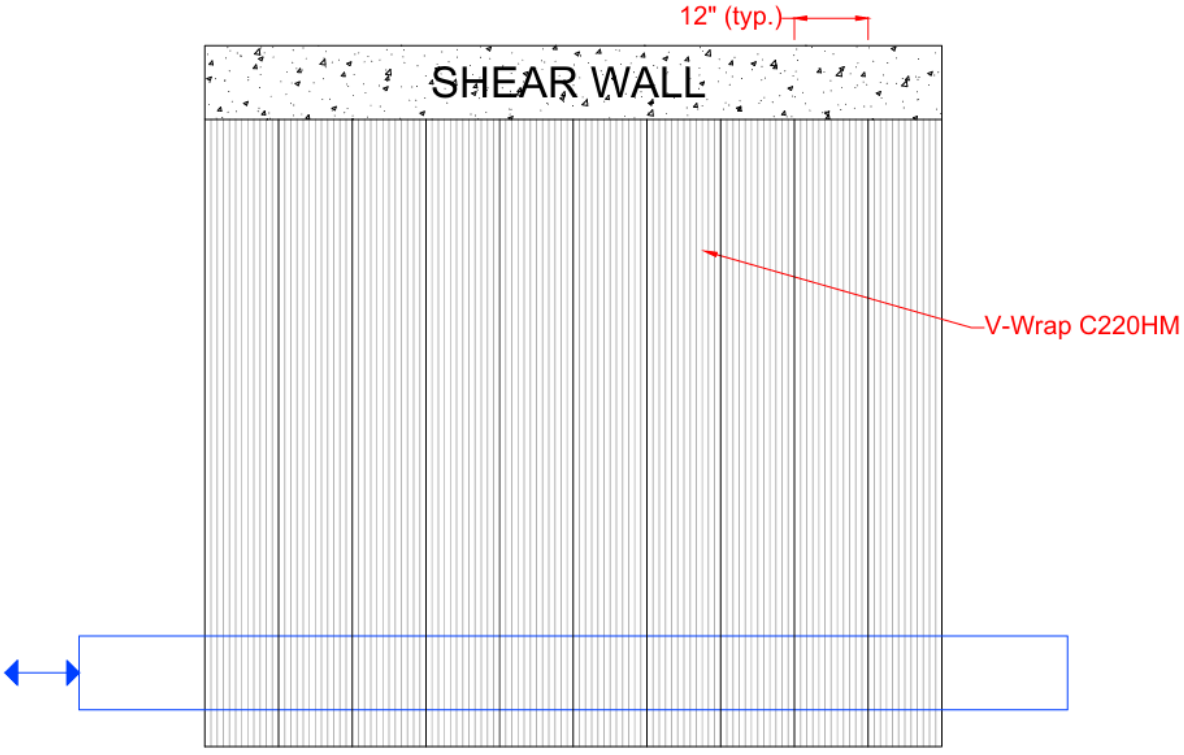

Figure 3-8. Second Layer of FRP Strengthening Applied to Specimen CD12.

3.2.7 CD13: 2 Layers CFRP with End and Intermediate Anchor Plates

FRP strengthening applied to Specimen CD13 is presented in Figure 3-9. Specimen CD13 was strengthened with two layers 6 in. wide layers of Tyfo SCH 41 spaced at 10 in. O.C. Both layers were oriented parallel to applied shear. Unlike all previous specimens, Specimen CD13 utilized the Duktil D8.25 Anchor System to provide mechanical anchorage to the FRP. This anchor system involves bonding a steel plate on top of the FRP sheets and fastening the plate to the concrete with six 1/4 in. screws. The manufacturer of this anchor system noted that the anchorage performance is similar regardless of which six holes in the steel plate contain screws. Because the thermosetting resin must harden before the screws are fastened, a propane heater was utilized to accelerate the curing process. More detail on this process is provided in Section 3.4.

Duktil D8.25 Anchor Plates were placed at the ends and in the middle of each FRP sheet. An additional 10 in. long sheet of Tyfo SCH 41 was placed beneath each anchor to provide additional reinforcement. The primary intention of this experimental test was to study the effect of the anchorage system, as the manufacturer believed the anchor plates possessed increased ductility compared to traditional fiber splay anchors, allowing the anchor plates to deform after debonding of the FRP sheets and delay anchorage failure.

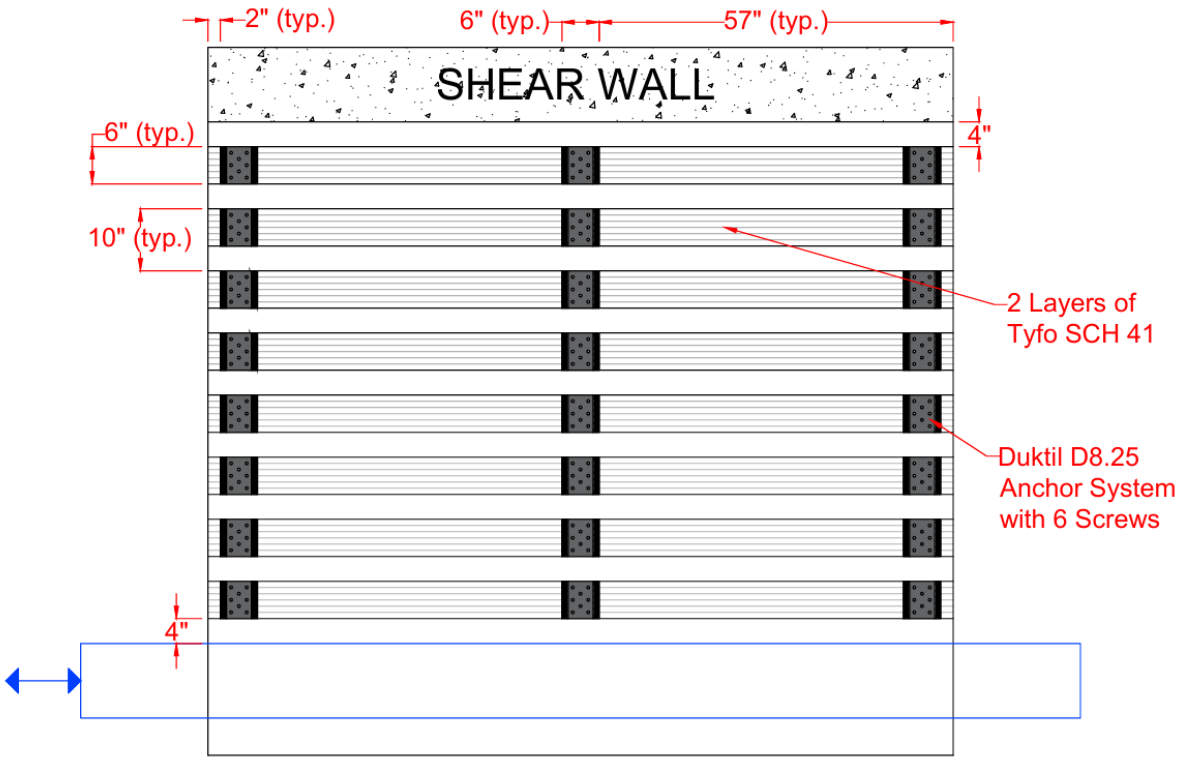

Figure 3-9. FRP Strengthening Applied to Specimen CD13.

3.2.8 CD14: 2 Layers CFRP with End and Alternating Intermediate Anchor Plates

FRP strengthening applied to Specimen CD14 is presented in Figure 3-10. Two layers of 6 in. wide sheets of Tyfo SCH 41 were installed throughout the specimen, parallel to applied shear. Although discrete 6 in. wide strips were used, the sponsors of this experimental test suggested that they would define this strengthening configuration as 12 in. wide strips placed at 22 in. O.C. in the context of the FRP shear capacity equations presented in ACI PRC-440.2R-23 (2023). Similar to Specimen CD13, Specimen CD14 utilized the Duktil D8.25 Anchor System with an additional 10 in. long sheet of Tyfo SCH 41 placed beneath each anchor. End anchors were applied for all sheets, while an alternating configuration of one and two intermediate anchors was utilized. As Specimen CD14 utilized a similar quantity of FRP to Specimen CD13, the primary intention of this experimental test was to isolate the effects of alternating intermediate anchorage in the diaphragm field.

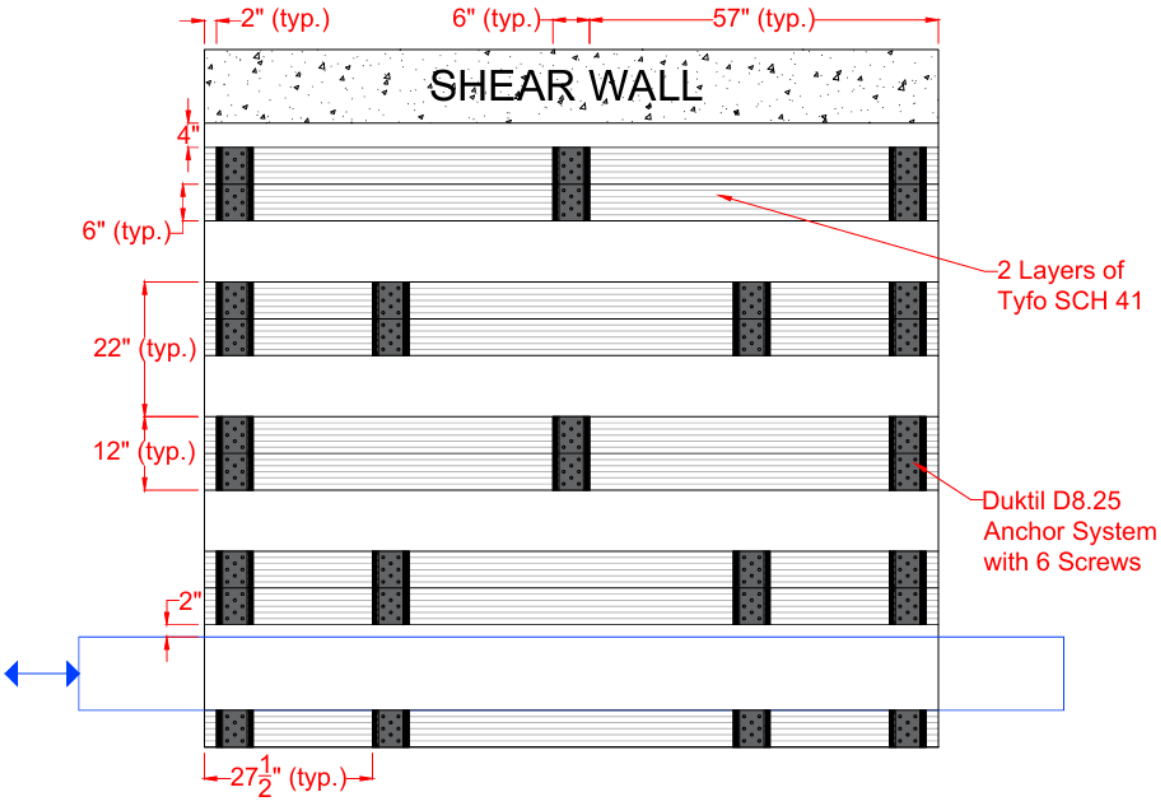

Figure 3-10. FRP Strengthening Applied to Specimen CD14.

3.3. Reinforced Concrete Specimen Details

Concrete and reinforcing steel details for Specimen CD7 and CD8 are presented in Figure 3-11, and concrete and reinforcing steel details for CD9-14 are presented in Figure 3-12. All specimens contained two chord beams with six #8 Gr. 60 longitudinal bars and #3 Gr. 60 stirrups with 135-degree hooks placed at 4 in. O.C. The chord beams were connected to the rection truss using #8 rebar couplers on each side of the reaction truss to allow the development of tension and compression during load reversals. All specimens contained one edge beam with ten #7 Gr. 60 longitudinal bars and #3 Gr. 60 stirrups with 135-degree hooks placed at 4 in. O.C. The edge beams were connected to the loading channels using ten shear transfer assemblies each containing four shear studs embedded into the concrete and four 3/4 in. bolts fastened to the loading channel.

All specimens contained a shear wall segment with eleven #8 Gr. 60 longitudinal bars and #4 Gr. 60 stirrups with crossties. All shear wall segments were connected to the reaction truss using segments of 3/4 in. threaded rod fastened with nuts on both sides of the reaction

truss, in addition to a nut secured to the rod on the embedded end using Loctite to allow the threaded rod to engage the concrete. Additionally, the shear wall segments were connected to the bearing beam using of 3/4 in. threaded rod fastened with nuts on both sides of the bearing beam, in addition to a nut secured to the rod on the embedded end using Loctite to allow the threaded rod to engage the concrete.

Several adjustments were made to the reinforcing steel details after Specimen CD7 and CD8. The distributed mesh of reinforcing steel in the field of the diaphragm specimen was adjusted from #3 Gr. 60 at 12 in. O.C. for Specimen CD7 and CD8 to #3 Gr. 60 at 18 in. O.C. for Specimen CD9 through CD14. Additionally, reinforcing steel in the edges of the slab protruding past the perimeter beams was included in Specimens CD9 through CD14, but was not included in Specimen CD7 or CD8. The reinforcing steel in the slab edges was #3 Gr. 60 U-bars placed at 4 in O.C. embedded at least the entire width of the beam. This reinforcing steel was intended to strengthen the specimen near the locations of FRP anchorage to prevent premature failure of the underlying specimen prior to the anchor fully engaging. Finally, fourteen 24 in. long pieces of #3 Gr. 60 reinforcing steel were placed diagonally in each direction along the interface between the edge beam and the field of the diaphragm specimen for specimens Specimen CD9 through CD14 but was not included in Specimen CD7 or CD8. This reinforcing steel was intended to strengthen the interface between the loading assembly and the diaphragm specimen to prevent premature direct shear failure along this interface prior to strut crushing or globalized debonding in the diaphragm field.

Complete sets of detailed drawings are included in Appendix A: and Appendix B:. For information regarding the design of the reaction truss, see Hutton et al. (2023).

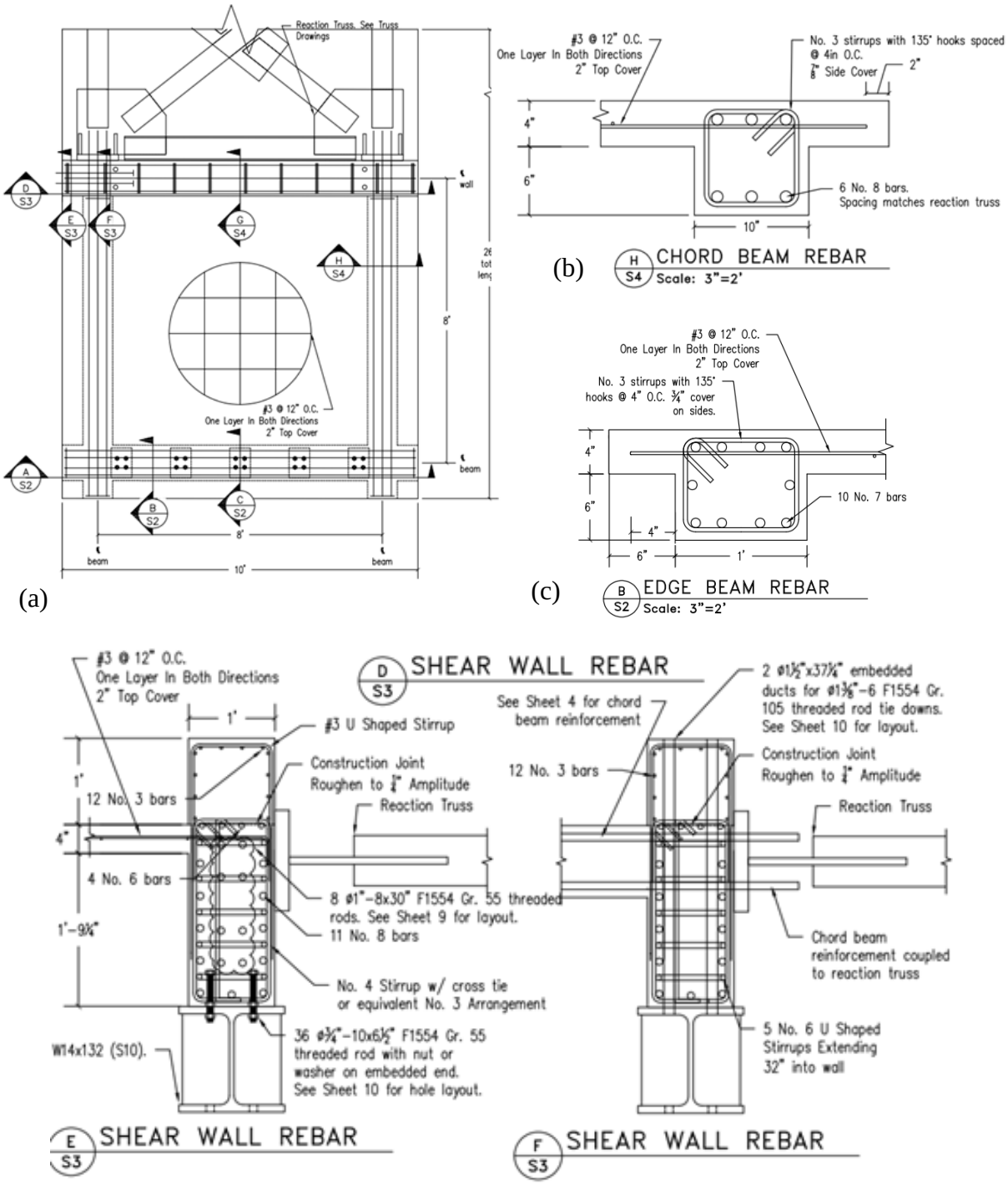

Figure 3-11. Specimen CD7 and CD8 Construction Details: (a) Plan View of the Specimen; (b) Chord Beam Reinforcement; (c) Edge Beam Reinforcement; (d) Shear Wall Segment Reinforcement.

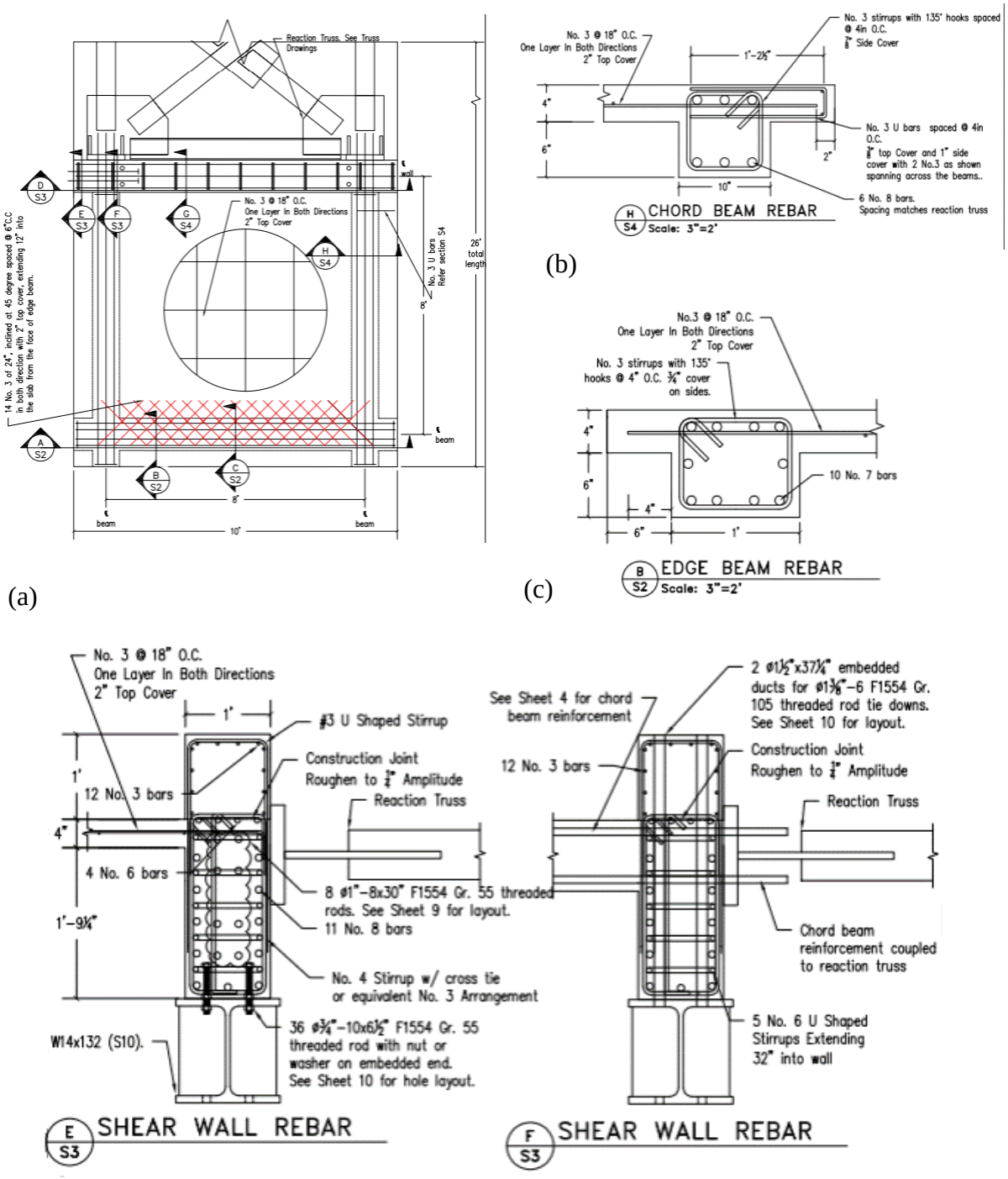

Figure 3-12. Specimen CD9-14 Construction Details: (a) Plan View of the Specimen; (b) Chord Beam Reinforcement; (c) Edge Beam Reinforcement; (d) Shear Wall Segment Reinforcement.

3.4. Specimen Construction Details

The specimen construction process began by placing wooden formwork. For full formwork drawings, see Hutton et al. (2023). A shoring system was used to elevate a series of 3/4 in. plywood panels supported by 2x4 dimensional lumber to the bottom elevation of the perimeter beams, as shown in Figure 3-13(a). A separate series of 3/4 in. plywood panels supported by 2x4 dimensional lumber was constructed to enclose the bottom of the shear wall segment. Prior to the placement of any reinforcing steel cages, segments of 6.5 in. long 3/4 in. thick threaded rod were placed at the bottom of the shear wall to connect the shear wall to the bearing beam beneath it. Each segment of threaded rod contained three nuts, one on each side of the bearing beam, and one on the end of the threaded rod protruding into the shear wall. The nut on the end of the threaded rod was fastened with Loctite to ensure it maintained its position during the pouring process.

Next, reinforcing steel cages were constructed. Shear wall and edge beam cages were constructed outside of the specimen and placed into the specimen using an overhead crane. The shear wall cage was constructed first and placed into the bottom shear wall form and around the segments of threaded rod, as shown in Figure 3-13(b). #3 U-bars in the top portion of the shear wall were placed, but longitudinal bars in the top portion of the shear wall were not placed at this time. The chord beam cages were constructed in place, as each longitudinal bar in the chord beam had to be carefully woven through the shear wall cage and the reaction truss. The interior rebar couplers on the longitudinal bars in the chord beams were fastened prior to placing the bars, while the exterior rebar couplers were placed after the bar had been woven through the shear wall cage and reaction truss. For Specimens CD11 through CD14, spacers were placed between the exterior rebar coupler and the reaction truss. These spacers were either slotted washers or slotted pieces of rebar couplers and were taped to the exterior rebar coupler to ensure they remained in place throughout the duration of the test. These spacers were intended to simplify the removal of the exterior couplers after the test, as the tape and spacers could be easily removed, and the longitudinal bar could be cut with a blowtorch.

Shear transfer assemblies were constructed outside of the specimen and consisted of a steel plate with four shear studs and four 3/4 in. bolts. Shear studs were stud welded onto the embedded side of the shear transfer assembly, while 3/4 in. bolts were placed through the steel

plate and fastened to the plate with Loctite to prevent slippage. Five shear transfer assemblies were then placed into the bottom loading channel. The edge beam cage was constructed outside of the specimen and woven into the edge beam and around the five bottom shear transfer assemblies, as shown in Figure 3-13(c).

After the shear wall, edge beam, and chord beam cages had been constructed and placed, additional wooden formwork was placed around the perimeter beams to create the exterior sides of these beams in addition to the bottom of the slab. In the center of the specimen, three layers of two in. thick insulating foam was cut and placed to create the interior sides of the perimeter beams, in addition to the bottom of the slab. A mat of reinforcement was placed throughout the slab, in addition to flange reinforcing bars and direct shear bars if they were present. Finally, segments of 2x6 dimensional lumber were fastened to existing formwork to form the edges of the slab. As much of the formwork was reused for each set of two specimens, formwork in contact with concrete was covered with 6 mm plastic sheeting to mitigate damage during formwork stripping operations. A photograph of a specimen directly before pouring concrete is shown in Figure 3-13(d).

While two specimens were cast simultaneously, the casting process involved two separate concrete placements. The first placement involved casting the entirety of the perimeter beams and slab, in addition to the lower portion of the shear wall up to the height of the top of the slab. Concrete was placed from the truck into a hopper and flown to the specimen using the overhead crane. Concrete was released from the hopper, distributed with shovels, and consolidated with a submersion vibrator, as shown in Figure 3-13(e). A vibratory screed was then used on the slab surface. The top surface of the shear wall concrete was roughened with a piece of #3 reinforcing steel to establish a construction joint for the secondary placement. A photograph taken directly after the first pour is shown in Figure 3-13(f). After an initial set, each specimen was covered with a sheet of 6 mm plastic to facilitate moisture curing.

The second placement involved casting the top portion of the shear wall. Prior to the placement, the longitudinal steel in this top portion was placed in addition to formwork around the edges of the top portion of the shear wall. Concrete was placed from the truck into a hopper and flown to the specimen using the overhead crane. Concrete was released from the hopper, distributed with shovels, consolidated with a submersion vibrator, and trowel finished. After

the concrete began to set, the top surface of the shear wall was covered with a sheet of 6 mm plastic to facilitate moisture curing.

(a)

(b)

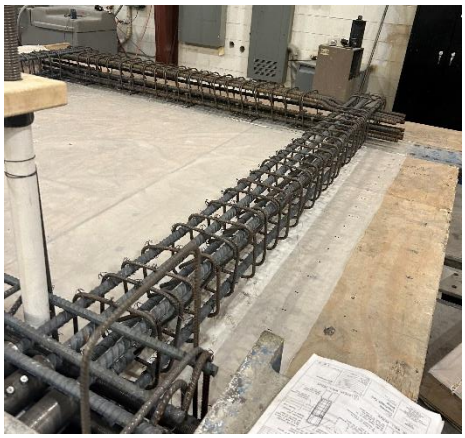

(c)

(d)

(e)

(f)

Figure 3-13. Photographs Taken During Specimen Construction: (a) Formwork Slab at Bottom of Beam Elevation; (b) Shear Wall Cage and Bottom Form; (c) Edge Beam and Chord Beam Cages; (d) Before First Pour; (e) During First Pour; (f) After First Pour.

The formwork was stripped from the specimen after at least seven days of moisture curing. The formwork was stripped in the reverse order of its installation and was occasionally damaged to facilitate removal. Once the formwork was removed, the process for preparing the specimen for FRP installation began.

Because FRP shear strengthening is a bond critical application, the surface was prepared according to the bond critical guidelines in ACI PRC-440.2R-23 (2023). The top surface of the diaphragm specimen was ground using a concrete diamond angle grinder to achieve at least Concrete Surface Profile 3. After the surface was ground, locations of FRP anchors were measured and marked. For specimens utilizing fiber splay anchors, anchor holes were drilled at a diameter of 1/8 in. greater than the diameter of the fiber splay anchor. The top of the anchor holes drilled for fiber splay anchors were rounded to a 3/4 in. radius with a diamond drill bit. Pieces of concrete surrounding the bottom side of the hole occasionally blew out during the drilling process. The holes were patched using a mixture of epoxy and sand. No holes were predrilled for specimens utilizing Duktil Anchor Plates. Finally, the top surface of the diaphragm was swept and vacuumed, and the anchor holes (if present) were vacuumed.

The externally bonded FRP was installed after the surface had been prepared, anchor holes had been drilled, and the specimen had cured for at least 14 days. First, the concrete surface was primed using resin. To fill voids and create a smooth surface, a layer of resin thickened with fumed silica was evenly spread over the primed area and each anchor hole. Before installation, each FRP sheet was pre-cut and hand-saturated with resin. The FRP sheets were then positioned on the specimen and a plastic drywall trowel was used to press the sheets into place, ensuring proper adhesion while removing excess epoxy and trapped air.

The following process was followed for specimens utilizing fiber splay anchors. A razor blade was used to create a small incision in the FRP sheet at each anchor hole location. The fiber anchors were manually saturated with resin before inserting the dowel into the predrilled hole. Then, the fiber fan was splayed to the specified dimensions. Finally, a uniform layer of thickened resin was applied over the FRP sheets and anchors, and additional thickened resin was placed into any anchor holes that were not fully filled.

The following process was followed for specimens utilizing the Duktil Anchor System. An additional hand-saturated 10 in. long strip of Tyfo SCH 41 was placed on top of the sheet being anchored at the location of the anchor plate. The anchor plate was then placed in the specified location, ensuring no air voids or excess epoxy were beneath the plate. The specimen was then heated using two propane heaters and a shroud constructed with plywood and insulating foam to accelerate the curing process. After the epoxy began to harden, 1/4 in. concrete screws were installed into the anchor plates. Each anchor plate had eight holes, and the manufacturer specified that any six of the eight holes needed to be fastened with screws. Six screws were installed in each anchor plate. For Specimen CD13, the two propane heaters and the shroud were also used after anchor installation to ensure a full cure of the FRP prior to testing. Additional heat after anchor installation was not applied to Specimen CD14.

3.5. Test Setup

A schematic of the test setup used is presented in Figure 3-14, retrieved from Hutton et al. (2023). Two specimens were constructed simultaneously and connected in the middle through a steel reaction truss. The steel reaction truss allowed both shear walls to produce reactions into the strong floor. This test setup was developed similar to Nakashima et al. (1981). Two MC12x31 loading channels were connected with bolts to shear transfer assemblies containing shear studs embedded in the concrete. The bottom loading channel rested on rollers supported by concrete pedestals to allow translation along the longitudinal direction of the loading channels.

Vertical translation was restrained in two locations. The actuator vertical translation resistance system is shown in Figure 3-15(a) and restrained uplift at the actuator head. The loading channel vertical translation resistance system is shown in Figure 3-15(b) and restrained uplift at the far end of the loading channel. Additionally, the shear wall segment of each diaphragm specimen rested on a W12X132 bearing beam. The bearing beam and the shear wall were connected using segments of 3/4 in. threaded rod, as discussed in Section 3.3. The reaction truss was fabricated with HSS 7x7x3/8 and W8x35 sections. For detailed drawings and design calculations of the test setup, see Hutton et al. (2023).

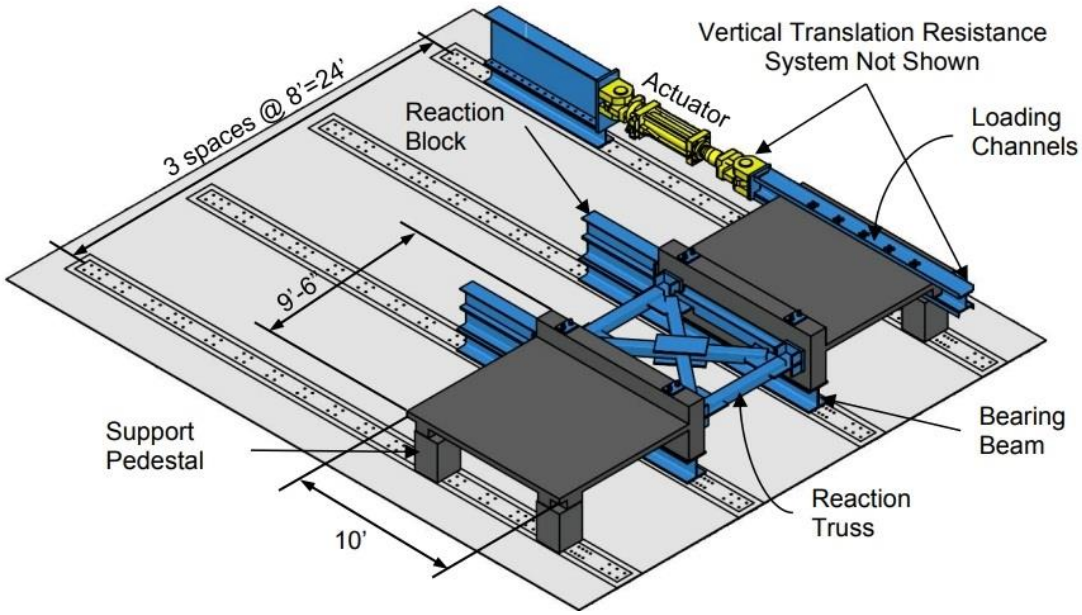

Figure 3-14. Schematic of Test Setup [From (Hutton et al. 2023)].

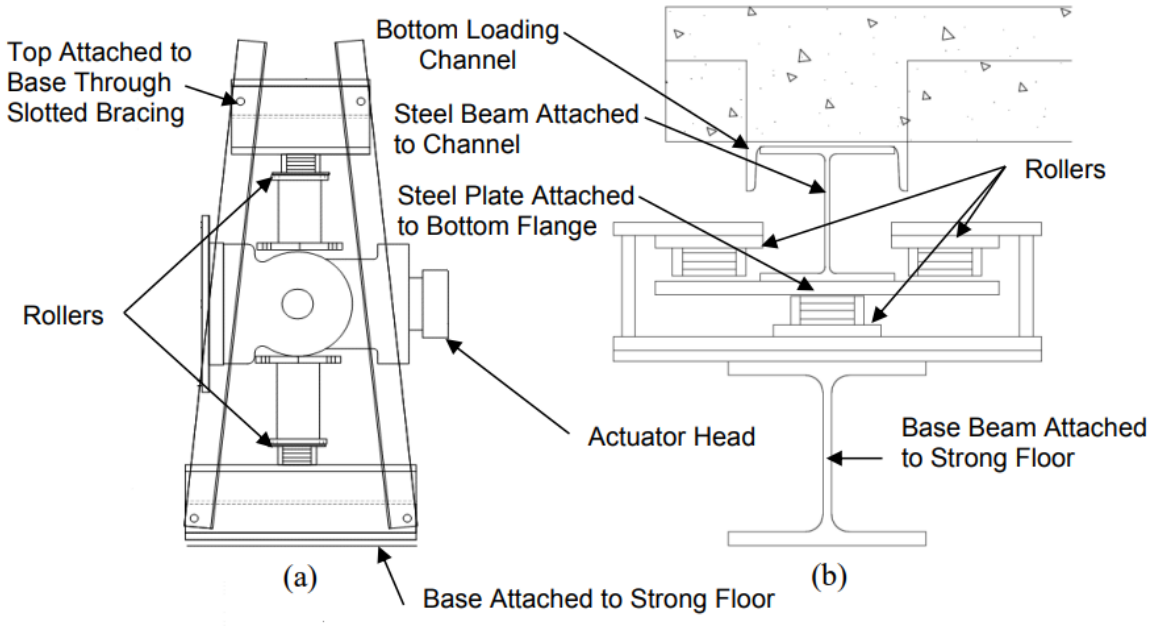

Figure 3-15. Vertical Translation Resistance Systems: (a) Actuator Out-of-plane Bracing [From (Avellaneda-Ramirez 2021)]; (b) Loading Channel Out-of-plane Bracing [From (Hutton et al. 2023)].

3.6. Test Procedure and Loading Protocol

The loading protocol is shown in Table 3-2. This protocol was developed following quasi-static cyclic testing guidelines in FEMA 461 (2007). According to these guidelines, two

cycles were conducted at each displacement step. The displacement at each step was 40% larger than the previous step. Positive displacements are associated with extension of the actuator and are referred to as a "push" load, while negative displacements are associated with retraction of the actuator and are referred to as a "pull" load. Subsequently, cycles are denoted with a plus or minus sign to indication whether the push or pull portion of that cycle is being referenced. For example, cycle 21+ refers to the push portion of the first cycle in step 11. The loading protocol presented in Table 3-2 was followed for all specimens except Specimen CD12. After cycle 25+, Specimen CD12 was subjected to two cycles at +/- 3 in. displacement. This was due to concerns with exceeding the actuator force capacity of 330 kips.

Table 3-2. Loading Protocol.

Step	Cycle	Disp. (in.)	Disp. (% of span)	Number of cycles	Rate (in./min)
1	1 2	0.038	0.040	2	0.061
2	3 4	0.054	0.056	2	0.086
3	5 6	0.075	0.078	2	0.120
4	7 8	0.105	0.109	2	0.169
5	9 10	0.148	0.154	2	0.236
6	11 12	0.207	0.215	2	0.331
7	13 14	0.289	0.301	2	0.463
8	15 16	0.405	0.422	2	0.648
9	17 18	0.567	0.591	2	0.907
10	19 20	0.794	0.827	2	1.270
11	21 22	1.111	1.157	2	1.778
12	23 24	1.556	1.621	2	2.000
13	25 26	2.178	2.269	2	2.000
14	27 28	3.049	3.176	2	2.000

Crack maps and FRP debonding maps were made at various cycles throughout the test. Crack maps were typically made at the peaks of cycles 15+, 15-, 21+, and 21-. Crack maps were made simply by observing crack locations from beneath the slab and marking them on a sheet of paper. Crack widths were measured with a crack card. FRP debonding maps were made at varying cycles between tests, as the progression of debonding during a cycle justified the creation of a debonding map at that cycle. To determine the location of debonded FRP, a large steel washer was tapped on the FRP surface and hollow sounds indicated debonding. Areas of debonding were marked on the FRP using a white paint pen and FRP debonding maps were transcribed from overhead photos taken during the test.

3.7. Instrumentation

Each test used ten string potentiometers, two laser transducers, and between thirteen and sixteen strain gages on the reaction truss, as shown in Figure 3-18. For specimens strengthened with FRP, between eight and eighteen strain gages were installed on the FRP to measure strain in the direction of the gaged sheet. The locations of the FRP strain gages are presented in Figure 3-16. Each strain gage was located at the center of the width of the gaged FRP sheet. Additionally, Specimen CD13 and CD14 each utilized sixteen strain gages on the internal reinforcing steel, eight of which were installed on the chord beam longitudinal reinforcement while the other eight gages were installed on the distributed reinforcement mesh in the slab. The locations of the reinforcing steel strain gages are presented in Figure 3-17. Each strain gage was installed to measure strain in the longitudinal direction of the gaged reinforcing steel. For the deck bar strain gages, the last two letters indicate the direction of measured strain, where “EW” refers to strain measured perpendicular to the loading channels and “NS” refers to strain measured parallel to the loading channels. The nominal gauge length and resistance of all strain gages was 5 mm and 120 Ω, respectively.

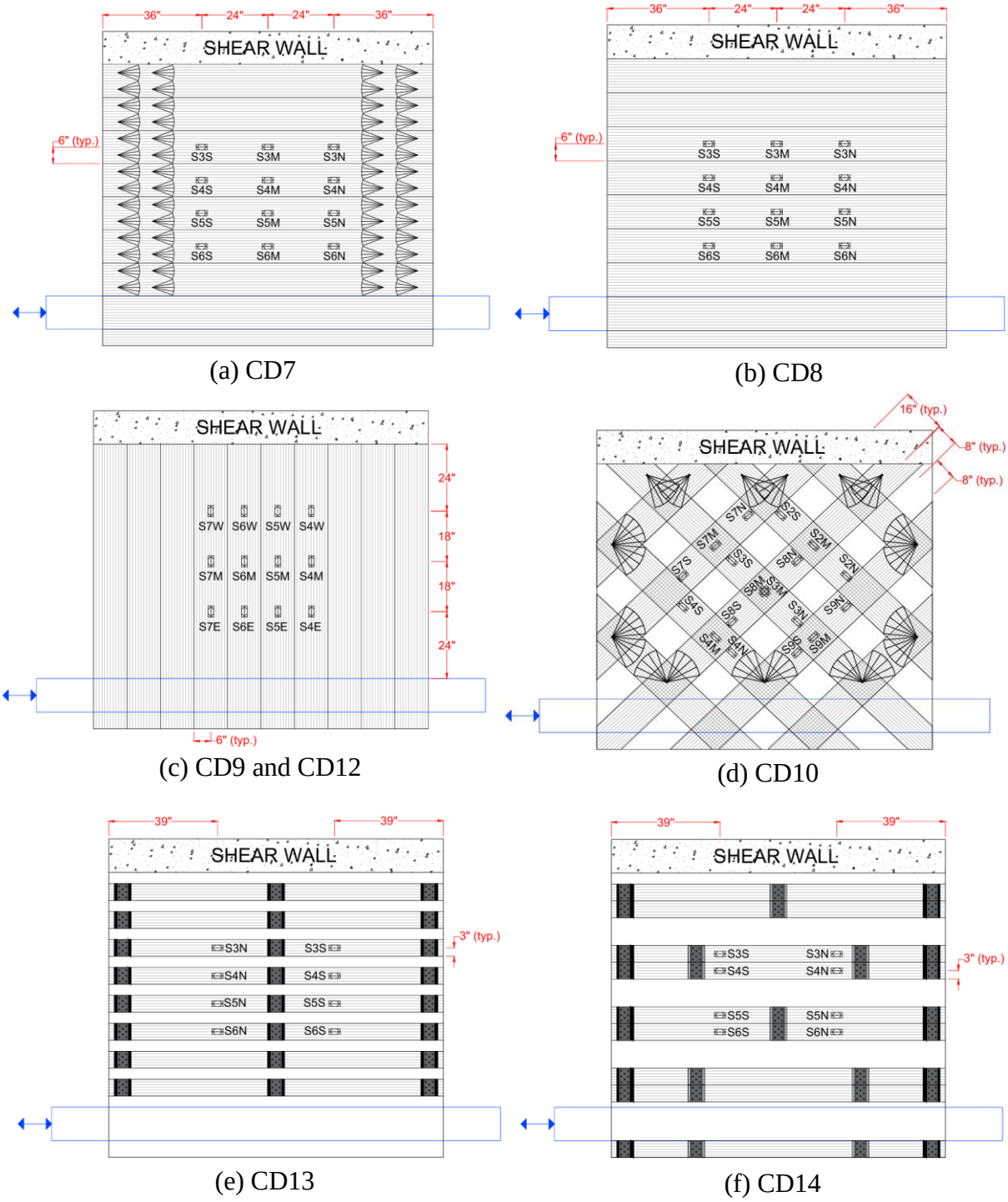

Figure 3-16. FRP Strain Gage Locations for Specimen: (a) CD7; (b) CD8; (c) CD9 and CD12; (d) CD10; (e) CD13; (f) CD14.

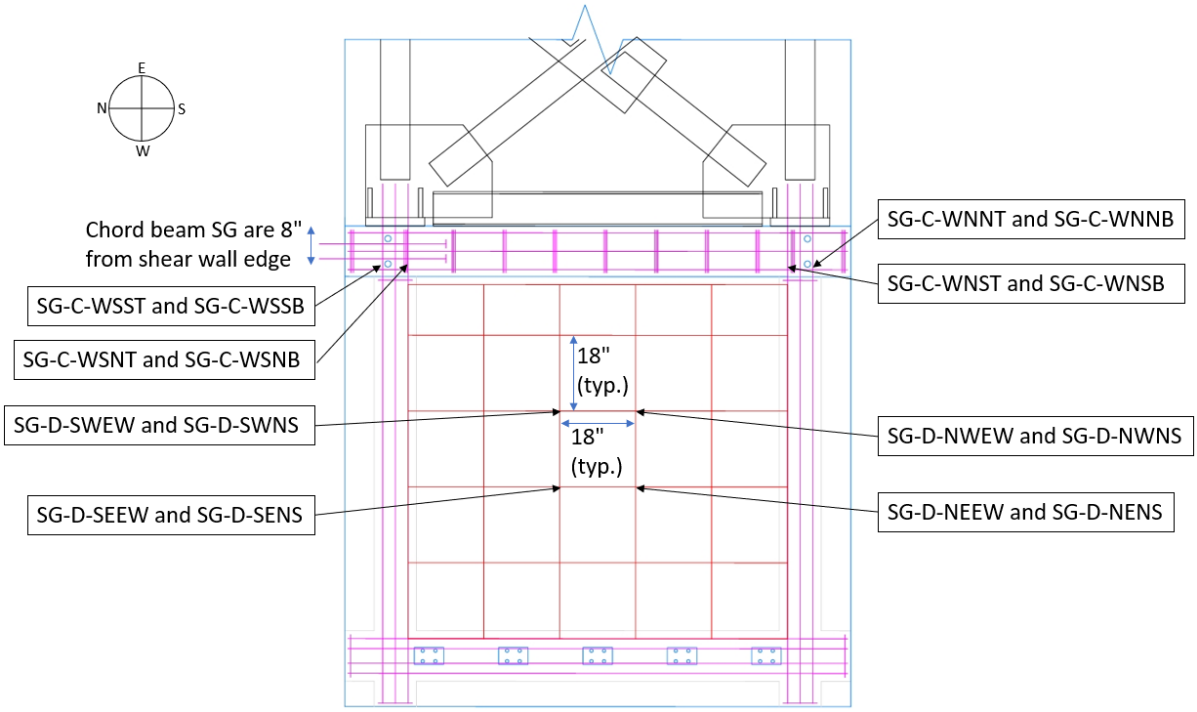

Figure 3-17. Reinforcing Steel Strain Gage Locations for Specimen CD13 and CD14.

Six string potentiometers were placed on the slab to measure local deformations of the diaphragm specimen. These string potentiometers were connected to wooden mounts and fastened to pieces of threaded rod embedded in the concrete. These string potentiometers were removed after the first observation of concrete spalling in the diaphragm to prevent potential damage to the sensors. Four string potentiometers were attached to edges of the diaphragm specimen and mounted to blocks attached to the ground to measure global deformations of the diaphragm specimen. The distances between string potentiometers, measured prior to testing, are provided in Appendix E:.

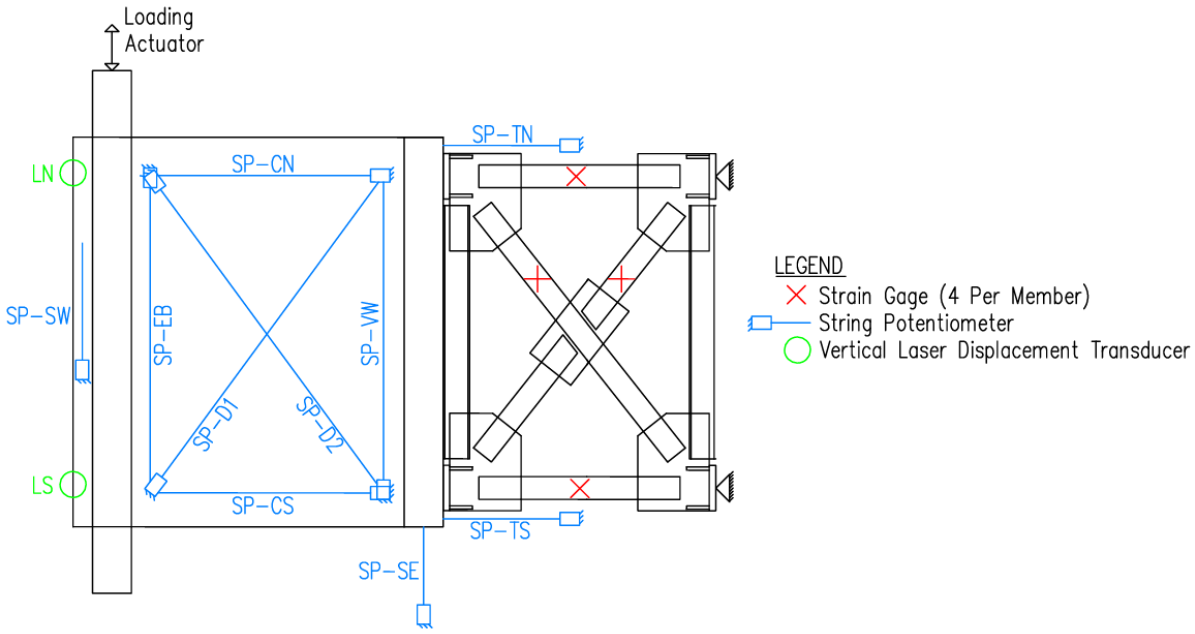

Figure 3-18. Schematic of Instrumentation Excluding FRP Strain Gages and Reinforcing Steel Strain Gages.

Measurements from the six string potentiometers on the slab were utilized to calculate the local shear angle throughout the duration of the test. Four different local shear angles can be measured using the Law of Cosines. For detailed equations on the calculation of the local shear angle, see Hutton et al. (2023). Measurements from the four string potentiometers fixed to a ground support were used to calculate the global shear angle throughout the duration of the test. The global shear angle is calculated using Eq. (16).

$$\gamma_g = \frac{\Delta SE - \Delta SW}{A} - \frac{\Delta TN - \Delta TS}{B} \tag{16}$$

where: γ_g is the global shear angle (rad); ΔSE is the displacement recorded by sensor SP-SE (in.); ΔSW is the displacement recorded by sensor SP-SW (in.); ΔTN is the displacement recorded by sensor SP-TN (in.); ΔTS is the displacement recorded by sensor SP-TS (in.); A is the center-to-center distance between sensors SP-SW and SP-SE (in.); and B is the center-to-center distance between sensors SP-TS and SP-TN (in.).

3.8. Material Properties

3.8.1 Concrete

The diaphragm specimens were constructed in four separate pairs. For specimens using LWC (Specimen CD11 and CD12), the concrete was specified to have a 28-day compressive strength of 3000 psi, and a unit weight of 114 lb/ft^3. For specimens using NWC, the concrete was specified to have a 28-day compressive strength of 2500 psi, and a unit weight of 150 lb/ft^3. The LWC mix used a 3/4 in. expanded shale aggregate in addition to an air entrainment agent, while the NWC mix uses a 3/8 in. crushed limestone aggregate. Both mix designs had a specified slump of 4 in.

The material properties of the concrete are presented in Table 3-3. Concrete cylinders were prepared following ASTM C31 (2022). On the day of each experimental test, the concrete cylinder compressive strength was determined following ASTM C39 (2022) and the concrete cylinder splitting tensile strength was determined following ASTM C496 (2017). The elastic modulus was calculated following ACI 318 (2019) Clause 19.2.2.1.b.

Table 3-3. Concrete Material Properties at Time of Testing.

Specimen ID	**4 in. x 8 in. Compressive Strength, f_{cm} (psi)**	**Splitting Tensile Strength, f_{sp} (psi)**	**Unit Weight (lb/ft^3)**	**Calculated Modulus of Elasticity, E_c (ksi)**
CD7	2650	250	139.7	2805
CD8	3050	265	139.7	3009
CD9	2980	Not tested	140.9	3013
CD10			137.3	2898
CD11	5620	355	116.9	3127
CD12	5690	380	116.9	3146
CD13	2980	Not tested	137.5	2905
CD14	3150	330	135.8	2931

3.8.2 Reinforcing Steel

All reinforcing steel used in the diaphragm specimens consisted of ASTM A615 Grade 60 rebar. The reinforcing steel was ordered in four separate batches, with each batch corresponding to a set of two specimens. Segments of #3 rebar from each batch was tested following

ASTM A370 (2022) to determine the yield strength, ultimate strength, and elongation. The average values of these material properties are presented in Table 3-4. The tabulated values represent the average of at least two experimental tests.

Table 3-4. Reinforcing Steel Material Properties.

Specimen ID	0.2% Yield Stress (ksi)	Ultimate Stress (ksi)	Elongation (%)
CD7 and CD8	73.6	111.3	15.7
CD9 and CD10	68.0	106.3	15.9
CD11 and CD12	82.3	94.9	11.2
CD13 and CD14	72.3	111.0	21.2

3.8.3 Externally Bonded FRP

Three different types of FRP were used in this experimental program, as shown in the test matrix in Table 3-1. Specimen CD7, CD8, CD9, and CD12 were strengthened with Simpson Strong-Tie and Structural Technology's V-Wrap C220HM. Specimen CD10 was strengthened with Simpson Strong-Tie and Structural Technology's V-Wrap C100HM. Specimen CD13 and CD14 were strengthened with Fyfe's Tyfo-SCH-41. All specimens were strengthened with CFRP. The manufacturer reported average FRP properties are presented in Table 3-5. Technical data sheets for each of the FRP systems used are provided in Appendix C:.

Table 3-5. Manufacturer Reported Material Properties.

Material	V-Wrap C220HM		V-Wrap C100HM		Tyfo-SCH-41	
Type	Dry Fiber	Compo-site	Dry Fiber	Compo-site	Dry Fiber	Compo-site
Tensile Strength (ksi)	670	152	790	216	620	171
Tensile Modulus (ksi)	37000	14700	42000	16700	36000	14600
Ultimate Elongation (%)	1.65	1.05	1.9	1.3	1.7	1.2
Thickness (in.)	-	0.04	-	0.02	-	0.04

Chapter 4. Experimental Results

Experimental results for the eight diaphragm specimens are included in this chapter. For all specimens, positive forces, displacements, and shear angles indicate that the actuator was pushing on the specimen, while negative values indicate that it was pulling.

4.1. CD7

Specimen CD7 was tested on September 13th, 2023. Figure 4-1 shows the hysteresis plot of the actuator load F versus the global shear angle γ_G. A portion of the global shear angle measurements for Specimen CD7 during post-peak displacement cycles required correction. This correction process is detailed in Appendix D:. Figure 4-2(a) shows a top view photograph of Specimen CD7 prior to testing. Figure 4-2(b-f) shows photographs of Specimen CD7 at different stages throughout testing. In Figure 4-1, callouts A through G are used to highlight key observations that are crucial for understanding the behavior and performance of the specimen:

- Callout A: The first crack near the shear wall corner was observed during the positive portion of cycle 13, corresponding to a global shear angle of $\gamma_G = 0.0009\,rad$ and actuator force $F = 124.4\,kips$.
- Callout B: Diagonal shear cracks within the field of the diaphragm were first observed during the positive portion of cycle 15, at a global shear angle of $\gamma_g = 0.0014\,rad$ and actuator force $F = 163.1\,kips$.
- Callout C: The first signs of debonding over a small area near the middle of sheet S4 were observed at a global shear angle of $\gamma_G = 0.0020\,rad$ and $F = 194.0\,kips$ during the positive portion of cycle 19. The area where the debonding was localized corresponded with a diagonal shear crack, which was identified upon inspecting the underside of the specimen.
- Callout D: The peak load of $F = 284.2\,kips$ was achieved at a global shear angle of $\gamma_G = 0.0049\,rad$ during the positive portion of cycle 22. Localized debonding in the field of the diaphragm of FRP sheets 2, 3, 4 was observed.

- Callout E: The actuator reached its maximum pull force, $F = -272.6\ kips$ at a global shear angle of $\gamma_G = -0.0053\ rad$ during the negative portion of cycle 22.
- Callout F: Several important behaviors were observed at this stage:
  - The FRP sheets numbered 4, 5, 6, and 7 experienced complete intermediate crack debonding in the areas between the FRP anchors.
  - Concurrently, the slab flanges, where the FRP anchors were installed, began exhibiting signs of flexural distress. This distress was a result of the tensile forces developed in the anchors, which exerted an upward force at the ends of the slab.
  - The specimen began exhibiting signs of direct shear cracks at the interface of the diaphragm slab and the edge beam.
  - Initial signs of concrete spalling were observed in the field of the diaphragm. The spalling was due to the intersecting network of opposing diagonal shear cracks which caused unsupported segments of concrete to fall out of the specimen. The extent of concrete loss increased as post-peak displacement grew.
- Callout G: A direct shear failure at the interface between the slab and the edge beam was clearly observed during the positive portion of cycle 24, at a global shear angle of $\gamma_G = 0.0149\ rad$. Concurrently, approximately 20% of the diaphragm's field had undergone spalling, a result of the progressively expanding network of diagonal shear cracks.

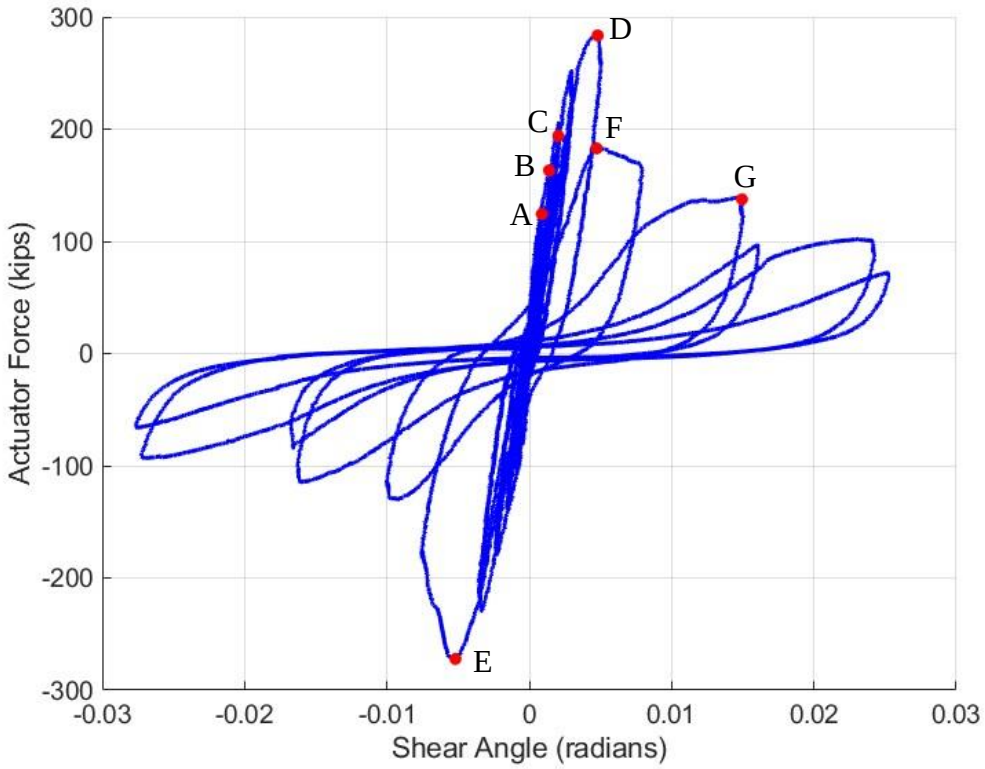

Figure 4-1. Corrected Hysteretic Shear Angle Response of Specimen CD7.

(a) (b)

(c) (d)

(e) (f)

Figure 4-2. Photographs of Specimen CD7: a) Prior to Testing; b) Post-test Condition of the Specimen; c) Shear Cracks in Concrete Observed from the Underside of the Slab; d) Anchor Pullout; e) FRP Debonding Near the Loading Beam; f) Spalling of Concrete Due to Out of Plane Bending.

Figure 4-3 shows the FRP strain measurements as recorded by the 12 strain gauges installed on sheets S3, S4, S5, and S6 plotted against the actuator load. Table 4-1 provides a summary of the FRP strains at peak load ε_f^{pk} from eight of the 12 FRP strain gauges. Strain readings from gauges S5M, S5S, S6M, and S6S were deemed unreliable (spurious) near peak

load and were consequently excluded from the evaluation. The average FRP strain at peak load, derived from the data of the remaining eight gauges, was determined to be 0.0019.

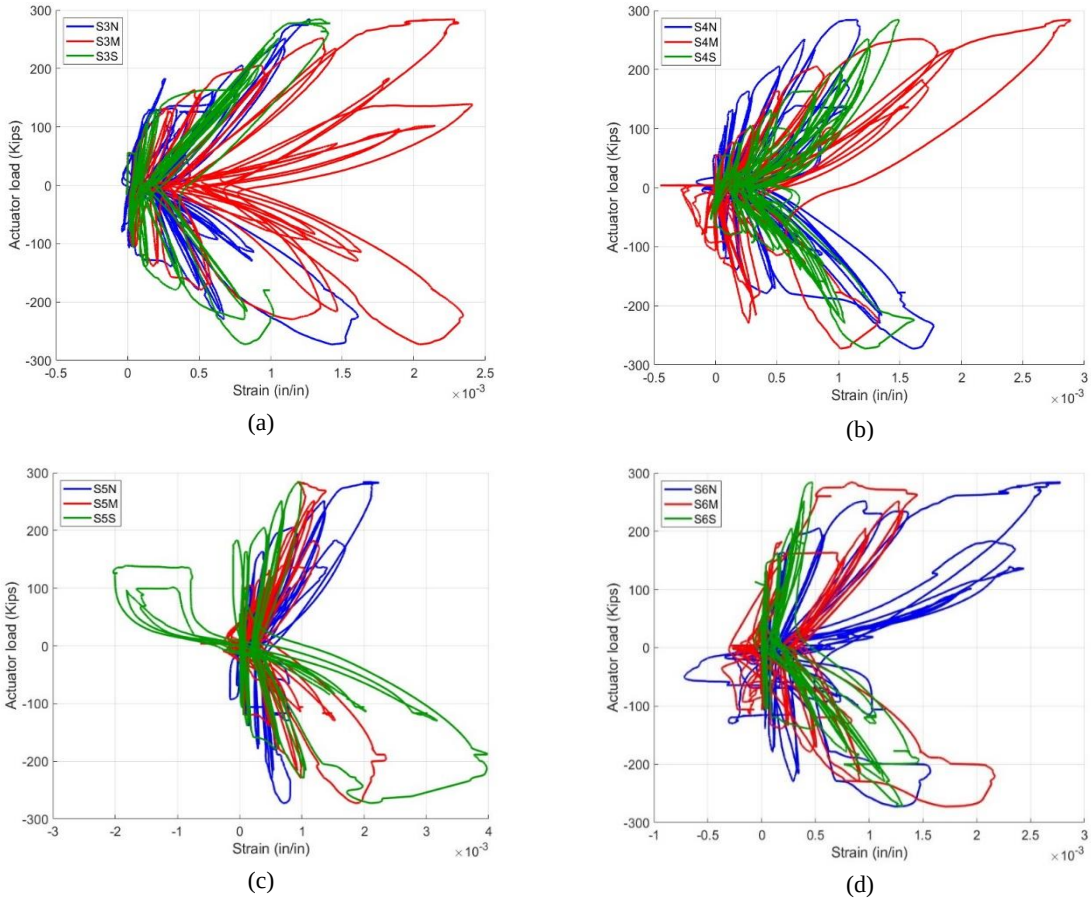

Figure 4-3. FRP Strain Measurements from Specimen CD7:
(a) Sheet S3; (b) Sheet S4; (c) Sheet S5; (d) Sheet S6.

Table 4-1. FRP Strains at Peak Load for Specimen CD7.

Strain gauge	**Strain at peak load, ε_f^{pk}**
S3N	0.0013
S3M	0.0023
S3S	0.0013
S4N	0.0011
S4M	0.0029
S4S	0.0015
S5N	0.0021
S6N	0.0027

Figure 4-4 shows the crack maps for Specimen CD7 taken at the peak push and pull actuator load for a given cycle. Cracks were marked and measured throughout the test, and maps were prepared to document each crack and associated width at cycles 16, 21 and 23. The first observation of debonding of FRP sheets was made during the positive portion of cycle 19. Diagonal tension cracks developed, with average widths of 0.35 mm to 0.90 mm. The specimen reached its peak capacity of 284.2 kips. At the peak load, FRP sheets S1 and S2 were 50% debonded and FRP sheets S3, S4, S5, S6, and S7 were fully debonded. Sheets S1 and S2 remained engaged due to anchor action. Cracks widths measured up to 1 mm after the debonding had occurred.

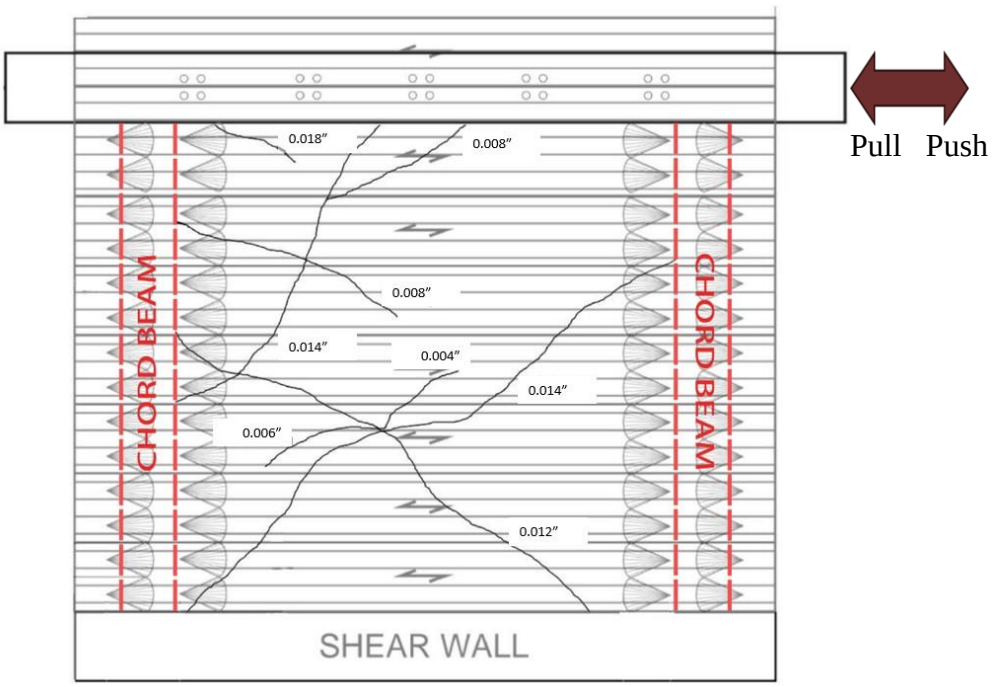

(a) Cycle 16 for a "push" load of 127 kips at $\gamma_G = 0.00067\ rad$ and for a "pull" load of -104 kips at $\gamma_G = -0.0011\ rad$.

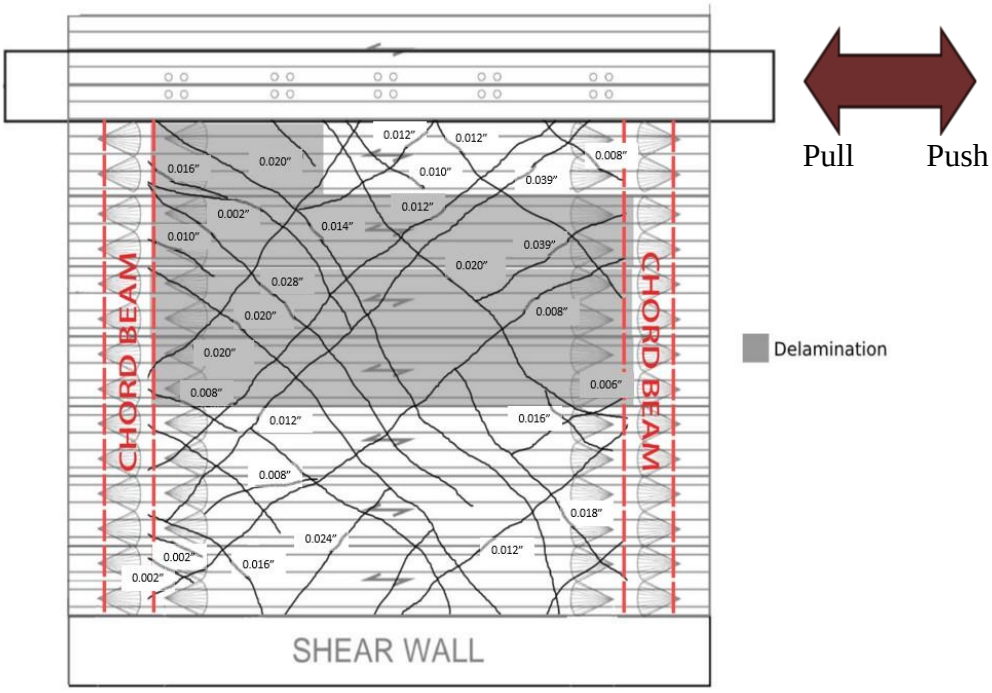

(b) Cycle 21 for a "push" load of 254 kips at $\gamma_G = 0.00267\ rad$ and for a "pull" load of -230 kips at $\gamma_G = -0.0037\ rad$.

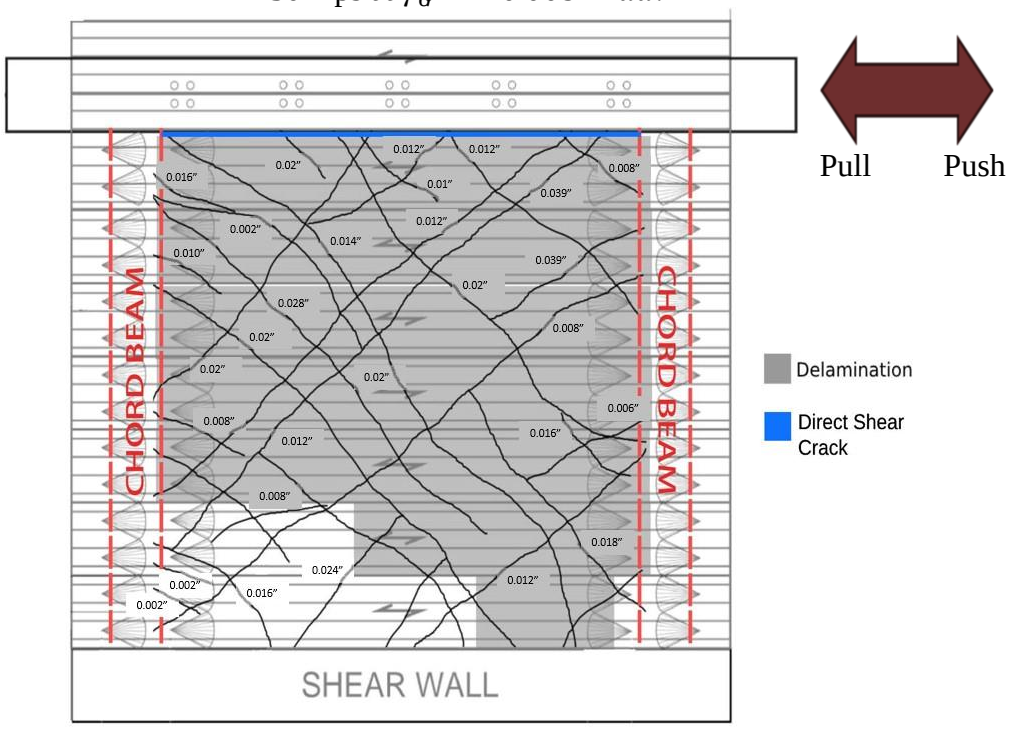

(c) Cycle 23 for a "push" load of 183 kips at $\gamma_G = 0.00726\ rad$ and for a "pull" load of -129 kips at $\gamma_G = -0.010\ rad$.

Figure 4-4. Crack and FRP Debonding maps for Specimen CD7.

4.2. CD8

Specimen CD8 was tested on October 28th, 2023. Figure 4-5 shows the hysteresis plot of the actuator load F versus the global shear angle γ_G. A portion of the global shear angle measurements during post-peak cycles required correction due to concrete spalling at the mounting point of sensors SP-TS and SP-SE. This correction process is detailed in Appendix D:. Figure 4-6(a) shows a top view photograph of Specimen CD8 prior to testing. Figure 4-6(b-f) shows photographs of Specimen CD8 at different stages throughout testing. In Figure 4-5, callouts A through G are used to highlight key observations that are crucial for understanding the behavior and performance of the specimen:

- Callout A: The first diagonal crack was observed during the positive portion of cycle 16, corresponding to a global shear angle of $\gamma_G = 0.0008\, rad$ and actuator load $F = 132.3\, kips$.
- Callout B: The first signs of FRP bulging on sheet 2 and sheet 6 were observed at a global shear angle of $\gamma_G = 0.0014\, rad$ and actuator load $F = 177.5\, kips$ during the positive portion of cycle 17. The area where the debonding was localized corresponded with a diagonal shear crack, which was identified upon inspecting the underside of the specimen.
- Callout C: Continued widening of diagonal shear cracks within the field of the diaphragm was observed during the negative portion of cycle 17, at a global shear angle of $\gamma_g = -0.0010\, rad$ and actuator load $F = -143.5\, kips$.
- Callout D: The FRP sheet 6 was completely debonded at a global shear angle of $\gamma_G = 0.0032\, rad$ and actuator force of $F = 281.5\, kips$ during the positive portion of 21. Debonding appeared to be instigated by an intermediate shear crack in the field of the diaphragm and propagated towards the end of the sheet. Localized debonding in the field of the diaphragm of FRP sheets 2, 3, 4 and 5 was observed. Initial spalling of concrete was observed at the midspan of the specimen.
- Callout E: The actuator reached its maximum pull force, $F = -255.2\, kips$ at a global shear angle of $\gamma_G = -0.0032\, rad$ during the negative portion of cycle 21.

- Callout F: Several important behaviors were observed at this stage as the actuator reached its maximum push load $F = 287.0\ kips$ at a global shear angle of $\gamma_G = 0.0046\ rad$ during the positive portion of cycle 23.
    - All the FRP sheets that were still bonded experienced a debonding failure due to intermediate crack debonding.
    - The first signs of spalling of concrete were observed in the field of the diaphragm. The spalling was due to the intersecting network of opposing diagonal shear cracks which caused unsupported segments of concrete to fall out of the specimen. The extent of concrete loss increased as post-peak displacement grew.
    - A narrow direct shear crack was noted along the intersection of the edge beam and the diaphragm slab.
- Callout G: Torsional rotation of loading beam was observed at a global shear angle of $\gamma_G = 0.0181\ rad$ and actuator load of $F = 73.2\ kips$ during the positive portion of cycle 26. Concurrently, approximately 40% of the diaphragm's field had undergone spalling, a result of the progressively expanding network of diagonal shear cracks.

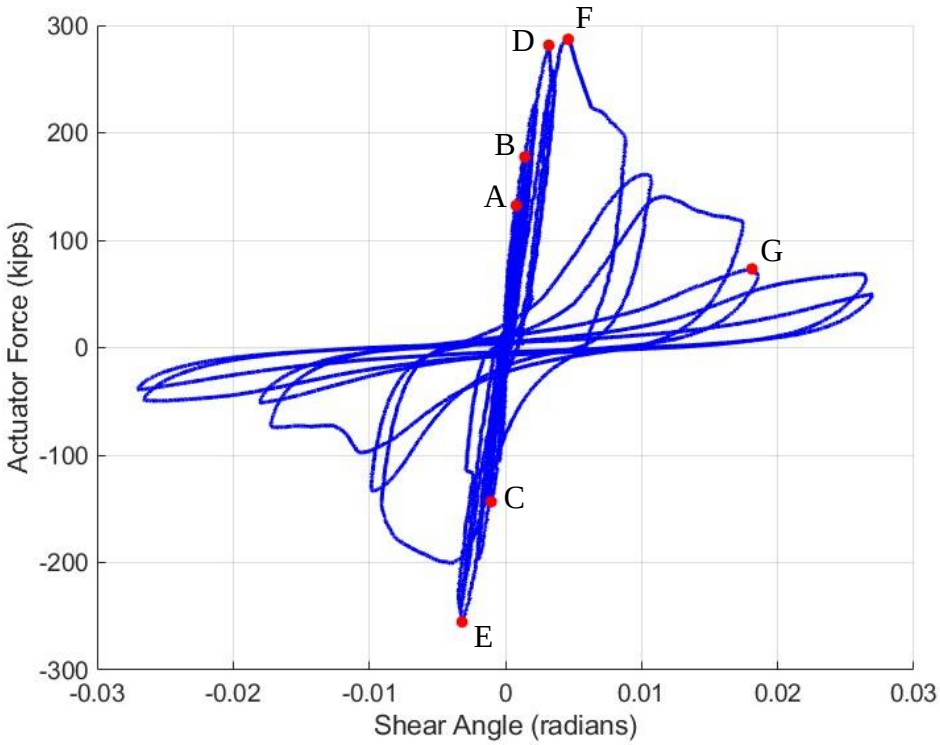

Figure 4-5. Corrected Hysteretic Shear Angle Response of Specimen CD8.

(a)

(b)

(c)

(d)

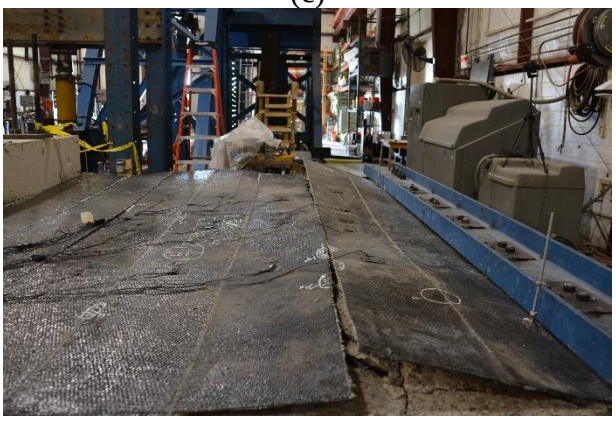

(e)

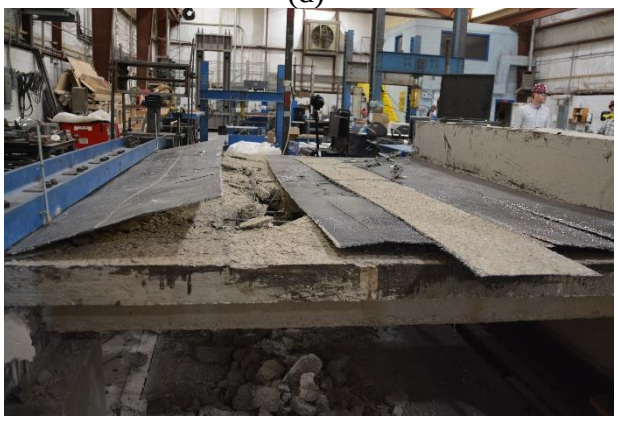

(f)

Figure 4-6. Photographs of Specimen CD8: a) Before Testing; b) Post-test Condition of the Specimen; c) Diagonal Tension Cracks and Section Loss in Concrete; d) Cracks in Chord Beam; e) FRP Debonding Near the Actuator; f) Spalling of Concrete Due after FRP Debonding.

Figure 4-7 displays the FRP strain measurements as recorded by the 12 strain gauges installed on sheets S3, S4, S5, and S6 plotted against the actuator load. Table 4-2 provides a summary of the FRP strains at peak load ε_f^{pk} from nine of the 12 FRP strain gauges. Strain readings from gauges S6N, S6M, and S6S were deemed unreliable (spurious) near peak load

and were consequently excluded from the evaluation. The average FRP strain at peak load, derived from the data of the remaining nine gauges, was determined to be 0.0019.

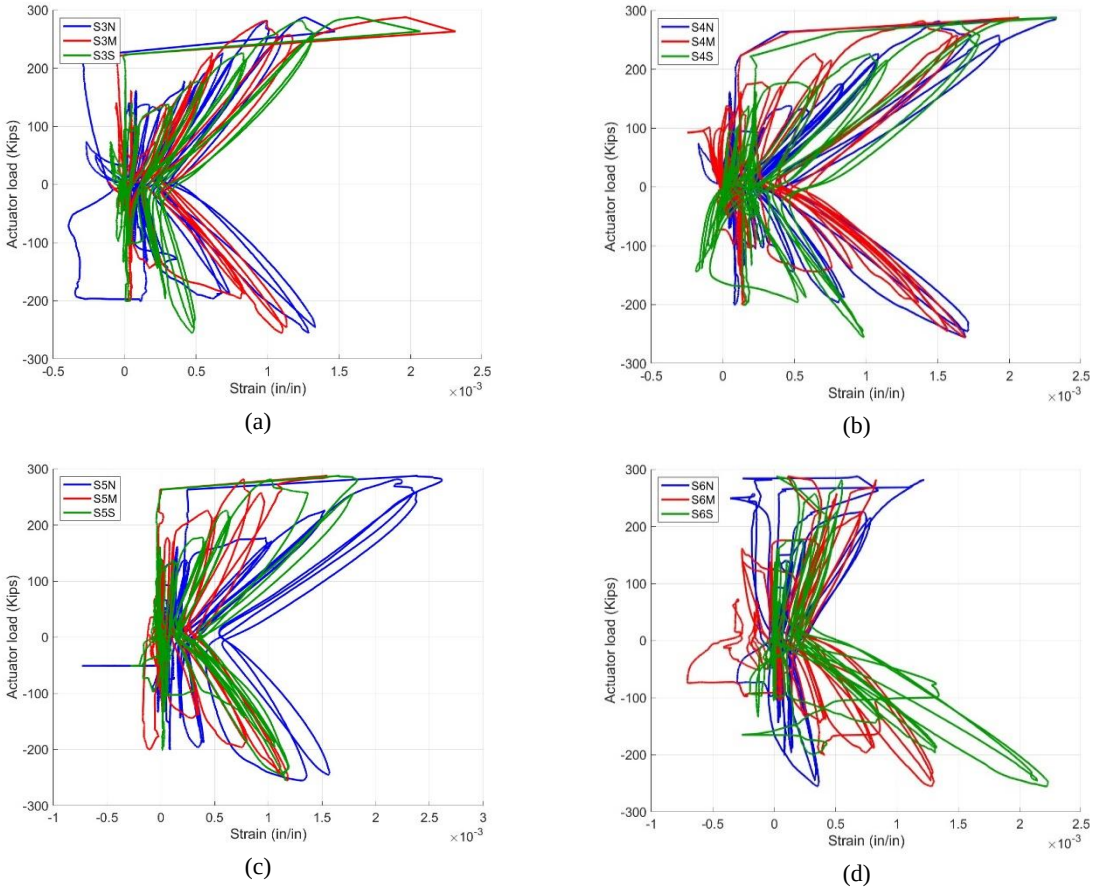

Figure 4-7. FRP Strain Measurements from Specimen CD8:
(a) Sheet S3; (b) Sheet S4; (c) Sheet S5; (d) Sheet S6.

Table 4-2. FRP Strains at Peak Load for Specimen CD8.

Strain gauge	**Strain at peak load, ε_f^{pk}**
S3N	0.0013
S3M	0.0019
S3S	0.0016
S4N	0.0023
S4M	0.0021
S4S	0.0023
S5N	0.0024
S5M	0.0015
S5S	0.0017

Figure 4-8 shows the crack maps for Specimen CD8 taken at the peak push and pull actuator load for a given cycle. Cracks were marked and measured throughout the test, and maps were prepared to document each crack and associated width at cycles 16 and 22. The first observation of debonding of FRP sheets was made during the positive portion of cycle 17. Diagonal tension cracks were observed at this load stage, with average widths of 0.35 mm to 1 mm. The specimen reached its peak capacity of 287 kips. At the peak load, all the FRP sheets had debonded.

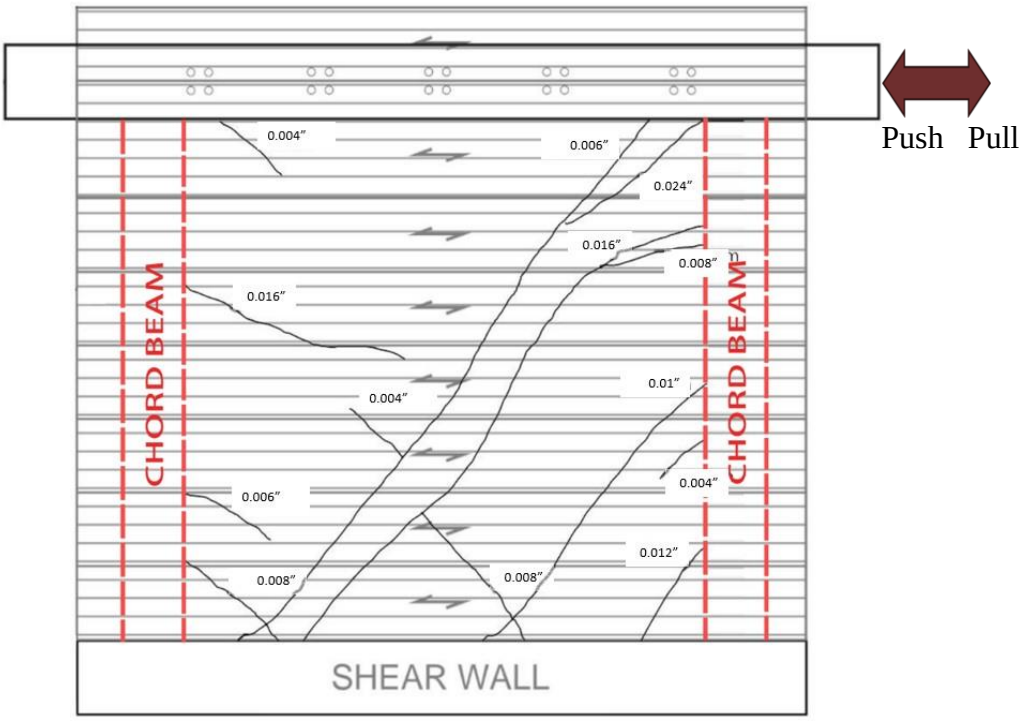

(a) Cycle 16 for a "push" load of 133 kips at $\gamma_G = 0.0009\ rad$ and for a "pull" load of -105 kips at $\gamma_G = -0.00037\ rad$.

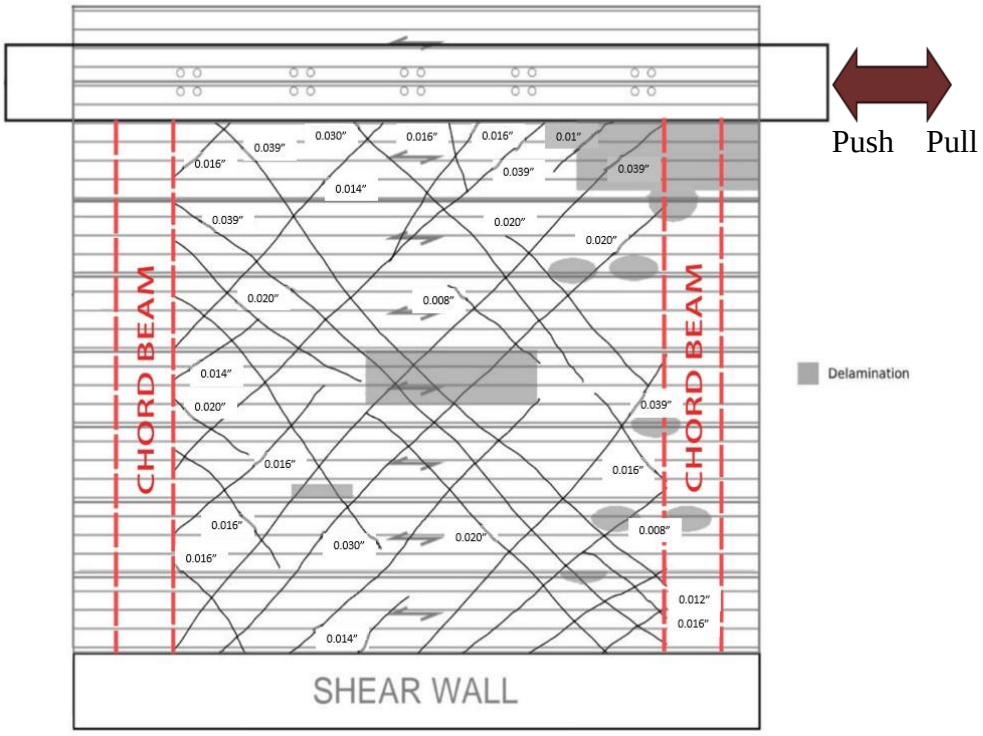

(b) Cycle 22 for a "push" load of 257 kips at $\gamma_G = 0.0035\ rad$ and for a "pull" load of -245 kips at $\gamma_G = -0.0033\ rad$.

Figure 4-8. Crack and FRP Debonding Maps for Specimen CD8.

4.3. CD9

Specimen CD9 was tested on March 21st, 2024. Figure 4-9 shows the hysteresis plot of the actuator load F versus the global shear angle γ_G. A portion of the global shear angle measurements for sensor SP-SE required correction due to concrete spalling at the sensor connection point (shown in Figure 4-10(d)) during the positive portion of cycle 25. This correction process is detailed in Appendix D:. Figure 4-10(a) shows a top view photograph of Specimen CD9 prior to testing. Figure 4-10(b-f) shows photographs of Specimen CD9 at different stages throughout testing. In Figure 4-9, callouts A through G are used to highlight key observations that are crucial for understanding the behavior and performance of the specimen:

- Callout A: The first flexural crack near the shear wall corner was observed during the negative portion of cycle 13, corresponding to a global shear angle of $\gamma_G = -0.00056\ rad$ and actuator force $F = -76.5\ kips$.

- Callout B: Diagonal shear cracks within the field of the diaphragm were first observed during the positive portion of cycle 15, at a global shear angle of $\gamma_g = 0.00056\,rad$ and actuator force $F = 130.9\,kips$.
- Callout C: The first signs of debonding over a small area near the middle of sheet S5 were observed at a global shear angle of $\gamma_G = 0.0027\,rad$ and $F = 244.0\,kips$ during the positive portion of cycle 21. The area where the debonding was localized corresponded with a diagonal shear crack, which was identified upon inspecting the underside of the specimen.
- Callout D: The peak load of $F = 318.6\,kips$ was achieved at a global shear angle of $\gamma_G = 0.0038\,rad$ during the positive portion of cycle 23. Localized debonding in the field of the diaphragm of FRP sheets 4, 5, 6, and 7 was observed. Debonding of FRP resulted in a loss of strength during subsequent cycles.
- Callout E: The actuator reached its maximum pull force, $F = -311.4\,kips$ at a global shear angle of $\gamma_G = -0.0049\,rad$ during the negative portion of cycle 23.
- Callout F: A direct shear crack at the interface between the slab and the shear wall was clearly observed during the positive portion of cycle 25, at a global shear angle of $\gamma_G = 0.0161\,rad$ and actuator load of $F = 110.2\,kips$.
- Callout G: Several important behaviors were observed during the negative portion of cycle 25, at a global shear angle of $\gamma_G = -0.0164\,rad$ and actuator load of $F = -90.5\,kips$:
    - The FRP sheets numbered 3, 4, 5, 6, and 7 experienced complete intermediate crack debonding in the areas between the FRP anchors.
    - Concurrently, the slab flanges, where the FRP anchors were installed, began exhibiting signs of flexural distress. This distress was a result of the tensile forces developed in the anchors, which exerted an upward force at the ends of the slab.
    - The chord beam further from the actuator began exhibiting diagonal cracks close to the shear wall likely due to torsional shear developed by flexural stress in the slab flange. At the peak displacement during the negative portion of cycle 25, concrete spalling occurred where torsional shear cracks had previously developed.

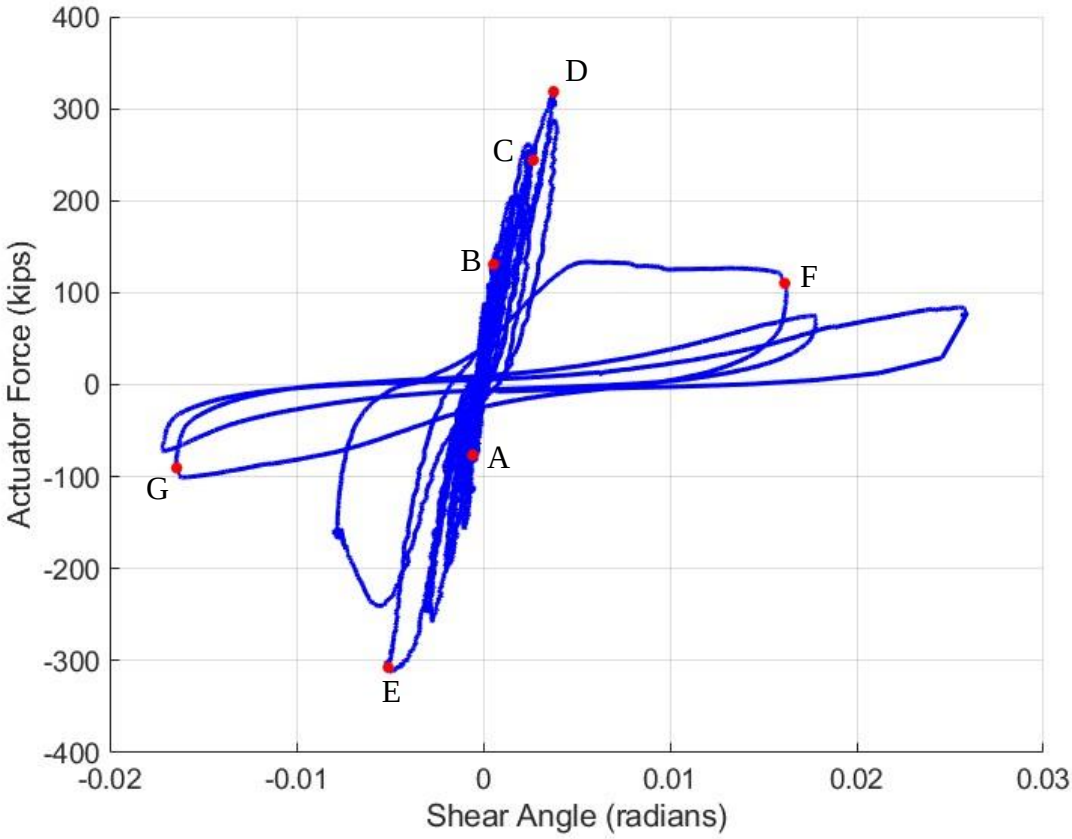

Figure 4-9. Corrected Hysteretic Shear Angle Response of Specimen CD9.

Figure 4-10. Photographs of Specimen CD9: a) Prior to Testing; b) After Testing; c) Shear Cracks in Concrete After Testing; d) Concrete Spalling at Shear Wall End After Testing; e) FRP Debonding Near the Shear Wall; f) Spalling of Concrete Due to Out of Plane Bending.

Figure 4-11 shows the FRP strain measurements as recorded by the 12 strain gauges installed on sheets S4, S5, S6 and S7 plotted against the actuator load. Table 4-3 provides a summary of the FRP strains at peak load ε_f^{pk} of the 12 FRP strain gauges. The average FRP strain recorded at peak load across the 12 strain gauges was 0.0022.

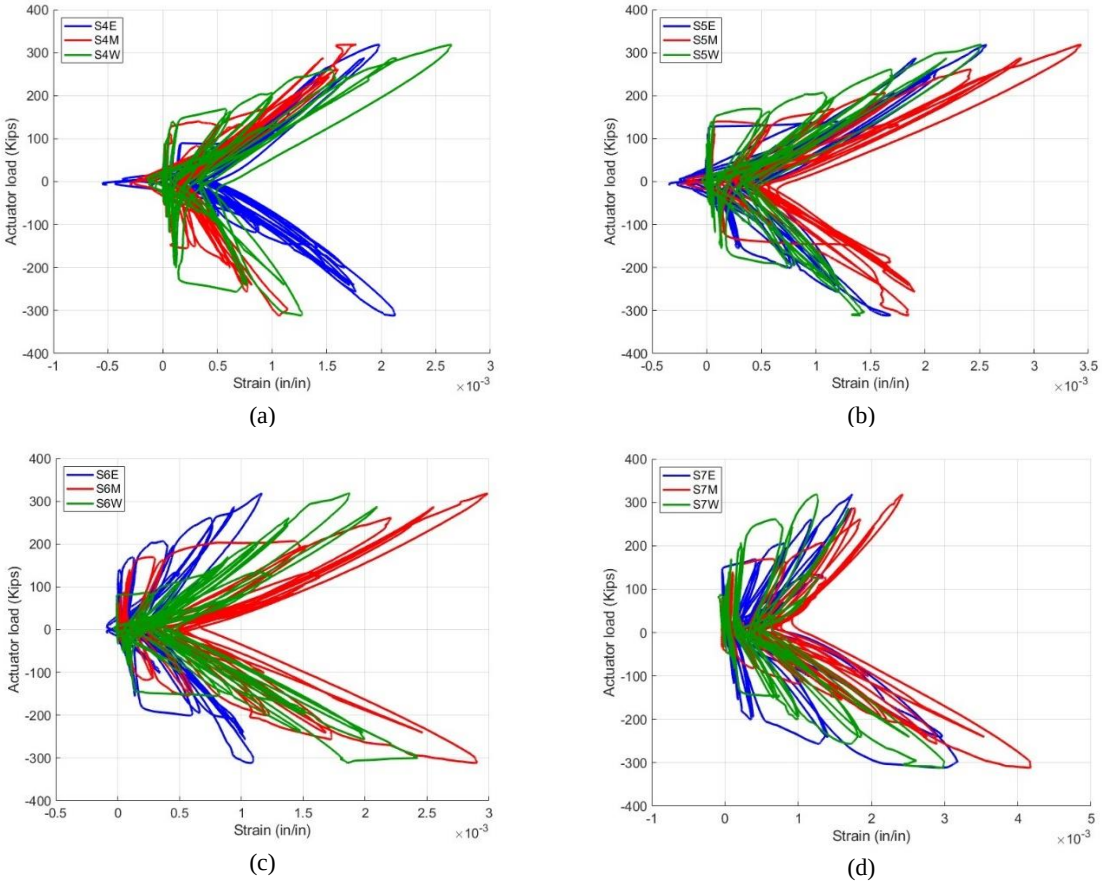

Figure 4-11. FRP Strain Measurements from Specimen CD9: (a) Sheet S4; (b) Sheet S5; (c) Sheet S6; (d) Sheet S7.

Table 4-3. FRP Strains at Peak Load for Specimen CD9.

Strain gauge	**Strain at peak load +318.6 kips, ε_f^{pk}**
S4E	0.0020
S4M	0.0018
S4W	0.0026
S5E	0.0026
S5M	0.0034
S5W	0.0025
S6E	0.0012
S6M	0.0030
S6W	0.0019
S7E	0.0017
S7M	0.0024
S7W	0.0013

Figure 4-12 shows the crack maps for Specimen CD9 taken at the peak push and pull actuator load for a given cycle. Cracks were marked and measured throughout the test, and maps were prepared to document each crack and associated width at cycles 15 and 21. Additionally, Figure 4-13 shows the debonding maps for Specimen CD9 also taken at the peak push and pull load for a given cycle.

The first flexural cracks were observed during the negative portion of cycle 13. Shear cracks appeared in the positive portion of cycle 15, with widths ranging from 0.15 mm to 0.3 mm, as shown in Figure 12(a). The initial debonding of the FRP sheets was noted in the positive portion of cycle 21. Diagonal tension cracks widened, reaching average widths of up to 1.25 mm in the positive portion of cycle 21 and up to 1.5 mm in the negative portion. During the negative portion of cycle 21, the FRP sheets continued to debond around the areas previously affected during the positive portion.

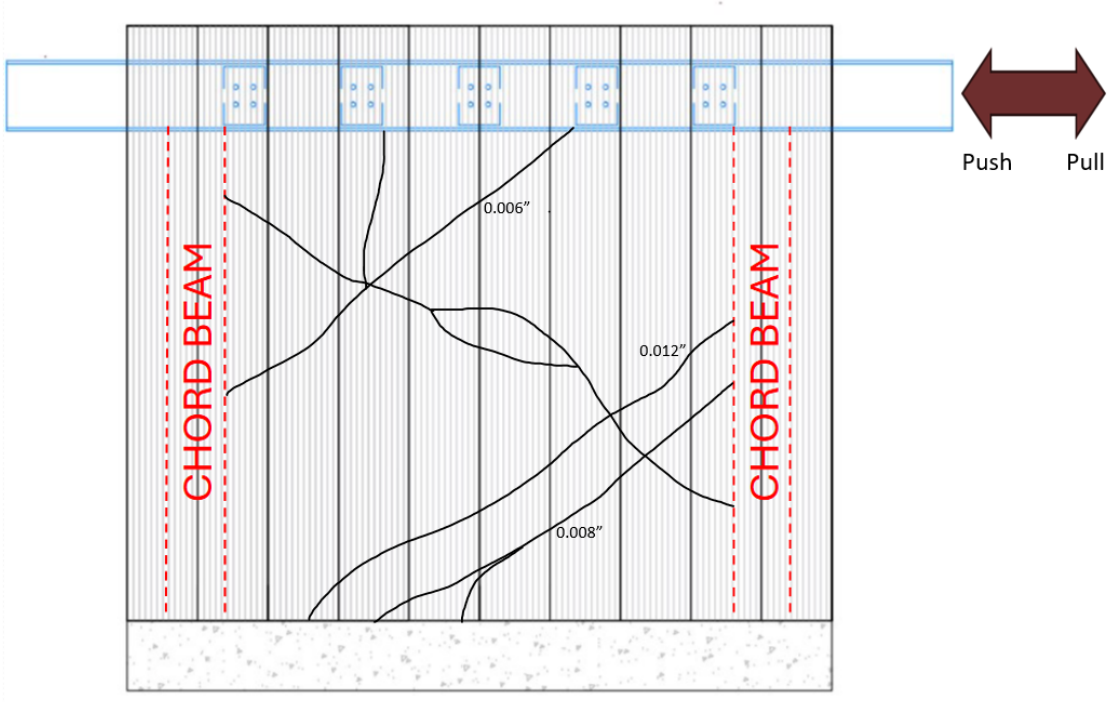

(a) Cycle 15 for a "push" load of 131 kips at $\gamma_G = 0.000557\ rad.$

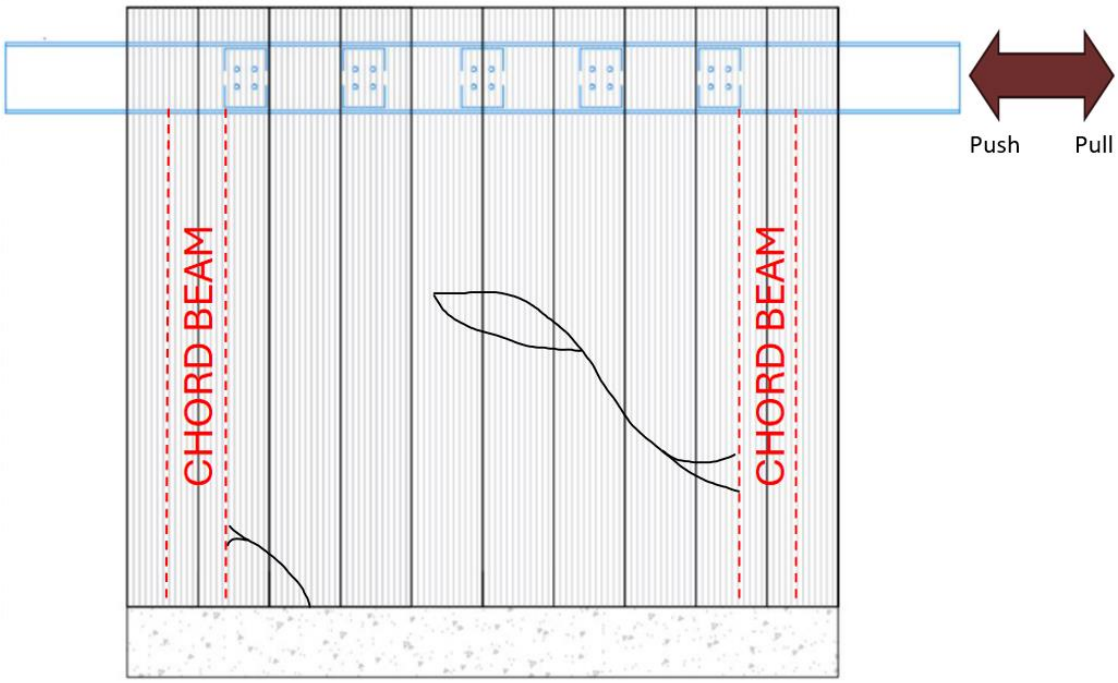

(b) Cycle 15 for a "pull" load of -113 kips at $\gamma_G = -0.00067\ rad.$

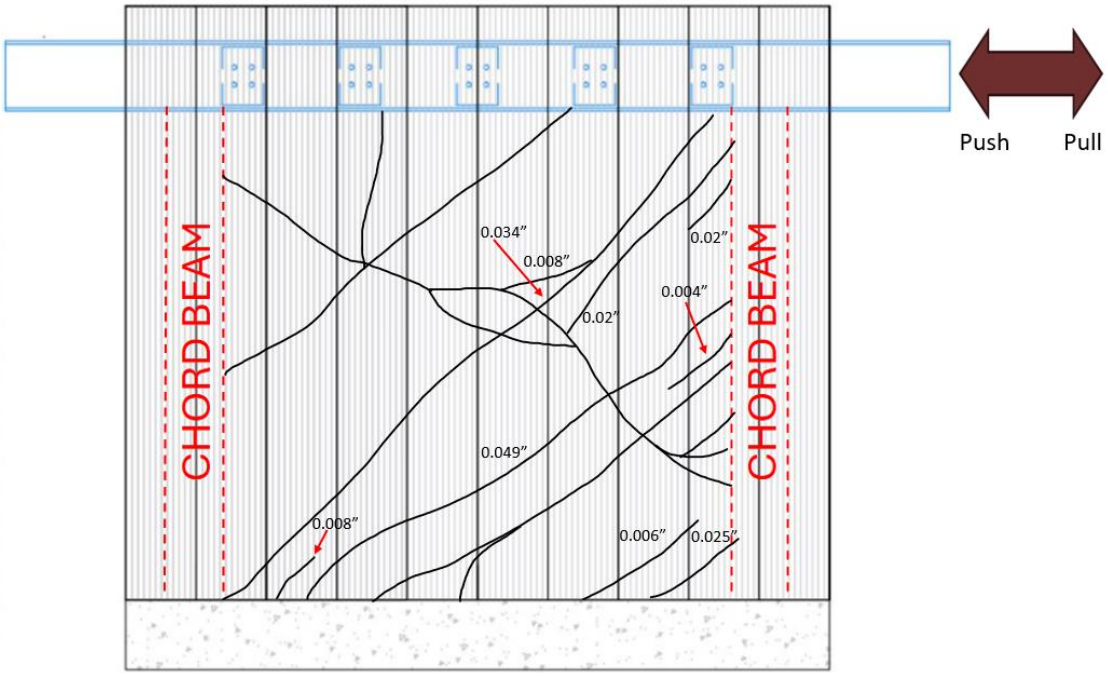

(c) Cycle 21 for a "push" load of 244 kips at $\gamma_G = 0.0027\ rad.$

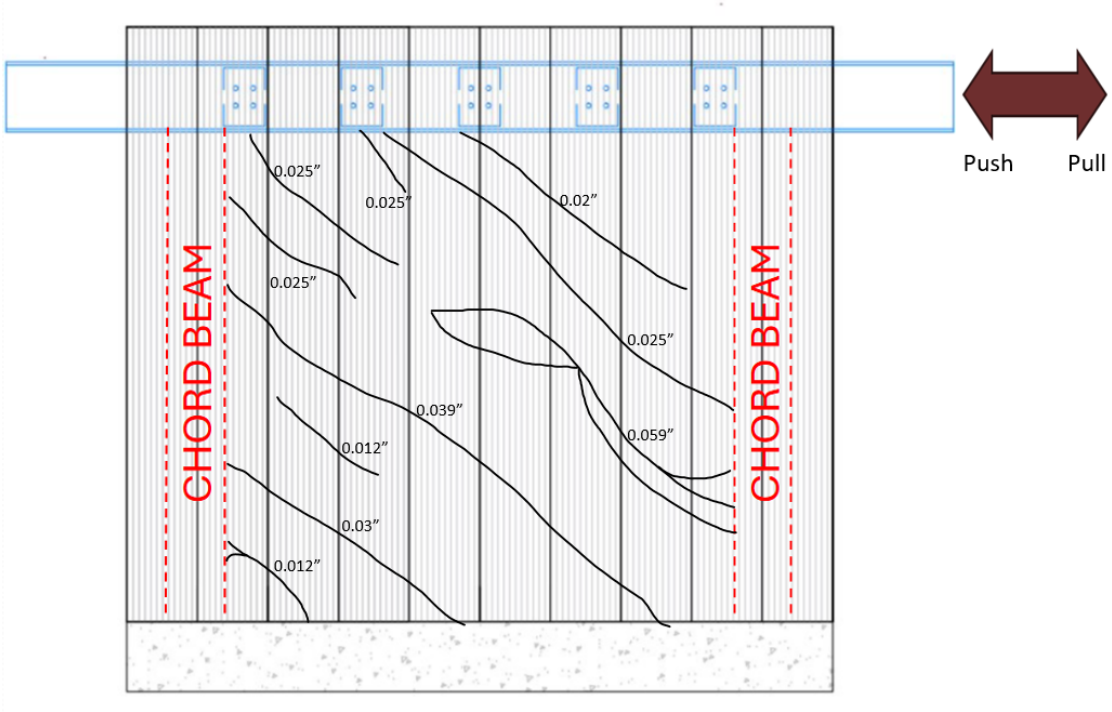

(c) Cycle 21 for a "pull" load of -243 kips at $\gamma_G = -0.003\ rad$.

Figure 4-12. Crack maps for Specimen CD9.

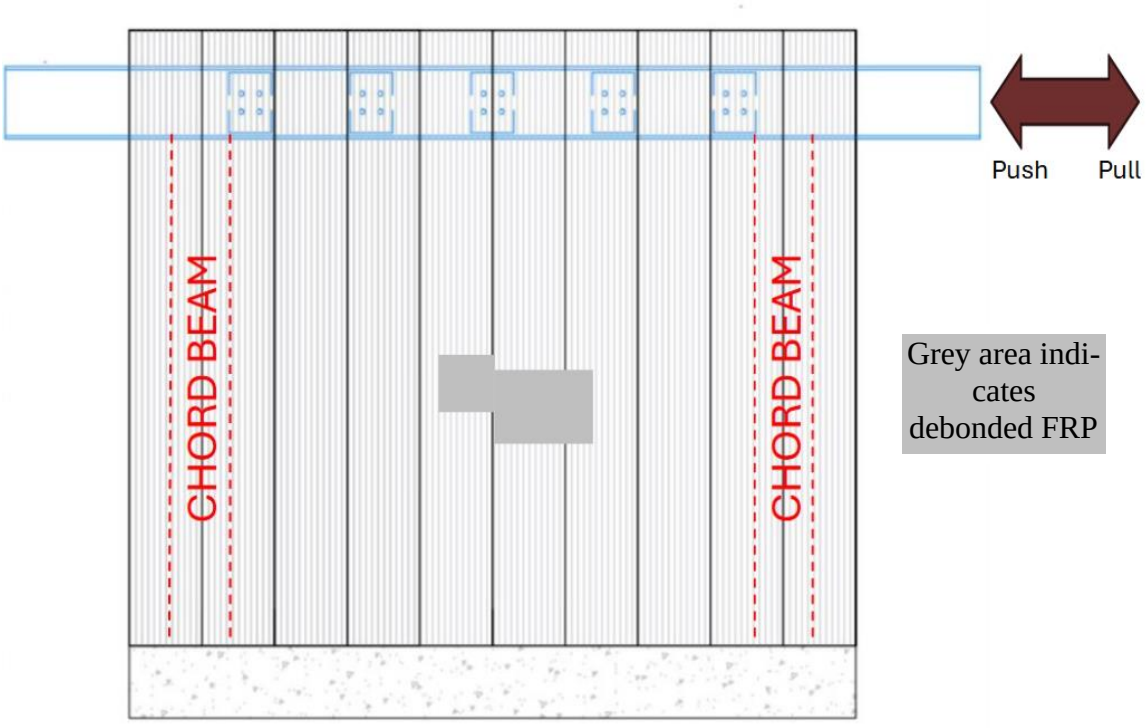

(a) Cycle 21 for a "push" load of 244 kips at $\gamma_G = 0.0027\ rad$.

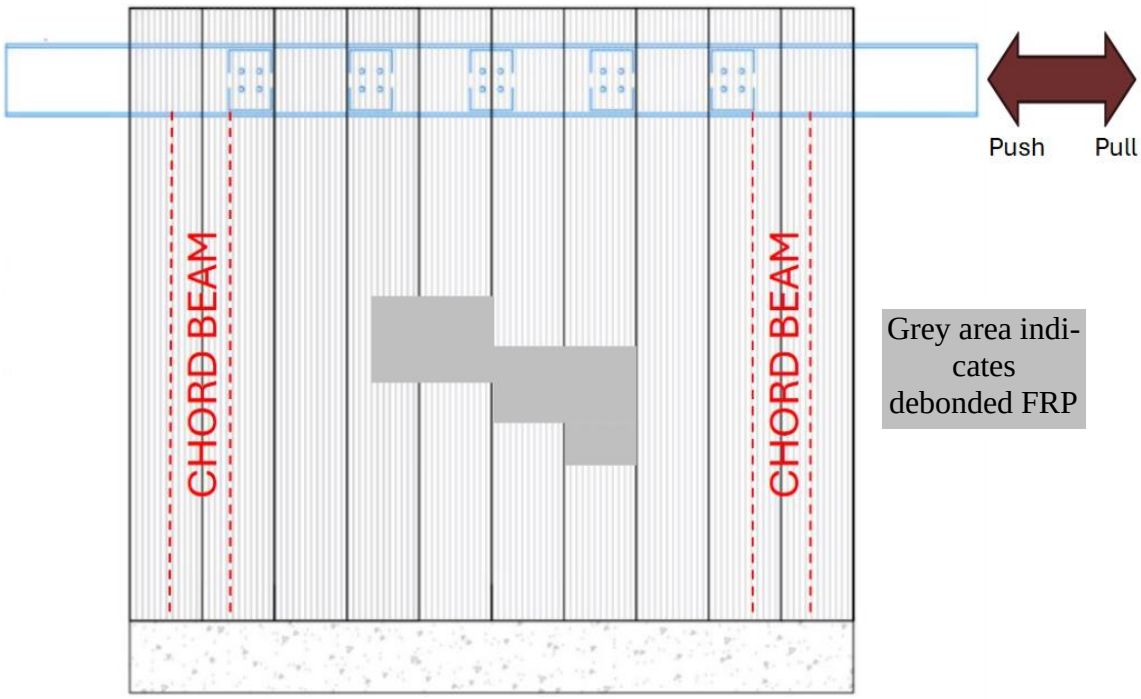

(b) Cycle 21 for a "pull" load of -243 kips at $\gamma_G = -0.003\ rad.$

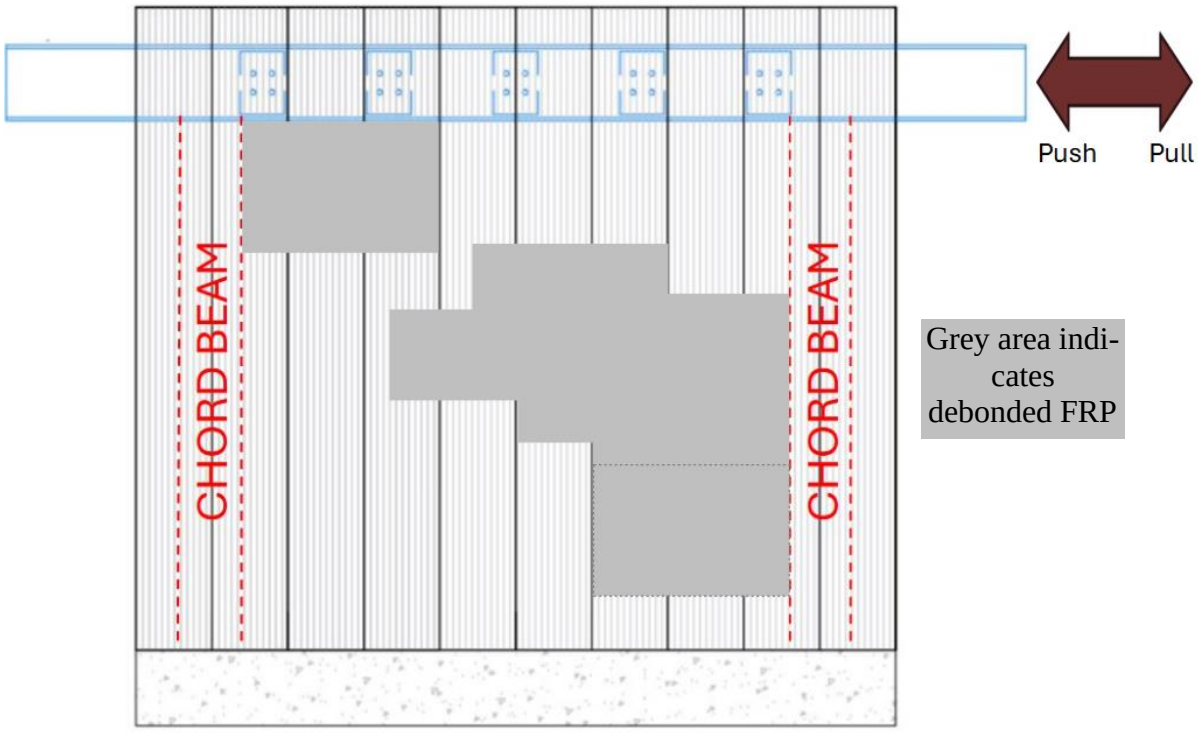

(c) Cycle 24 for a "pull" load of -240 kips at $\gamma_G = -0.0056\ rad.$

Figure 4-13. FRP debonding maps for Specimen CD9.

4.4. CD10

Specimen CD10 was tested on April 9th, 2024. Figure 4-14 shows the hysteresis plots of the actuator load F versus the global shear angle γ_G. A portion of the global shear angle measurements required correction due to concrete spalling at the sensor connection for SP-SE, as shown in Figure 4-15(a). This correction process is detailed in Appendix D:. Figure 4-15(a-b) show pre and post-test conditions of Specimen CD10. FRP rupture is shown in in Figure 4-15(e) and global debonding of all FRP sheets is shown in in Figure 4-15(f). In Figure 4-14, callouts A through I are used to highlight key observations that are crucial for understanding the behavior and performance of the specimen:

- Callout A: The first diagonal shear cracks in the field of the diaphragm were observed during the negative portion of cycle 13, corresponding to a global shear angle of $\gamma_G = -0.00037\ rad$ and actuator force $F = -65.6\ kips$.
- Callout B: Diagonal cracks continued to form and widen during the positive portion of cycle 15, corresponding to a global shear angle of $\gamma_G = 0.00049\ rad$ and actuator force $F = 111.0\ kips$. Diagonal cracks were measured at 0.003 in., 0.008 in., and 0.02 in..
- Callout C: Localized debonding was first observed during the positive portion of cycle 17, corresponding to a global shear angle of $\gamma_G = 0.00096\ rad$ and actuator force $F = 139.9\ kips$. The debonding was localized to a small area of FRP near strain gage S3S.
- Callout D: More localized debonding was observed during the positive portion of cycle 19, corresponding to a global shear angle of $\gamma_G = 0.0015\ rad$ and actuator force $F = 183.3\ kips$. The debonding was localized to the edge of sheet S3.
- Callout E: Debonding was observed to have propagated further by the positive portion cycle 21, corresponding to a global shear angle of $\gamma_G = 0.0026\ rad$ and actuator force $F = 236.4\ kips$. The majority of the debonding was contained to sheets S6, S7, S8, and S9, between sheets S3 and S2. The widest diagonal shear crack was also observed in this location.
- Callout F: The specimen reached its peak actuator load during the positive portion of cycle 23, corresponding to a global shear angle of $\gamma_G = 0.0034\ rad$ and actuator force

$F = 280.2\ kips$. As the specimen reached peak load, the FRP sheets S6, S7, and S8 ruptured between sheets S2 and S3.

- Callout G: The specimen reached its peak pull actuator load during the negative portion of cycle 23, corresponding to a global shear angle of $\gamma_G = -0.0050\ rad$ and actuator force $F = -271.0\ kips$.
- Callout H: FRP Sheet S9 ruptured between sheets S2 and S3 during the positive portion of cycle 24, corresponding to a global shear angle of $\gamma_G = 0.0067\ rad$ and actuator force $F = 170.5\ kips$.
- Callout I: Large portions of concrete in the diaphragm field were observed to spall by the positive portion of cycle 27, corresponding to a global shear angle of $\gamma_G = 0.0215\ rad$ and actuator force $F = 79.5\ kips$. The majority of the voids left in the diaphragm field were located near the location of the primary diagonal shear crack earlier in the test, which was also the location of FRP rupture observed in the positive portions of cycle 23 and 24.

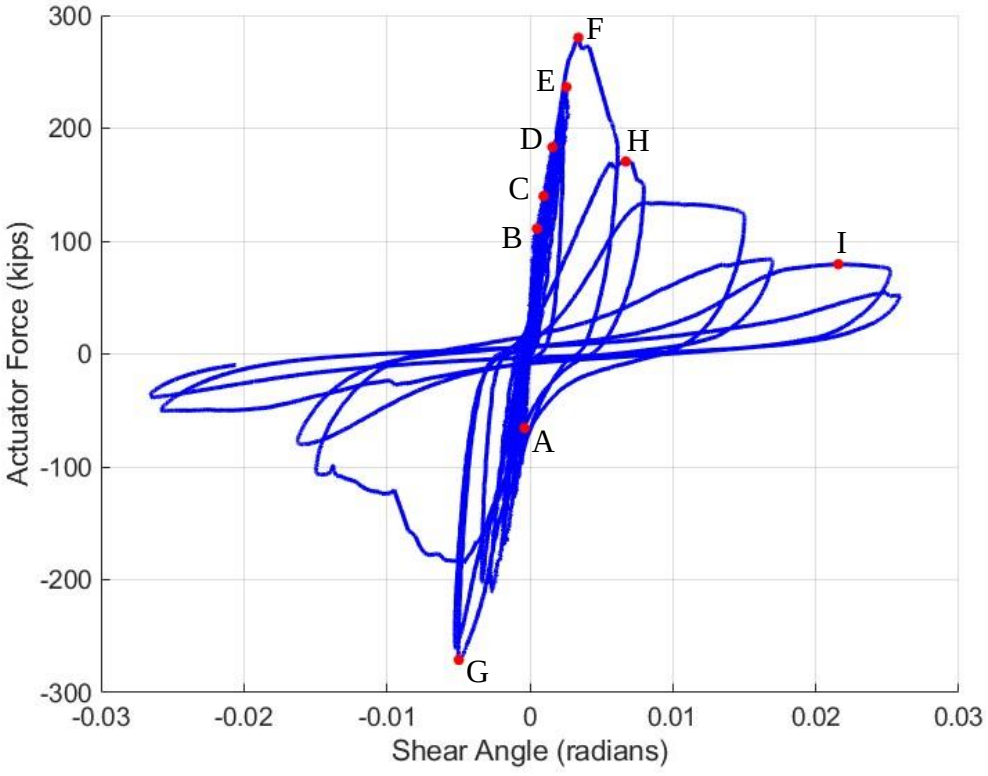

Figure 4-14. Corrected Hysteretic Shear Angle Response of Specimen CD10.

Figure 4-15. Photographs of Specimen CD10: a) Prior to Testing; b) Post-test Condition of the Specimen; c) Concrete Spalling Yielding Sensor SP-SE Unreliable; d) Shear Cracks in the Concrete; e) FRP Rupture of Sheets S6, S7, and S8; f) Post-test Condition Showing Global Debonding of the FRP.

Figure 4-16 shows the FRP strain measurements as recorded by the 18 strain gauges installed on sheets S2, S3, S4, S7, S8, and S9 plotted against the actuator load. Some of the data in the plots are truncated to better visualize FRP strain. The truncation point of the data was typically associated with large steps where the gage was deemed unreliable.

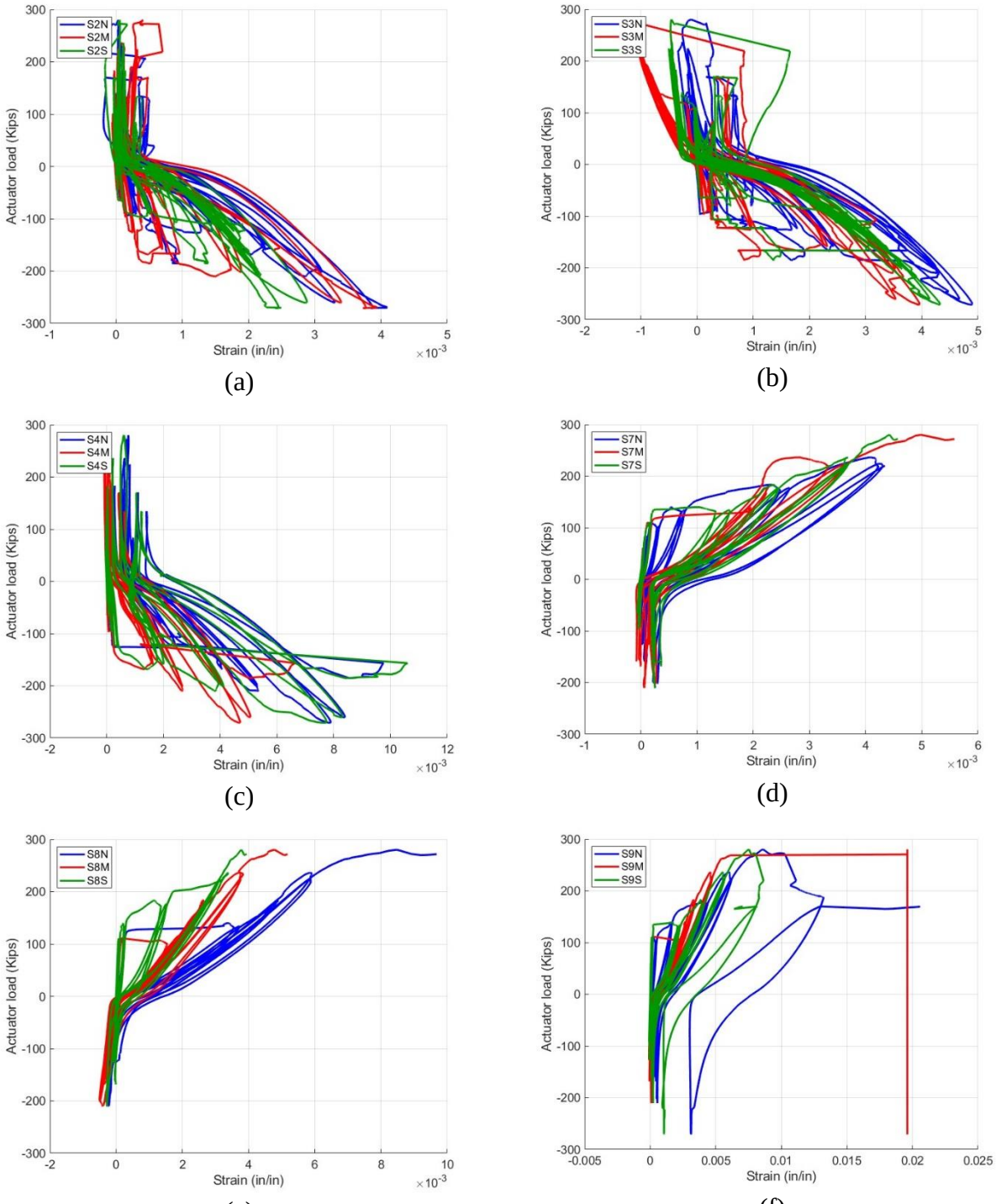

Figure 4-16. FRP Strain Measurements from Specimen CD10: a) Sheet S2; b) Sheet S3; c) Sheet S4; d) Sheet S7; e) Sheet S8; f) Sheet S9.

Assuming a state of pure shear stress in the diaphragm field and considering that FRP has negligible compressive strength, only the FRP sheets oriented parallel to the direction of principal tensile stress contributed to diaphragm shear strength. This assumption was generally

confirmed by the plots in Figure 4-16, as each gauge recorded much higher strains in one direction of applied load. Therefore, only FRP strain gauges along sheets S7, S8, and S9 were analyzed at peak load. Table 4-4 provides a summary of the FRP strains at peak load ε_f^{pk} of the seven reliable FRP strain gauges on sheets assumed to contribute to diaphragm shear strength in the push direction. Strain readings from gauges S7N and S9M were deemed unreliable (spurious) near peak load and were consequently excluded from the evaluation. The average FRP strain recorded at peak load across the seven reliable strain gauges was 0.0061.

Table 4-4. FRP Strains at Peak Load for Specimen CD10.

Strain gauge	**Strain at peak load, ε_f^{pk}**
S7M	0.0050
S7S	0.0044
S8N	0.0085
S8M	0.0048
S8S	0.0038
S9N	0.0086
S9S	0.0075

4.5. CD11

Specimen CD11 was tested on July 15th, 2024. As shown in Table 3-3, the concrete compressive strength was 5620 psi at the time of testing, although the specified compressive strength of the concrete was 3000 psi. This was attributed to the expanded shale aggregate likely absorbing water from the mix, resulting in a lower water cement ratio than specified. Figure 4-17 shows the hysteresis plot of the actuator load F versus the global shear angle γ_G. A portion of the global shear angle measurements required correction due to concrete spalling at the sensor connection for SP-SE (cycle 23, negative) and sensor cabling damage for SP-SW (cycle 25, positive), as shown in Figure 4-18(d). This correction process is detailed in Appendix D:. Figure 4-18(a) shows a top view photograph of Specimen CD11 prior to testing. Figure 4-18(b-d) shows photographs of Specimen CD11 at different stages throughout testing. In Figure 4-17, callouts A through G are used to highlight key observations that are crucial for understanding the behavior and performance of the specimen:

- Callout A: Both the first diagonal shear cracks in the field of the diaphragm and the first flexural cracks in the slab flanges were observed during the positive portion of cycle 13, corresponding to a global shear angle of $\gamma_G = 0.00081\, rad$ and actuator force $F = 84.7\, kips$.
- Callout B: Diagonal shear cracks in the diaphragm field in the negative direction were first observed during the negative portion of cycle 13, at a global shear angle of $\gamma_g = -0.00040\, rad$ and actuator force $F = -88.5\, kips$. Fewer diagonal shear cracks were observed in the negative direction compared to the positive portion of cycle 13.
- Callout C: Existing diagonal shear cracks opened while few new diagonal shear cracks formed during the positive portion of cycle 15, at a global shear angle of $\gamma_g = 0.0013\, rad$ and actuator force $F = 120.8\, kips$. The primary diagonal shear crack measured 0.035 in. in width, while other diagonal cracks measured between 0.003 in. and 0.008 in.
- Callout D: Existing diagonal shear cracks opened while several new diagonal shear cracks formed during the negative portion of cycle 15, at a global shear angle of $\gamma_g = -0.0013\, rad$ and actuator force $F = -102.6\, kips$. The primary diagonal shear cracks measured 0.02 in. and 0.016 in. in width, while other diagonal cracks measured 0.003 in. and 0.008 in.
- Callout E: The actuator reached its maximum push force $F = 225.5\, kips$ during the positive portion of cycle 21, corresponding to a global shear angle of $\gamma_g = 0.0039\, rad$.
- Callout F: The actuator reached its maximum pull force $F = -234.1\, kips$ during the negative portion of cycle 21, corresponding to a global shear angle of $\gamma_g = -0.0053\, rad$. After reaching peak strength, the specimen exhibited post-peak strength decay as diagonal tension shear cracks widened, leading to a loss of aggregate inter-lock. The residual strength was primarily governed by reinforcing steel bridging the cracks and the diagonal capacity of concrete struts along the crack paths.
- Callout G: Large portions of concrete in the field of the diaphragm spalled during the positive portion of cycle 25, leaving large voids in the field of the diaphragm. This was

associated with a push force $F = 77.6\,kips$ and a global shear angle of $\gamma_g = 0.0164\,rad$.

Unlike previously tested NWC diaphragm specimens, the diagonal shear cracks in the LWC Specimen CD11 tended to shear through the lightweight aggregate, resulting in relatively smooth crack planes. In contrast, cracks in NWC specimens were more jagged and meandered around the aggregates.

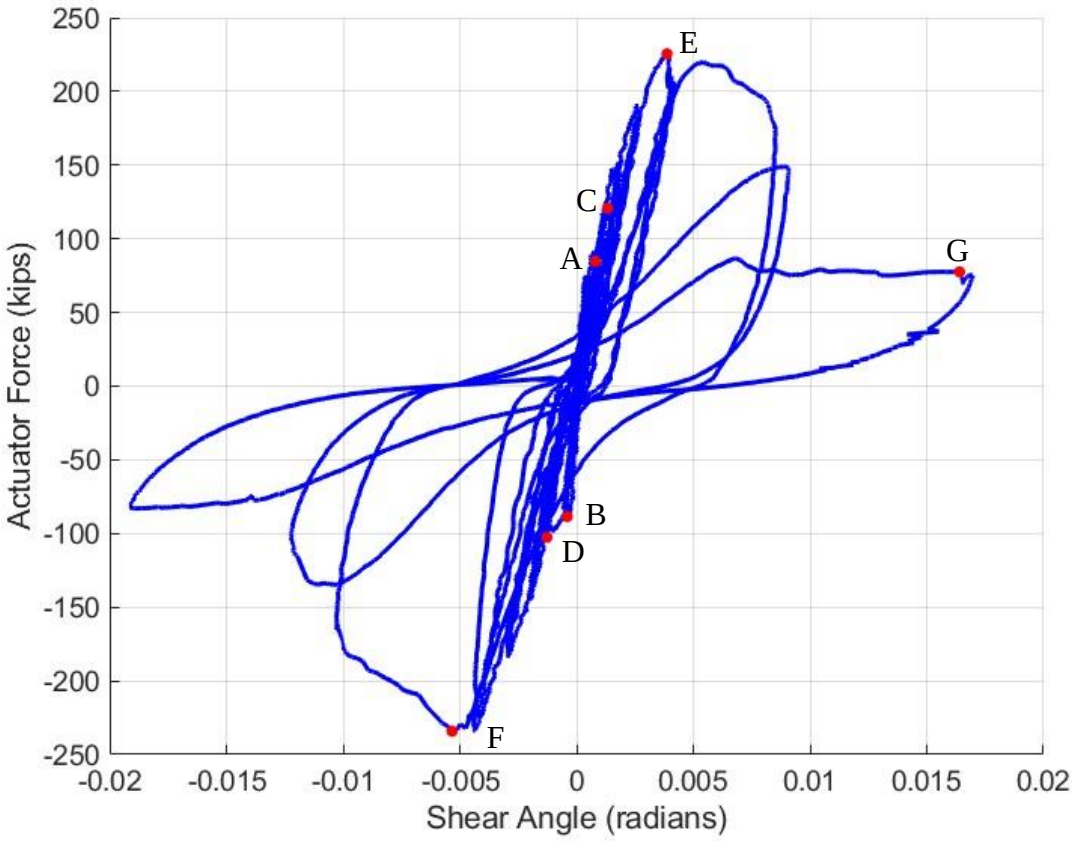

Figure 4-17. Corrected Hysteretic Shear Angle Response of Specimen CD11.

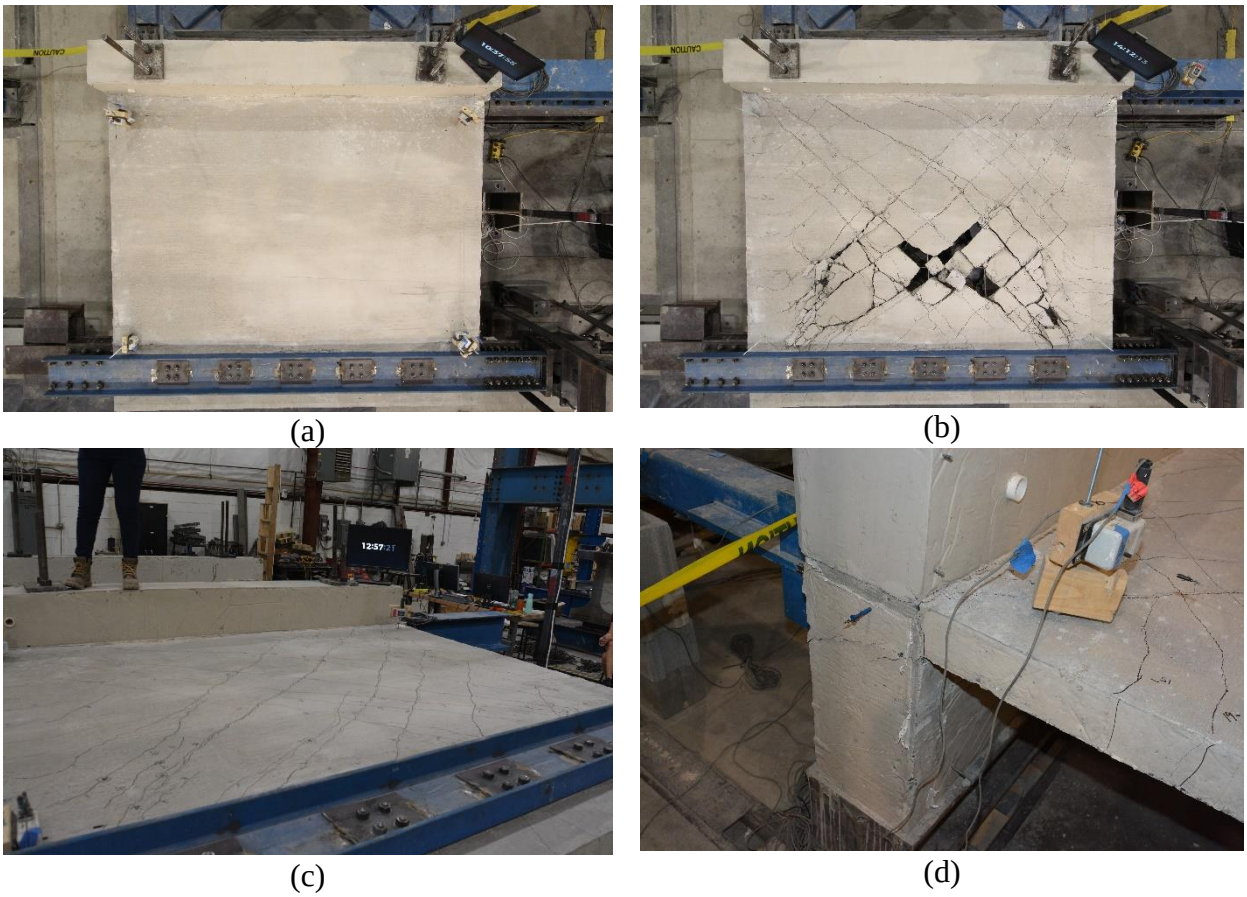

(a) (b)

(c) (d)

Figure 4-18. Photographs of Specimen CD11: a) Prior to Testing; b) Post-test Condition of the Specimen; c) Shear Cracks in Concrete; d) Concrete Spalling at Shear Wall End.

Figure 4-19 shows the crack maps for Specimen CD11 taken at the peak push and pull actuator load for a given cycle. Cracks were marked and measured throughout the test, and maps were prepared to document each crack and associated width at cycles 15 and 21.

The first flexural cracks were observed during the positive portion of cycle 13. The first shear cracks were also observed during the positive portion of cycle 13. During the positive portion of cycle 15, existing cracks widened while new cracks formed. The primary diagonal shear crack measured 0.035 in. wide, while other diagonal shear cracks measured between 0.03 in. and 0.08 in. wide. During the negative portion of cycle 15, diagonal tension cracks widened and formed measuring between 0.003 in. to 0.02 in. wide. Shear and flexural cracks continued to propagate throughout the rest of the test, finally causing large portions of concrete to spall from the center of the slab, leaving large voids.

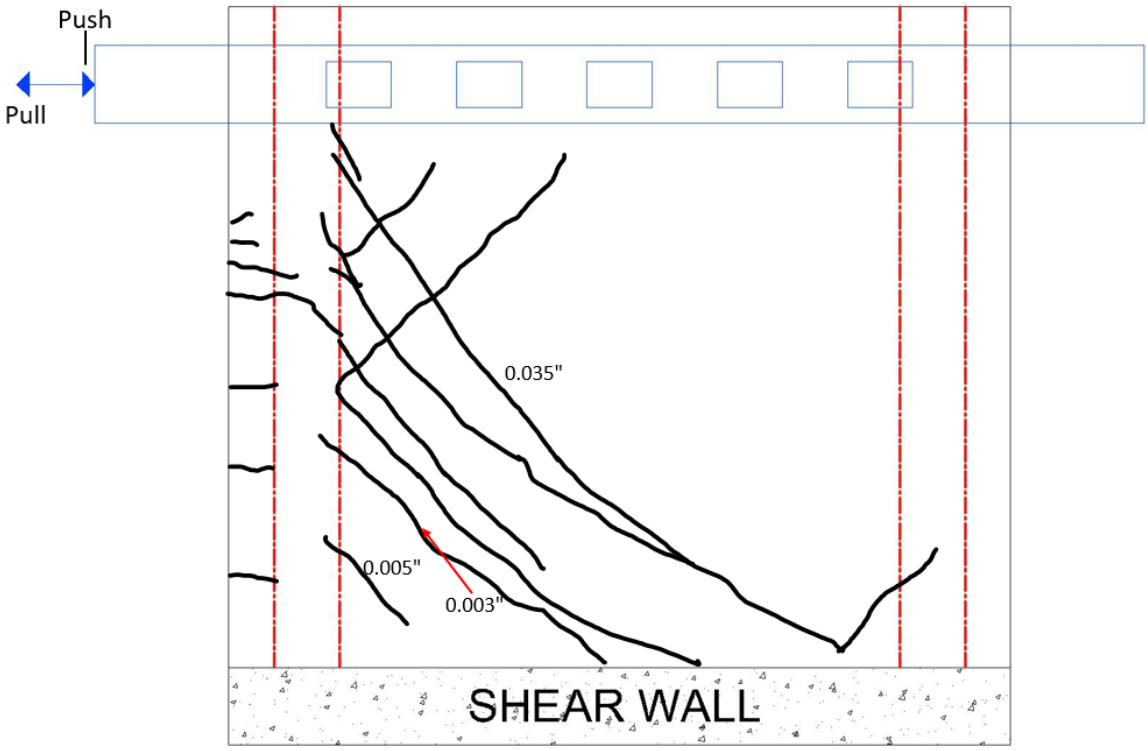

(a) Cycle 15 for a "push" load of 120.8 kips at $\gamma_G = 0.0013\ rad.$

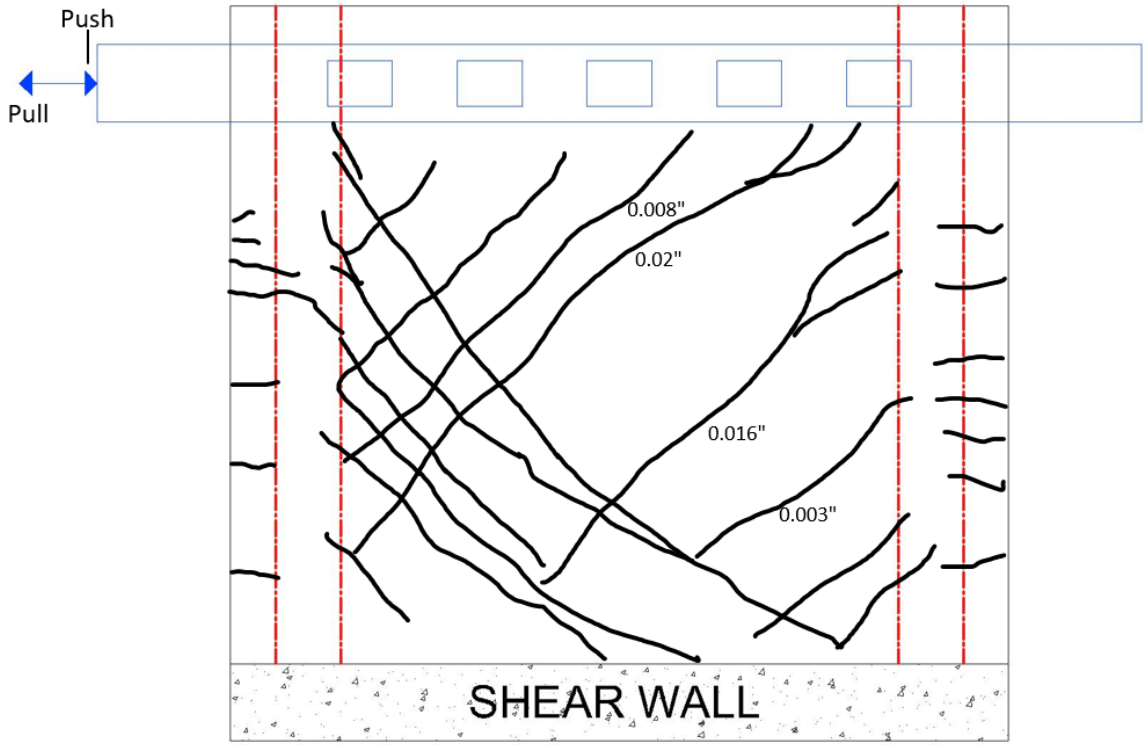

(b) Cycle 15 for a "pull" load of -102.6 kips at $\gamma_G = -0.0013\ rad.$

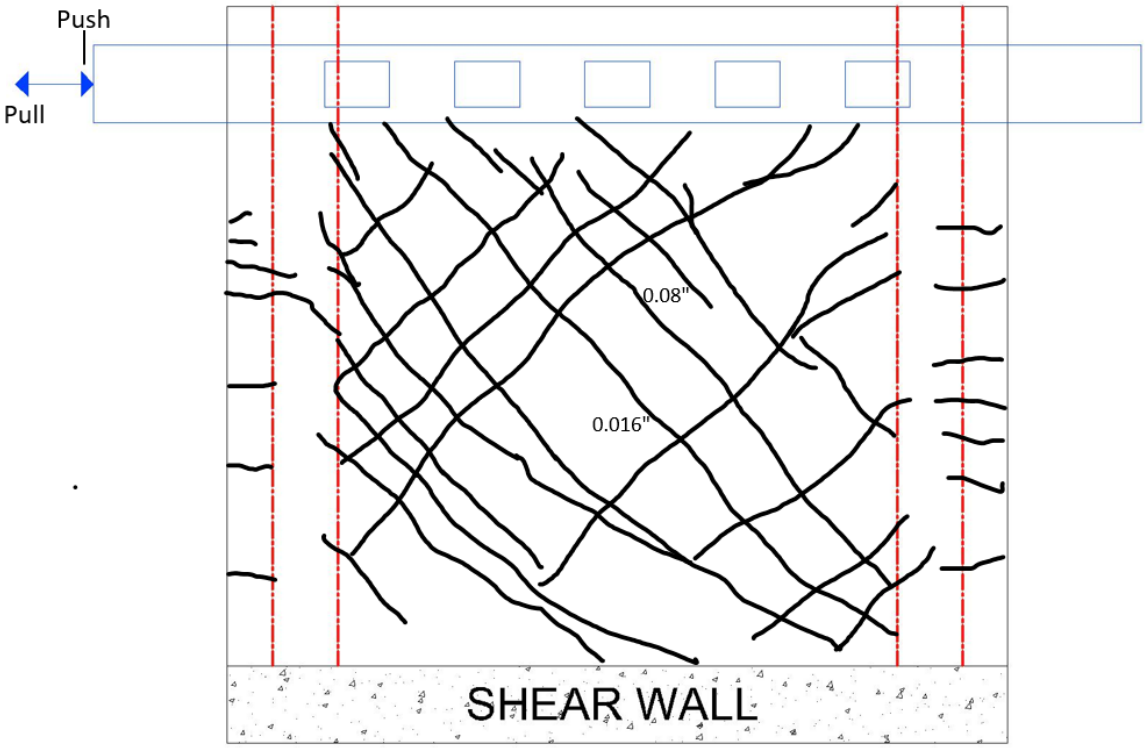

(c) Cycle 21 for a "push" load of 225.5 kips at $\gamma_G = 0.0039\ rad.$

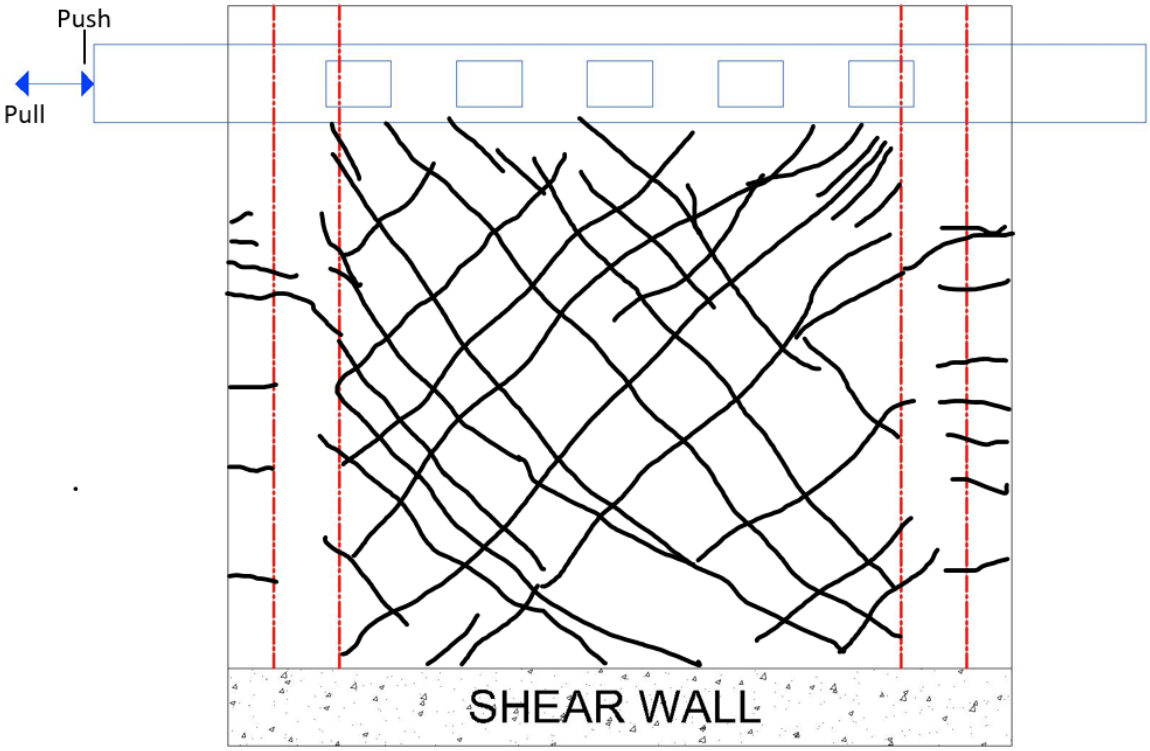

(c) Cycle 21 for a "pull" load of -234.1 kips at $\gamma_G = -0.0053\ rad.$

Figure 4-19. Crack maps for Specimen CD11.

4.6. CD12

Specimen CD12 was tested on August 26th, 2024. Similar to CD11, the concrete compressive strength (shown in Table 3-3) was 5690 psi at the time of testing, although the specified compressive strength of the concrete was 3000 psi. This was attributed to the expanded shale aggregate likely absorbing water from the mix, resulting in a lower water cement ratio than specified. Figure 4-20 shows the hysteresis plot of the actuator load F versus the global shear angle γ_G. A portion of the global shear angle measurements for sensor SP-SE required correction due to concrete spalling at the sensor connection point (shown in Figure 4-21(d)) during the negative portion of cycle 19. This correction process is detailed in Appendix D:. Figure 4-21(a) shows a top view photograph of Specimen CD12 prior to testing. Figure 4-21(b-f) shows photographs of Specimen CD12 at different stages throughout testing. In Figure 4-20, callouts A through G are used to highlight key observations that are crucial for understanding the behavior and performance of the specimen:

- Callout A: Both the first diagonal shear cracks and the first flexural cracks were observed during the positive portion of cycle 11, corresponding to a global shear angle of $\gamma_G = 0.00023\ rad$ and actuator force $F = 67.5\ kips$. Diagonal cracks measured between 0.03 in. and 0.08 in.
- Callout B: Existing diagonal shear cracks opened while new diagonal shear cracks formed during the positive portion of cycle 13, at a global shear angle of $\gamma_g = 0.00033\ rad$ and actuator force $F = 98.5\ kips$. The widest diagonal shear crack was measured at 0.012 in.
- Callout C: A direct shear crack along the interface between the slab and the shear wall was first observed during the positive portion of cycle 21 at a global shear angle of $\gamma_g = 0.0030\ rad$ and actuator force $F = 264.2\ kips$. Global shear angle data indicate that slip at the interface first occurred during the negative portion of cycle 19, at a global shear angle of $\gamma_g = -0.0018\ rad$ and actuator force $F = -187.1\ kips$.
- Callout D: The first occurrence of localized FRP debonding occurred during the negative portion of cycle 21 at a global shear angle of $\gamma_g = -0.0032\ rad$ and actuator force $F = -246.4\ kips$. Most of the debonding was observed along the loading channel, but

areas of localized debonding approximately 4 in. wide were observed in sheets S3 and S4. Most of the FRP remained bonded to the substrate at this load step.

- Callout E: Additional localized FRP debonding was observed in the diaphragm field during the positive portion of cycle 23 at a global shear angle of $\gamma_g = 0.0048\ rad$ and actuator force $F = 322.1\ kips$.
- Callout F: The actuator reached its maximum force $F = 346.2\ kips$ during the positive portion of cycle 25, corresponding to a global shear angle of $\gamma_g = 0.0090\ rad$.
- Callout G: Direct shear failure was observed at the interface between the slab and the shear wall during the positive portion of cycle 26 (the first 3 in. displacement cycle) at a global shear angle of $\gamma_g = 0.0108\ rad$ and actuator force $F = 338.7\ kips$. Slip was also observed at the interface between the slab and the bottom of the chord beam.

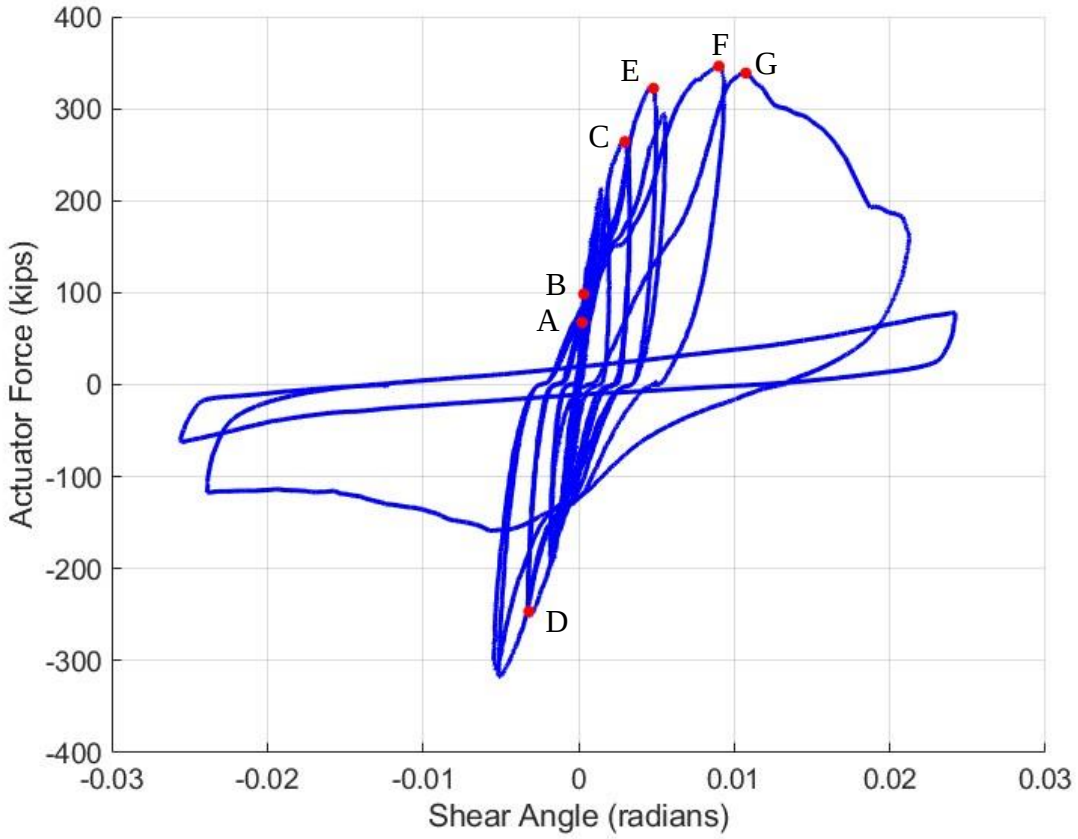

Figure 4-20. Corrected Hysteretic Shear Angle Response of Specimen CD12.

Figure 4-21. Photographs of Specimen CD12: a) Prior to Testing; b) Post-test Condition of the Specimen; c) Shear Cracks in Concrete; d) Concrete Crushing at the Toe; e-f) Sliding Shear Failure at the Wall-slab Interface;

Figure 4-22 shows the FRP strain measurements recorded by the 12 strain gauges installed on sheets S4, S5, S6 and S7 plotted against the actuator load. Table 4-5 provides a summary of the peak FRP strains recorded by each strain gage. Due to an error in the strain range of the FRP strain gages, most of the sensors were unable to measure strain above a certain value and thus did not capture the peak strain. Because of the range issue, these strains

should be interpreted as a lower bound for strain at peak load. The actual strain in the FRP was larger at peak load.

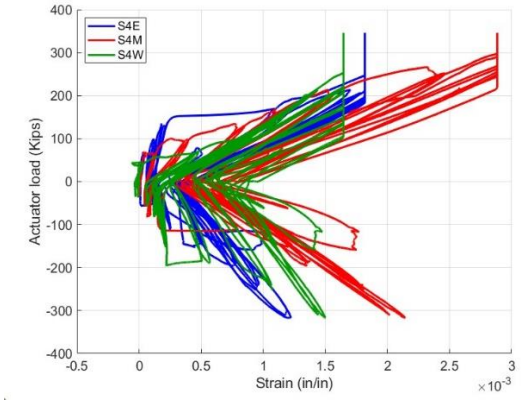

(a) Sheet S4

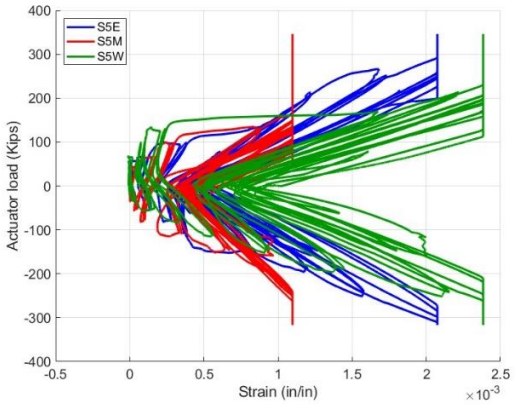

(b) Sheet S5

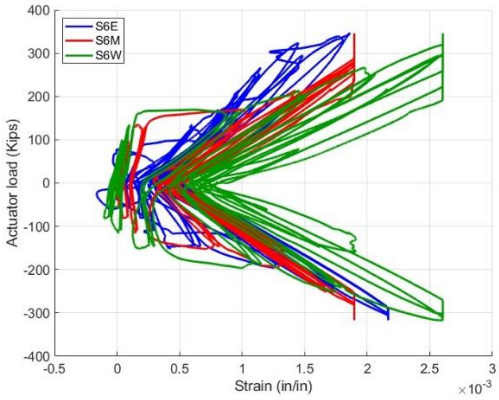

(c) Sheet S6

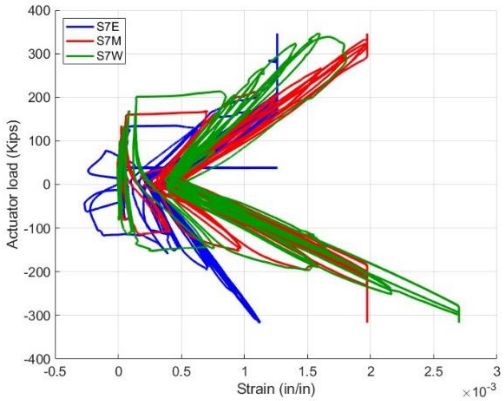

(d) Sheet S7

Figure 4-22. FRP Strain Measurements from Specimen CD12: (a) Sheet S4; (b) Sheet S5; (c) Sheet S6; (d) Sheet S7.

Table 4-5. Maximum Recorded FRP Strains for Specimen CD12.

Strain gauge	Maximum recorded strain, ε_f^{pk}
S4E	> 0.0018
S4M	> 0.0029
S4W	> 0.0016
S5E	> 0.0021
S5M	> 0.0011
S5W	> 0.0024
S6E	> 0.0019
S6M	> 0.0019
S6W	> 0.0026
S7E	> 0.0013
S7M	> 0.0020
S7W	> 0.0016

(>) indicates that the strains were limited by sensor range

Figure 4-23 shows the crack maps for Specimen CD12 taken at the peak push and pull actuator load for a given cycle. Cracks were marked and measured throughout the test, and maps were prepared to document each crack and associated width at cycles 15 and 21. Additionally, Figure 4-24 shows the debonding maps for Specimen CD12 also taken at the peak push and pull load for a given cycle.

The first flexural and shear cracks were observed during the positive portion of cycle 11. Cracks were first mapped during cycle 15, where diagonal shear cracks measured between 0.008 in. and 0.016 in. in width (Figure 4-23(a-b)). During cycle 21, diagonal cracks continued to form, as illustrated in Figure 4-23(c-d). The initial debonding of the FRP sheets was noted in the negative portion of cycle 21 (Figure 4-23(a)). Debonding during the negative portion of cycle 21 was localized to small areas of sheets S3 and S4, and near the loading channel. More debonding was observed on sheets S3 and S2 during the positive portion of cycle 23, as illustrated in Figure 4-24(b). During the positive portion of cycle 26, more debonding was observed as shown in Figure 4-24(c).

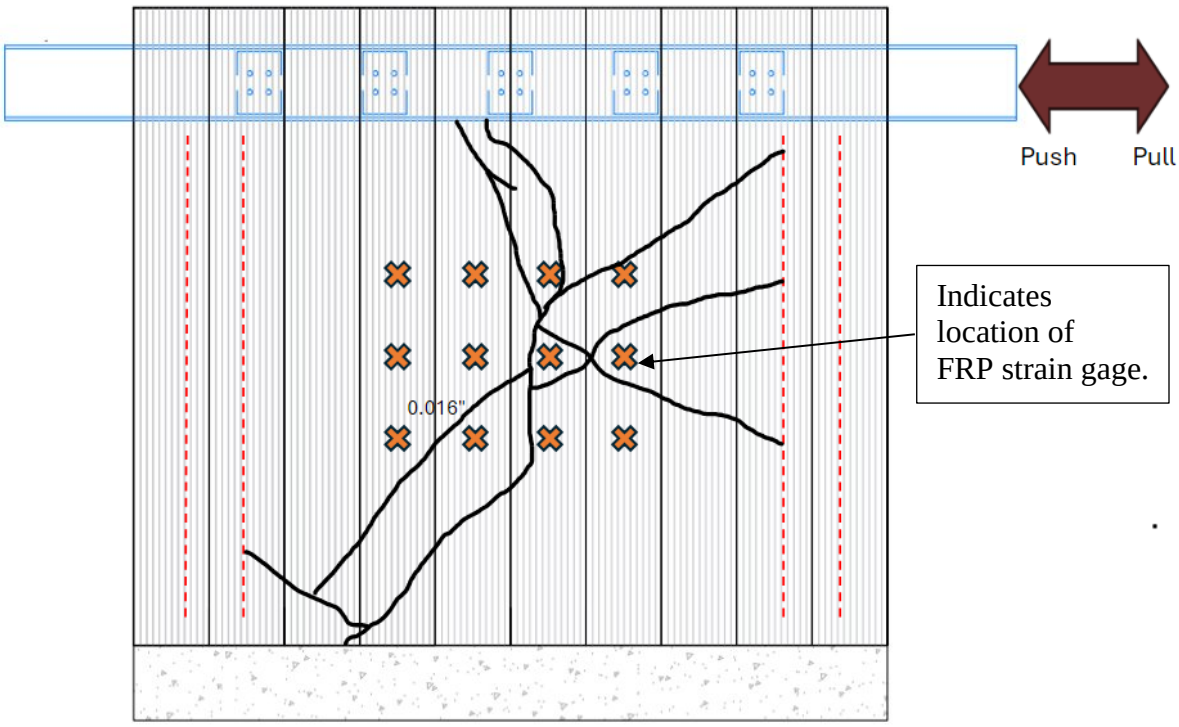

(a) Cycle 15 for a "push" load of 134.6 kips at $\gamma_G = 0.0006\ rad$.

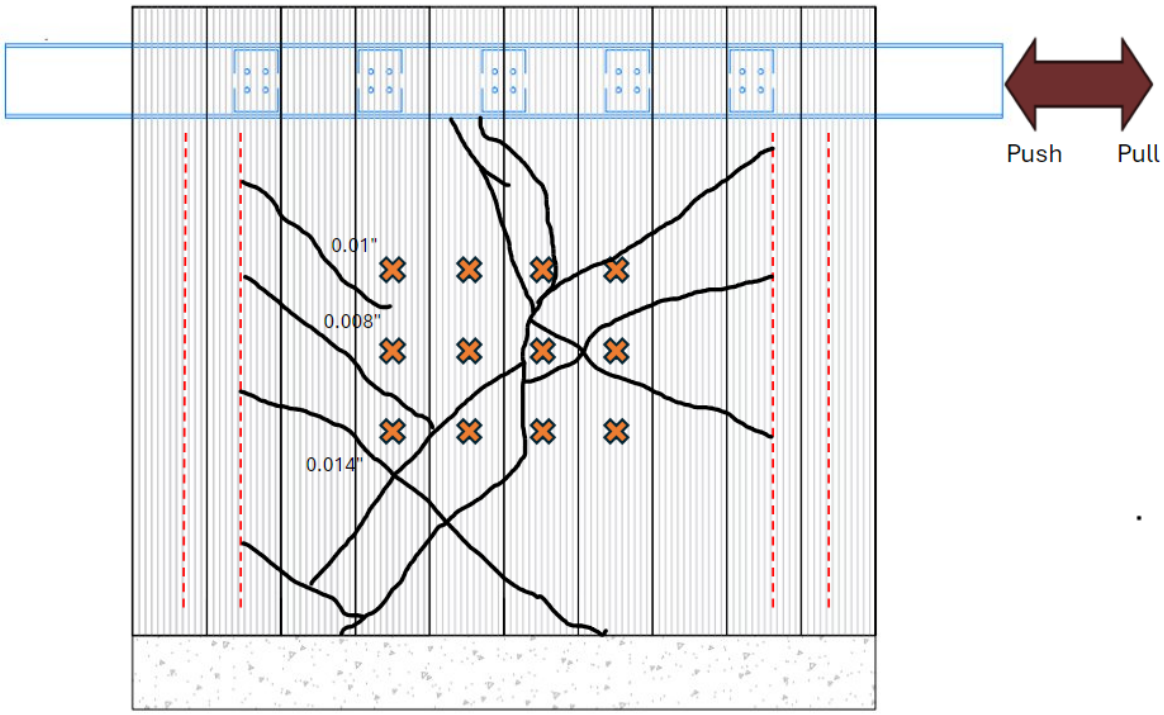

(b) Cycle 15 for a "pull" load of -114.9 kips at $\gamma_G = -0.0006\ rad$.

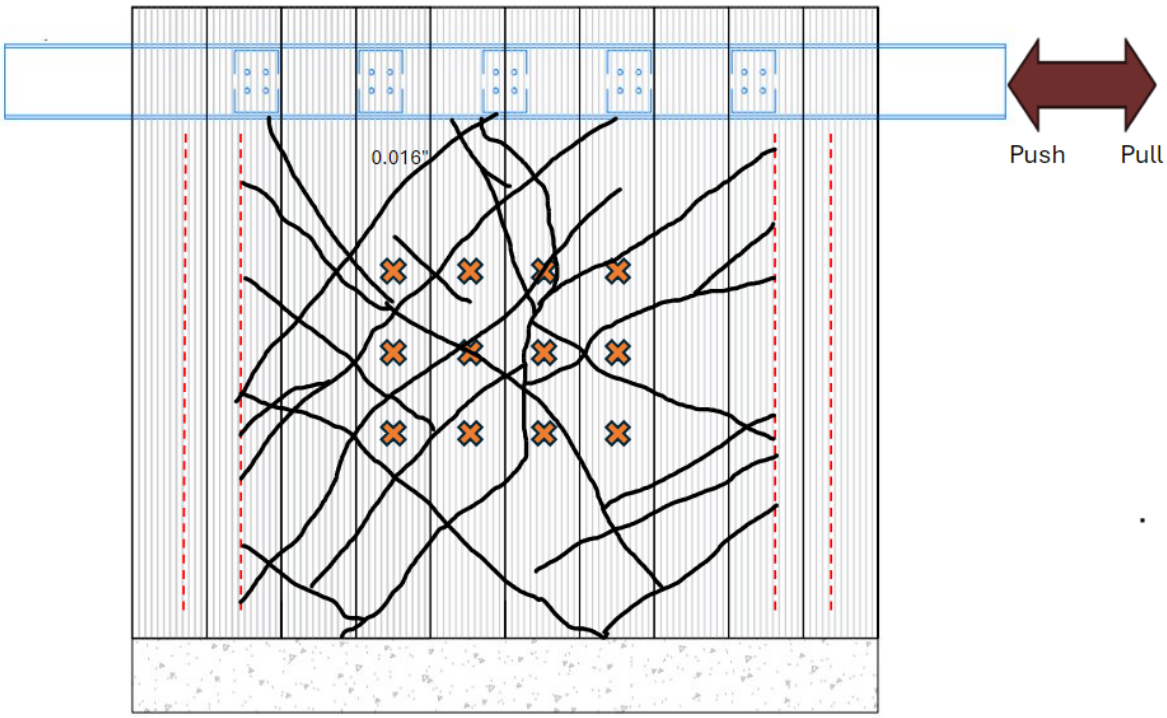

(c) Cycle 21 for a "push" load of 264.2 kips at $\gamma_G = 0.0025\ rad$.

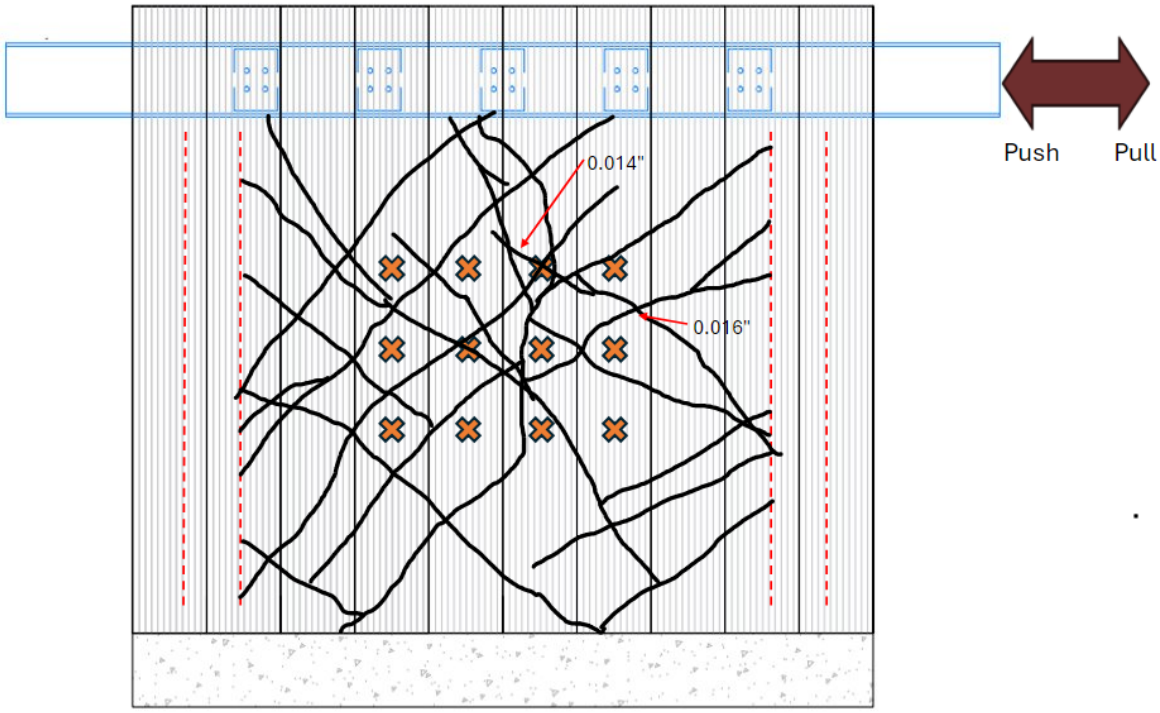

(d) Cycle 21 for a "pull" load of -246.4 kips at $\gamma_G = 0.0020\ rad$.

Figure 4-23. Crack Maps for Specimen CD12.

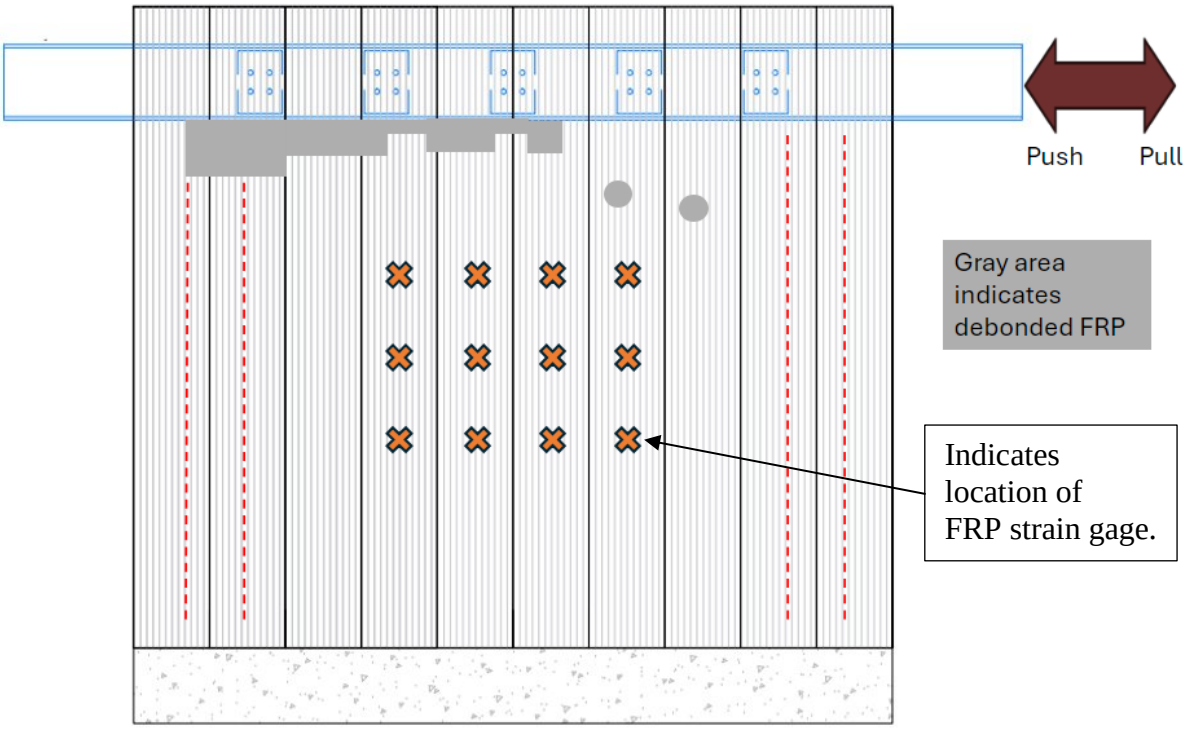

(a) Cycle 21 for a "pull" load of -246.4 kips at $\gamma_G = 0.0020\ rad.$

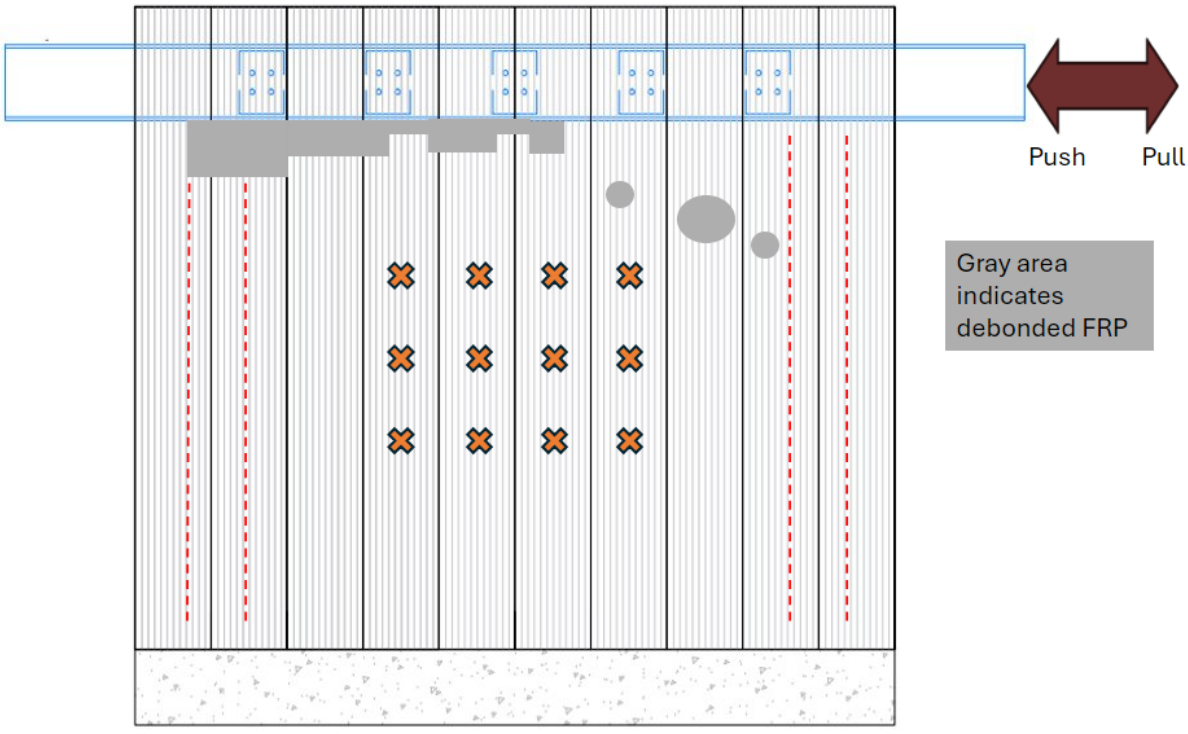

(b) Cycle 23 for a "push" load of 323.4 kips at $\gamma_G = 0.0037\ rad.$

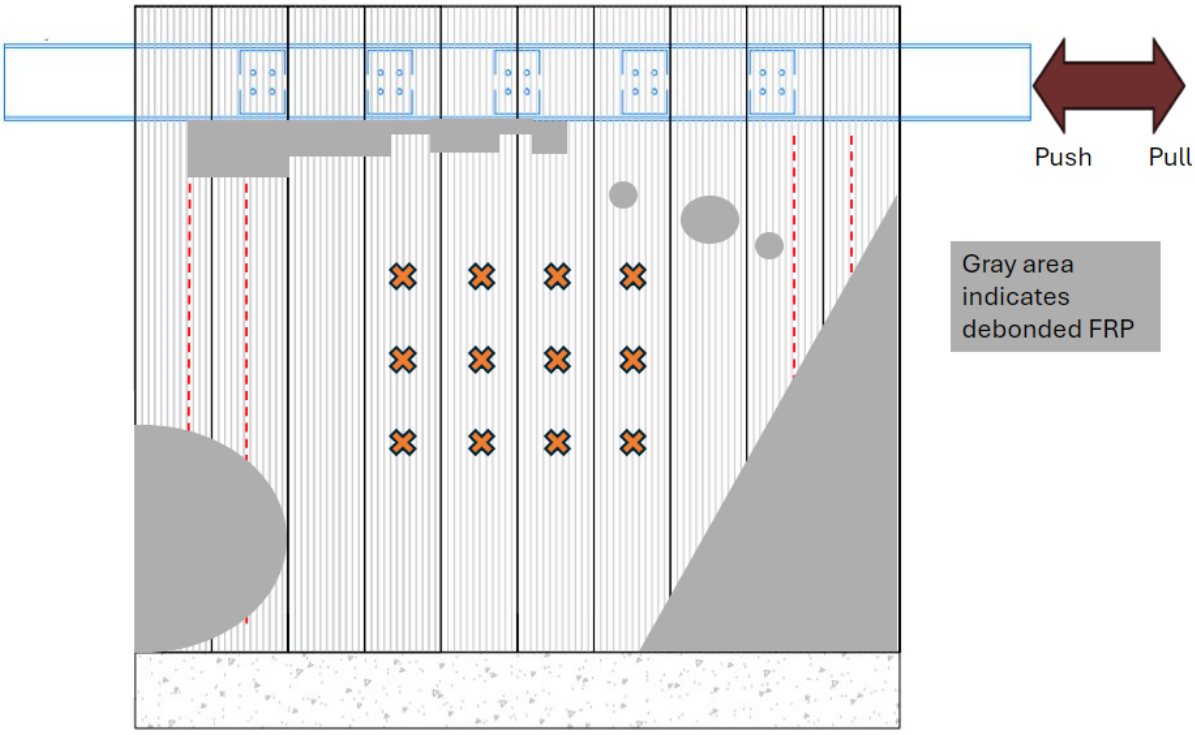

(c) Cycle 26 for a "push" load of 338.7 kips at $\gamma_G = 0.0060\ rad$.

Figure 4-24. FRP Debonding Maps for Specimen CD12.

4.7. CD13

Specimen CD13 was tested on December 11th and December 12th, 2024. Figure 4-25 shows the hysteresis plot of actuator load F versus the global shear angle γ_G. A portion of the global shear angle measurements for Specimen CD13 required correction due to concrete spalling at the sensor SP-SW mounting point. The correction process is detailed in Appendix D:. Figure 4-26(a) shows a top view photograph of Specimen CD13 prior to testing. Figure 4-26(b-f) shows photographs of Specimen CD13 at different stages throughout testing. In Figure 4-25, callouts A through G are used to highlight key observations that are crucial for understanding the behavior and performance of the specimen:

- Callout A: The first flexural cracks and first diagonal shear cracks were observed during the positive portion (actuator push) of cycle 13, corresponding to a global shear angle of $\gamma_G = 0.0003\ rad$ and actuator force $F = 110.5\ kips$. The largest diagonal crack was measured 0.008 in. wide, while other diagonal cracks were measured around 0.003 in. wide. After strain redistribution following peak load in this cycle, strain gage

S3N recorded the highest FRP strain at 0.00006. No debonding of sheets or anchorage was observed.

- Callout B: The first flexural cracks and first diagonal shear cracks were observed during the negative portion of cycle 15, corresponding to a global shear angle of $\gamma_G = -0.0006\ rad$ and actuator force $F = -119.6\ kips$. The primary diagonal cracks were measured 0.005 and 0.012 in. wide. Strain gage S6N recorded the highest FRP strain at 0.0005. No debonding of sheets or anchorage was observed.
- Callout C: The first signs of debonding over small areas near of sheets S3, S4, S5, S6 and S7 were observed at a global shear angle of $\gamma_G = -0.0023\ rad$ and $F = -200.4\ kips$ during the negative portion of cycle 19. The area where the debonding was located corresponded with diagonal shear cracks, and strain gage S6N recorded the highest FRP strain at 0.0024 during the peak load of this cycle. Debonding extending the full width of sheets S3 and S7 was observed on one side of the intermediate anchorage. No visible movement of the Duktil anchorage was observed.
- Callout D: More localized debonding of all sheets except S1 was observed at a global shear angle of $\gamma_G = 0.0031\ rad$ and $F = 262.6\ kips$ during the positive portion of cycle 21. Following the redistribution of FRP strains after the peak load in this cycle, the highest recorded FRP strains were 0.0035 in strain gages S4N and S4S. A portion of sheet S5 had fully debonded on both sides of the intermediate anchor plate. All intermediate and end anchorage remained secured to the underlying concrete.
- Callout E: The actuator reached its maximum push force, $F = 263.1\ kips$ at a global shear angle of $\gamma_G = 0.0045\ rad$ during the positive portion of cycle 23. Sheets S4, S5, and S6 had entirely debonded, while sheets S2, S3, S7, and S8 had partially debonded. Instantaneously at the peak load, strain gages S4N and S4S continued to record the highest FRP strain at 0.0044 and 0.0042, respectively. The lowest recorded FRP strain was 0.0012 in strain gage S3N. Strain at this point from all FRP strain gages is presented in Table 4-6.
- Callout F: At a push force of $F = 259.1\ kips$ and global shear angle of $\gamma_G = 0.0060\ rad$, Specimen CD13 began to experience a drop in strength, despite the FRP maintaining strain while being unbonded between anchor points. The underlying reinforced concrete diaphragm underwent excessive crack opening, leading to a loss of

aggregate interlock and a reduced concrete shear contribution. This, combined with the failure of the compressive strut, resulted in progressive unloading as the shear angle increased. As the specimen began to unload, strain gages S4N and S4S continued to record the highest FRP strain at 0.0052 and 0.0047, respectively. The lowest recorded FRP strain was 0.0011 in strain gage S3N. Strain at this point immediately prior to unloading from all FRP strain gages is presented in Table 4-6. Debonding of the FRP beneath the intermediate anchor plates was observed in sheets S3, S5, S7 and S8. While bond between the FRP beneath the anchor plate and concrete was lost in these sheets, the screws engaged the plate to maintain anchorage.

- Callout G: The actuator reached its maximum pull force, $F = -264.0\ kips$ at a global shear angle of $\gamma_G = -0.0051\ rad$ during the negative portion of cycle 23. FRP sheets S7 and S8 experienced complete intermediate crack induced debonding, leaving only sheets S2 and S3 partially bonded, while sheet S1 was still fully bonded. Additionally, concrete spalling was observed near the loading channels due to the widening network of intersecting cracks. Instantaneously at the peak load, strain gages S4N and S3N recorded the highest FRP strain at 0.0042 and 0.0035, respectively. The lowest recorded FRP strain was 0.0012 in strain gage S6N. Strain at this point from all FRP strain gages is presented in Table 4-6. Debonding of the FRP beneath the intermediate anchor plates was observed in all sheets except S1. While bond between the FRP beneath the anchor plate and concrete was lost in these sheets, the screws engaged the plate to maintain anchorage.
- Callout H: Concrete in the diaphragm field had undergone spalling due to the widening network of intersecting diagonal shear cracks by the positive portion of cycle 27, at a global shear angle of $\gamma_G = 0.026\ rad$ and $F = 69.7\ kips$. At this point in the test, FRP strains recorded by the gages were deemed unreliable due to flexural buckling of the sheets. Intermediate anchorage on sheets S3, S4, S5, S6, S7, and S8 was observed to separate from the underlying concrete, as shown in Figure 4-26(d).

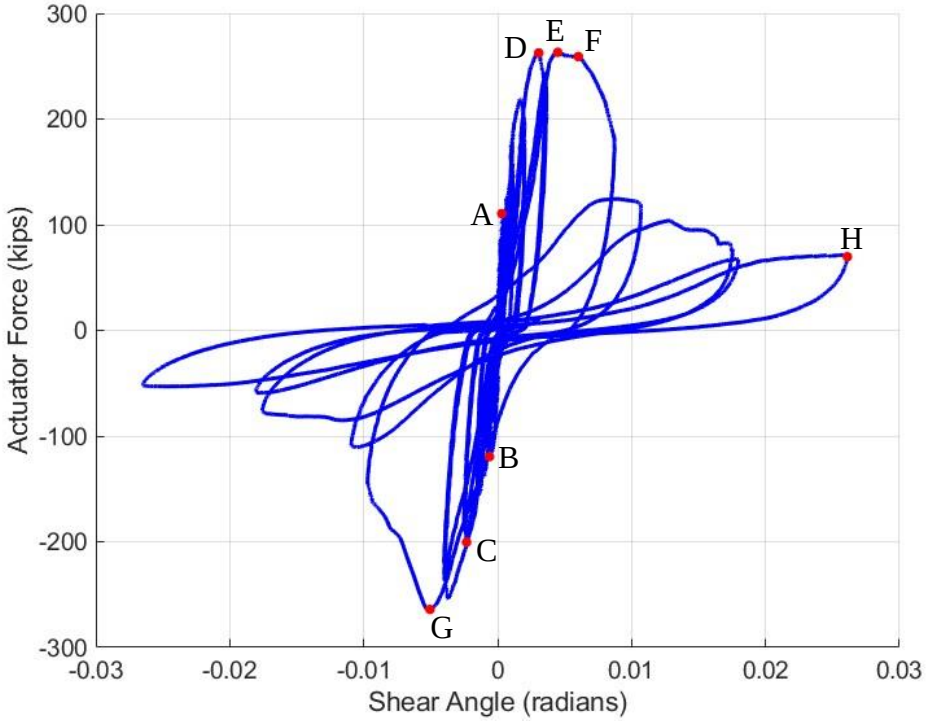

Figure 4-25. Corrected Hysteretic Shear Angle Response of Specimen CD13.

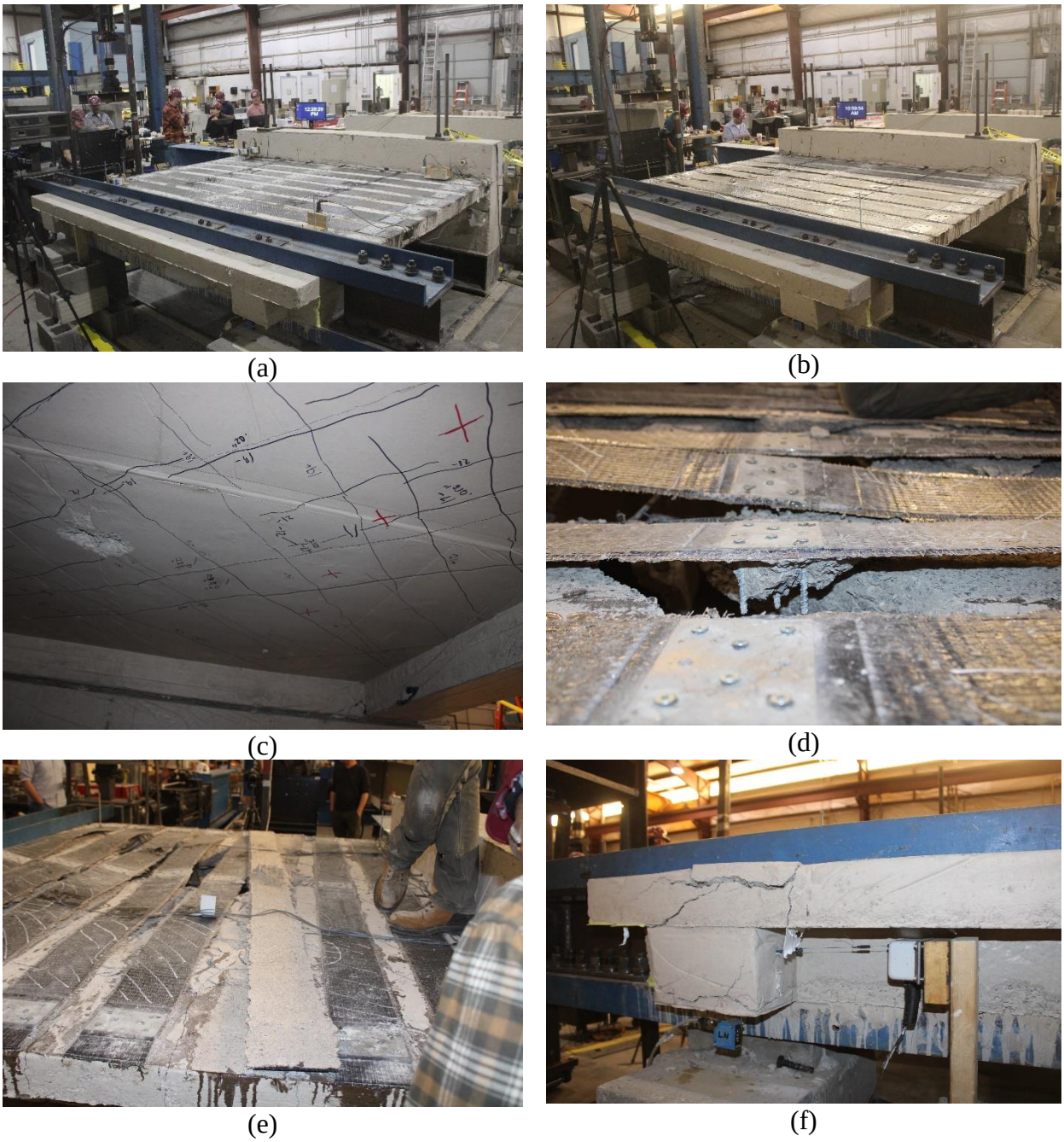

Figure 4-26. Photographs of Specimen CD13: a) Prior to Testing; b) Post-test Condition of the Specimen; c) Shear Cracks in Concrete; d) Anchor Pullout; e) Underside of Debonded FRP Sheet; f) Spalling of Concrete at Sensor SP-SW Mounting Point.

Figure 4-27 shows the FRP strain measurements as recorded by the eight strain gages installed on sheets S3, S4, S5, and S6 plotted against the actuator load. Table 4-6 provides a summary of the FRP strains at peak pull load, $\varepsilon_f^{pk,pull}$, at peak push load, $\varepsilon_f^{pk,push}$, and strain at the end of the end of push direction strength plateau, $\varepsilon_f^{pk,plat}$, from the FRP strain gages. The average FRP strain at the absolute peak load, based on data from eight gages, was 0.0025,

with a coefficient of variation of 41%. The minimum and maximum recorded FRP strains at peak load were 0.0012 and 0.0042, respectively.

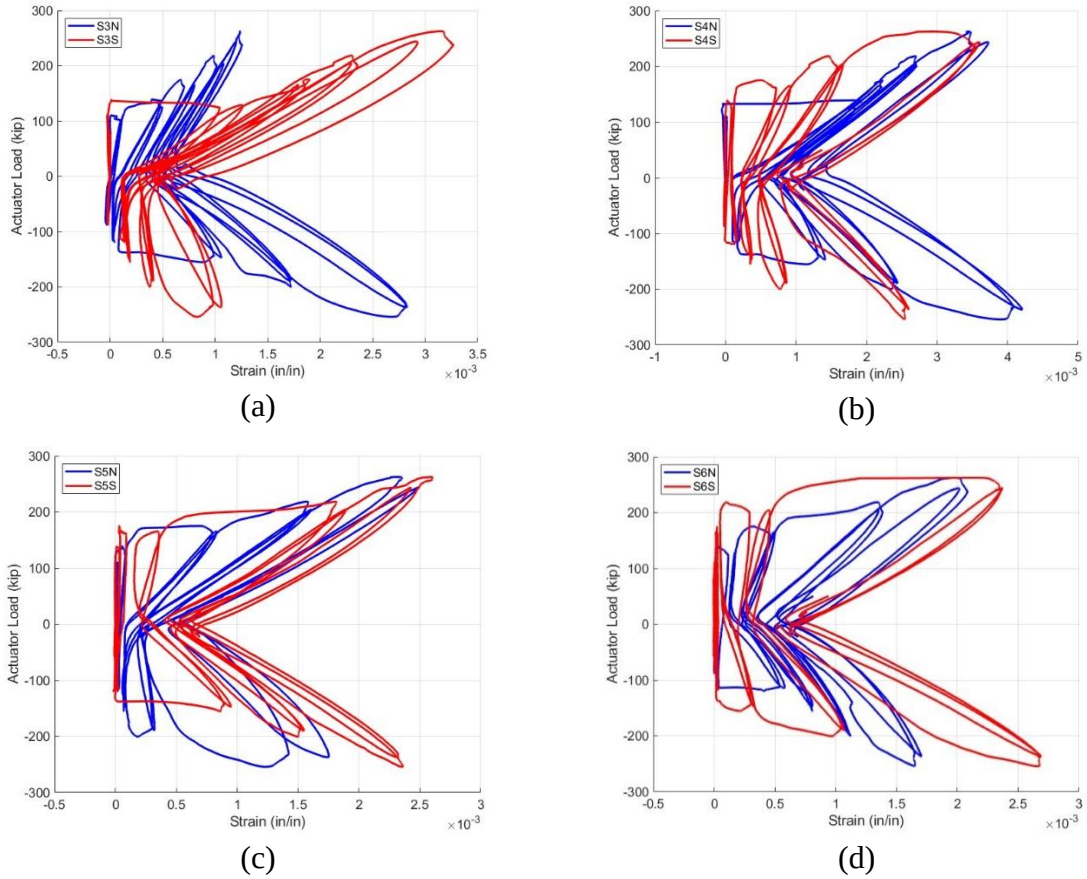

Figure 4-27. FRP Strain Measurements from Specimen CD13: a) Sheet S3; b) Sheet S4; c) Sheet S5; d) Sheet S6.

Table 4-6. FRP Strains for Specimen CD13.

Strain gage	**Strain at peak pull load, ε_f^{pk}**	**Strain at peak push load, $\varepsilon_f^{pk,push}$**	**Strain at end of push direction strength plateau $\varepsilon_f^{pk,plat}$**
S3N	0.0035	0.0012	0.0011
S3S	0.0018	0.0035	0.0041
S4N	0.0042	0.0044	0.0052
S4S	0.0027	0.0042	0.0047
S5N	0.0014	0.0028	0.0032
S5S	0.0024	0.0028	0.0031
S6N	0.0012	0.0027	0.0031
S6S	0.0031	0.0026	0.0028

Figure 4-28 shows the reinforcing steel strain measurements from the strain gages installed on the chord beam longitudinal reinforcement. Although eight strain gages were installed, one of the gages on the south chord beam was damaged while casting the specimen and was consequently not included in the experiment. Figure 4-29 shows the reinforcing steel strain measurements from the strain gages installed on the distributed mesh of reinforcement in the diaphragm field. Similarly, one of the southwest gages was damaged while casting the specimen and was consequently not included in the experiment. shows the reinforcing steel strain measurements at peak pull load from the 13 strain gages on the reinforcing steel that were functioning at peak load. The average deck bar strain at peak pull load was 0.0060, the average north (compression at peak load) chord bar strain at peak pull load was 0.0008, and the average south (tension at peak load) chord bar strain at peak pull load was 0.0016. Reinforcing steel train data indicate that chord steel and deck bar steel do not carry high compressive stress, and that the deck bar steel begins yielding prior to reaching peak load while the chord steel remains elastic throughout the duration of the test.

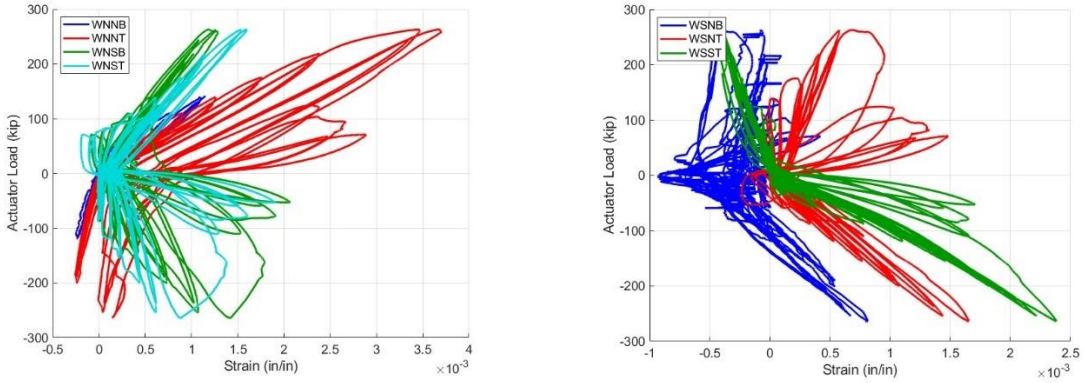

(a) (b)

Figure 4-28. Chord Beam Longitudinal Reinforcement Strains from Specimen CD13: (a) North Chord Beam; (b) South Chord Beam.

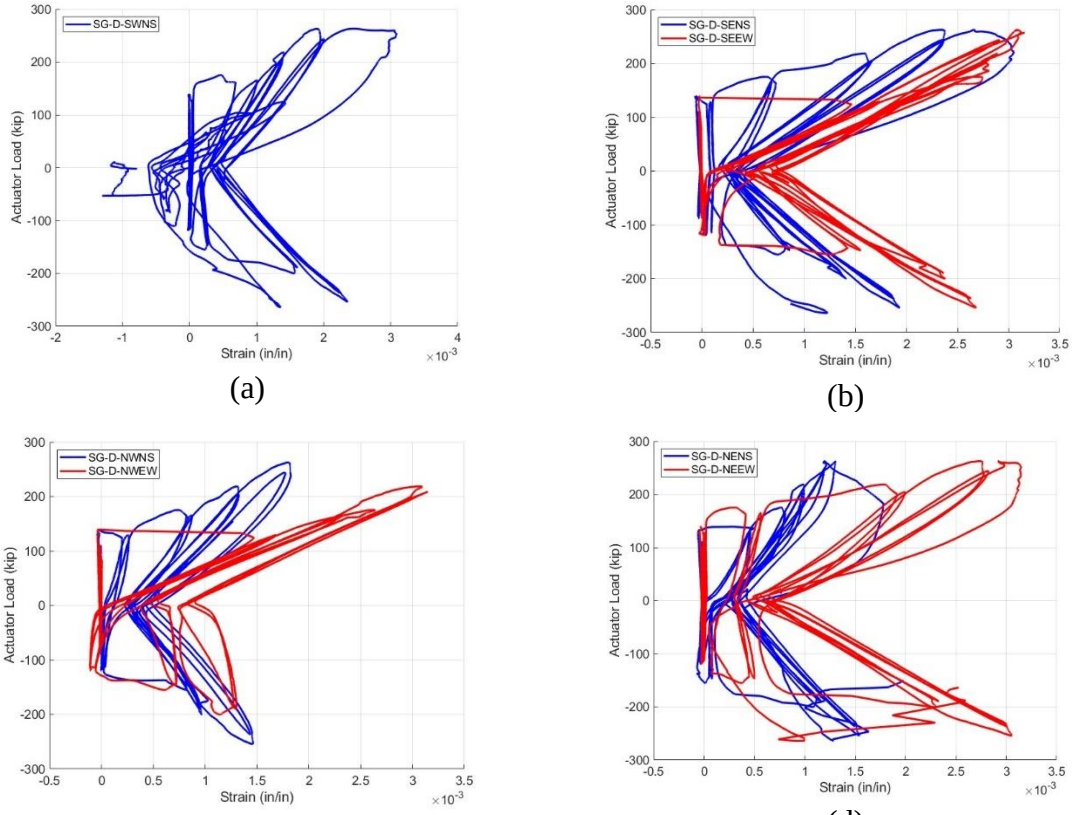

Figure 4-29. Deck Bar Reinforcement Strains from Specimen CD13: (a) SW Deck Bars; b) SE Deck Bars; (c) NW Deck Bars; (d) NE Deck Bars.

Table 4-7. Reinforcing Steel Strains at Peak Load for Specimen CD13.

Strain gage	Strain at peak pull load, ε_f^{pk}	Strain at peak push load, $\varepsilon_f^{pk,push}$
C-WSST	0.0024	-0.0004
C-WSNB	0.0008	-0.0004
C-WSNT	0.0017	0.0007
C-WNSB	0.0014	0.0012
C-WNST	0.0009	0.0016
C-WNNT	0.0001	0.0037
D-NWEW[1]	0.0169	0.0151
D-SWNS	0.0014	0.0025
D-NWNS[1]	0.0064	0.0024
D-SEEW[1]	0.0143	0.0032
D-NENS	0.0013	0.0012
D-NEEW	0.0010	0.0029
D-SENS	0.0012	0.0027

[1] Gage reading was limited by sensor range. Actual strain may have been higher.

Figure 4-30 shows the crack maps for Specimen CD13 taken at the peak push and pull actuator load for a given cycle. Cracks were marked and measured throughout the test, and maps were prepared to document each crack at cycles 19 and 21. Figure 4-31 shows the debonding maps for Specimen CD13 taken at the peak push and pull actuator load for a given cycle. The first observation of debonding of FRP sheets was made during the negative portion of cycle 19. Diagonal tension cracks developed at this cycle, with the largest widths around 0.016 in. The specimen reached its peak capacity of 264.0 kips. At the peak load, approximately 80% of the FRP sheet area in the diaphragm field had debonded between anchor locations.

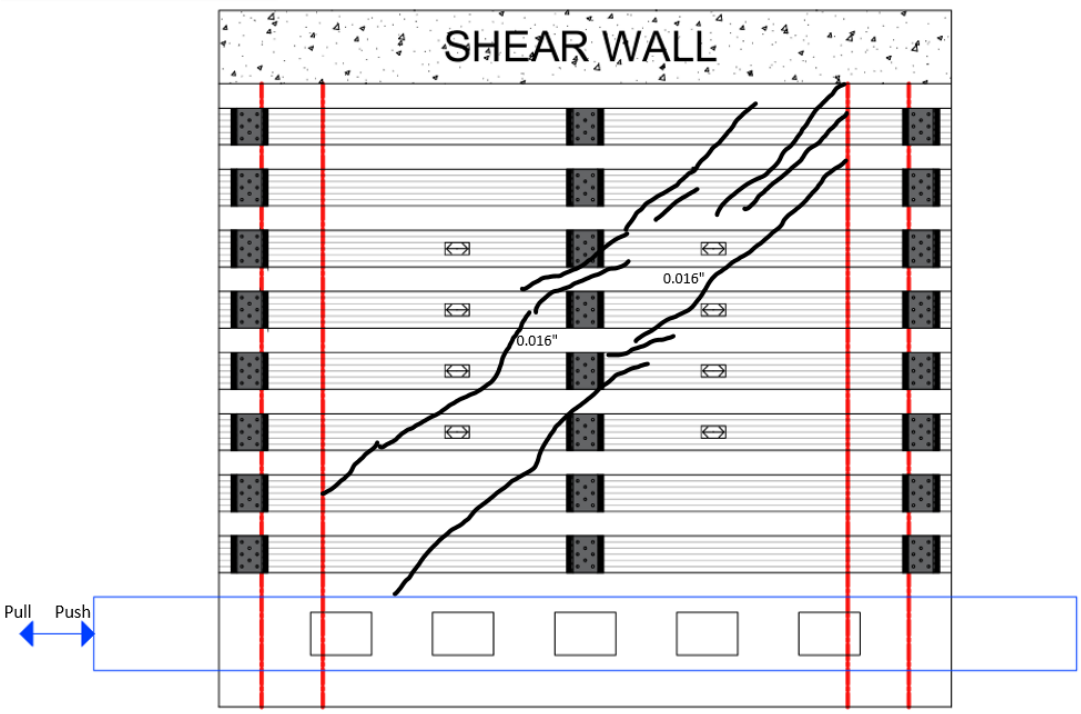

(a) Cycle 19 for a "push" load of 218.6 kips at $\gamma_G = 0.0017$ rad.

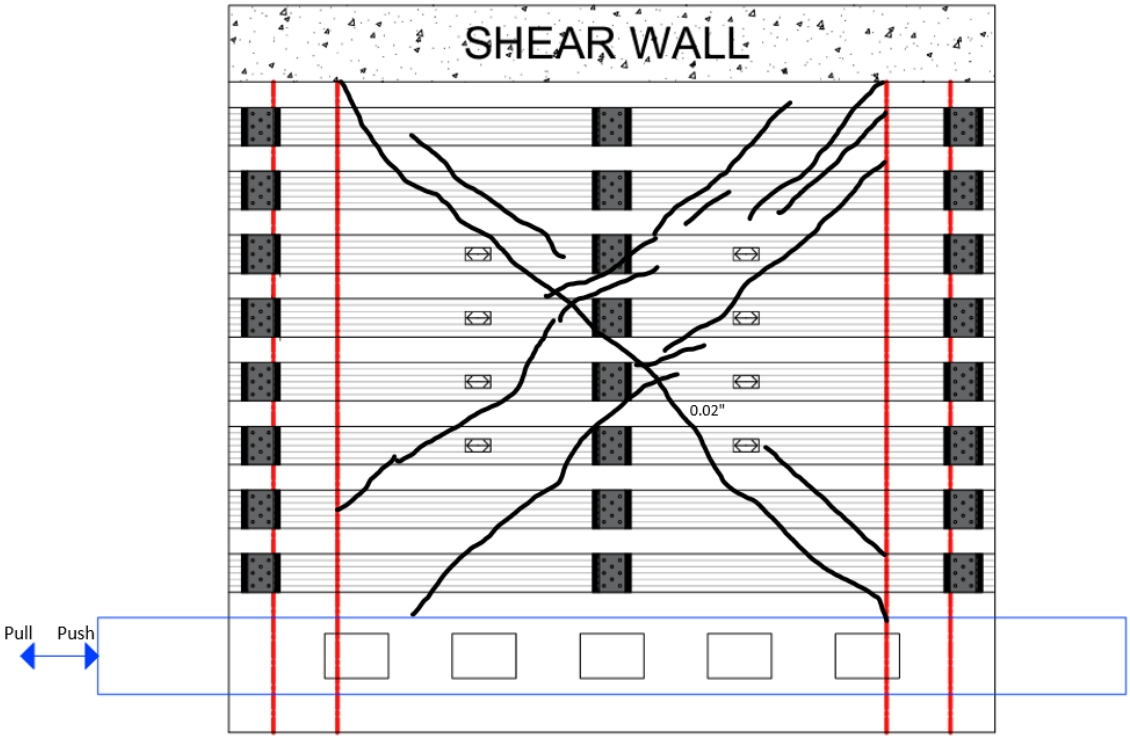

(b) Cycle 19 for a "pull" load of -200.4 kips at $\gamma_G = -0.0023$ rad.

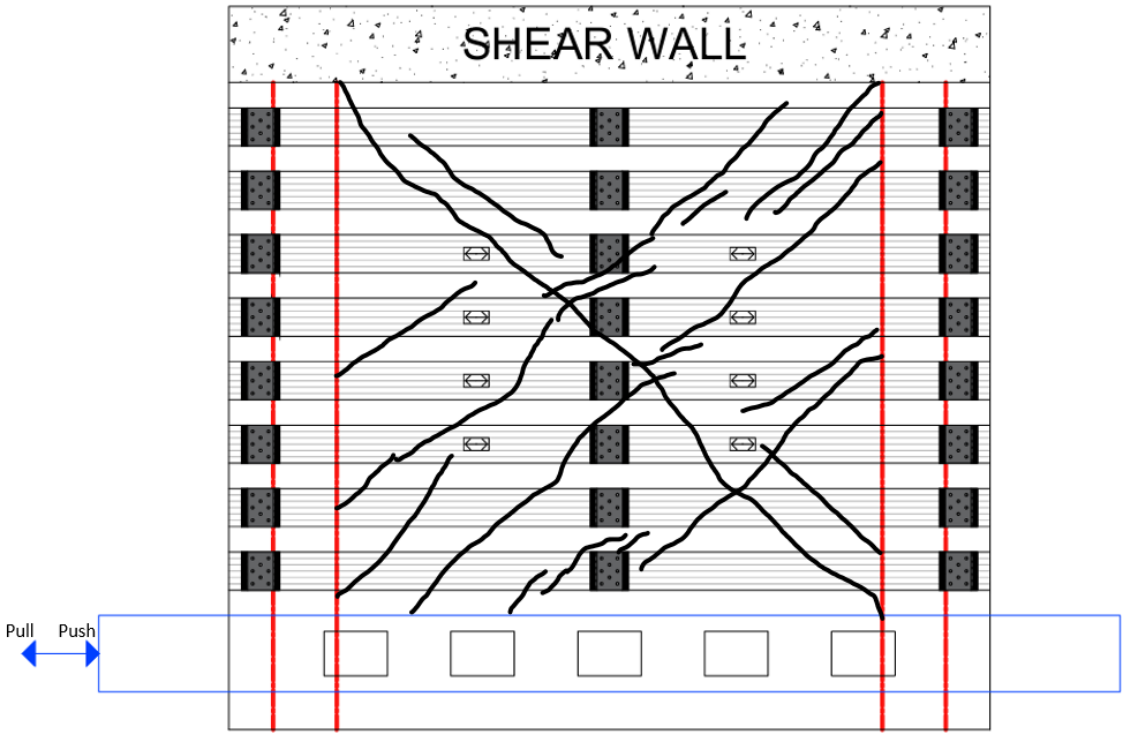

(c) Cycle 21 for a "push" load of 262.6 kips at $\gamma_G = 0.0031$ rad.

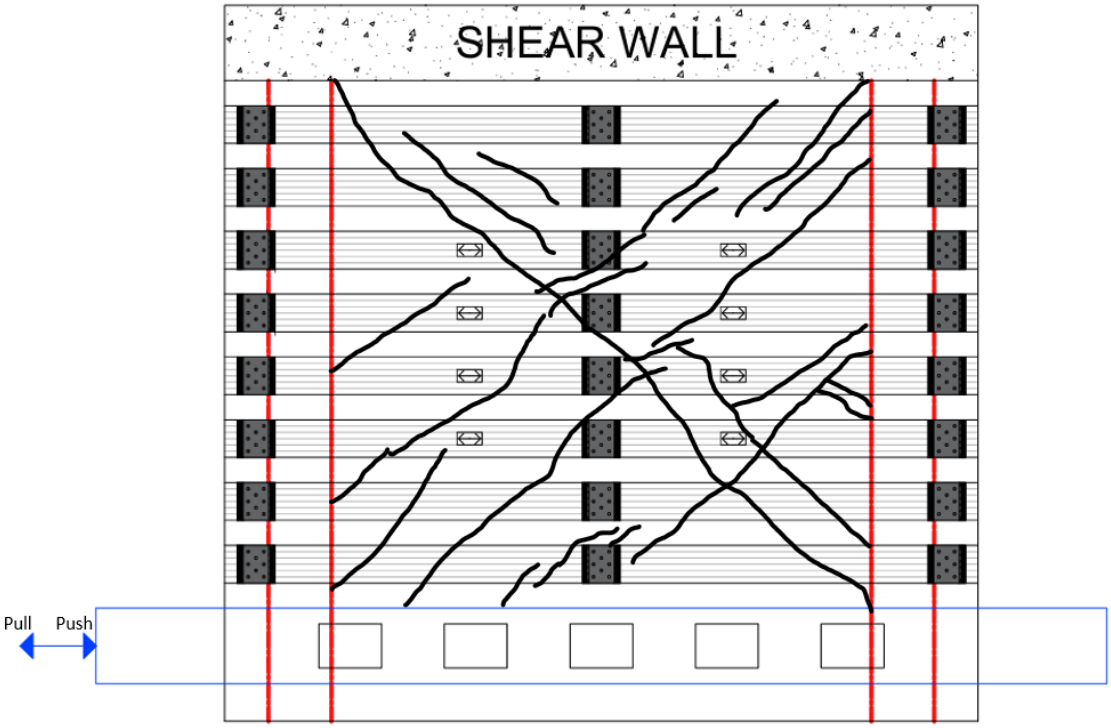

(d) Cycle 21 for a "pull" load of -254.2 kips at $\gamma_G = -0.0037$ rad.

Figure 4-30. Crack maps for Specimen CD13.

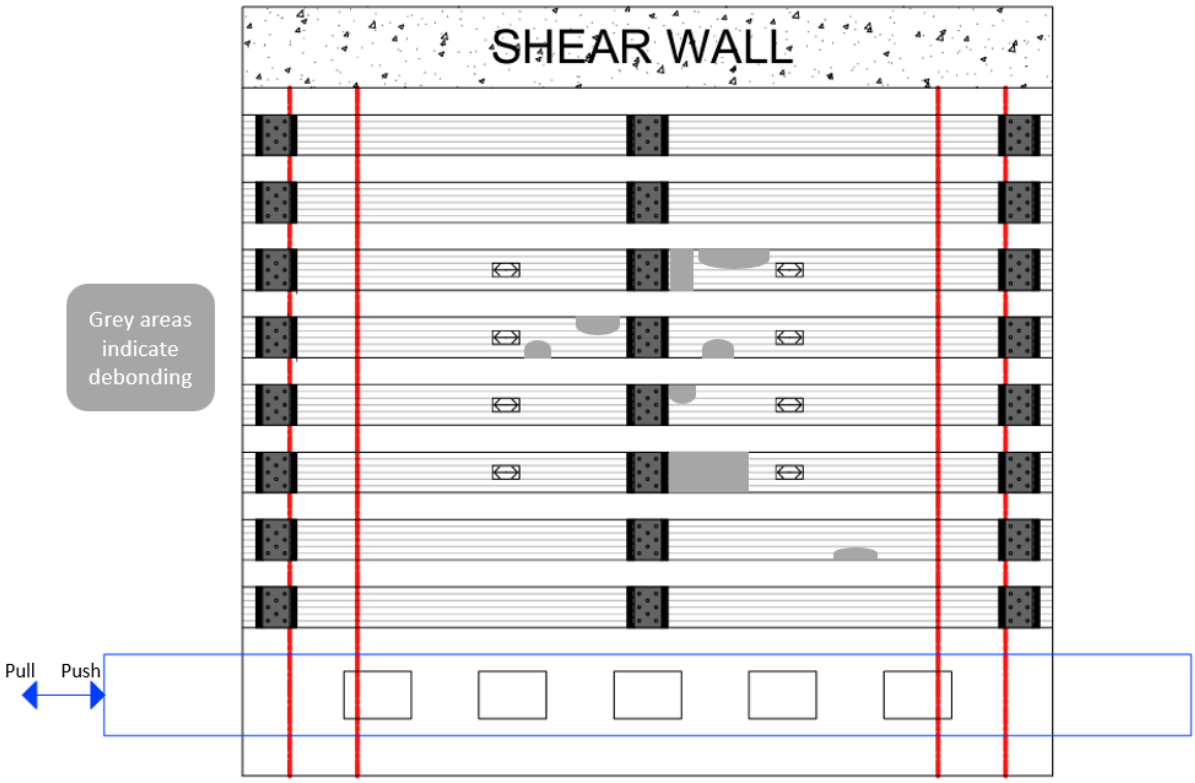

(a) Cycle 19 for a "pull" load of -200.4 kips at $\gamma_G = -0.0023$ rad.

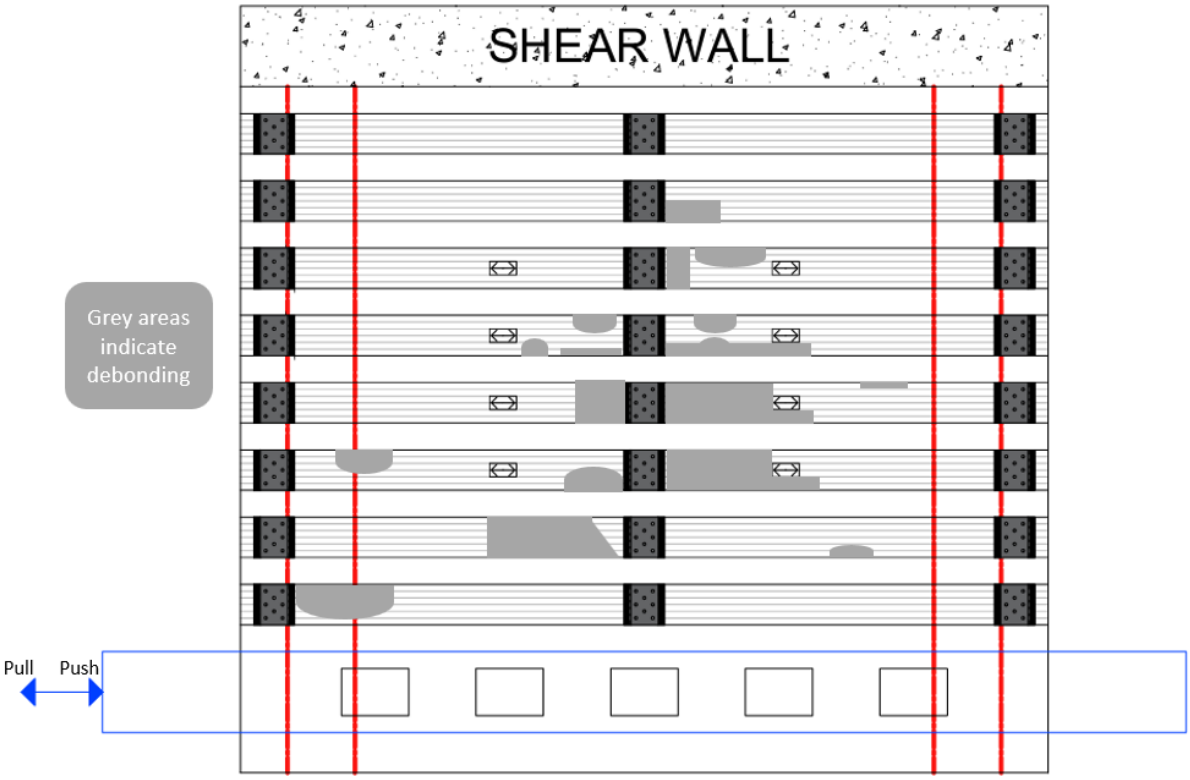

(b) Cycle 21 for a "push" load of 262.6 kips at $\gamma_G = 0.0031$ rad.

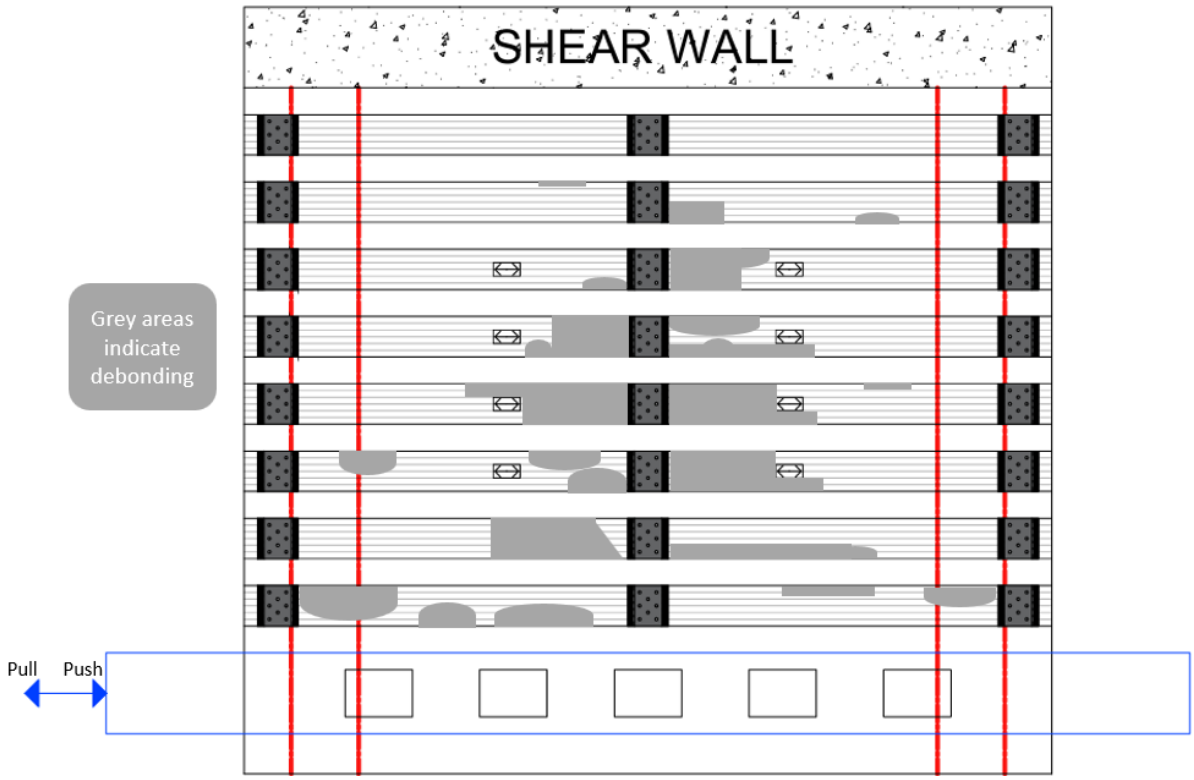

(c) Cycle 21 for a "pull" load of -254.2 kips at $\gamma_G = -0.0037$ rad.

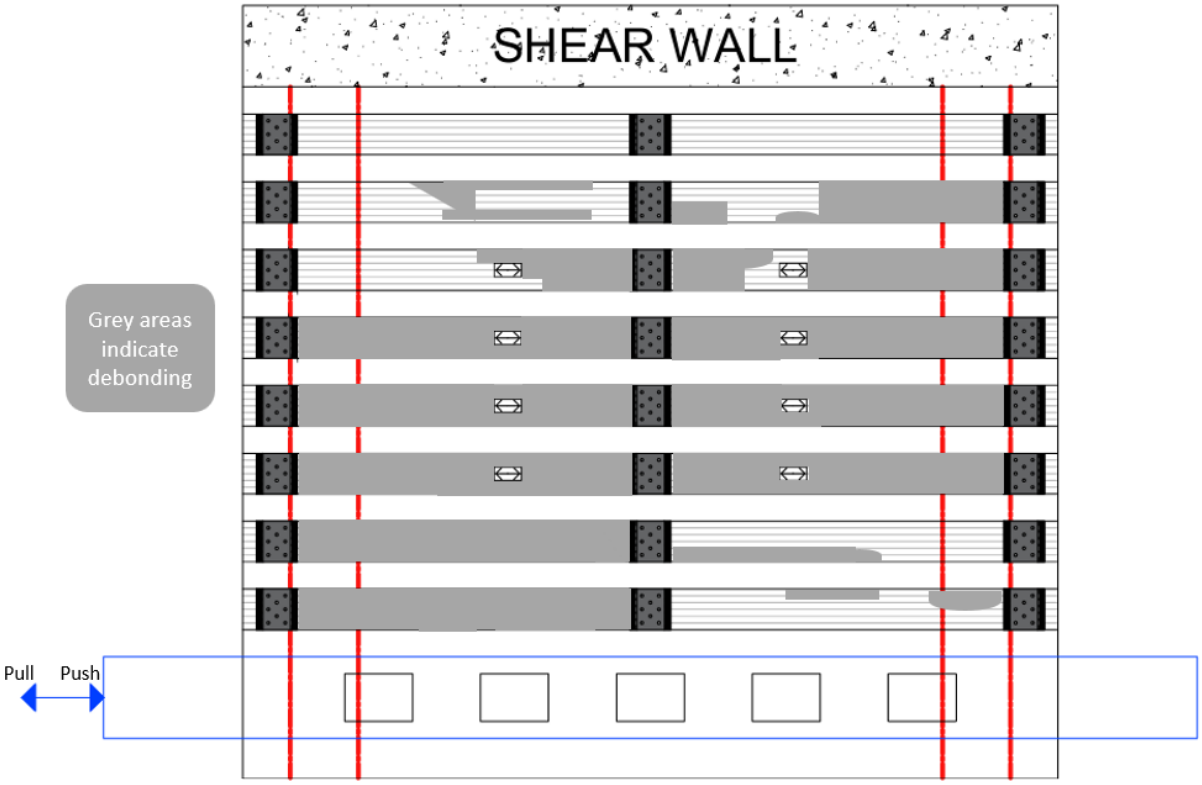

(d) Cycle 23 for a "push" load of 263.1 kips at $\gamma_G = 0.0045$ rad.

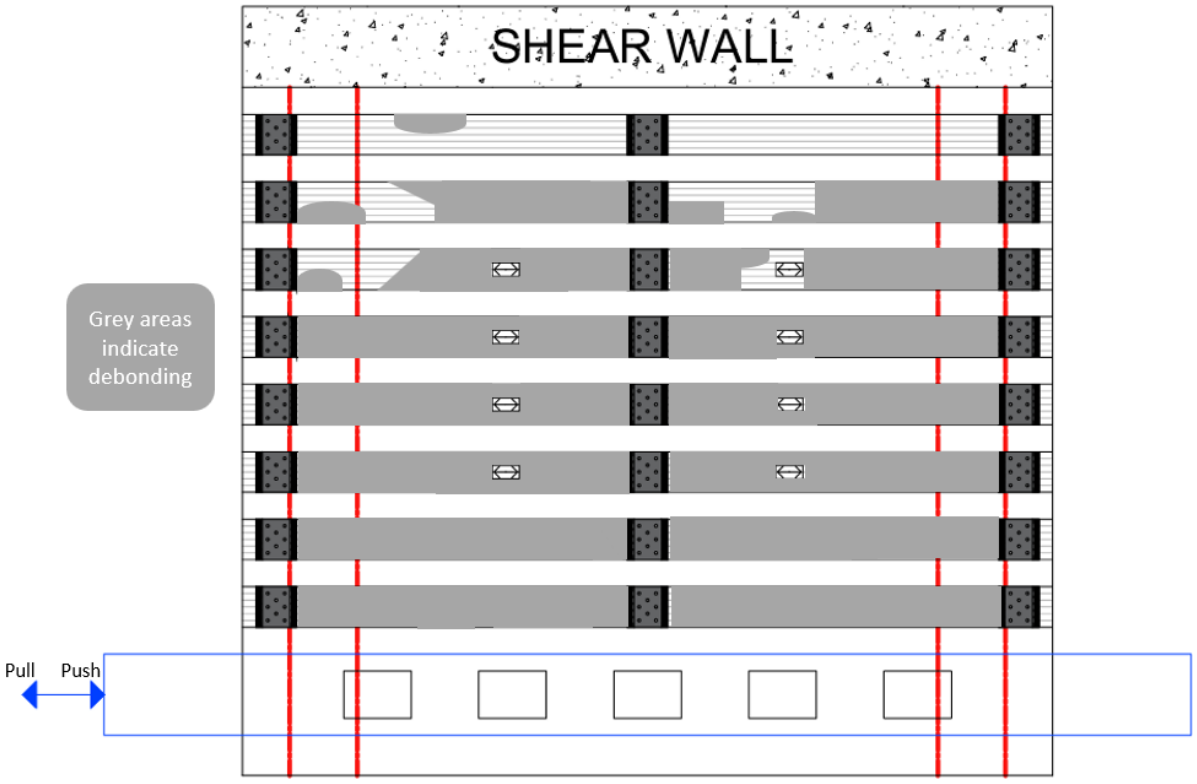

(e) Cycle 23 for a "pull" load of -264.0 kips at $\gamma_G = -0.0051$ rad.

Figure 4-31. FRP Debonding Maps for Specimen CD13.

4.8. CD14

Specimen CD14 was tested on January 29th, 2025. Figure 4-32 shows the hysteresis plot of the actuator load F versus the global shear angle γ_G. A portion of the global shear angle measurements for Specimen CD14 required correction due to concrete spalling off at one of the displacement measurement locations. The correction process is detailed in Appendix D:. Figure 4-6(a) shows a top view photograph of Specimen CD14 prior to testing. Figure 4-6(b-f) shows photographs of Specimen CD14 at different stages throughout testing. In Figure 4-32, callouts A through G are used to highlight key observations that are crucial for understanding the behavior and performance of the specimen:

- Callout A: The first flexural cracks and first diagonal shear cracks were observed during the positive portion of cycle 13, corresponding to a global shear angle of $\gamma_G = 0.0005$ rad and actuator force $F = 91.2$ kips. Following the redistribution of FRP strains after the peak load in this cycle, strain gage S3N recorded the highest FRP strain at 0.00009. No debonding of sheets or anchorage was observed.
- Callout B: The first flexural cracks and first diagonal shear cracks in the actuators pull direction were observed during the negative portion of cycle 13, corresponding to a global shear angle of $\gamma_G = -0.0005$ rad and actuator force $F = -75.8$ kips. Following the redistribution of FRP strains after the peak load in this cycle, all strain gages recorded strains between -0.00004 and 0.00001. No debonding of sheets or anchorage was observed.
- Callout C: The first signs of debonding over small areas near the edges of sheets S2, S3, S4, S5, and S6 were observed at a global shear angle of $\gamma_G = 0.0015$ rad and $F = 158.5$ kips during the positive portion of cycle 17. The area where the debonding was localized corresponded with diagonal shear cracks. Following the redistribution of FRP strains after the peak load in this cycle, strain gages S6N and S4S recorded the highest FRP strains at 0.0012 and 0.0008, respectively. No visible movement of intermediate or end anchorage was observed.
- Callout D: More debonding of sheets S2, S3, S4, S5, and S6 was observed at a global shear angle of $\gamma_G = 0.0021$ rad and $F = 204.3$ kips during the positive portion of cycle 19. The area near the middle of sheets S3 and S4 had debonded across the entire 12

in. width, while debonding in other sheets was localized to smaller areas. Following the redistribution of FRP strains after the peak load in this cycle, strain gages S6N and S4S recorded the highest FRP strains both at 0.0015. All end and intermediate anchor plates remained bonded and no visible movement was observed.

- Callout E: The actuator reached its maximum pull force, $F = -288.7$ kips at a global shear angle of $\gamma_G = -0.0070$ rad during the negative portion of cycle 23. Complete global debonding of sheets S5 and S6 was observed, while the remaining FRP sheets were between 50% and 75% debonded. Instantaneously at the peak pull load, strain gages S3N and S5S recorded the highest strains at 0.0052 and 0.0042, respectively. Strain at this point from all FRP strain gages is presented in Table 4-8. By this point, debonding extending the entire width of sheets S5, S6, S7, and S8 was observed on both sides of a row of intermediate anchor plates on the respective sheets. After the debonding of the FRP on both sides of the intermediate anchor, the FRP beneath the anchor plate debonded from the underlying concrete. While bond between the FRP beneath the anchor plate and concrete was lost at these locations, the screws engaged the plate to maintain anchorage.
- Callout F: The actuator reached its maximum push force, $F = 301.2$ kips at a global shear angle of $\gamma_G = 0.0055$ rad during the positive portion of cycle 25. Instantaneously at the peak push load, strain gages S3N and S4N recorded the highest strains at 0.0087 and 0.0058, respectively. Strain at this point from all FRP strain gages is presented in Table 4-8. Anchor plates at the previously debonded intermediate anchorage locations remained engaged to the concrete through the anchor screws.
- Callout G: At a global shear angle of $\gamma_G = 0.0077$ rad and actuator push force of $F = 293.3$ kips, Specimen CD14 began to experience a drop in strength, despite the FRP maintaining strain while being unbonded between anchor points. The underlying reinforced concrete diaphragm underwent excessive crack opening, leading to a loss of aggregate interlock and a reduced concrete shear contribution. This, combined with the failure of the compressive strut, resulted in progressive unloading as the shear angle increased. As the specimen began to unload, strain gages S3N and S4N recorded the highest strains at 0.0094 and 0.0064, respectively. Strain at this point from all FRP strain gages is presented in Table 4-8.

- Callout H: Concrete in the diaphragm field had undergone spalling due to the widening network of opposing diagonal shear cracks by the positive portion of cycle 28, at a global shear angle of $\gamma_G = 0.0023$ rad and F = 57.0 kips. At this point in the test, FRP strains recorded by the gages were deemed unreliable due to flexural buckling of the sheets. Both rows of intermediate anchorage on sheets S5 and S6 had separated from the underlying concrete. All other anchorage remained engaged either through bond to the concrete or through the group of anchor screws. After the test, the screws on the end anchorage of sheets S3 and S4 were removed, as shown in Figure 4-33(f). The head of each screw was observed to have deformed inelastically.

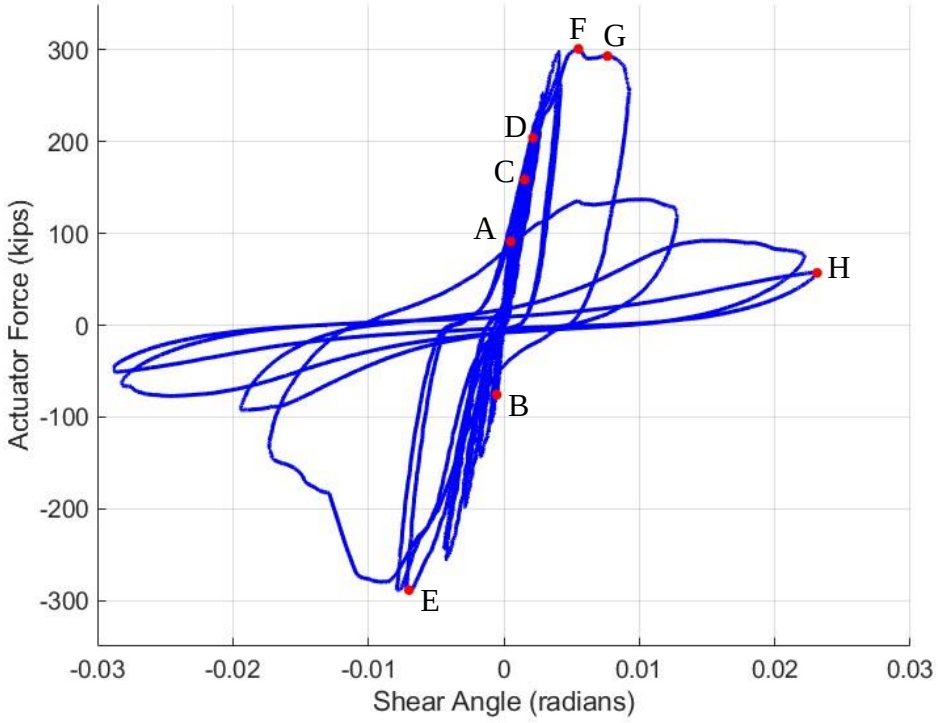

Figure 4-32. Corrected Hysteretic Shear Angle Response of Specimen CD14.

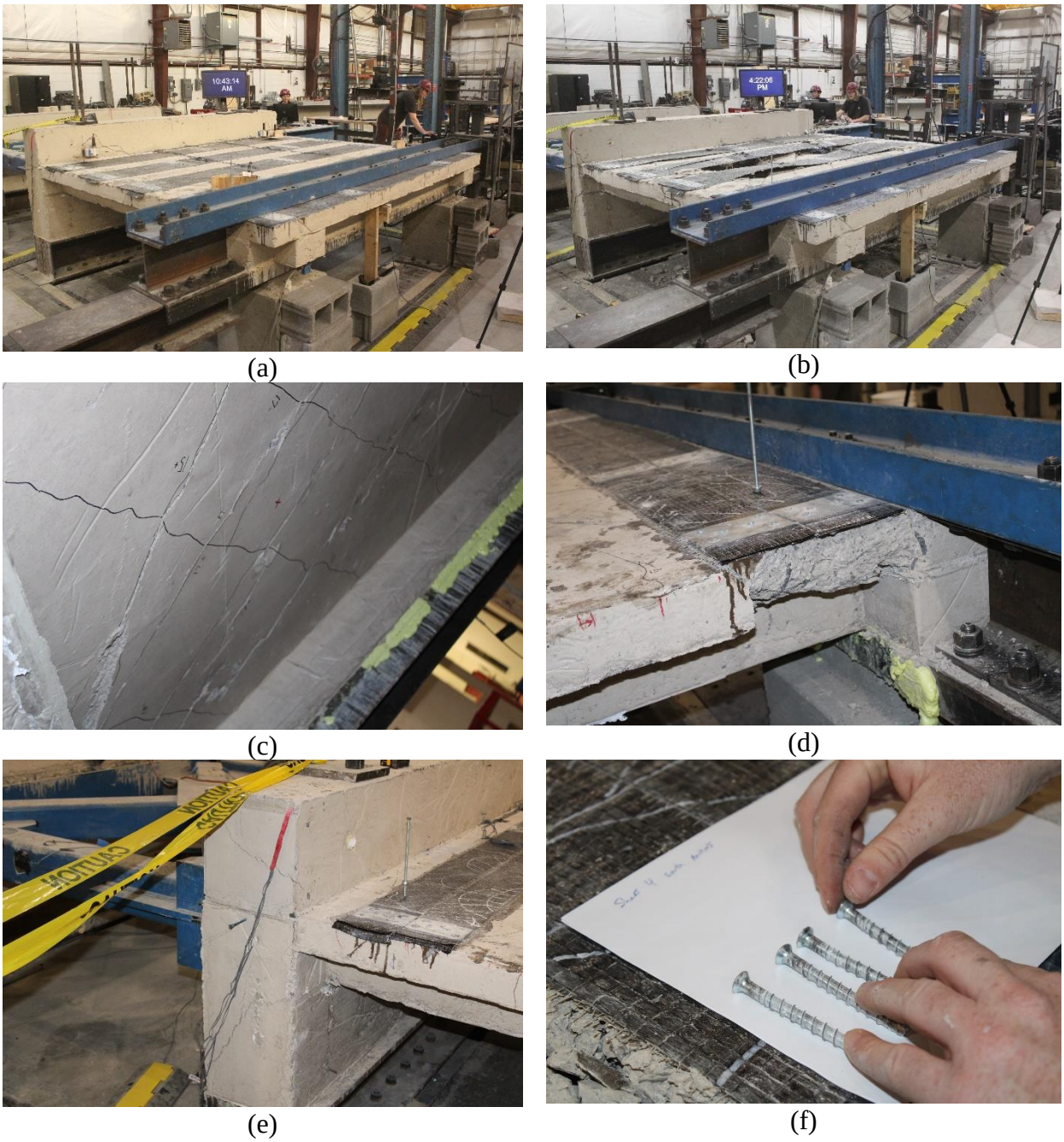

Figure 4-33. Photographs of Specimen CD14: (a) Before Testing; (b) Post-test Condition of the Specimen; (c) Underside Diagonal Tension Cracks; (d) Loss of Concrete in Edge of Slab; (e) Concrete Spalling near Sensor SP-SE Mounting Point; (f) Post-test Condition of Concrete Screws from an End Anchor on Sheet S4.

Figure 4-34 shows the FRP strain measurements as recorded by the seven functioning strain gages installed on sheets S3, S4, S5, and S6 plotted against the actuator load. S5N yielded erroneous data and was consequently removed from analysis. Table 4-8 provides a summary of the FRP strains at peak load ε_f^{pk} from the FRP strain gages. The average FRP strain at peak push load, derived from the data of the seven gages, was determined to be 0.0046,

with a coefficient of variation of 50%. The minimum and maximum recorded FRP strains at peak push load were 0.0021 and 0.0087, respectively.

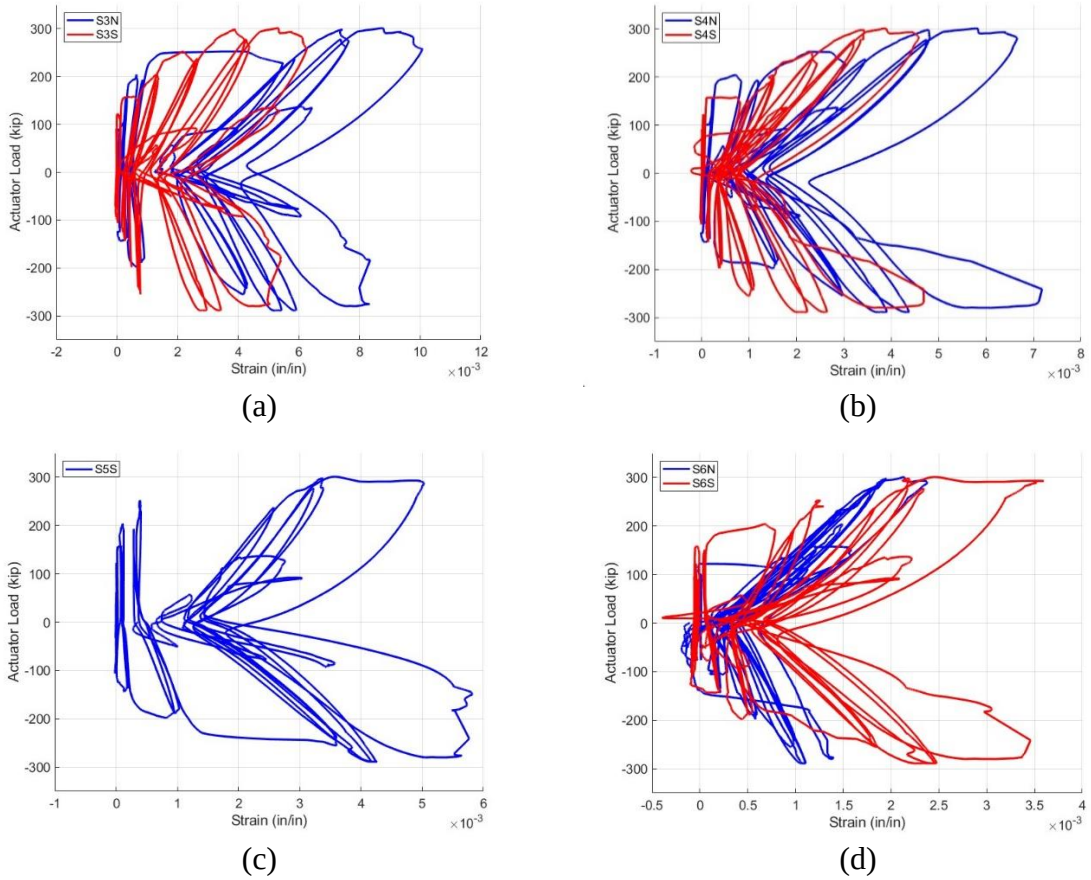

Figure 4-34. FRP Strain Measurements from Specimen CD14: a) Sheet S3; b) Sheet S4; c) Sheet S5; d) Sheet S6.

Table 4-8. FRP Strains for Specimen CD14.

Strain gage	Strain at peak push load, ε_f^{pk}	Strain at peak pull load, $\varepsilon_f^{pk,pull}$	Strain at end of push direction strength plateau $\varepsilon_f^{pk,plat}$
S3N	0.0087	0.0052	0.0094
S3S	0.0053	0.0028	0.0058
S4N	0.0058	0.0038	0.0064
S4S	0.0039	0.0021	0.0044
S5S	0.0036	0.0042	0.0049
S6N	0.0021	0.0011	0.0023
S6S	0.0025	0.0023	0.0035

Figure 4-35 shows the reinforcing steel strain measurements from the strain gages installed on the chord beam longitudinal reinforcement. Figure 4-36 shows the reinforcing steel strain measurements from the strain gages installed on the distributed mesh of reinforcement in the diaphragm field. Table 4-9 shows the reinforcing steel strain measurements at peak pull load from the 16 strain gages on the reinforcing steel. The average deck bar strain at peak load was 0.0080, the average north (tension at peak load) chord bar strain at peak load was 0.0024, and the average south (compression at peak load) chord bar strain at peak load was -0.0001. Reinforcing steel train data indicate that chord steel and deck bar steel do not carry high compressive stress, and that the deck bar steel begins yielding prior to reaching peak load while the chord steel remains elastic throughout the duration of the test.

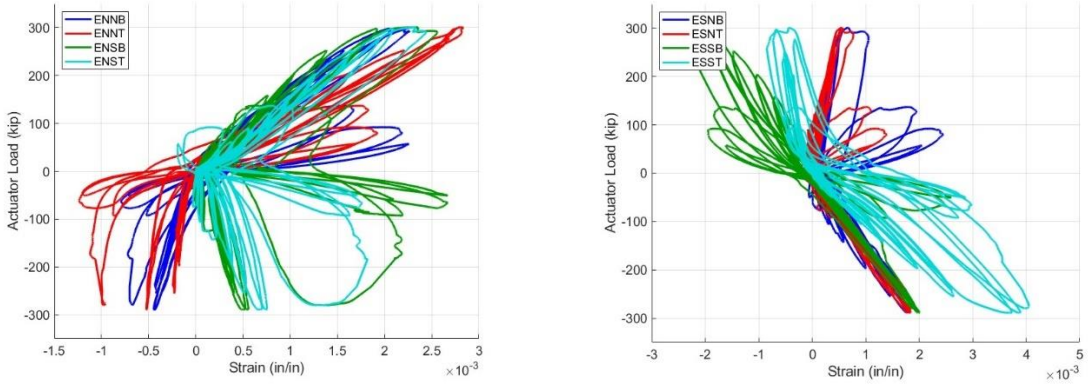

(a) (b)

Figure 4-35. Chord Beam Longitudinal Reinforcement Strains from Specimen CD14: a) North Chord Beam; b) South Chord Beam.

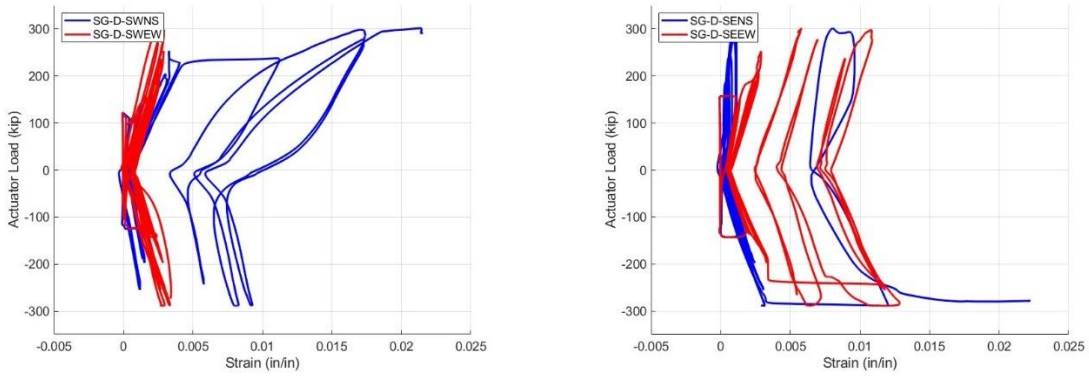

(a) (b)

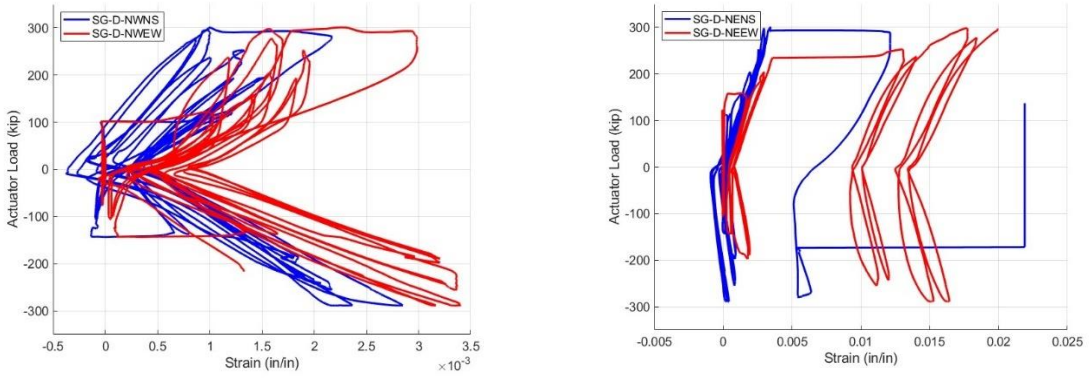

(c) (d)

Figure 4-36. Deck Bar Reinforcement Strains from Specimen CD14: a) SW Deck Bars; b) SE Deck Bars; c) NW Deck Bars; d) NE Deck Bars.

Table 4-9. Reinforcing Steel Strains at Peak Load for Specimen CD14.

Strain gage	**Strain at peak push load, ε_f^{pk}**	**Strain at peak pull load, $\varepsilon_f^{pk,pull}$**
C-ESST	0.0004	0.0037
C-ESNB	0.0007	0.0018
C-ESNT	0.0006	0.0018
C-ENSB	0.0023	0.0005
C-ENST	0.0023	0.0007
C-ENNT	0.0028	-0.0005
C-ESSB	-0.0021	0.0020
C-ENNB	0.0022	-0.0004
D-NWEW	0.0023	0.0034
D-SWNS	0.0213	0.0081
D-NWNS	0.0010	0.0022
D-SEEW	0.0058	0.0116
D-NENS	0.0034	0.0004
D-NEEW[1]	0.0198	0.0151
D-SENS	0.0080	0.0032
D-SWEW	0.0023	0.0028

[1] Gage reading was limited by sensor range. Actual strain may have been higher.

Figure 4-8 shows the crack maps for Specimen CD14 taken at the peak push and pull actuator load for a given cycle. Cracks were marked and measured throughout the test, and maps were prepared to document each crack and associated width at cycles 15 and 21. Figure 4-38 shows the debonding maps for Specimen CD14 taken at the peak push and pull actuator load for a given cycle. The first observation of debonding of FRP sheets was made during the

positive portion of cycle 17. The specimen reached its peak capacity of 301.2 kips. At the peak load, approximately 75% of the FRP sheet areas in the field of the diaphragm had debonded.

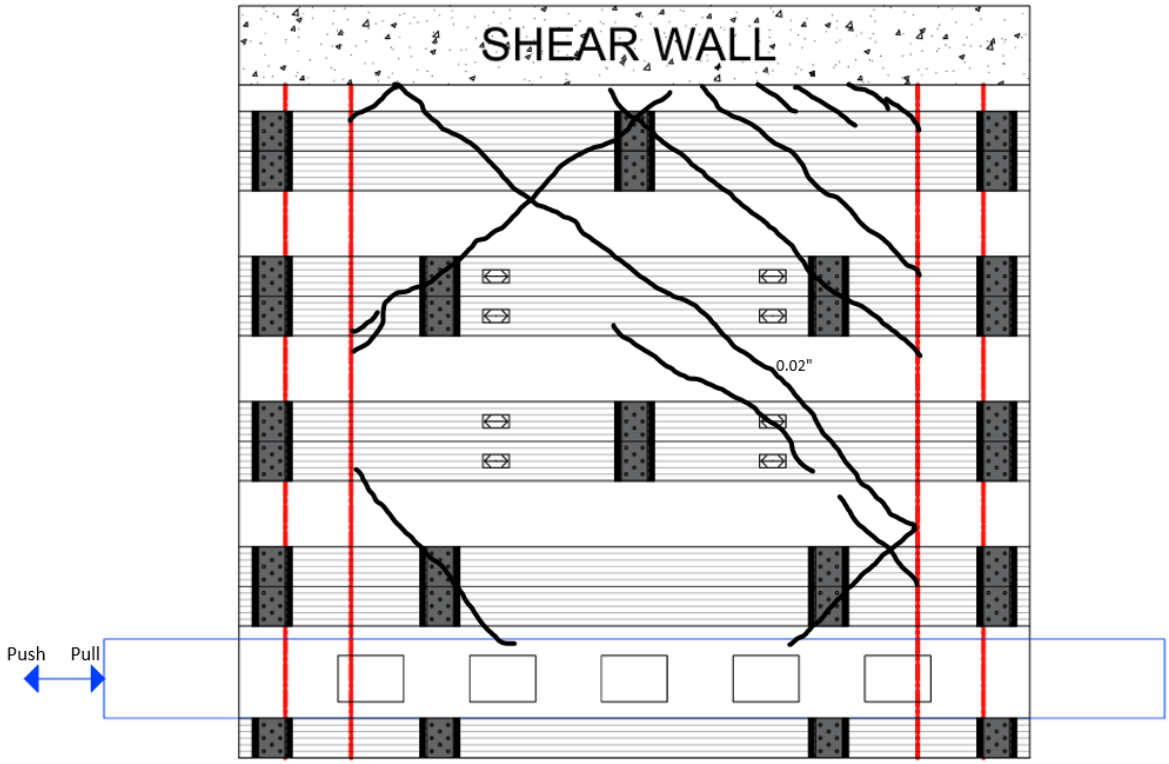

(a) Cycle 15 for a "push" load of 121.9 kips at $\gamma_G = 0.0010$ rad.

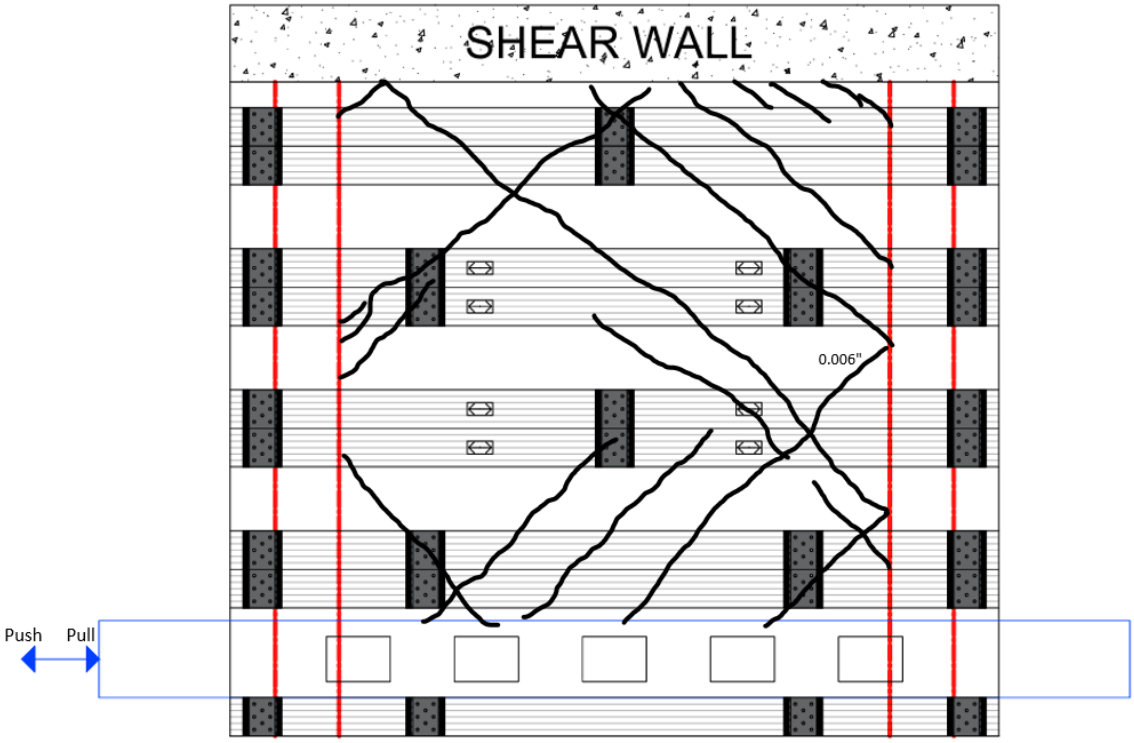

(b) Cycle 15 for a "pull" load of -105.4 kips at $\gamma_G = 0.0010$ rad.

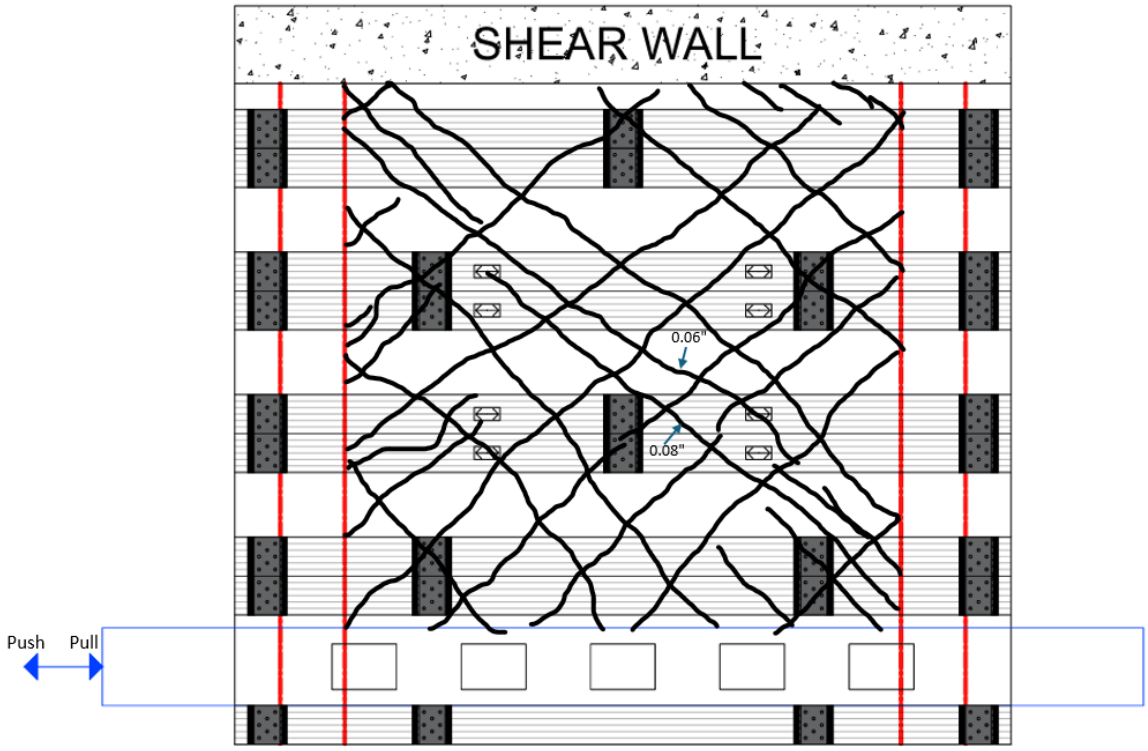

(c) Cycle 21 for a "push" load of 252.1 kips at $\gamma_G = 0.0029$ rad.

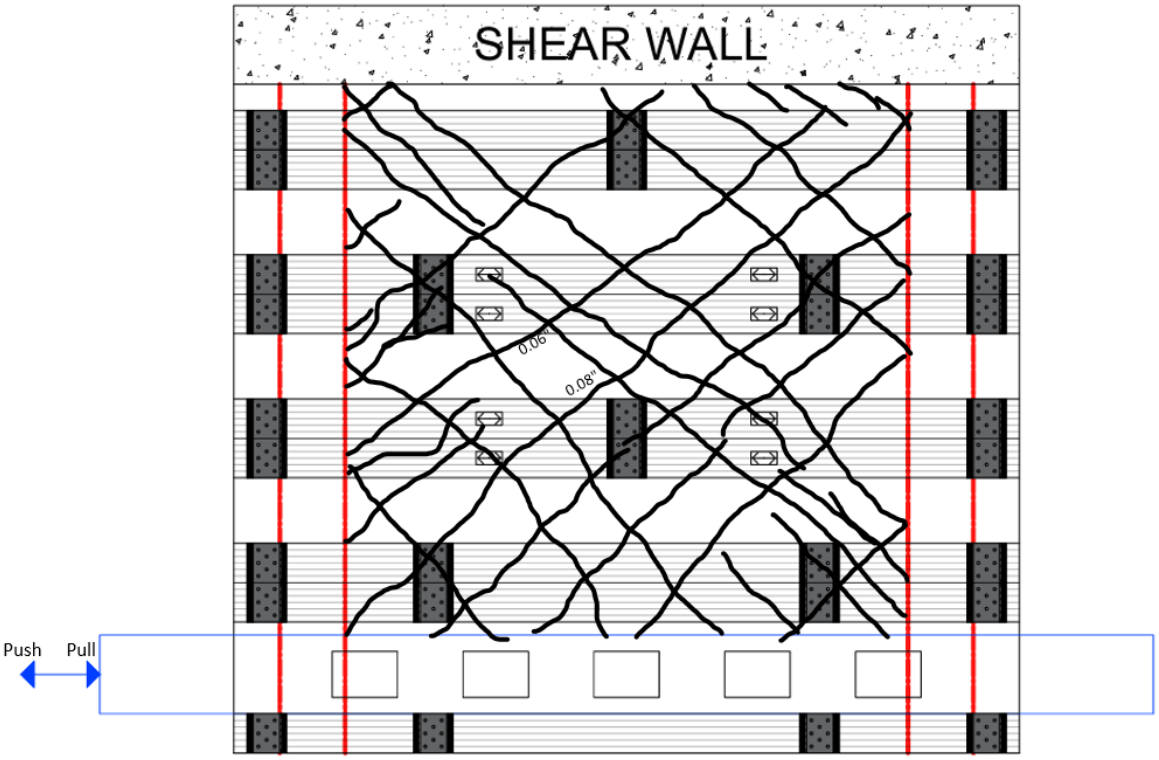

(d) Cycle 21 for a "pull" load of -255.2 kips at $\gamma_G = -0.0043$ rad.

Figure 4-37. Crack maps for Specimen CD14.

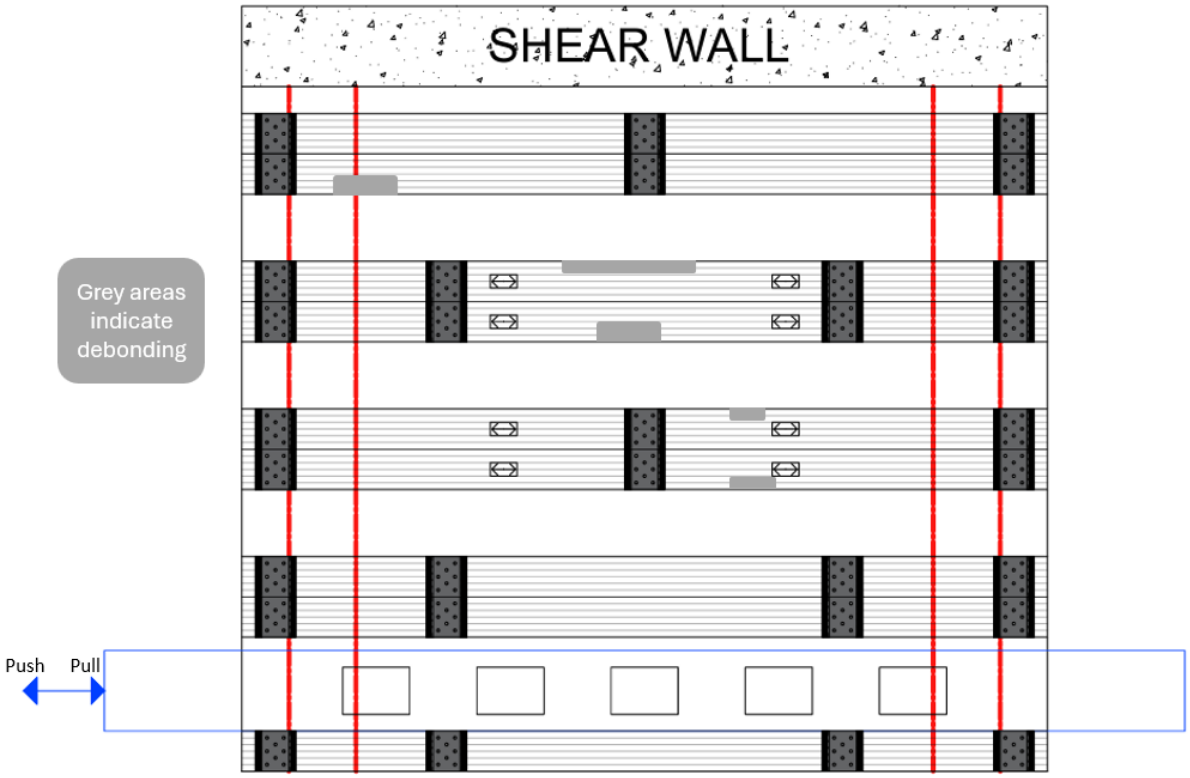

(a) Cycle 17 for a "push" load of 158.5 kips at $\gamma_G = 0.0015$ rad.

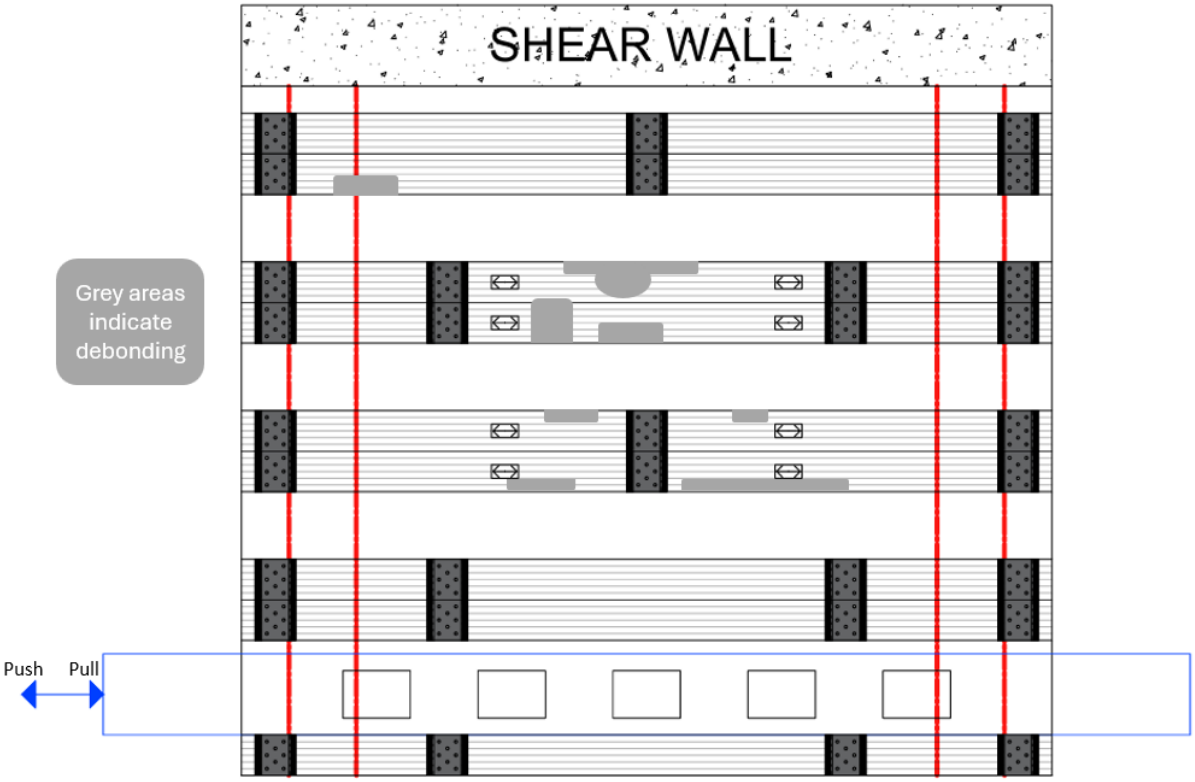

(b) Cycle 17 for a "pull" load of -143.3 kips at $\gamma_G = -0.0017$ rad.

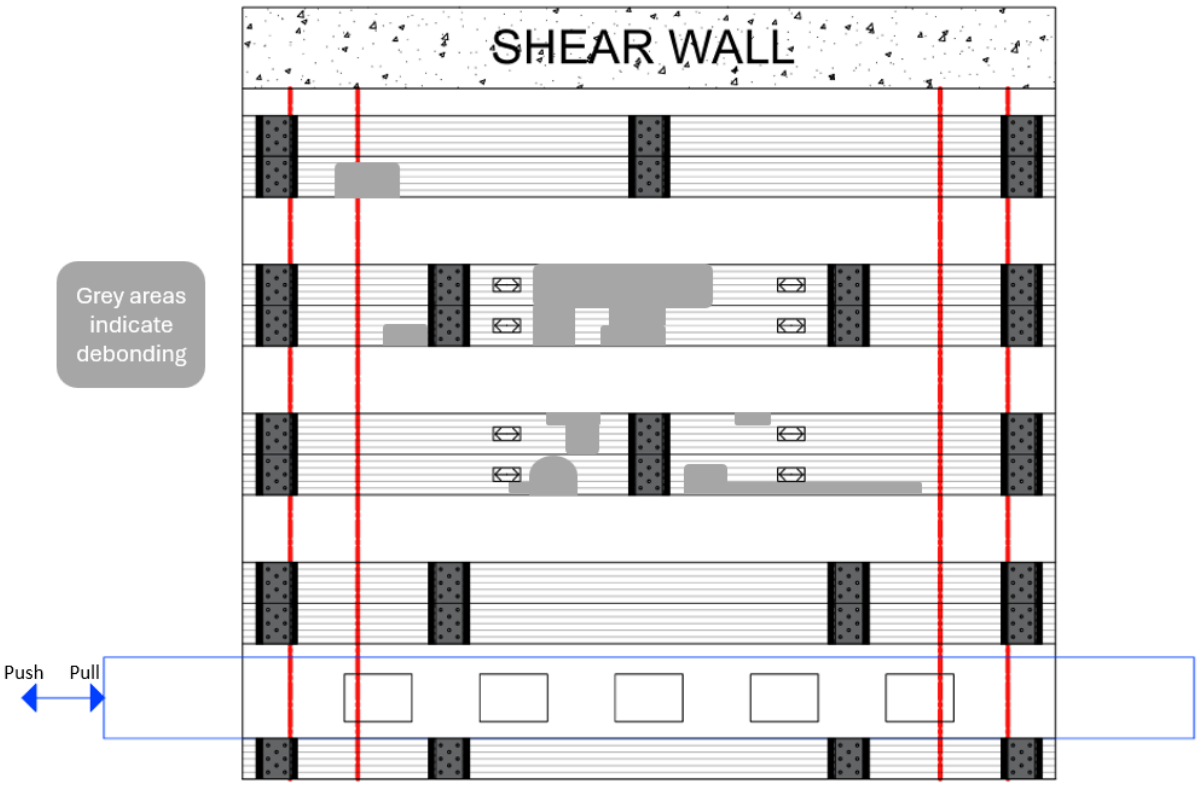

(c) Cycle 19 for a "push" load of 204.3 kips at $\gamma_G = 0.0021$ rad.

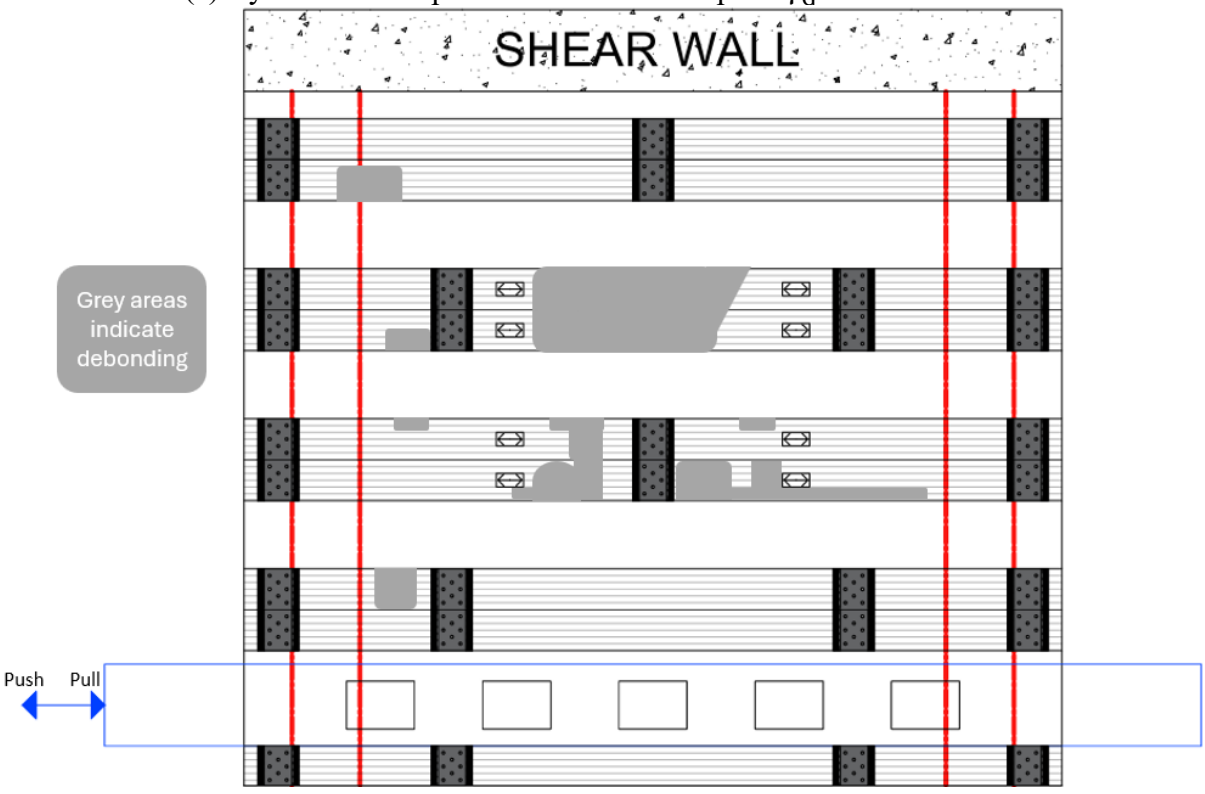

(d) Cycle 19 for a "pull" load of -197.6 kips at $\gamma_G = -0.0030$ rad.

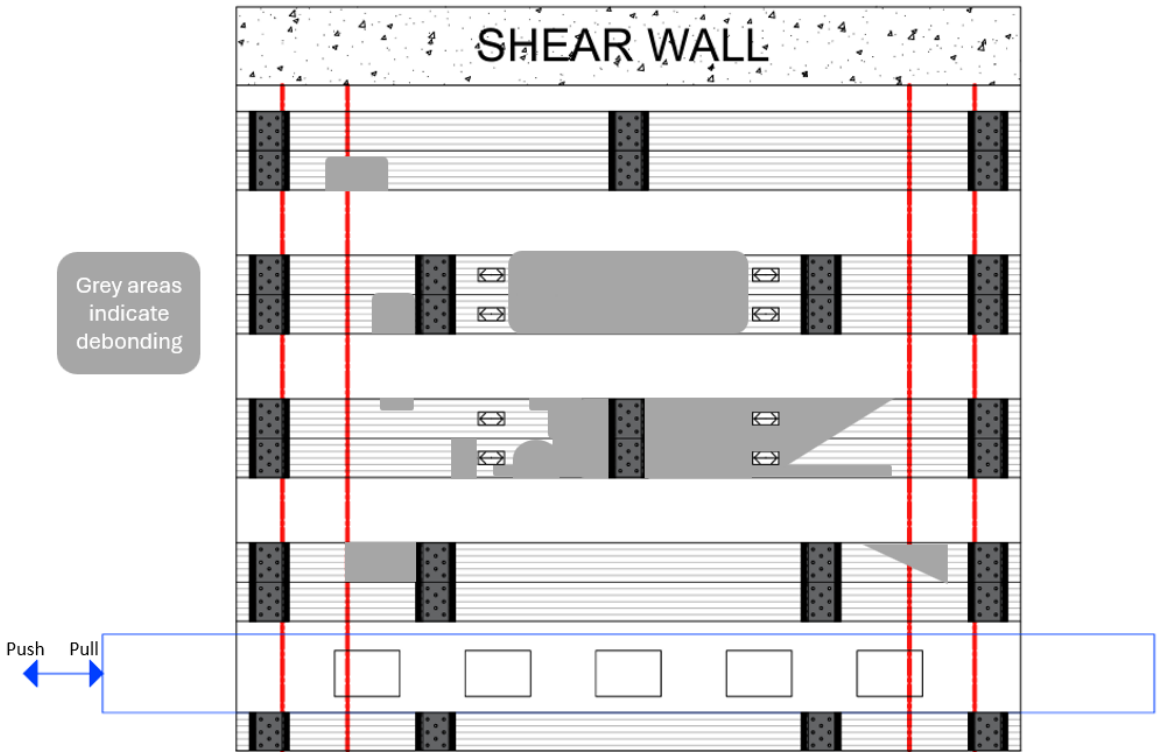

(e) Cycle 21 for a "push" load of 252.1 kips at $\gamma_G = 0.0029$ rad.

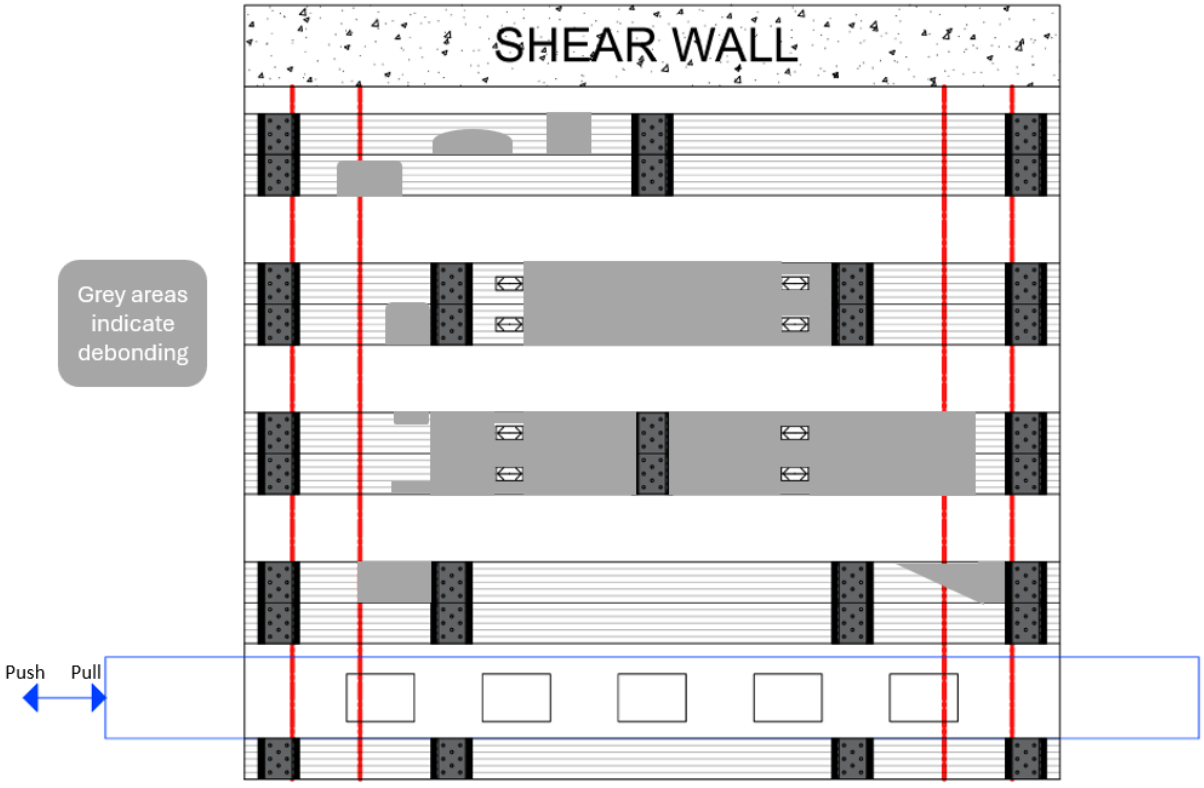

(f) Cycle 21 for a "pull" load of -255.2 kips at $\gamma_G = -0.0043$ rad.

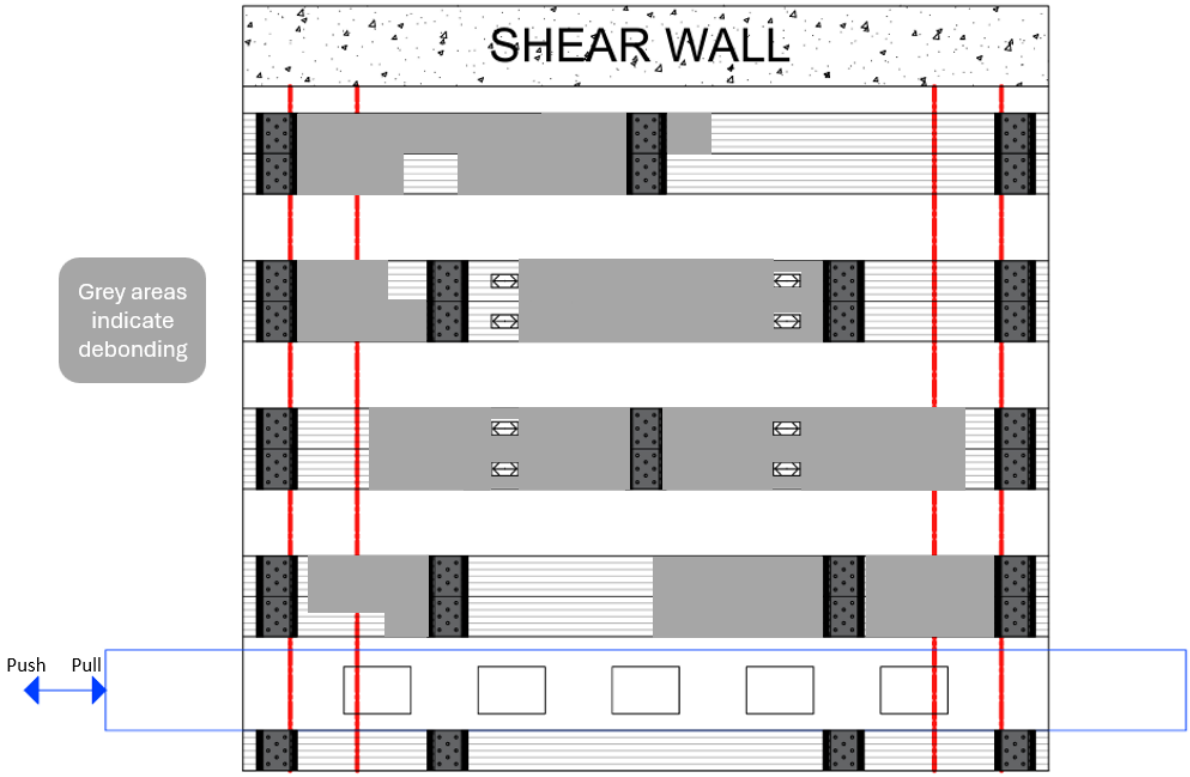

(g) Cycle 23 for a "push" load of 298.1 kips at $\gamma_G = 0.0041$ rad.

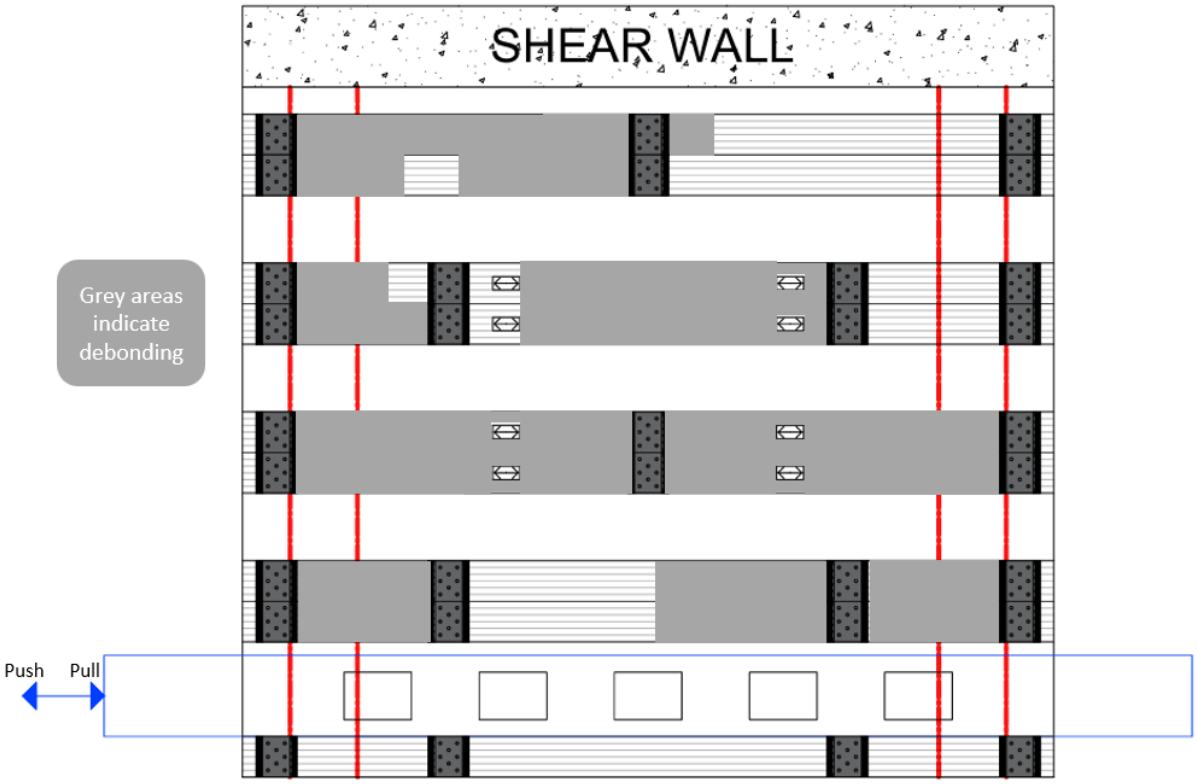

(h) Cycle 23 for a "pull" load of -288.7 kips at $\gamma_G = -0.0070$ rad.

Figure 4-38. FRP Debonding Maps for Specimen CD14.

Chapter 5. Analysis of Database

5.1. Overview of Diaphragm Specimen Database

A database of FRP strengthened diaphragm test results was assembled to better inform the design recommendations proposed in this thesis. The database includes five simply supported specimens described in Aryan et al. (2022), six cantilever specimens described in Hutton et al. (2023), and eight new cantilever specimens described herein. Existing experimental programs were reviewed in Section 2.3, while new specimens were described in Chapter 3 and Chapter 4. Among the 19 diaphragm specimens, 16 were strengthened with FRP while the remaining three control specimens served to establish a baseline. Specimen construction information is shown in Table 5-1, experimental results are shown in Table 5-2, and load-deformation envelopes are shown in Figure 5-1. The results of the 19 specimens are used in this chapter to quantify aspects of behavior, and then the results are discussed in detail in Chapter 6 to understand the effect of key design variables on behavior and make specific design recommendations.

All but two specimens were constructed with NWC, and the concrete compressive strength varies from 2650 psi to 5690 psi. The steel transverse reinforcement ratio varies from 0.0015 to 0.0023, while the FRP ply stiffness, $K_f = nt_f w_f E_f$, ranges from 900-14000 kip/(in./in.). Among the 16 strengthened specimens, 12 were strengthened parallel to applied shear, one was strengthened perpendicular to applied shear, and three were strengthened with an orthogonal grid. 13 specimens were strengthened with CFRP and three specimens were strengthened with GFRP. End mechanical anchorage of the FRP was provided by end wrapping for four specimens from Aryan et al. (2022), while the cantilever diaphragm specimens utilized fiber splay anchors for nine specimens and steel plate anchors for two specimens. One strengthened cantilever specimen contained no anchorage. Intermediate mechanical anchorage was provided in two of the nine specimens containing fiber splay anchors, and in both specimens containing steel plate anchors.

Reversed cyclic loading protocols were applied to all 19 diaphragm specimens. For the specimens in Hutton et al. (2023) and described in this thesis, the reversed cyclic protocol was entirely displacement controlled with two cycles per displacement step, following quasi-static

guidelines in FEMA 461 (2007). For the specimens described in Aryan et al. (2022), the reversed cyclic protocol was force controlled until the applied force reached 1.6 times the strength of the control, Specimen 3-0. Then, the protocol switched to displacement control. For the specimens described in Aryan et al. (2022), one cycle was conducted for the first three load-controlled steps, while three cycles were conducted for all other steps.

Table 5-1. Diaphragm Specimen Database: Specimen Construction Information.

Specimen ID	Concrete Compressive Strength (psi)	Transverse Reinforcing Ratio	Steel Yield Stress (ksi)	FRP Material	FRP Strengthening Scheme	Orientation, α	Anchorage Scheme
3-0 (A)	5280	0.00153	75.4	N/A	N/A	N/A	N/A
3-H-1 (A)	5280	0.00153	75.4	C200H	1 ply 3 in. wide at 24 in. O.C.	90°	Wrapped around both edges
3-H2-1 (A)	5280	0.00153	75.4	C200HM	1 ply 3 in. wide at 24 in. O.C.	90°	Wrapped around both edges
3-G-1 (A)	5280	0.00153	75.4	EG50	1 ply 6 in. wide at 24 in. O.C.	90°	Wrapped around both edges
3-G-2 (A)	5280	0.00153	75.4	EG50	1 ply 6 in. wide at 24 in. O.C.[1]	90°	Wrapped around both edges
CD1 (H)	4760	0.00205	88.3	N/A	N/A	N/A	N/A
CD2 (H)	4570	0.00205	88.3	C100HM	1 ply 12 in. wide at 24 in. O.C.	90°	Splay anchors at ends
CD3 (H)	3670	0.00205	88.3	SCH-11UP	1 ply 14.5 in. wide at 23.2 in. O.C.	90°	Intermediate & end splay anchors
CD4 (H)	3670	0.00205	88.3	SEH-51A	1 ply 21 in. wide at 21 in. O.C.	90°	Splay anchors at ends
CD5 (H)	3950	0.00205	88.3	C200HM	1 ply 7 in. wide at 25.7 in. O.C.	90°	Splay anchors at ends
CD6 (H)	4470	0.00205	88.3	C100HM	1 ply 12 in. wide at 24 in. O.C.	0°	Intermediate & end splay anchors
CD7	2650	0.00229	73.6	C220HM	2 plies 12 in. wide at 12 in. O.C.	90°	2 rows of splay anchors at ends
CD8	3050	0.00229	73.6	C220HM	2 plies 12 in. wide at 12 in. O.C.	90°	N/A
CD9	2980	0.00153	68.0	C220HM	2 orthogonal plies 12 in. wide at 12 in. O.C.	0°/90°	Perimeter splay anchors between layers
CD10	2980	0.00153	68.0	C100HM	2 orthogonal plies 12 in. wide at 24 in. O.C.	47°/-47°	Splay anchors at ends
CD11	5690 (LW)	0.00153	82.3	N/A	N/A	N/A	N/A
CD12	5690 (LW)	0.00153	82.3	C220HM	2 orthogonal plies 12 in. wide at 12 in. O.C.	0°/90°	Perimeter splay anchors between layers
CD13	2980	0.00153	72.3	SCH-41	2 plies 6 in. wide at 10 in. O.C.	90°	Intermediate & end anchor plates
CD14	3150	0.00153	72.3	SCH-41	2 plies 12 in. wide at 22 in. O.C.	90°	Alternating intermediate & end anchor plates

[1]Specimen 3-G-2 was strengthened on both sides. All other specimens strengthened on one side only.
(A) - Aryan et al. (2022); (H) - Hutton et al. (2023)

Table 5-2. Diaphragm Specimen Database: Experimental Results.

Specimen ID	Cracking Strength (kips)	Maximum Recorded FRP Strain at Peak Load (%)	Shear Angle at Peak Load (rad)	Peak Actuator Load, $V_{u,exp}$ (kips)	Failure Mode(s) at Peak Load[2]	Post-Peak Failure Mode(s)[2]
3-0 (A)	Unknown[3]	N/A	0.0051	133	CDS	N/A
3-H-1 (A)	Unknown[3]	0.50	0.0056	167	FD	CDS
3-H2-1 (A)	Unknown[3]	0.50	0.0051	176	FD	CDS
3-G-1 (A)	Unknown[3]	N/A	0.0059	170[1]	FD	CDS
3-G-2 (A)	Unknown[3]	0.75	0.0057	186	Concrete crushing at load point	N/A
CD1 (H)	55	N/A	0.0085	203	CDS	N/A
CD2 (H)	110	0.37	0.0069	280	FD & AR	CDS & SR
CD3 (H)	100	0.45	0.0047	259	FD, FR & AP	CDS & SR
CD4 (H)	80	0.47	0.0076	263	FD, AP & AR	CDS & SR
CD5 (H)	95	0.36	0.0064	240	FD & AP	CDS & SR
CD6 (H)	110	0.48	0.0085	250	FD & AP	CDS & SR
CD7	75	0.29	0.0052	284	FD, CDS & DS at edge beam	FF
CD8	70	0.24	0.0053	287	FD, CDS & DS at edge beam	N/A
CD9	110	0.34	0.0040	319	FD & CDS	FF & DS at shear wall
CD10	110	0.86	0.0042	280	FR	FD & CDS
CD11	50	N/A	0.0053	234[1]	CDS	N/A
CD12	65	0.29	0.0157	346	DS at shear wall	CBC
CD13	75	0.42	0.0051	264[1]	FD	CDS & intermediate AP
CD14	60	0.87	0.0093	301	FD	CDS

[1]Peak load happens in pull direction. Otherwise, peak load happens in push direction.
[2]FD = FRP Debonding; FR = FRP Rupture; CDS = Concrete Diagonal Shear; AR = Anchor Rupture; AP = Anchor Pullout; DS = Direct Shear; SR = Reinforcing Steel Rupture; FF = Anchorage-induced Flange Failure; CBC = Chord Beam Crushing.
[3]Unable to determine cracking strength from available data.
(A) - Aryan et al. (2022); (H) - Hutton et al. (2023)

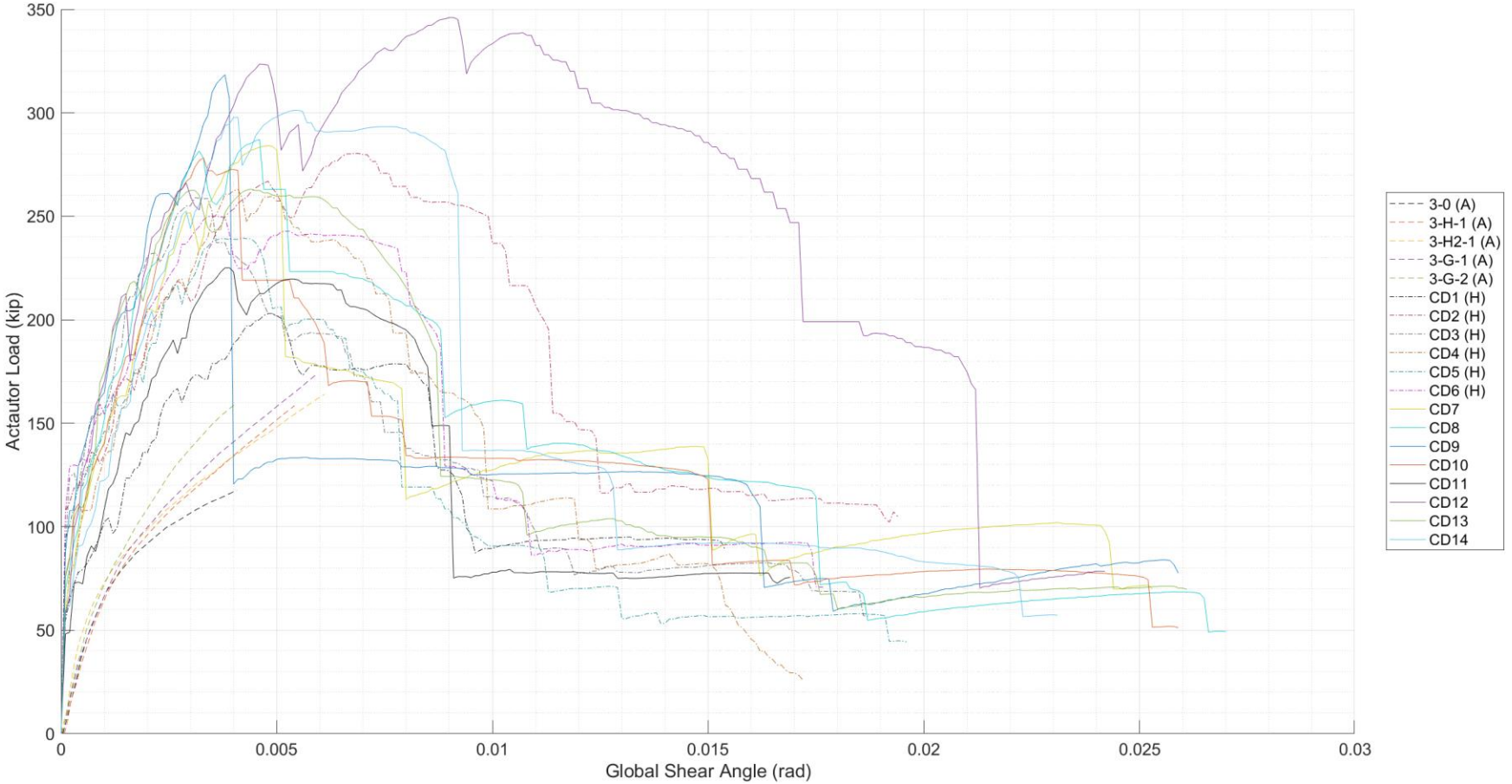

Figure 5-1. Diaphragm Specimen Load-Deformation Envelopes. (A) - Aryan et al. (2022); (H) - Hutton et al. (2023)

5.2. Steel and Concrete Contribution to Shear Strength

The experimental strength of the three control Specimens, 3-0, CD1, and CD11, is compared to the design equations in ACI 318 (2019) and predictions from Response2000 to evaluate these beam-based approaches for predicting diaphragm shear strength. In ACI 318 (2019), the steel and concrete contributions are evaluated separately, ignoring any potential interaction between steel and concrete, and are assumed to occur at the same time. The design concrete contribution to diaphragm shear strength is calculated using Eq. (17):

$$V_c = A_{cv} 2\lambda \sqrt{f_c'} \tag{17}$$

where: V_c is the concrete contribution to shear capacity (lbs); A_{cv} is the gross concrete section (in.^{2}); λ is the LWC reduction factor; and f_c' is the concrete compressive strength (psi).

The design steel contribution to diaphragm shear strength is calculated using Eq. (18):

$$V_s = A_{cv} \rho_t f_y \tag{18}$$

where: V_s is the internal reinforcing steel contribution to shear capacity (lbs); A_{cv} is the gross concrete section (in.^{2}); ρ_t is the area ratio of internal steel reinforcement parallel to the direction of in-plane shear; and f_y is the yield stress of the internal steel reinforcement (psi). Additionally, steel oriented perpendicular to in-plane shear is typically not considered to have an effect on shear capacity.

In this analysis, the gross concrete area A_{cv} corresponds with the cross-sectional area in which diagonal shear cracks were observed during the experimental test. The slab thickness is 4 in. for all specimens in the database. For the specimens described in Aryan et al. (2023), hereafter referred to as "Aryan specimens", shear cracks were observed to extend the entire diaphragm depth (60 in.) so $A_{cv} = 240\ in.^2$ is used. For the specimens described in this thesis and in Hutton et al. (2023), hereafter referred to as "CD specimens", shear cracks were observed to extend between the centerlines of the chord beams (96 in.) so $A_{cv} = 384\ in.^2$ is used. A comparison between design strength and experimental strength for the three control specimens is shown in Table 5-3.

Table 5-3. Control Specimen ACI 318-19 Design Strengths.

Specimen ID	V_c (kip)	V_s (kip)	$V_c + V_s$ (kip)	$V_{u,exp}$ (kip)	$\frac{V_{u,exp}}{V_c + V_s}$
3-0 (A)	35	28	125[1]	133	1.06
CD1 (H)	53	69	122	203	1.66
CD11	50	48	99	234	2.37
				Average	1.70
				COV	39%

[1]Multiplied by two to represent 3-point loading test setup.
(A) - Aryan et al. (2022); (H) - Hutton et al. (2023)

The design equations in ACI 318 (2019) are conservative for the three control diaphragm specimens as the experimental strength is on average 70% greater than the design strength. However, a coefficient of variation (COV) of 39% indicates high variance between the three specimens. Although typically ignored in design, the contribution of steel reinforcement oriented perpendicular to applied shear is included in a second set of calculations to investigate the level of conservatism of this approach, in addition to any change in COV relative to the conventional approach. In the second approach, $V_{s,1}$ is the shear strength contribution of transverse reinforcement and $V_{s,2}$ is the shear strength contribution of longitudinal reinforcement. A different A_{cv} is used in the $V_{s,2}$ calculation. It is equivalent to the diaphragm depth times the distance between the edge of the support and the edge of the loading channel, 320 in.^{2} for Aryan specimens and 336 in.^{2} for CD specimens. The results from this analysis are shown in Table 5-4.

Table 5-4. Control Specimen Design Strengths Including Longitudinal Steel.

Specimen ID	V_c (kip)	$V_{s,1}$ (kip)	ρ_2[1]	$V_{s,2}$ (kip)	$V_c + V_{s,1} + V_{s,2}$ (kip)	$V_{u,exp}$ (kip)	$\frac{V_{u,exp}}{V_c + V_{s,1} + V_{s,2}}$
3-0 (A)	35	28	0.00229	55	236[2]	133	0.56
CD1 (H)	53	69	0.00205	61	183	203	1.11
CD11	50	48	0.00153	42	141	234	1.66
						Average	1.11
						COV	49%

[1]Reinforcement ratio of longitudinal steel in the distributed mesh of reinforcement.
[2]Multiplied by two to represent 3-point loading test setup.
(A) - Aryan et al. (2022); (H) - Hutton et al. (2023)

Including longitudinal steel in the design strength calculation results in a conservative approximation for Specimen CD1 and CD11, but is highly unconservative for Specimen 3-0,

with an experimental strength 44% less than design. Additionally, this method has a higher COV (49%) relative to the conventional method (39%). Results from these analyses indicate that the beam approach for quantifying diaphragm shear strength results in high variance due to an oversimplification of diaphragm behavior, and the inclusion of longitudinal steel does not result in more accurate design strengths or less variation in the results.

In addition to the code approach, the modified compression field theory (MCFT) was investigated as an alternative method for predicting the behavior of the control specimens. MCFT calculations were facilitated in the software program Response2000 version 1.9.6 (Bentz 2001). Although Response2000 uses a beam-based approach, it was thought that the MCFT may produce more accurate results as it treats cracked concrete as an orthotropic material and accounts for tension stiffening and compression softening. Two input files were prepared for each of the three control specimens, one with and one without distributed longitudinal reinforcement, denoted as $V_{R2K,2}$ and $V_{R2K,1}$, respectively. Results from the analysis are shown in Table 5-5.

Table 5-5. Control Specimen MCFT Analysis in Response2000.

Specimen ID	$V_{u,exp}$ **(kip)**	$V_{R2K,2}$ **(kip)**	$V_{R2K,1}$ **(kip)**	$\frac{V_{u,exp}}{V_{R2K,2}}$	$\frac{V_{u,exp}}{V_{R2K,1}}$
3-0 (A)	133	152	149	0.87	0.89
CD1 (H)	203	174	170	1.17	1.19
CD11	234	150	147	1.56	1.59
			Average	1.20	1.22
			COV	29%	29%

(A) - Aryan et al. (2022); (H) - Hutton et al. (2023)

The MCFT analyses in Response2000 demonstrate higher accuracy and lower variance relative to the ACI 318 (2019) approach. When longitudinal steel is included in the model, experimental strengths are on average 20% greater than predicted, with a COV of 29%. When longitudinal steel is not included, the reduction in strength is very small, resulting in experimental strengths that are 22% greater than predicted, on average, also with a COV of 29%. Although the MCFT provides more accurate predictions than the approach in ACI 318 (2019), the MCFT analyses are still inconsistent with experimental results, likely due to the inability of the MCFT as implemented in Response2000 to capture biaxial behavior.

For application in this thesis, the MCFT as implemented Response2000 is used to approximate the contribution of steel and concrete to diaphragm shear strength for specimens without directly comparable controls. For the CD specimens, the shear strength contribution of the perimeter beams acting as a portal frame is also considered. In cases where directly comparable control specimens exist (with similar reinforcement layouts and material properties), the control specimen strength is taken as the steel and concrete contribution for the corresponding FRP-strengthened specimens.

5.3. Diaphragm Shear Strength

As shown in Eq. (1), diaphragm shear strength is typically expressed as a superposition of steel, concrete, and FRP contributions. To analyze the effect of externally bonded FRP strengthening on diaphragm shear strength, the contribution to shear strength attributed to FRP was estimated by approximating and removing the other contributions. Section 5.3.1 demonstrates the procedure for approximating an additional contribution to shear strength, the frame action contribution, relevant to specimens with perimeter beams. Section 5.3.2 demonstrates the procedure for approximating steel and concrete contributions using the MCFT in Response2000. Section 5.3.3 presents estimated FRP contributions to diaphragm shear strength.

5.3.1 Frame Action Contribution to Diaphragm Strength

The frame action contribution refers to the behavior of the chord beams and edge beam in the CD specimens behaving as a single-bay moment frame. As there were no perimeter beams in the Aryan specimens, no frame action contributions were approximated for these specimens. The procedure for quantifying frame action was adopted from Hutton et al. (2023). For detailed information on this procedure, see Hutton et al. (2023). A brief overview is provided in the following paragraphs.

The frame contribution was idealized with an elastic perfectly plastic load-deformation relationship, shown in Figure 5-2 from Hutton et al. (2023). The edge beam was assumed to be rigid, while the chord beams were assumed to have fixed supports to both the edge beam and shear wall. The frame stiffness was calculated using Eq. (19), the plastic shear capacity of the frame was calculated using Eq. (20), and results are summarized in Table 5-6.

$$K_{Frame} = 2 \cdot \frac{12E_cI_e}{h^3} \tag{19}$$

where: K_{Frame} is the frame stiffness (k/in.); E_c is the concrete elastic modulus; I_e is the effective moment of inertia of the chord beams, taken as 0.7 times the gross moment of inertia plus 0.3 times the cracked moment of inertia; and h is the length of the chord beam from the face of the shear wall to the free end (102 in.).

$$V_p = 2 \cdot \frac{2M_n}{h} \tag{20}$$

where: V_p is the plastic shear capacity of the frame (kip); M_n is the chord beam moment capacity (k-in.); h is the length of the chord beam from the face of the shear wall to the free end (102 in.).

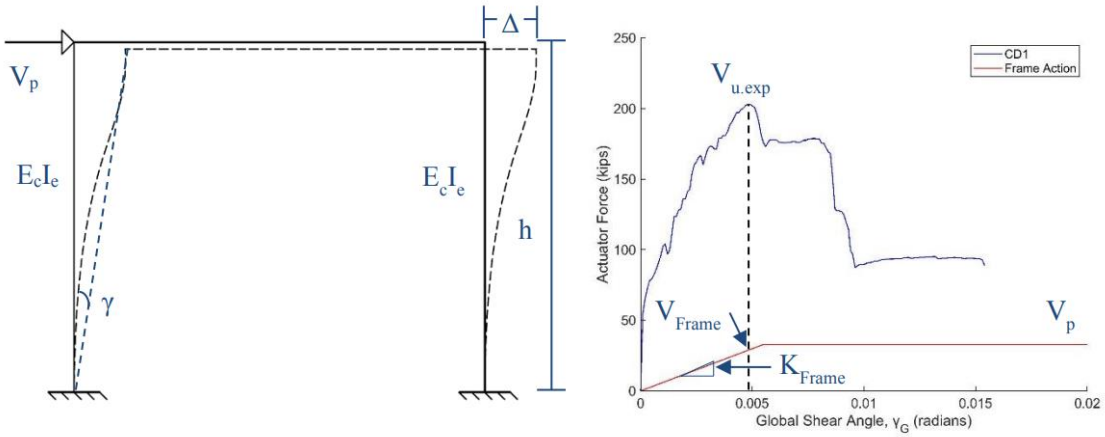

Figure 5-2. Frame Action: (a) Frame Model; (b) Procedure for Quantifying Frame Action for Specimen CD1 [From (Hutton et al. 2023)].

Table 5-6. Summary of Frame Action Contribution for CD Specimens.

Specimen ID	Cracked Moment of Inertia, I_{cr} (in.^{4})	Gross Moment of Inertia, I_g (in.^{4})	Frame Stiffness, K_{Frame} (k/in.)	Plastic Shear Capacity, V_p (kip)	Global Shear Angle at Peak Load (rad)	Frame Contribution, V_{Frame} (kip)
CD1 (H)	489	833	58.6	33	0.0049	30
CD2 (H)	510		56.3	32	0.0069	32
CD3 (H)	531		54.2	31	0.0033	18
CD4 (H)	531		54.2	31	0.0041	23
CD5 (H)	492		58.3	31	0.0043	25
CD6 (H)	479		59.9	32	0.0036	22
CD7	591		48.3	31	0.0044	24
CD8	562		51.2	31	0.0046	24
CD9	561		51.2	31	0.0038	20
CD10	577		49.6	31	0.0035	18
CD11	544		53.1	36	0.0053	29
CD12	544		53.1	37	0.0090	37
CD13	576		49.7	31	0.0051	26
CD14	573		50.1	32	0.0055	28

5.3.2 Steel and Concrete Contribution to Diaphragm Strength

Although each experimental program contained an unstrengthened control specimen, for some specimens the experimental FRP contribution to shear strength could not be calculated as the difference between the control specimen experimental strength and the strengthened specimen experimental strength. This was due to variations in the concrete and steel material properties, as well as the steel reinforcement layout, between strengthened specimens and their relevant control specimen. Therefore, a method for predicting the concrete and steel contribution to shear strength was necessary for specimens without a directly comparable control.

Similar to the frame contribution, the methodology for quantifying the steel and concrete contribution was adopted from Hutton et al. (2023). A brief overview is provided in this section. The MCFT was used to approximate the steel and concrete contribution in lieu of the equation in ACI 318 (2019) due to the conservatism of the code. MCFT calculations were facilitated in the software program Response2000 version 1.9.6 (Bentz 2001). As described previously, the MCFT was only utilized for specimens without a directly comparable control

specimen. Because the strengthened Aryan specimens and CD12 had directly comparable control specimens, the MCFT was not used in their analysis.

The Response2000 input parameters were identical to the input parameters described in Hutton et al. (2023). Only the concrete material properties, steel material properties, and steel reinforcement layout were adjusted between specimens. The concrete material properties shown in Table 3-3, steel material properties shown in Table 3-4, and steel reinforcement layouts shown in Figure 3-11 and Figure 3-12 were used as input parameters for the MCFT calculations. See Hutton et al. (2023) for more detailed information on the input parameters. Approximations of the steel and concrete contribution to shear strength, $(V_c + V_s)_{R2K}$, for specimens without a directly comparable control are shown in Table 5-7.

Table 5-7. Approximation of Steel and Concrete Contributions using Response2000.

Specimen ID	**Approximation of Steel and Concrete Contribution to Shear Strength, $(V_c + V_s)_{R2K}$ (kip)**
CD1	172
CD2	171
CD3	162
CD4	162
CD5	166
CD6	170
CD7	148
CD8	151
CD9	117
CD10	117
CD13	119
CD14	121

5.3.3 FRP Contribution to Diaphragm Strength

To estimate the FRP contribution to diaphragm shear strength, $V_{f,exp}$, two separate equations were used. For specimens with a directly comparable control (Specimen CD12 and Aryan specimens), Eq. (21) was used. The control strength could be directly removed from the strengthened specimen strength because concrete and steel material properties, as well as steel reinforcement layouts, were similar between specimens. For specimens without a directly comparable control (CD specimens except Specimen CD12), Eq. (22) was used. The process

for approximating the frame contribution and contribution from steel and concrete is described in the previous sections. Estimated experimental contributions of FRP to shear strength are shown in Table 5-8.

$$V_{f,exp} = V_{u,exp} - V_{u,control} \quad (21)$$

where: $V_{f,exp}$ is the experimental contribution of FRP to shear strength (kip); $V_{u,exp}$ is the maximum force applied to the strengthened specimen (kip); $V_{u,control}$ is the maximum force applied to the control specimen with similar material properties and steel reinforcement layout as the strengthened specimen (kip).

$$V_{f,exp} = V_{u,exp} - V_{Frame} - (V_c + V_s)_{R2K} \quad (22)$$

where: $V_{f,exp}$ is the experimental contribution of FRP to shear strength (kip); $V_{u,exp}$ is the maximum force applied to the strengthened specimen (kip); V_{Frame} is the contribution of frame action to shear strength (kip); $(V_c + V_s)_{R2K}$ is the contribution of steel and concrete to shear strength calculated using Response2000 (kip).

Table 5-8. Estimated Experimental FRP Contribution to Shear Strength.

Specimen ID	Ultimate Experimental Strength, $V_{u,exp}$ (kip)	Ultimate Control Specimen Strength, $V_{u,control}$ (kip)	Frame Contribution, V_{Frame} (kip)	Steel and Concrete Contribution to Shear Strength, $(V_c + V_s)_{R2K}$ (kip)	Experimental FRP Shear Strength Contribution $V_{f,exp}$ (kip)
3-0 (A)	133		N/A	N/A	0
3-H-1 (A)	167	133	N/A	N/A	34
3-H2-1 (A)	176	133	N/A	N/A	43
3-G-1 (A)	170	133	N/A	N/A	38[1]
3-G-2 (A)	186	133	N/A	N/A	53
CD1 (H)	203		30	172	1
CD2 (H)	280	N/A	32	171	77
CD3 (H)	259	N/A	18	162	79
CD4 (H)	263	N/A	23	162	78
CD5 (H)	240	N/A	25	166	48
CD6 (H)	250	N/A	22	170	58
CD7	284	N/A	22	148	114
CD8	287	N/A	24	151	112
CD9	319	N/A	20	117	181[1]
CD10	280	N/A	18	117	145
CD11	234		N/A	N/A	0
CD12	346	234	N/A	N/A	112
CD13	264	N/A	26	119	119
CD14	301	N/A	28	121	152

[1]Inconsistent with subtracting whole numbers due to precision not shown in table.
(A) - Aryan et al. (2022); (H) - Hutton et al. (2023)

5.4. Effective FRP Strain

As FRP is assumed to have a linear constitutive relationship, it is simple to analyze the performance of FRP strengthening using effective strains, thus the effective stress in the FRP is simply the product of the effective strain and mean elastic modulus of the FRP composite reported by the manufacturer. In this section, three types of effective strain are compared. The design effective strain associated with debonding from the concrete substrate is calculated using guidance adopted from ACI PRC-440.2R-23 (2023) in Section 5.4.1. FRP strains measured by strain gages installed on the FRP are summarized in Section 5.4.2. Estimated FRP strains using $V_{f,exp}$ as described in Section 5.3.3 are calculated in Section 5.4.3. These three types of

strains are compared to each other and to the 0.4% limit from ACI PRC-440.2R-23 (2023) in Chapter 6.

5.4.1 Design Effective Strain

The design effective strain, ε_{fe}, is calculated following the guidance in ACI PRC-440.2R-23 (2023) for shear strengthening of beams which is often adopted for use in diaphragm shear strengthening (Ormeno et al. 2019). Following the design recommendation proposed in Hutton et al. (2023), the wrapping scheme modification factor $k_2 = 1.0$, as it approaches 1.0 using the equation in ACI PRC-440.2R-23 (2023) as the active bond length is typically two to three orders of magnitude less than the effective depth.

ACI PRC-440.2R-23 (2023) provides two equations for the effective strain in the FRP: one associated with FRP rupture and one associated with debonding of the FRP. Because diaphragm retrofits do not typically enclose the entire section, ACI PRC-440.2R-23 (2023) indicates that Eq. (23) should be used as FRP in unenclosed retrofits typically debonds prior to the loss of aggregate interlock in the concrete.

$$\varepsilon_{fe} = \kappa_t \varepsilon_{fu} \leq 0.004 \tag{23}$$

where: ε_{fe} is the effective strain in the FRP; κ_t is the bond-reduction coefficient for shear; and ε_{fu} is the ultimate fiber strain in the FRP.

The calculation procedure for the bond-reduction coefficient is adopted from bond mechanism equations presented in Khalifa et. al (1998), where researchers applied experimental data on direct tension tests of concrete-bonded FRP (Maeda et al. 1997) to calibrate an equation for the reduction in effective stress associated with the debonding failure mode. According to Khalifa et al. (1998), the bond-reduction coefficient is affected by the concrete strength, the FRP configuration and the stiffness of the FRP laminate. The bond-reduction coefficient is calculated using Eq. (24).

$$\kappa_t = \frac{k_1 k_2 L_e}{468 \varepsilon_{fu}} \leq 0.75 \tag{24}$$

where: κ_t is the bond-reduction coefficient for shear; k_1 is the concrete strength modification factor; k_2 is the wrapping scheme modification factor, equal to 1.0 for diaphragm shear strengthening; L_e is the active bond length (in.); and ε_{fu} is the ultimate fiber strain in the FRP.

The active bond length refers to the length over which bond stresses are maintained (ACI 2019). An active bond length, as opposed to the total bonded length, is used because FRP debonding typically propagates progressively from the loading point. For an idealized FRP strip in pure tension, debonding first occurs due to concrete cracking near the loading point. As debonding occurs, the active bond length shifts down the total bonded length of the FRP sheet until the entire sheet debonds (Khalifa et al. 1998). The active bond length is calculated using Eq. (25).

$$L_e = \frac{2500}{\left(nt_f E_f\right)^{0.58}} \tag{25}$$

where: L_e is the active bond length (in.); n is the number of layers of FRP sheets; t_f is the thickness of the FRP laminate (in.); and E_f is the tensile modulus of the FRP (psi). When strengthening with an orthogonal grid of unidirectional FRP, the active bond length should be calculated independently for each orientation as the layers are assumed to not share stiffness. For example, to calculate the effective bond length of two orthogonal layers of unidirectional FRP, one would set $n = 1$, t_f as the thickness of one layer, and E_f as the tensile elastic modulus of one layer, ignoring any contribution of transverse stiffness from the other layer.

The concrete strength modification factor can be calculated using Eq. (26).

$$k_1 = \left(\frac{f_c'}{4000}\right)^{\frac{2}{3}} \tag{26}$$

where: k_1 is the concrete strength modification factor; and f_c' is the compressive strength of the concrete (psi).

The equations above are used to calculate the design effective strain for the 16 strengthened specimens in the database. Design effective strains and relevant parameters in the calculation procedure are shown in Table 5-9.

Table 5-9. Effective Design Strain Calculations.

Specimen ID	Active Bond Length, L_e (in.)	Concrete Modification Factor, k_1	Wrapping Scheme Modification Factor, k_2	FRP Rupture Strain, ε_{fu} (%)	Bond Reduction Coefficient, κ_t	Design Effective Strain, $\varepsilon_{fe} = \kappa_t \varepsilon_{fu}$ (%)
3-H-1 (A)	1.35	1.20	1.00	1.70	0.20	0.35
3-H2-1 (A)	1.15	1.20	1.00	1.27	0.23	0.30
3-G-1 (A)	2.44	1.20	1.00	2.13	0.29	0.63[1]
3-G-2 (A)	2.44	1.20	1.00	2.13	0.29	0.63[1]
CD2 (H)	1.56	1.09	1.00	1.30	0.28	0.37
CD3 (H)	1.74	0.94	1.00	1.00	0.35	0.35
CD4 (H)	2.19	0.94	1.00	1.80	0.25	0.44[1]
CD5 (H)	1.15	0.99	1.00	1.27	0.19	0.24
CD6 (H)	1.56	1.08	1.00	1.30	0.28	0.36
CD7	0.75	0.76	1.00	1.05	0.12	0.12
CD8	0.75	0.83	1.00	1.05	0.13	0.13
CD9	1.13	0.82	1.00	1.05	0.19	0.20
CD10	1.56	0.82	1.00	1.30	0.21	0.27
CD12	1.13	1.26	1.00	1.05	0.29	0.30
CD13	0.76	0.82	1.00	0.90	0.15	0.13
CD14	0.76	0.85	1.00	0.90	0.15	0.14

[1]Exceeds the 0.4% limit on design effective strain. Specimen is strengthened with GFRP.
(A) - Aryan et al. (2022); (H) - Hutton et al. (2023)

5.4.2 Measured FRP Strain

The measured FRP strain, $\varepsilon_{f,SG}$, refers to strain measured by strain gages installed on the FRP during the duration of the test. It should be noted that the strain gages installed on Specimen CD9 and CD12 measured strain of FRP sheets oriented perpendicular to applied shear, while gages installed on Specimen CD10 measured strain of FRP sheets in each orientation (+47° and -47°). In all other strengthened specimens, the strain gages measured strain of FRP sheets oriented parallel to applied shear. For specimens in this experimental program, strain gage layouts are provided in Section 3.7, and strain data are presented in Chapter 4. For information on the other specimens, see Aryan et al. (2022) and Hutton et al. (2023). The maximum recorded strain at peak load for all strengthened diaphragm specimens, except 3-G-1, is shown in Table 5-2. Specimen 3-G-1 is not included as the FRP strain data were not recorded during the test.

5.4.3 Estimated Effective Strain

The estimated effective strain, $\varepsilon_{f,exp}$, is the strain associated with the experimental FRP shear strength contribution, $V_{f,exp}$, which was calculated in Section 5.3.3. The equations for the design FRP shear strength contribution and effective FRP stress, Eq. (4) and Eq. (5), are rearranged to isolate $\varepsilon_{f,exp}$ as shown in Eq. (27). Eq. (27) assumes all FRP, except for FRP oriented approximately parallel to the compression strut (see Specimen CD10), achieves the same strain at peak load. Eq. (27) was used to determine the estimated effective strain for all 16 FRP-strengthened diaphragm specimens. The two cases in Eq. (27) are visualized in Figure 5-3 for clarity. The results of this analysis and relevant input parameters are shown in Table 5-10.

$$\varepsilon_{f,exp} = \begin{cases} \dfrac{V_{f,exp} s_f}{A_{fv} E_f} \left(\dfrac{1}{d_{fv,1}} + \dfrac{1}{d_{fv,2}} \right) & for\ sheets\ both \parallel and\ \perp \\ \dfrac{V_{f,exp} s_f}{A_{fv} E_f} \left(\dfrac{1}{(\sin \alpha_1 + \cos \alpha_1)\, d_{fv,1}} \right) & for\ all\ other\ cases \end{cases} \tag{27}$$

where: $\varepsilon_{f,exp}$ is the estimated effective strain in the FRP; $V_{f,exp}$ is the experimental FRP shear strength contribution (kip); s_f is the center-to-center spacing of FRP sheets (in.); A_{fv} is the area of an FRP sheet (in.^{2}); E_f is the manufacturer-reported average tensile elastic modulus (ksi); α_1 is the FRP sheet orientation relative to the longitudinal axis (degrees); $d_{fv,1}$ is the effective depth of the FRP, defined in this analysis as the transverse depth with which shear cracks were observed during the experiment (96 in. for CD specimens, 60 in. for Aryan specimens); and $d_{fv,2}$ is the effective depth of FRP oriented perpendicular to applied shear (84 in. for CD specimens, N/A for Aryan specimens). The trigonometric term is not included in the equation for specimens with perpendicular and parallel FRP orientations, as it reduces to 1.0 for both 0° and 90°. For Specimen CD10, with sheets oriented at 47° and -47°, only the positive angle is considered (i.e., $\alpha_1 = 47°$) as sheets oriented nearly parallel to the compression strut experienced negligible strain relative to sheets oriented in the other direction.

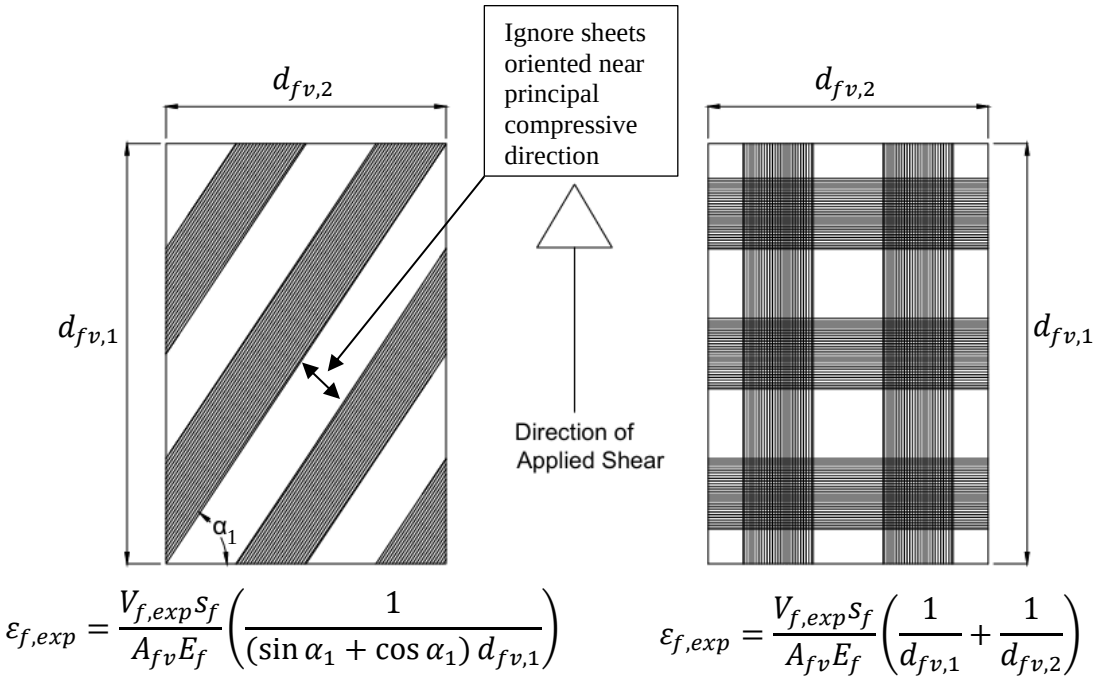

Figure 5-3. Visualization of Procedure for Estimating Experimental Effective FRP Strain.

Table 5-10. Estimated Effective FRP Strain Analysis.

Specimen ID	Experimental FRP Shear Strength Contribution $V_{f,exp}$ (kip)	O.C. Spacing of FRP Sheets, s_f (in.)	Area of FRP Sheet, A_{fv} (in.^{2})	FRP Tensile Elastic Modulus, E_f (ksi)	Orientation, α_1 (deg)	Estimated Effective FRP Strain, $\varepsilon_{f,exp}$ (%)
3-H-1 (A)	17[1]	24.0	0.12	10700	90	0.53
3-H2-1 (A)	21[1]	24.0	0.12	14240	90	0.50
3-G-1 (A)	19[1]	24.0	0.24	3870	90	0.81
3-G-2 (A)	26[1]	24.0	0.24	3870	90	1.13
CD2 (H)	77	24.0	0.24	16700	90	0.48
CD3 (H)	79	23.2	0.29	13900	90	0.47
CD4 (H)	78	21.0	1.05	3730	90	0.44
CD5 (H)	49	25.7	0.28	14240	90	0.33
CD6 (H)	58	24.0	0.24	16700	0	0.36
CD7	114	12.0	0.96	14700	90	0.10
CD8	112	12.0	0.96	14700	90	0.10
CD9	181	12.0	0.48	14700	90/0	0.69
CD10	149	24.0	0.24	16700	47	0.64
CD12	112	12.0	0.48	14700	90/0	0.43
CD13	119	10.0	0.48	14600	90	0.18
CD14	152	22.0	0.96	14600	90	0.25

[1]Half of $V_{f,exp}$ is used, assuming each shear span contributes to shear strength equally.
(A) - Aryan et al. (2022); (H) - Hutton et al. (2023)

5.5. Global Response

Envelope curves for the 19 diaphragm specimens were compared to access key differences in cracking strength, post-cracking stiffness, and diaphragm ductility. The envelope curves, as opposed to the hysteretic response, were compared as the load-deformation relationship is simpler to analyze using the envelope curves. However, the hysteretic shear angle response was used to quantify dissipated energy for the CD specimens. The initial stiffnesses of the uncracked diaphragm specimens were not compared as this parameter was difficult to quantify for CD specimens due to quantization error (error due to low resolution) in the sensor readings at such low displacements. The envelope curves are shown in Figure 5-1. As mentioned previously, the effect of key design parameters on these behavioral aspects are discussed in detail in the next chapter along with design recommendations.

5.5.1 Cracking Strength

Cracking strengths for CD specimens are shown in Table 5-2. The cracking strength of the unstrengthened control specimens is consistently less than the cracking strength of each relative strengthened specimen. As described in Hutton et al. (2023), the average cracking strength of Specimen CD2 through CD6 was 96 kips, which was an 85% increase relative to Specimen CD1. Limited information is available regarding the cracking strength of the Aryan specimens. However, the initial stiffness recorded by Aryan et al. indicated no change between control and strengthened specimens. These findings regarding FRP strengthening having no effect on initial stiffness were corroborated in Hutton et al. (2023).

For specimens constructed with NWC, the cracking strength was consistently higher for strengthened specimens relative to Specimen CD1, although varying steel reinforcement layouts make comparing these specimens difficult. The cracking strength was reduced for specimens constructed with LWC, likely due to the reduced tensile strength of LWC relative to NWC.

5.5.2 Post-cracking Stiffness

As visualized in Figure 5-1, FRP strengthened specimens were consistently more stiff after cracking than their relative control. However, there is little variance between the post-

cracking stiffness of the four strengthened Aryan specimens, and the 12 strengthened CD specimens. This observation indicates that, while FRP strengthening does increase post-cracking stiffness, it is not affected by FRP modulus, orientation, ply configuration, and surface coverage.

5.5.3 Ductility

Ductility ratios for the 19 diaphragm specimens are presented in Table 5-11, where ductility is quantified as the quotient of the critical point deformation and the yield point deformation. For the Aryan specimens, the yield point was quantified by fitting a line to the peak loads of the first three cycles and finding the intersection of that line and a second line fitted to the peak values of the following cycles, while the critical point was simply defined as the displacement at peak load (Aryan et al. 2022). A different approach was utilized for the CD specimens, in which the 75% secant stiffness was calculated and the intersection of this line and the peak push load was defined as the yield point, while the critical point was the post-peak shear angle in which the actuator load decreased to 80% of the peak load. For detailed in formation on the ductility analyses, see Aryan et al. (2022) and Hutton et al. (2023). Because of the variances of these two approaches, ductility comparisons between Aryan specimens and CD specimens should be made with caution.

Aryan et al. (2022) noted that the four strengthened specimens in their experimental program experienced higher ductility in the push or pull direction relative to the reference specimen. Additionally, they noted higher ductility in their CFRP strengthened specimens, as the low modulus of GFRP increases the yield point, in addition to increased surface coverage in their GFRP specimens relative to their CFRP specimens. Hutton et al. (2023) found that FRP strengthening perpendicular to applied shear had a negligible effect on ductility. However, they did note increased ductility in Specimen CD6, which had FRP plies oriented perpendicular to applied shear.

Data from this experimental program indicate that heavily strengthened specimens (two 50-100% coverage layers of CFRP) exhibit reduced ductility. Specimen CD12 is a notable exception, likely due to its global shear angle response being heavily influenced by slip at the interface between the diaphragm and the shear wall. The average ductility ratio of the other

heavily strengthened specimens: Specimen CD7, CD8, CD9, and CD10 is 1.73, nearly 40% less than Specimen CD1, despite Specimen CD1 being constructed with cold-drawn reinforcement as opposed to A615 reinforcing steel in Specimen CD7 through CD10.

Table 5-11. Ductility Analysis.

Specimen ID	Yield Point Shear Angle (rad)	Critical Point Shear Angle (rad)	Ductility Ratio
3-0 (A)	0.0011[3]	0.0051[3]	4.78
3-H-1 (A)	0.0007[3]	0.0056[3]	7.80
3-H2-1 (A)	0.0011[3]	0.0051[3]	4.59
3-G-1 (A)	0.0013[3]	0.0042[3]	3.34
3-G-2 (A)	0.0011[3]	0.0057[3]	5.26
CD1 (H)	0.0031	0.0085	2.80
CD2[1] (H)	N/A	N/A	N/A
CD3 (H)	0.0019	0.0047	2.45
CD4 (H)	0.0029	0.0076	2.61
CD5 (H)	0.0026	0.0064	2.41
CD6 (H)	0.0023	0.0085	3.62
CD7	0.0030	0.0052	1.71
CD8	0.0025	0.0053	2.09
CD9	0.0026	0.0040	1.53
CD10	0.0027	0.0042	1.58
CD11	0.0028	0.0085	3.08
CD12	0.0036	0.0157	4.40[2]
CD13	0.0017	0.0082	4.77
CD14	0.0032	0.0093	2.87

[1]Specimen CD2 was not considered in the ductility analysis in Hutton et al. (2023).
[2]Critical shear angle for Specimen CD12 was affected by slip at the shear wall interface.
[3]Shear angle calculated by dividing actuator displacement by 90 in. distance to support.
(A) - Aryan et al. (2022); (H) - Hutton et al. (2023)

5.5.4 Energy Dissipation

Energy dissipation was analyzed to assess the seismic performance of the diaphragm specimens. For the CD specimens, the methodology for quantifying the cumulative shear angle and associated energy from Hutton et al. (2023) was adopted. For more information on this methodology, see Hutton et al. (2023). Aryan et al. (2023) exclusively reports the total energy dissipated by their specimens throughout the duration of the loading protocol. Energy dissipation for CD specimens is shown in Figure 5-4, and total dissipated energy for the Aryan specimens is presented in Table 5-12.

(a)

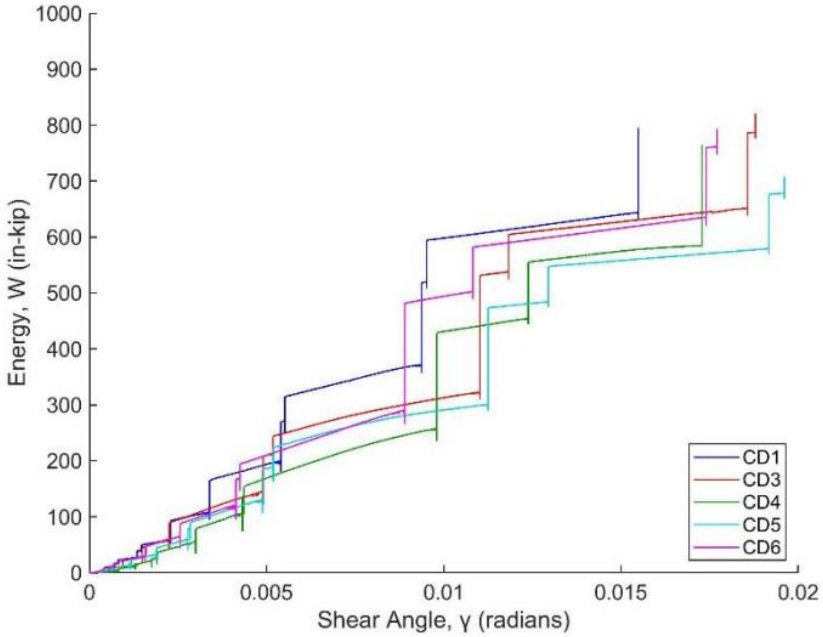

(b)

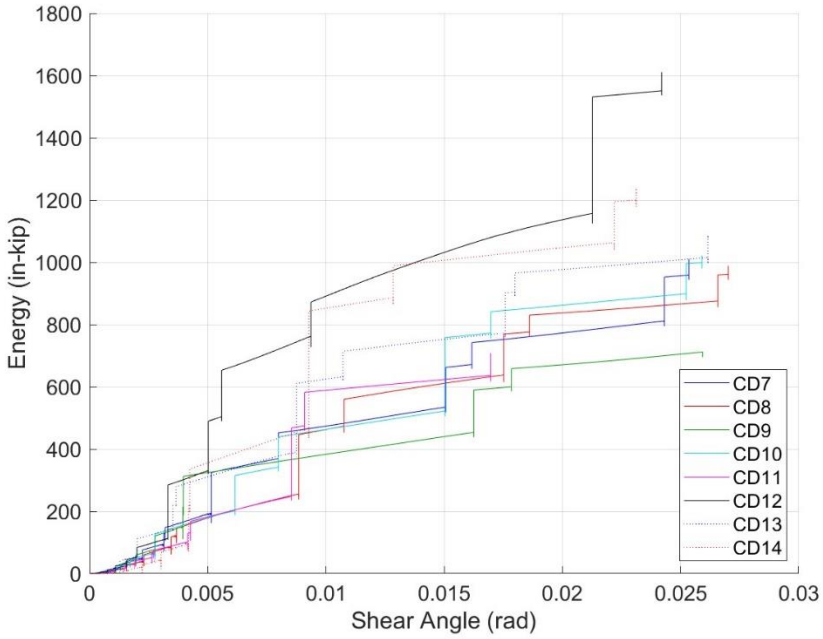

Figure 5-4. Energy Dissipation for: a) Specimen CD1-6 [From (Hutton et al. 2023)]; b) Specimen CD7-14.

Table 5-12. Total Energy Dissipated for Aryan Specimens.

Specimen ID	Total Energy Dissipated (in.-kip)
3-0 (A)	107.3
3-H-1 (A)	171.1
3-H2-1 (A)	211.6
3-G-1 (A)	248.6
3-G-2 (A)	238.9

Similar to the ductility ratio, energy dissipation for Specimen CD12 is influenced by slip at the interface between the diaphragm and shear wall captured in the global shear angle data. Additionally, the total energy dissipated by the diaphragm specimens can vary with peak strength and due to the inconsistent number of displacement cycles applied to each specimen.

Chapter 6. Discussion and Design Recommendations

This section contains discussion on the diaphragm specimen database analyzed in Chapter 5 and design recommendations relevant to reinforced concrete diaphragms strengthened with externally bonded FRP. In particular, these design considerations are for unidirectional FRP applied using a wet layup procedure. These design considerations are specifically for strengthening diaphragm shear zones and do not address strengthening other elements in a diaphragm, such as chords or collectors. These design considerations are developed to modify existing design guidance in ACI PRC-440.2R-23 (2023) and build upon the design recommendations presented in Hutton et al. (2023).

6.1. Effective FRP Design Strain

A comparison of design and estimated FRP strains is shown in Figure 6-1. The estimated effective strain from experiments, $\varepsilon_{f,exp}$ (presented in Table 5-10), exceeded the design effective strain (presented in Table 5-9) in all but three specimens (Specimen CD4, CD7, and CD8) by an average of 51% with a COV of 44%. Among Specimen CD4, CD7, and CD8, the estimated effective strain was on average 15% less than the design effective strain. The governing failure mode affects the estimated strain, as the design strain is associated with global debonding of the FRP. Therefore, Figure 6-1 also indicates the governing failure mode(s) of each specimen. Generally, this shows that the approach for quantifying the design effective strain in Section 11.4.1.2 of ACI PRC-440.2R-23 (2023) is a good lower bound for diaphragm shear strengthening.

To assess the accuracy of the approach for quantifying the design effective strain, a linear best-fit line was established for specimens in FRP debonding is one of the governing failure modes (all strengthened specimens except CD10, CD12 and 3-G-2). As shown in Figure 6-2, the trendline indicates moderate agreement between estimated and design strains, with an R^2 value of 0.52. Therefore, it is recommended to calculate the design effective strain, ε_{fe}, using the approach described in Section 11.4.1.2 of ACI PRC-440.2R-23 (2023) while adopting the recommendation from Hutton et al. (2023) that the wrapping scheme modification factor $k_2 = 1.0$. The k_2 factor approaches 1.0 using Eq. (10) as the active bond length is typically

two to three orders of magnitude less than the effective depth of the diaphragm (Hutton et al. 2023). As shown in Figure 6-1, the recommended approach for quantifying the design effective strain is conservative for the majority of specimens in the database. However, the approach is not conservative for Specimen CD7 (with anchors) and CD8 (without anchors), which were strengthened with two full-coverage CFRP layers oriented in the same direction, indicating the approach may yield unconservative design strains for high surface coverage applications using CFRP.

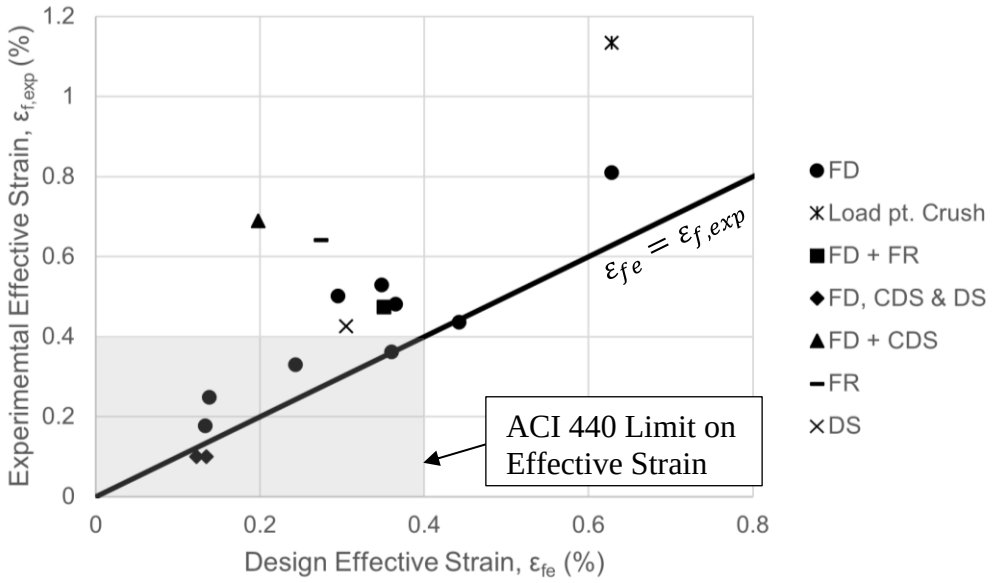

Figure 6-1. Design and Effective Strain Comparison All Strengthened Specimens. DS Indicates Direct Shear Failure, CDS Indicates Concrete Diagonal Shear, FD Indicates FRP Debonding, and FR Indicates FRP Rupture.

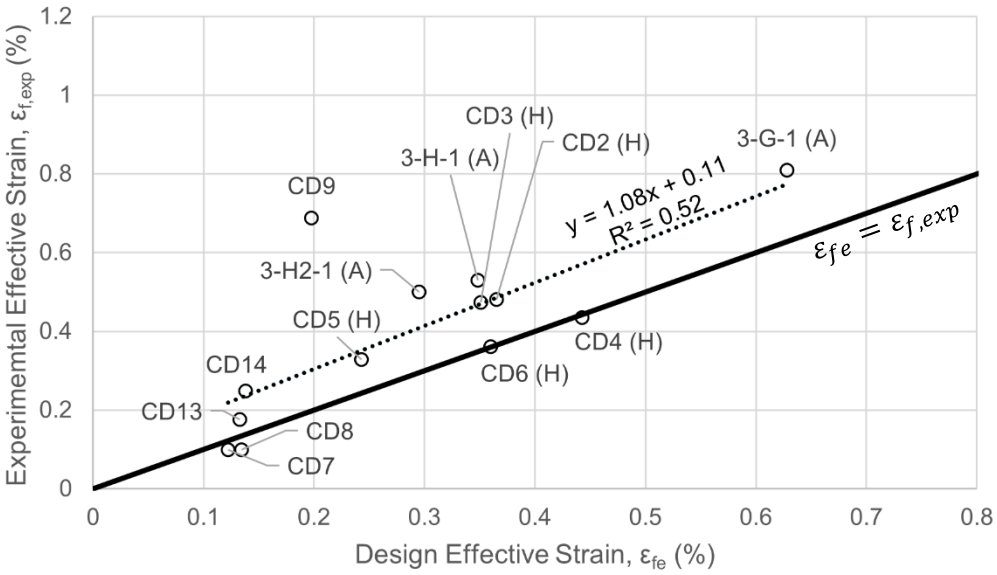

Figure 6-2. Design and Effective Strain Comparison for Specimens Governed or Partially Governed by FRP Debonding with Linear Trendline.

A comparison of design and measured FRP strains is shown in Figure 6-3. Measured FRP strains are based on the largest strains from any strain gage at the time of peak load as described in Section 5.4.2 and summarized in Table 5-2. The maximum recorded strain at peak load, $\varepsilon_{f,SG}$, exceeded the design strain in all but one specimen (Specimen CD12) by an average of 100% with a COV of 69%. The maximum recorded strain is likely very high in some specimens due to stress concentrations in the FRP at a crack forming near a strain gage. It is likely that $\varepsilon_{f,SG}$ for Specimen CD12 did not exceed the design strain as the specimen did not experience global debonding of the FRP. Therefore, the maximum recorded strain may not be representative of the design effective strain due to local effects or failure modes other than FRP debonding.

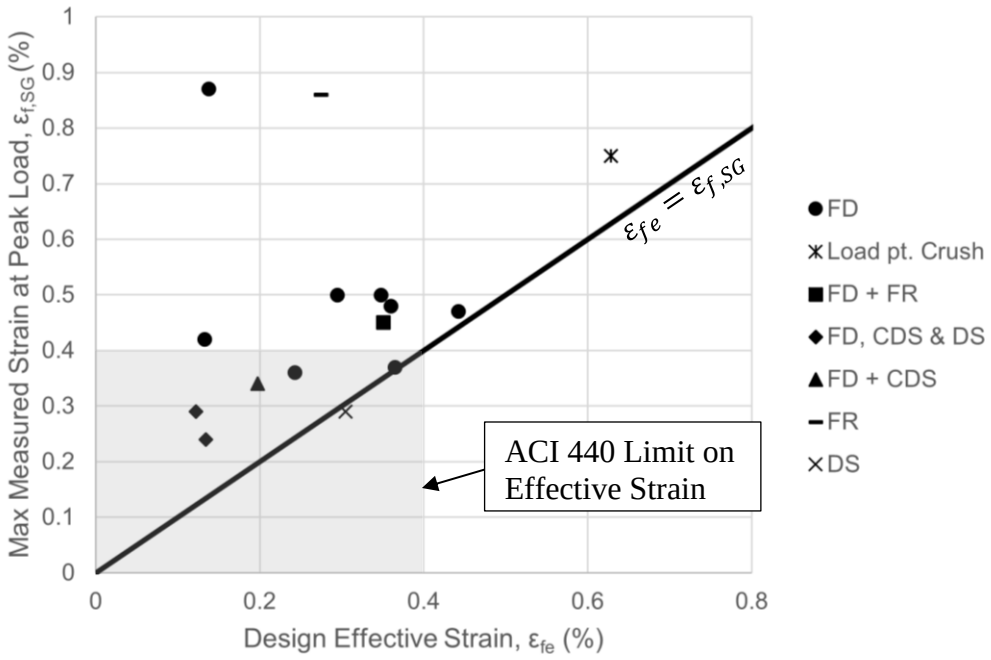

Figure 6-3. Design and Measured Strain Comparison All Strengthened Specimens. DS Indicates Direct Shear Failure, CDS Indicates Concrete Diagonal Shear, FD Indicates FRP Debonding, and FR Indicates FRP Rupture.

Although the 0.004 limit on effective design strain presented in ACI PRC-440.2R-23 (2023) is exceeded by measured and estimated FRP strains in many of the specimens in the database, insufficient experimental data exist to propose a higher limit. Among the 16 strengthened specimens, the 0.004 limit is only exceed by three specimens (Specimen 3-G-1, 3-G-2, and CD4, all strengthened with GFRP). The 0.004 limit is not exceeded by the design effective strain of any specimen strengthened with CFRP.

The approach for quantifying the effective strain associated with debonding from the concrete substrate was developed by Khalifa et al. (1998) using experimental data from direct tension tests of concrete-bonded FRP conducted by Maeda et al. (1997). Because the approach was developed using data for FRP in pure tension, it may be over idealized for FRP used in shear strengthening applications due to the network of diagonal cracks forming stress concentrations and multiple debonding fronts. Additionally, the bond characteristics of an orthogonal grid of FRP may have implications on the effective strain, as the top layer is either completely bonded to the bottom layer (in the case of full coverage layers) or bonded to both concrete and the bottom layer in varying locations.

6.2. Effect of Ply Orientation

Dhakal et al. (2022) indicated that FRP oriented perpendicular to the direction of applied shear is typically ignored in design scenarios, as steel oriented in this direction is also not considered to contribute to shear strength. A similar design recommendation was proposed in Hutton et al. (2023), despite the observation that Specimen CD6 (with FRP oriented perpendicular to applied shear) achieved approximately 75% of the shear strength of Specimen CD3 (similar ply stiffness oriented parallel to applied shear). Similar evidence was observed in more recent specimens with Specimen CD9 achieving a strength that is 180% of the design strength calculated neglecting the sheets that are not parallel to the applied shear.

A comparison between Specimen CD7, CD8, and CD9, shown in Figure 6-4, suggests that applying an orthogonal grid of FRP may result in an increased shear strength contribution relative to applying an identical quantity of FRP entirely parallel to applied shear. Comparison between the peak experimental strengths of these specimens is difficult due to variations in the layout of the distributed mesh of steel reinforcement in the diaphragm field between the specimens. However, a comparison of $V_{f,exp}$ is possible due to the removal of approximate frame, concrete, and steel contributions.

Despite identical quantities of the same FRP material in the shear span, Specimen CD7 and CD8 (with FRP parallel to applied shear) achieved an experimental FRP contribution of 112 kips, relative to 181 kips in Specimen CD9 (with an orthogonal grid of FRP). Considering the bond-based approach presented in Khalifa et al. (1998) and adopted by ACI PRC-440.2R-23 (2023), the relative 60% increase is likely due to the reduced stiffness of the individual orthogonal layers in Specimen CD9. When two layers are oriented in the same direction, their combined stiffness reduces the active bond length, reducing the effective stress in the FRP. Conversely, when two layers of unidirectional FRP are oriented orthogonally, they are idealized to deform independently of each other. Therefore, the stiffness can be considered per layer, allowing each layer to achieve a greater active bond length and effective stress.

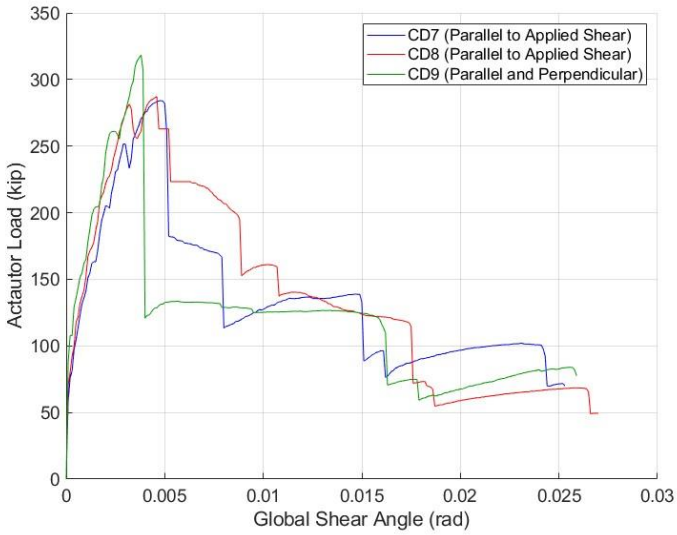

Figure 6-4. Global Shear Angle Envelope Comparison between Specimen CD7, CD8, and CD9.

Specimen CD10 was strengthened with an orthogonal grid of FRP at approximately +/- 45° relative to the direction of applied shear, and experienced FRP rupture along three separate sheets at peak load. Each layer provided 50% surface coverage, as the clear spacing of the FRP sheets was identical to their width. This resulted in varied bond characteristics along the length of each FRP sheet, where in some locations the FRP was bonded to the concrete, and in some locations bonded to both the concrete and the other layer of FRP. It is likely that the stress concentrations related to these varied bond characteristics lead to rupture of the FRP sheets.

The following methodology has been developed to account for the contribution of FRP oriented in any direction. The shear strength contribution of FRP, V_f, is defined as the sum of the contributions of the independent orthogonal layers, shown in Eq. (28):

$$V_f = \sum V_{f,i} = \left[\sum \frac{A_{fv} f_{fe} k_{\alpha,i}}{s_f}\right] d \tag{28}$$

where: V_f is the total FRP contribution to shear strength (lbs); $V_{f,i}$ is the contribution of layer i of FRP to shear strength (lbs); A_{fv} is the cross-sectional area of FRP, defined as the product of width, thickness, and the number of stacked sheets per layer (in.^{2}); f_{fe} is the effective stress

of the FRP (psi); $k_{\alpha,i}$ is the directionality factor for layer i; s_f is the center-to-center spacing of FRP sheets (in.); and d is the effective depth of the diaphragm (in.).

To reflect the 19 specimens in the database, Eq. (28) is only recommended when A_{fv}, f_{fe}, and s_f are constant between orthogonal layers. Additionally, the breadth of experimental data also introduces the limitation that the two layers must be orthogonal to each other, consist of the same FRP material and configuration, and orthogonal layers cannot consist of multiple stacked FRP plies. If these limitations are met, the only parameter that varies between layers is the directionality factor $k_{\alpha,i}$.

The directionality factor is introduced in Eq. (28) in lieu of the $\sin(\alpha) + \cos(\alpha)$ term used in Chapter 11 of ACI PRC-440.2R-23 (2023). The $\sin(\alpha) + \cos(\alpha)$ term reduces to 1.0 for sheets both perpendicular and parallel to applied shear, reaches a maximum at $\sqrt{2}$ for sheets oriented perpendicular to the anticipated direction of diagonal shear cracks, and reduces to zero for sheets oriented parallel to the anticipated direction of diagonal shear cracks. The $\sin(\alpha) + \cos(\alpha)$ term was deemed sufficient for three of these four orientations. For sheets oriented perpendicular to applied shear, reducing the term to 1.0 resulted in unconservative strength predictions for Specimen CD6 and CD9. Hutton et al. (2023) indicated that 0.75 may be sufficient, but 0.5 is taken here to reflect the limited experimental data with which the directionality factor was calibrated. If referencing the orientation α_i to the longitudinal axis of the member, the calculation procedure for the directionality factor $k_{\alpha,i}$ is visualized in Figure 6-5:

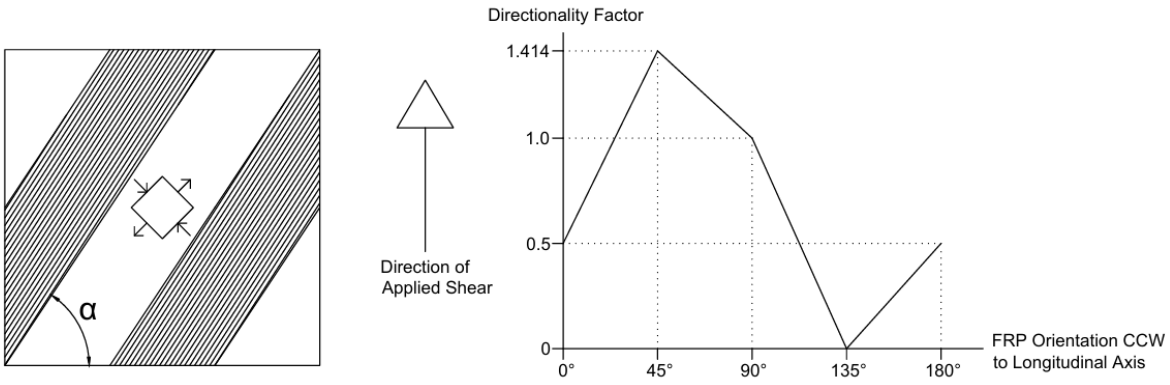

Figure 6-5. Calculation Procedure for Directionality Factor, k_α.

Because experimental data is unavailable for orientations other than 0°, 45°, 90°, and 135°, it is recommended to use linear interpolation (as shown in Figure 6-5) between these points for other orientations. The effective depth of the diaphragm, d, is isolated in Eq. (28) to facilitate a comparison of demand and capacity in terms of unit shear per length, where the unit shear capacity is the term inside brackets in Eq. (28).

To demonstrate the design methodology, the design FRP contribution to shear strength is presented in Table 6-1 for specimens in the database that contain FRP sheets oriented in any direction other than parallel to applied shear. The effective stress is calculated using Eq. (23) through (26), and the term $(A_{fv}f_{fe})/s_f$ is included as this parameter is constant between orthogonal sheets with identical FRP configurations. These results are compared to the experimental strength in Section 6.7 to show the efficacy of the proposed approach.

Table 6-1. FRP Shear Strength Contributions with Recommended Design Methodology.

Specimen ID	$\frac{A_{fv}f_{fe}}{s_f}$ (k/in.)	α_1 (deg.)	$k_{\alpha,1}$	α_2 (deg.)	$k_{\alpha,2}$	d (in.)	V_f (kip) Eq. (28)
CD6 (H)	0.603	0	0.500	N/A	N/A	96	28.9
CD9	1.167	90	1.000	0	0.500	96	168.1
CD10	0.460	47	1.396	133	0.044	96	63.6
CD12	1.797	90	1.000	0	0.500	96	258.7

(H) - Hutton et al. (2023)

6.3. Effect of Surface Coverage

Surface coverage is quantified as the percentage of surface area in the shear span that is covered in externally bonded FRP. For the CD specimens, the shear span is defined as the portion of the specimens between the interior edge of the loading channel and the edge of the shear wall. For Aryan specimens, the shear span is similarly defined as the portion of the specimens between the edge of the steel loading plate and the edge of the concrete in the support. The surface area in the shear span is 4800 in.^{2} and 10080 in.^{2} for Aryan specimens and CD specimens, respectively.

Aryan et al. (2022) noted that surface coverage has an inverse relationship with ductility, a trend that is generally observed in the dataset, as shown in Figure 6-6. As visualized in the envelope curves in Figure 5-1, specimens with greater surface coverage typically

experience more abrupt post-peak strength decay, leading to reduced ductility. This reduced ductility is not seen in Specimen CD13 and CD14, as their ductility was primarily attributed to their anchorage.

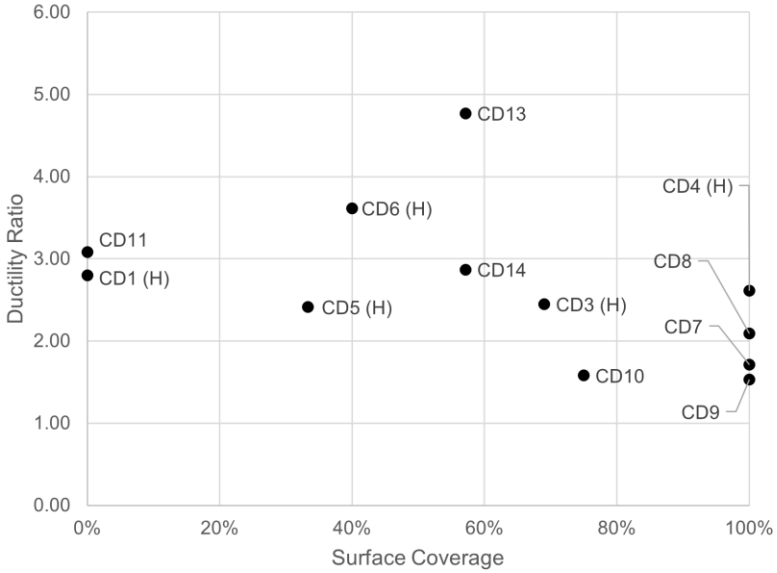

Figure 6-6. Ductility Ratio vs. Surface Coverage for CD Specimens.

In Khalifa et al. (1998), the effective strain of bonded FRP was defined as a function of ply stiffness, ply configuration, and concrete strength. Specimens with high surface coverage often have larger total ply stiffnesses then specimens with low surface coverage simply due to the higher quantity of FRP in the shear span. The total ply stiffness in the shear span was compared to the shear strength contribution of FRP, as shown in Figure 6-7. The experimental shear strength contribution of FRP has a direct relationship with the total stiffness of FRP in the shear span. However, for total ply stiffness values exceeding 60000 kips/in./in., the shear strength contribution plateaus. This highlights a key limitation of strengthening with high surface coverage: the underlying strength of the concrete diaphragm may become the controlling factor. Crushing of the diagonal compression strut is addressed by the current ACI 318 (2019) $8A_{cv}\sqrt{f_c'}$ limit on nominal shear strength, but other failure modes such as direct shear failure can also govern, especially in specimens with total ply stiffness values exceeding 60000 kips/in./in.

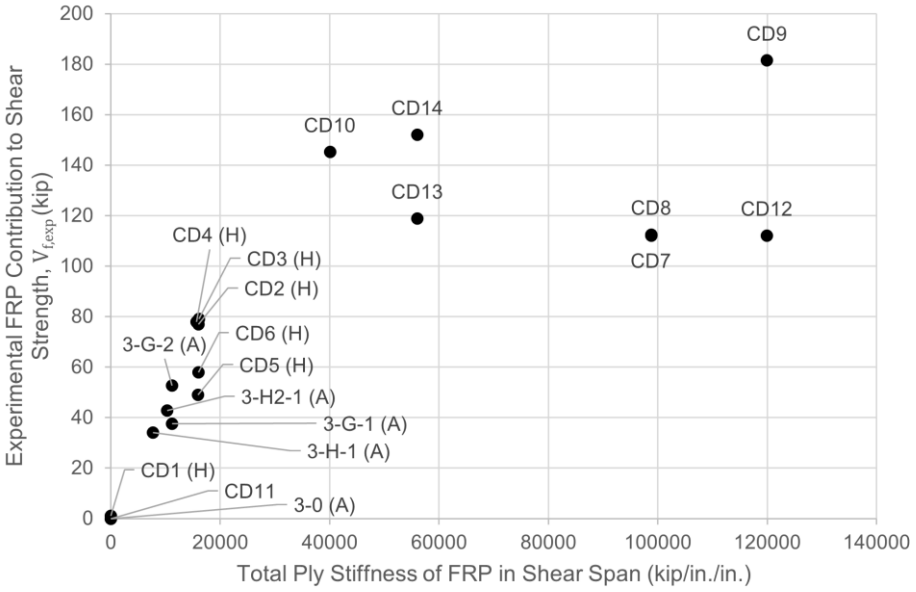

Figure 6-7. $V_{f,exp}$ vs. Total Ply Stiffness of FRP in Shear Span.

In addition to directly contributing to shear strength, FRP also plays a crucial role in limiting crack widths in concrete. Excessive cracking in concrete diaphragms is associated with inelastic strains in steel reinforcement, reduced aggregate interlock, and propagation of FRP debonding (Hutton et al. 2023). Clear spacing of the FRP sheets has a direct relationship with surface coverage. Hutton et al. (2023) recommended that this clear spacing be limited to three times the diaphragm thickness, as Specimen CD5 (with a normalized clear spacing of 4.7) exhibited a lower experimental FRP shear strength contribution, $V_{f,exp}$, relative to specimens with normalized clear spacings below three strengthened in the same direction with similar axial ply stiffnesses. However, although these specimens have similar ply stiffnesses, the reduced FRP contribution in CD5 is captured in the design methodology, as the difference in the term $A_{fv}f_{fe}/s_f$ for these specimens is proportional to their experimental FRP contributions to shear capacity. Therefore, the difference in $V_{f,exp}$ should not be attributed solely to clear spacing. This limit was revisited using the 16 strengthened specimens in the database by investigating the effect of clear spacing on achieving design strains.

Figure 6-8 presents the ratio of estimated to design FRP strain, $\varepsilon_{f,exp}/\varepsilon_{fe}$, against the clear spacing normalized to the diaphragm thickness. Contrary to the proposed limit, specimens featuring clear spacing up to 5.25 times the diaphragm thickness were still able to exceed their design strains. Conversely, three specimens featuring no clear spacing were unable to

achieve their design strains. Similar to high surface coverage and total ply stiffness, a low clear spacing is associated with relatively high FRP contributions to shear strength. In highly strengthened specimens, the underlying concrete diaphragm can become the limiting factor, as anchorage failures, direct shear, and crushing of the compression strut can occur prior to or with global debonding of the FRP, limiting the ability to achieve design strains.

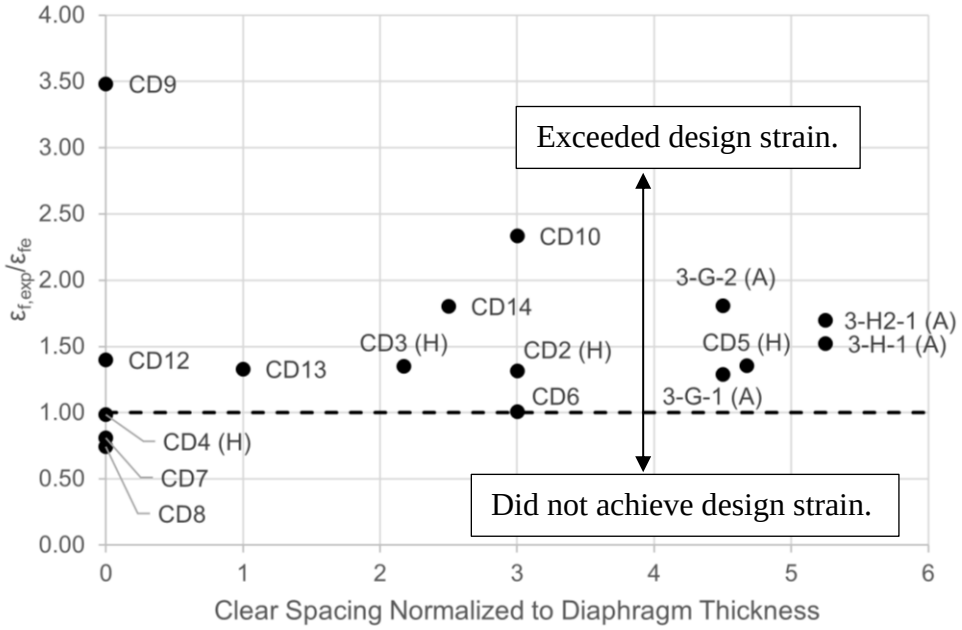

Figure 6-8. $\varepsilon_{f,exp}/\varepsilon_{fe}$ vs. Clear Spacing Normalized to Diaphragm Thickness.

6.4. Reinforcement Limits

Experimental shear strengths were normalized to $A_{cv}\sqrt{f_{cm}}$ to investigate the nominal shear strength limit of $8A_{cv}\sqrt{f_c'}$ presented in ACI 318 (2019). Although other limits in Chapter 11 and Chapter 13 of ACI PRC-440.2R-23 (2023) can be adopted for reinforced concrete diaphragm shear strengthening, the limit in ACI 318 (2019) controls, so only this limit is analyzed in this section.

The normalized strengths and relevant inputs are shown in Table 6-2. The procedure for normalizing shear strength involves removing the frame contribution from the specimens where it is relevant to achieve the experimental strength, $V_{n,exp}$. The experimental strength is

then divided by $A_{cv}\sqrt{f_{cm}}$, where f_{cm} is the concrete compressive strength at the time of testing reported in Table 3-3, and A_{cv} is the gross concrete area defined in Section 5.2.

Table 6-2. Experimental and Design Shear Strength Normalized to $A_{cv}\sqrt{f_{cm}}$.

Specimen ID	Experimental Shear Strength, $V_{n,exp}$ (kip)	Design Shear Strength, $V_{n,des}$ (kip)	Concrete strength, f_{cm} (psi)	Normalized Experimental Strength, $\frac{V_{n,exp}}{(A_{cv}\sqrt{f_{cm}})}$	Normalized Design Strength, $\frac{V_{n,des}}{(A_{cv}\sqrt{f_{cm}})}$	Failure Mode(s) at Peak Load[3]
3-0 (A)	66[1]	63[1]	5280	3.8	3.6	CDS
3-H-1 (A)	83[1]	71[1]	5280	4.8	4.1	FD
3-H2-1 (A)	88[1]	72[1]	5280	5.0	4.1	FD
3-G-1 (A)	85[1]	70[1]	5280	4.9	4.0	FD
3-G-2 (A)	93[1]	78[1]	5280	5.3	4.5	LPC
CD1 (H)	173	122	4760	6.5	4.6	CDS
CD2 (H)	248	165	4570	9.6	6.4	FD/AR
CD3 (H)	241	160	3670	10.4	6.9	FD/FR/AP
CD4 (H)	240	170	3670	10.3	7.3	FD/AP/AR
CD5 (H)	215	145	3950	8.9	6.0	FD/AP
CD6 (H)	228	140	4470	8.9	5.4	FD/AP
CD7	263	208	2650	13.2	10.5	FD/CDS/DS
CD8	263	221	3050	12.4	10.4	FD/CDS/DS
CD9	299	203	2980	14.3	9.7	FD/CDS
CD10	266	143	2980	12.5	5.9	FR
CD11	205	92	5620[2]	7.1	3.2	CDS
CD12	310	278	5690[2]	10.7	9.6	DS
CD13	238	152	2980	11.4	7.2	FD
CD14	273	149	3150	12.7	6.9	FD

[1]For the Aryan specimens, half of the experimental strength is used based off the assumption that half the applied shear is transferred to each side of the loading point.
[2]Specimen constructed with LWC.
[3]FD = FRP Debonding; FR = FRP Rupture; CDS = Concrete Diagonal Shear; AR = Anchor Rupture; AP = Anchor Pullout; DS = Direct Shear; LPC = Concrete Crushing at Load Point. (A) - Aryan et al. (2022); (H) - Hutton et al. (2023)

The average normalized design and experimental strength is 6.3 and 9.1, respectively, both with a COV of 37%. The $8A_{cv}\sqrt{f_c'}$ limit is exceeded in design by four specimens: Specimen CD7, CD8, CD9, and CD12, with an average design normalized strength of 10.1. The experimental normalized strength of each of these specimens exceeded the $8A_{cv}\sqrt{f_c'}$ limit, reaching $12.6A_{cv}\sqrt{f_c'}$ on average. Specimen CD7, CD8, and CD9 experienced both FRP

debonding and crushing of the diagonal compression strut at peak load, while Specimen CD12 experienced a direct shear failure. Additionally, the reinforcement limit was exceeded during the experiment by seven specimens in which the reinforcement limit was not exceeded in design.

The $8A_{cv}\sqrt{f_c'}$ limit is intended to guard against crushing of the diagonal concrete compression strut. This limit was developed for diaphragms reinforced with steel only, so its applicability to diaphragms strengthened with FRP is analyzed as a function of the design FRP contribution to shear strength, V_f, relative to the nominal shear strength, V_n. The relative contribution of FRP to nominal shear strength is calculated by dividing V_f by V_n using values from Table 6-3. The normalized strengths plotted against the portion of nominal shear strength attributed to FRP is shown in Figure 6-9, with markers indicating failure mode.

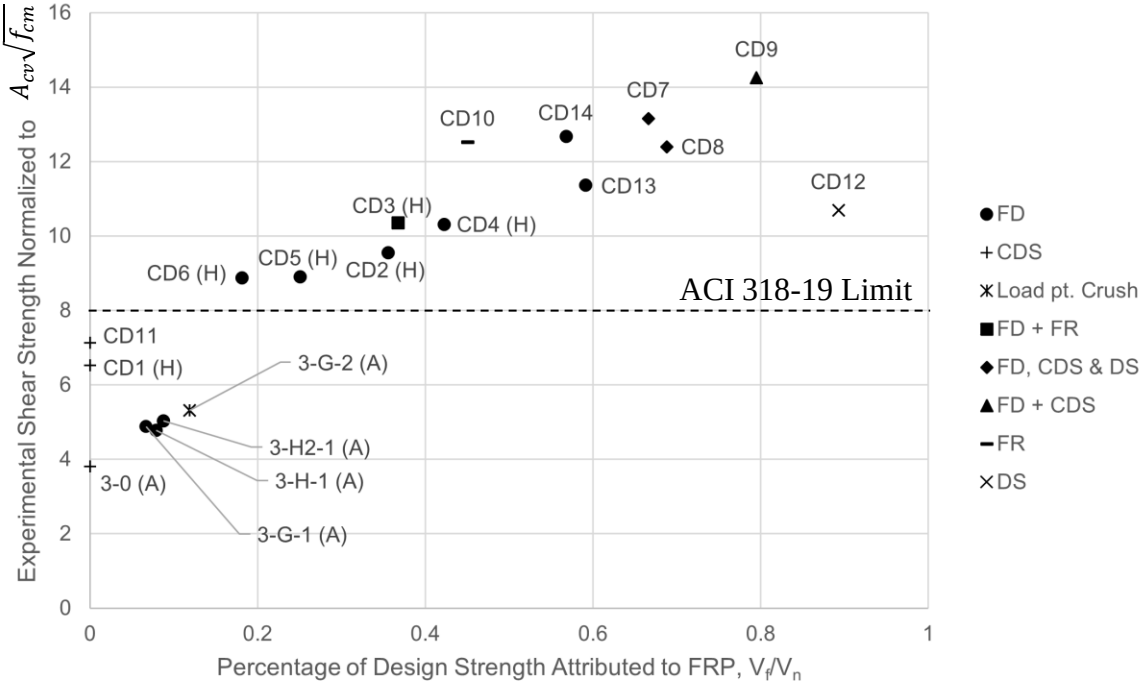

Figure 6-9. Normalized Strengths Against Percentage of Design Strength Attributed to FRP. DS Indicates Direct Shear Failure, CDS Indicates Concrete Diagonal Shear, FD Indicates FRP Debonding, and FR Indicates FRP Rupture.

The $8A_{cv}\sqrt{f_c'}$ limit is exceeded by all specimens in which FRP contributes at least 15% of the design shear strength. Additionally, all specimens in which FRP contributes at least 50% of the design shear strength exceed $10A_{cv}\sqrt{f_c'}$. A higher relative FRP contribution is associated

with increased surface coverage and reduced clear spacing. These parameters are effective in restraining crack widths, thus maintaining aggregate interlock in the concrete and allowing the compression strut to continue to contribute to shear strength at shear stresses above $8A_{cv}\sqrt{f_c'}$. Additionally, FRP may reduce principal strains in the concrete and mitigate compression softening behavior. In lieu of more extensive experimental data, particularly for specimens with higher steel reinforcement ratios and those designed to exceed this threshold, the $8A_{cv}\sqrt{f_c'}$ limit is recommended to guard against crushing of the compressive strut.

6.5. Effect of Anchorage Type and Scheme

Dhakal et al. (2022) indicated that designers often provide mechanical anchorage to promote favorable bond conditions between FRP and concrete. Aryan et al. (2022) wrapped FRP around the ends of the diaphragm specimens in lieu of an anchorage system and recommended future research to investigate FRP anchorage systems for diaphragm strengthening. Hutton et al. (2023) partially addressed this research gap through the use of varying configurations of end and intermediate fiber splay anchors in their strengthened specimens. Hutton et al. (2023) concluded that, while end anchorage can prevent end peeling prior to crack induced debonding, intermediate anchorage can propagate damage due to their influence on the stress distribution in the diaphragm field. Subsequently, Hutton et al. (2023) recommended to design intermediate anchorage to 50% of the area required to develop the full tensile strength of the FRP, while end anchors should be designed to 150%. Additionally, Hutton et al. (2023) concluded that neither end or intermediate anchorage has an effect on diaphragm in-plane shear capacity.

Experimental results for Specimen CD7 and CD8 also suggest that end anchorage does not have an effect on shear capacity. The specimens have identical reinforcement layouts, ply configurations, and similar concrete strengths. They are most dissimilar in their anchorage, where Specimen CD7 contains two rows of end anchors on the ends of each FRP sheet, while Specimen CD8 contains no anchorage. Despite the variance in anchorage, Specimen CD7 and CD8 have identical $V_{f,exp}$ components, at 112 kips. Furthermore, strain gages installed on the FRP indicate the same average FRP strain at peak load for both specimens, 0.0019.

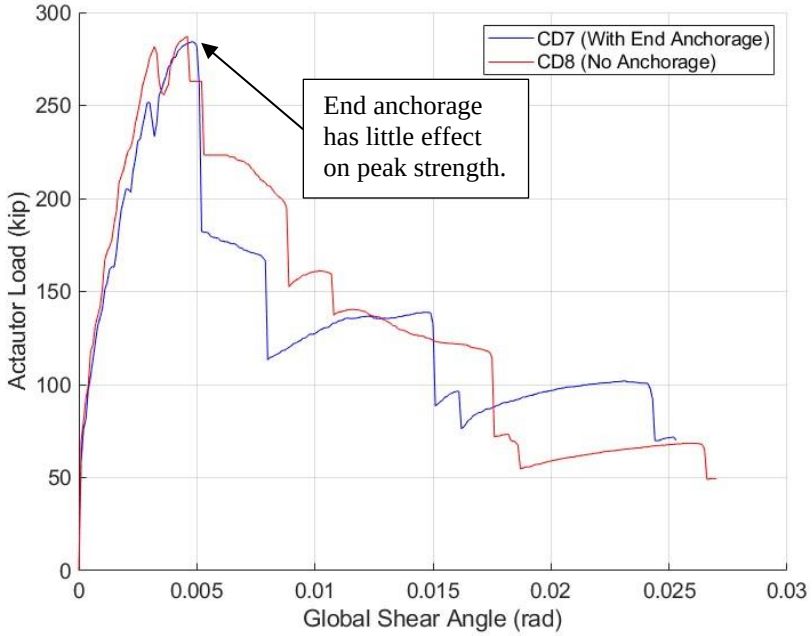

Figure 6-10. Comparison of Global Shear Angle Envelopes for Specimen CD7 and CD8.

The effectiveness of anchorage is also influenced by the strength of the underlying concrete. Anchorage can pullout from the underlying concrete or cause failure of concrete elements due to the large tensile force transferred to the concrete, such as the flange failures seen in Specimen CD7 and CD8. This effect can be more prominent in diaphragms constructed with low-strength concrete; a common material seen in existing buildings constructed before 1970. Therefore, in retrofit design, consideration should be given to the concrete diaphragms ability to resist anchorage forces in addition to the effect of the anchorage forces on the stress distribution in the diaphragm.

Hutton et al. (2023) recommended designing end anchorage to 1.5 times the tensile capacity of the anchored FRP sheet, and designing intermediate anchorage to 0.5 times the tensile capacity. The recommendation for designing intermediate anchorage for a lesser demand addresses the potential for stress concentrations to develop in the FRP leading to potential FRP rupture, such as that seen in Specimen CD3. To distribute intermediate anchorage forces into the diaphragm field, it is recommended to orient intermediate anchorage in an alternating configuration, as shown in Figure 6-11. An alternating intermediate anchorage scheme is preferable to a linear intermediate anchorage scheme to limit the effect of anchorage forces on the shear stress distribution in the diaphragm field. Additionally, mechanical

anchorage should be provided at the ends of the FRP sheets or at the effective depth of the FRP, d_{fv}, whichever is less (Hutton et al. 2023).

When providing mechanical anchorage to an orthogonal grid of FRP sheets, it is recommended to use a perimeter of end anchorage, each designed to 1.5 times the tensile capacity of the anchored sheet, between the orthogonal layers. An example of this anchorage scheme is shown in Figure 6-11. Placing anchorage between the layers allows each layer to engage the anchorage directly.

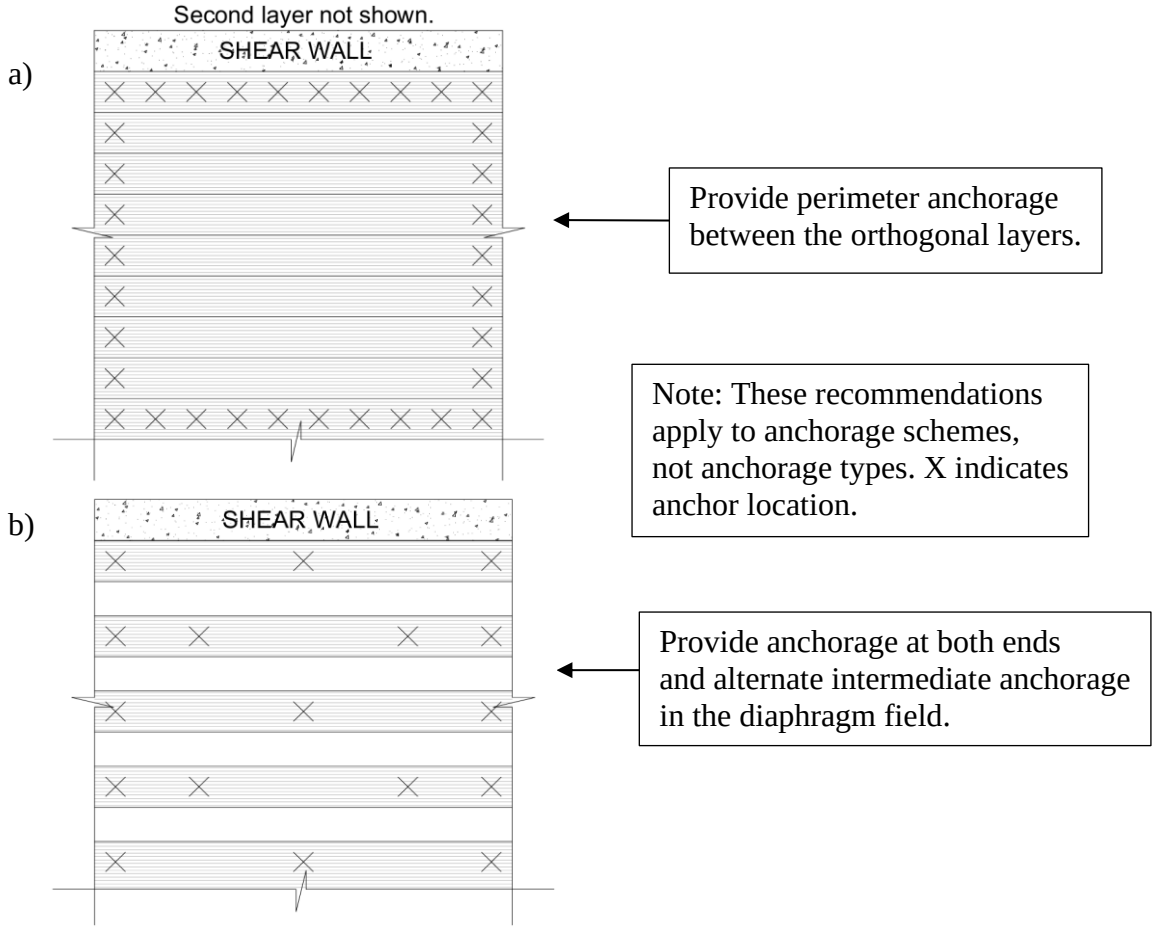

Figure 6-11. Recommended Anchorage Schemes for a Bay of the Diaphragm Near a Shear Wall: a) Strengthening with an Orthogonal Grid; b) All Sheets Oriented in the Same Direction.

6.6. Effect of Concrete Density

Specimen CD11 and CD12 were constructed with LWC, while all other specimens in the database were constructed with NWC. However, high variance in concrete strength, reinforcement layout, or FRP strengthening scheme between LWC and NWC specimens yield unreliable comparisons between concrete weight and the efficacy of diaphragm shear strengthening with FRP. In lieu of more comparable NWC and LWC specimens, the λ reduction factor for LWC is recommended for use in concrete diaphragms strengthened with externally bonded FRP. The λ reduction factor addresses reduced aggregate interlock and tensile strength in LWC. Reduced aggregate interlock can influence the ability of the concrete to transfer shear stress along a crack. This effect is witnessed in both Specimen CD11 and CD12, where flexural and shear cracks were observed to develop through the expanded shale aggregate as shown in Figure 6-12, as opposed to around the aggregate in NWC specimens. Further research is recommended on the interaction between the FRP and concrete shear strength contributions for varying concrete weights.

Figure 6-12. Cracks Forming Through Aggregate in LWC.

Furthermore, the LWC used in Specimen CD11 and CD12 was specified to have a 3000-psi nominal compressive strength at 28 days. However, cylinder tests revealed the compressive strength at 28 days to exceed 5000 psi, likely due to the expanded shale aggregate absorbing water and reducing the water-cement ratio of the concrete. Therefore, when using expanded aggregate, it is recommended to soak the aggregate prior to mixing to ensure similar water-cement ratios than those determined in design.

6.7. Validation of Nominal Shear Strength Design Recommendations

The nominal shear strength, V_n, of an FRP-strengthened reinforced concrete diaphragm can be calculated using Eq. (29). The gross concrete section, A_{cv}, should be calculated as the product of diaphragm thickness and diaphragm depth, where the diaphragm depth is the center-to-center distance between bounding perimeter beams in the direction of analysis. A modification to the ACI PRC-440.2R-23 (2023) methodology for the FRP contribution to shear strength is presented previously in this chapter and is reflected in Eq. (29). In lieu of a reliability analysis on the FRP strength reduction factor ψ_f, the existing design recommendation presented in Hutton et al. (2023) is recommended, where $\psi_f = 0.75$ for one-sided diaphragm strengthening. This value was obtained through an extrapolation of existing values in ACI PRC-440.2R-23 (2023) for two-sided, three-sided, and completely wrapped reinforced concrete beams (Hutton et al. 2023).

Following the conventional ACI 318 (2019) approach, the contribution of longitudinal reinforcement to shear strength is not considered in Eq. (29). In the truss model, longitudinal reinforcement is assumed to resist flexure only, and their role in shear is indirectly included through strain compatibility. While more rigorous analytical models, such as the MCFT, consider the shear resistance provided by longitudinal steel through dowel action and its influence on the inclination of the compression strut, these effects are complex and difficult to capture in closed-form equations. MCFT calculations conducted for the control specimens in Section 5.2 indicated minor variance between peak strengths with and without longitudinal reinforcement, where including longitudinal reinforcement was found to increase shear strength by an average of 2%.

$$V_n = V_c + V_s + \psi_f V_f = \left[b_w \left(2\lambda \sqrt{f_c'} + \rho_t f_y \right) + \psi_f \sum \frac{A_{fv} f_{fe} k_{\alpha,i}}{s_f} \right] d \qquad (29)$$

The effective depth of the diaphragm, d, is isolated in Eq. (29) to facilitate a comparison of demand and capacity in terms of unit shear per length, where the unit shear capacity is the term inside brackets in Eq. (29). The effective depth of the diaphragm varies based on the model used to analyze the diaphragm. In the beam model, d is typically defined as the distance from the extreme compression fiber to the centroid of the tension chord. In the SPM, d could

be defined as the panel edge dimension in the direction of analysis. There may be other ways to define d for other modeling techniques. Regardless of the model used in analysis, the effective depth, d, times the diaphragm thickness should be equivalent to the gross concrete area, A_{cv}.

Validation of the proposed design recommendations for nominal shear strength is shown in Table 6-3 and visualized with experimental failure modes in Figure 6-13. The superposition and lack of interaction between steel, concrete, and FRP contributions to shear strength is conservative for the 19 specimens in this database. The experimental strength, $V_{n,exp}$, is on average 43% higher than the design strength with a COV of 21%. The design strengths are identical to those calculated per ACI 318 (2019) Clause 12.5.3.3 for control specimens, as no modifications to the steel or concrete contribution to shear strength are recommended. The design strengths are identical to those calculated per ACI PRC-440.2R-23 (2023) Section 11.4 for specimens strengthened only parallel to applied shear. The proposed methodology reduces the contribution of FRP to nominal shear strength relative to the ACI PRC-440.2R-23 (2023) Section 11.4 procedure for specimens strengthened in any direction other than parallel to applied shear to maintain conservatism.

Using the proposed methodology, the experimental strength is on average 51% greater than the design strength for specimens strengthened with an orthogonal grid (Specimen CD9, CD10, and CD12), with a COV of 32%. Using the proposed methodology, the experimental strength of Specimen CD6 (the only specimen strengthened only perpendicular to applied shear) is 60% greater than the design strength. The level of conservatism is more consistent across varying FRP orientations, as the experimental strength is on average 43% greater than design, with a COV of 21%, across all specimens included in the database.

Table 6-3. Design Shear Strengths using Proposed V_f Methodology.

Specimen ID	V_c (kip)	V_s (kip)	V_f (kip)	V_n (kip)	$V_{n,exp} = V_{u,exp} - V_{frame}$ (kip)	$\frac{V_{n,exp}}{V_n}$
3-0 (A)	34.9	27.7	0.0	125.1	133	1.06
3-H-1 (A)	34.9	27.7	11.2	142.0	167	1.17
3-H2-1 (A)	34.9	27.7	12.6	144.1	176	1.22
3-G-1 (A)	34.9	27.7	9.3	139.1	170	1.23
3-G-2[1] (A)	34.9	27.7	18.6	156.7	186	1.18
CD1 (H)	53.0	69.4	0.0	122.3	173	1.41
CD2 (H)	51.9	69.4	58.8	165.3	248	1.50
CD3 (H)	46.5	69.4	58.7	159.9	241	1.51
CD4 (H)	46.5	69.4	71.6	169.6	240	1.42
CD5 (H)	48.3	69.4	36.3	144.9	215	1.48
CD6 (H)	51.3	69.4	28.9	142.4	228	1.60
CD7	39.5	64.7	138.6	208.2	260	1.25
CD8	42.4	64.7	152.3	221.3	263	1.19
CD9	41.9	40.0	168.1	207.9	299	1.44
CD10	41.9	40.0	63.6	129.6	262	2.03
CD11	50.5	48.4	0.0	98.8	205	2.08
CD12[2]	50.8	48.4	258.7	293.2	310	1.06
CD13	41.9	42.5	89.7	151.7	238	1.57
CD14	43.1	42.5	84.6	149.0	273	1.83

[1]Specimen 3-G-2 failed due to concrete crushing at load point.
[2]Specimen CD12 failed in direct shear at the shear wall.
(A) - Aryan et al. (2022); (H) - Hutton et al. (2023)

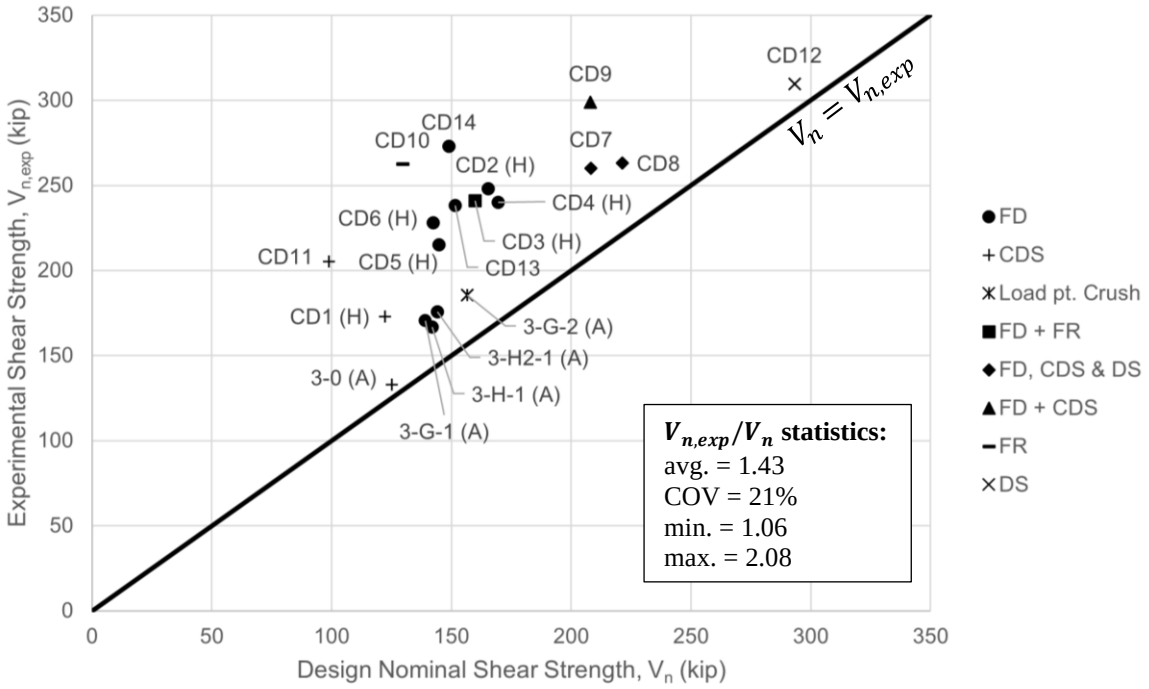

Figure 6-13. Comparison of $V_{n,exp}$ to V_n calculated per Eq. (29). DS Indicates Direct Shear Failure, CDS Indicates Concrete Diagonal Shear, FD Indicates FRP Debonding, and FR Indicates FRP Rupture.

Chapter 7. Methods for Determining Demands

Seismic design of reinforced concrete building diaphragms is one of the most complex challenges in a structural engineering design office (Godínez et al. 2024). Several analytical methods for both including diaphragms in a structural model and determining diaphragm demands exist. The selected analytical method can influence both the internal forces in the diaphragm and the interaction with the vLFRS (Godínez et al. 2024). Assuming the diaphragm is rigid in-plane relative to the vLFRS and subsequently lumping mass at a master node is a commonly used analytical method for reinforced concrete diaphragms due to its computational ease.

When conducting a rigid diaphragm analysis, internal forces in the diaphragm do not arise as the diaphragm is assumed to be perfectly rigid and all deformation is occurring in the vLFRS elements supporting the diaphragm. To establish internal diaphragm forces, the design engineer must analyze the diaphragm independently. This is most commonly done with an EBM, where the vLFRS reactions from the rigid diaphragm analysis are used to establish loading and the diaphragm is analyzed as a continuous simply-supported beam. Several issues have been identified with this analysis technique (Godínez et al. 2024). Diaphragms have different geometry, aspect ratios, and reinforcement layouts than beams, so applying the beam model is often met with concern from the design engineer.

The SPM is an analytical technique that has been applied in the modeling of reinforced concrete building diaphragms over recent years (Godínez et al. 2023). The linear model consists of stringers which permit pure axial deformation, and panels which permit pure shear deformation. Each panel is bounded by four stringers, which transfer a linearly varying force between the stringers and panels through compatibility. This chapter explores the application of the linear SPM in reinforced concrete diaphragm design through use of a design example. Side-by-side comparisons between design demands from the beam model and the SPM are compared, and key differences between the analytical techniques are identified.

7.1. Overview of CRSI Diaphragm Design Example

The Concrete Reinforcing Steel Institute's (CRSI) *Design Guide for Reinforced Concrete Diaphragms* provides design aids, worked-out examples, and other explanatory material for building diaphragms designed according to ACI 318. The design guide includes five worked-out examples, and Example 10.2 is selected here for use in a side-by-side comparison with the SPM. A plan view of the reinforced concrete diaphragm is shown in Figure 7-1. The diaphragm is located at the roof level of a seven-story office building and is classified as Seismic Design Category B. As this chapter focuses on the analytical methods used for determining diaphragm demands, other aspects of the design process are not reviewed. For detailed information, see the CRSI *Design Guide for Reinforced Concrete Diaphragms.*

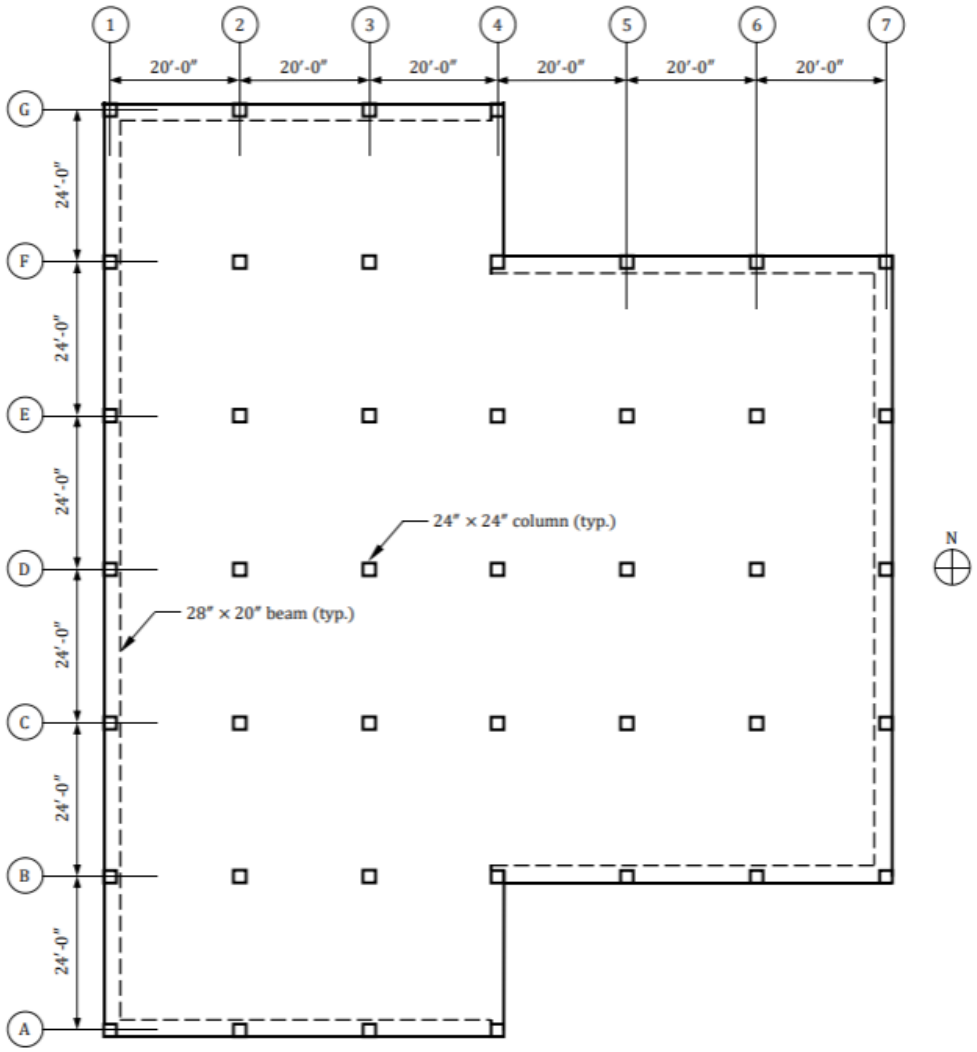

Figure 7-1. Plan View of CRSI Design Guide Example 10.2 Diaphragm [From (CRSI 2019)].

The materials used in the diaphragm design are 4000 psi NWC and Gr. 60 steel reinforcement. Considering minimum diaphragm thickness for serviceability, two-way shear, and fire-resistance requirements, a diaphragm thickness of 8 in. is selected. The equivalent static method is used to determine the design diaphragm seismic forces, and the design seismic force on the roof diaphragm is determined to be 127.5 kips (CRSI 2019).

Considering the conditions in ASCE/SEI 12.31.2, the diaphragm is determined to have sufficient span-to-depth ratios for classification as a rigid diaphragm, but does not satisfy the requirements related to reentrant corner irregularities. Therefore, a three-dimensional model is constructed and analyzed using structural analysis software. The model revealed that in-plane forces from the rigid diaphragm assumption are essentially identical to those in the model, justifying the use of the rigid diaphragm assumption in this design example. Subsequently, the corrected EBM with spring supports is selected for determining diaphragm demands (CRSI 2019).

The diaphragm is supported by perimeter moment frames, as indicated by dashed lines in Figure 7-1. The stiffness of the perimeter moment frames was determined using Eq. (30). The center of mass and center of rigidity were determined using typical techniques. An accidental torsional moment was applied to check for a torsional irregularity, which was determined not to exist in this diaphragm.

$$k_i = \frac{12E_c}{h_i^2\left(\frac{1}{\sum k_c + \sum k_b}\right)} \tag{30}$$

where: k_i is the moment frame stiffness along column line i considered in the diaphragm analysis (k/in.); E_c is the modulus of elasticity of the concrete (ksi); h_i is the story height beneath the diaphragm (in.); k_c is equivalent to the quotient of the gross moment of inertia of the column and h_i (in.^{3}); and k_b is equivalent to the quotient of the gross moment of inertia of the beam and the center-to-center beam length (in.^{3}).

For seismic force in the south direction, frame forces from the rigid diaphragm analysis are shown in Figure 7-2. “Term 1 Force” refers to force accumulated due to direct shear, while “Term 2 Force” refers to force accumulated due to torsional shear. The forces are summed to

determine reaction forces in the EBM. The reaction forces are used to solve for distributed loads, $w_{1,S}$ and $w_{2,S}$, acting on the equivalent beam, as shown in Figure 7-3. Typical beam theory is utilized to determine the internal shear and moment in the equivalent beam, as shown in Figure 7-3.

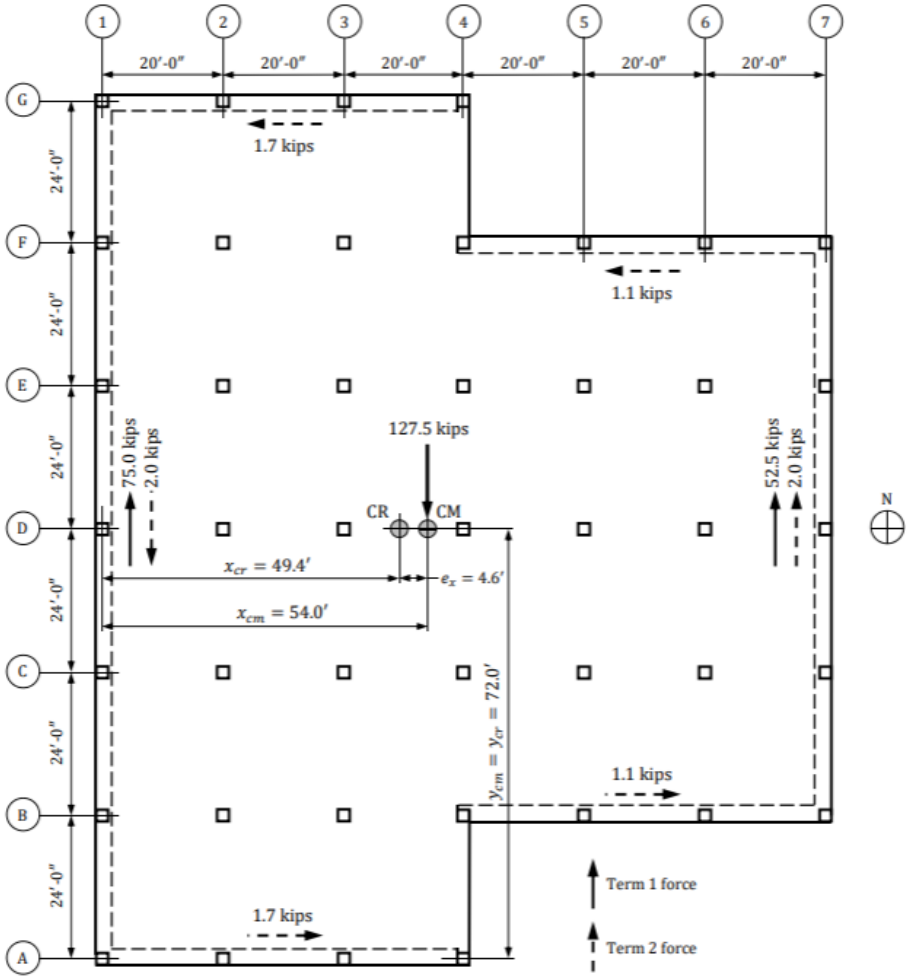

Figure 7-2. Force Allocation to the Frames from Rigid Diaphragm Analysis [From (CRSI 2019)].

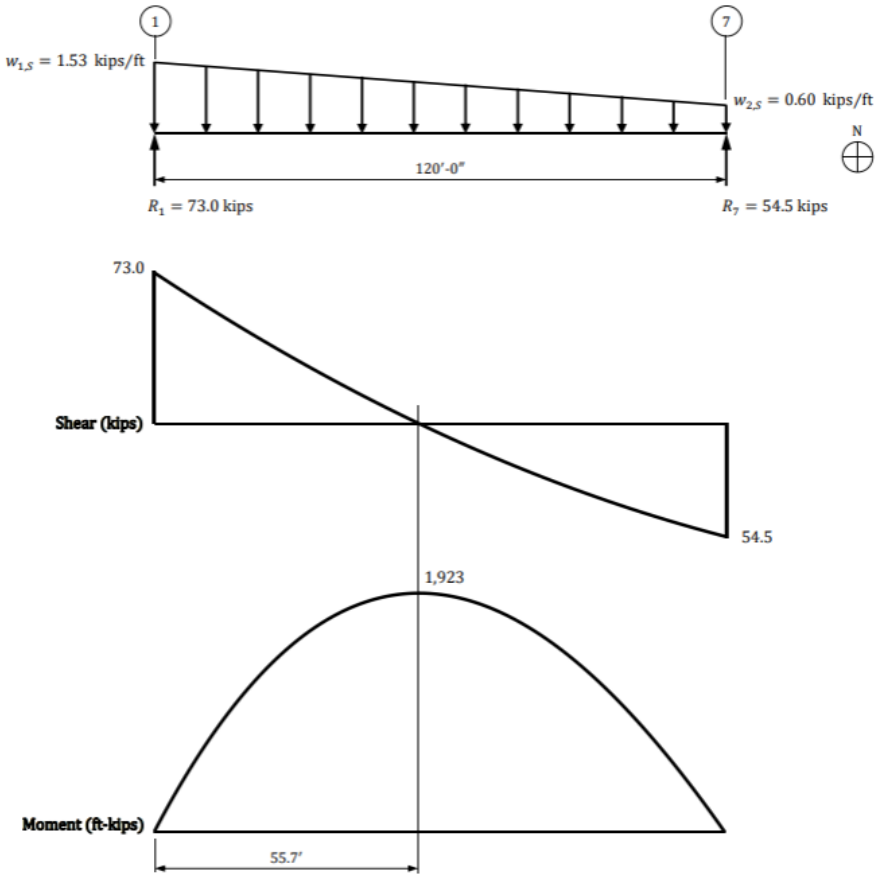

Figure 7-3. EBM and Internal Shear/Moment Diagrams [From (CRSI 2019)].

The shear and moment diagrams from the EBM are used to determine diaphragm demands. The unit shear demand is determined using Eq. (31), where critical sections are taken at locations of maximum shear and wherever there is a change in the diaphragm depth in the direction of analysis. The chord demand is determined using Eq. (32), where critical sections are taken at locations of maximum moment and wherever there is a change in the diaphragm depth in the direction of analysis. Although no collectors are identified for South-direction loads using the EBM, collector forces are determined using Eq. (33).

$$v_{u,i} = \frac{V_i}{d_i} \tag{31}$$

where: $v_{u,i}$ is the unit shear demand along column line i (k/ft); V_i is the internal shear along column line i from the EBM (kip); and d_i is the diaphragm depth in the direction of analysis along column line i (ft).

$$T_u = C_u = \frac{M_u}{d} \tag{32}$$

where: T_u is the tensile chord force demand at a critical section (kip); C_u is the compressive chord force demand at a critical section (kip); M_u is the internal moment at a critical section from the EBM (k-ft); and d is the moment arm, often assumed to be 95% of the diaphragm depth to account for the anticipated location of reinforcing steel within the exterior column lines (ft).

$$F_{u,i} = v_{n,i} \cdot L_{collector} \tag{33}$$

where: $F_{u,i}$ is the collector axial force demand along column line i (kip); $v_{n,i}$ is the net unit shear force along column line i (k/ft); and $L_{collector}$ is the length of the collector (ft).

Chord, collector, and diaphragm shear demands at vLFRS supports are shown for loads in the South and West directions in Figure 7-4. Diaphragm shear demands are reported by panel to facilitate more effective comparisons with the SPM. The panel demand is reported in psi and calculated as the maximum unit shear force along the panel divided by the diaphragm thickness. Chords are located along exterior column lines perpendicular to the direction of applied load, while collectors are located along parallel interior lines containing vLFRS elements. Tension and compression are considered positive and negative, respectively.

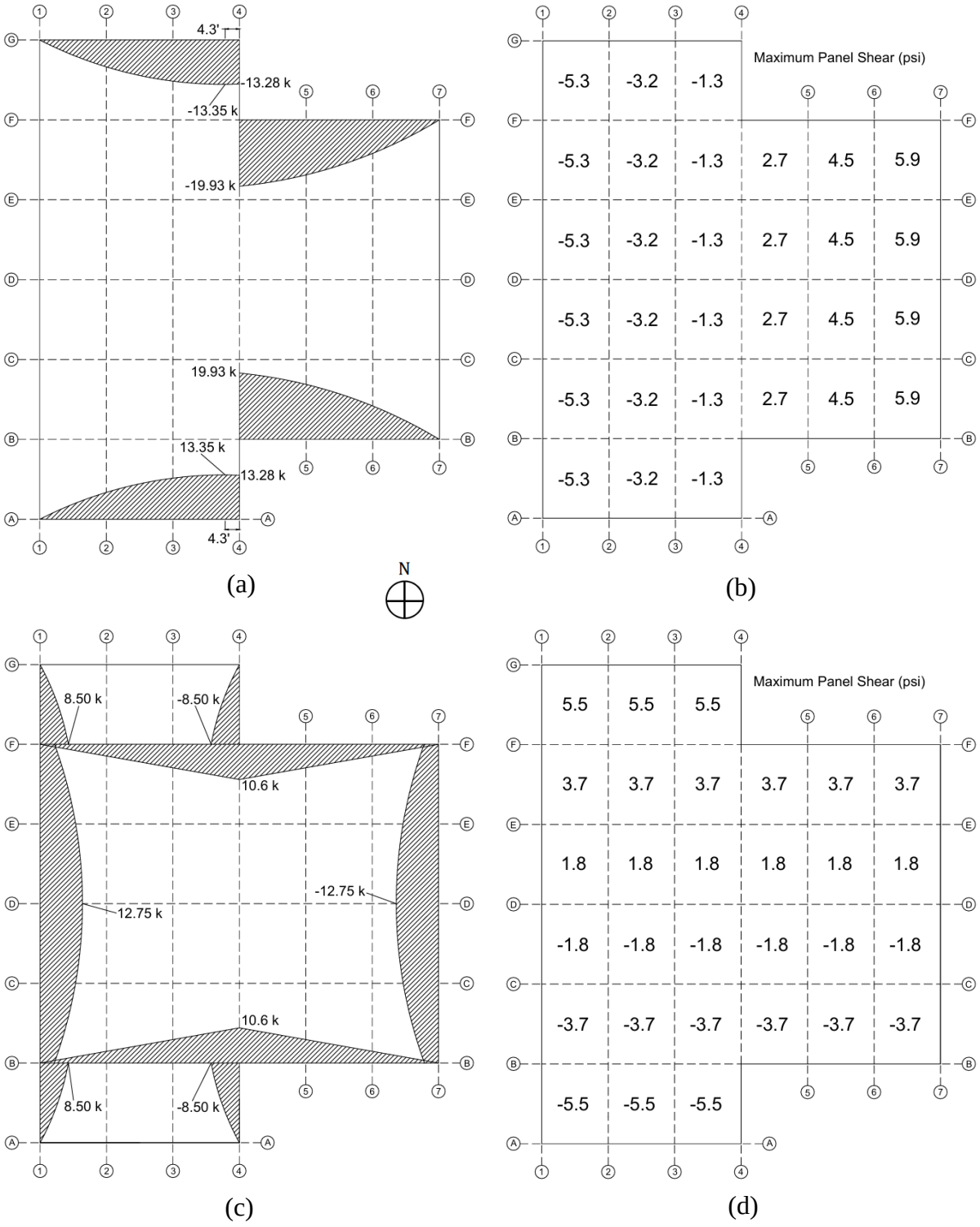

Figure 7-4. Demands from EBM: a) South Direction Axial Demands; b) South Direction Panel Demands; c) West Direction Axial Demands; d) West Direction Panel Demands.

7.2. Linear Stringer-Panel Model

The linear SPM is solved using the SPM analysis software Boring Square v4.1 (Jacques 2025). The input file is prepared and stringer-panel analysis is solved in Visual Studio Code using Python, and the model is visualized in FreeCAD. For a linear elastic analysis, the software uses force-controlled Newton-Raphson iteration, where the solution converges based off residual force. The SPM is discretized such that panels are associated with each 20 ft by 24 ft bay, as described in Section 7.2.1. Spring stiffnesses associated with the perimeter moment frames are distributed to the columns using tributary length, as described in Section 7.2.2. The 127.5-kip design seismic force is distributed using tributary area, as described in Section 7.2.3. SPM outputs for seismic load in the South and West directions are presented in Section 7.2.4.

7.2.1 Discretization

The SPM is discretized such that each panel is associated with each 20 ft by 24 ft bay shown in Figure 7-1. Stringers are simply included around the edges of every panel. All panels have identical dimensions: 24 ft in the North-South direction, 20 ft in the East-West direction, and an 8 in. thickness corresponding to the diaphragm thickness determined in the CRSI example. Stringers in the East-West direction are 24 ft long, while stringers in the North-South direction are 20 ft long. Stringers that are part of a perimeter moment frame have identical dimensions to the moment frame beams: 20 in. deep and 28 in. wide. Stringers that are not part of a perimeter moment frame are 24 in. wide (corresponding to the column widths) and 8 in. deep (corresponding to the diaphragm thickness).

The elastic modulus of the stringers is defined as $57000\sqrt{f_c'}$ per ACI 318 (2019) Clause 19.2.2.1.b. Considering the specified compressive strength of $f_c' = 4000\ psi$, the elastic modulus is determined to be 3605 ksi. Using the relation between shear modulus and elastic modulus, and considering a Poisson's ratio of 0.25, the shear modulus of the panels is determined to be 1442 ksi. Finally, the panel elastic modulus, although theoretically zero, was defined as 0.001 psi to assist the software in modeling deformed shapes.

In a linear SPM, stringers typically have three degrees of freedom (DOFs) and panels typically have four DOFs. While the amount of active DOFs in stringers and panels is three and four, respectively, the SPM was created with DOFs in the horizontal and vertical direction

at every vertex to assist the software in modeling deformed shapes. Subsequently, stringers have six degrees of freedom (three of which are active), and panels have eight degrees of freedom (four of which are active). The final SPM, shown in Figure 7-5, contains 115 vertices, 230 DOFs, 30 panels, and 72 stringers.

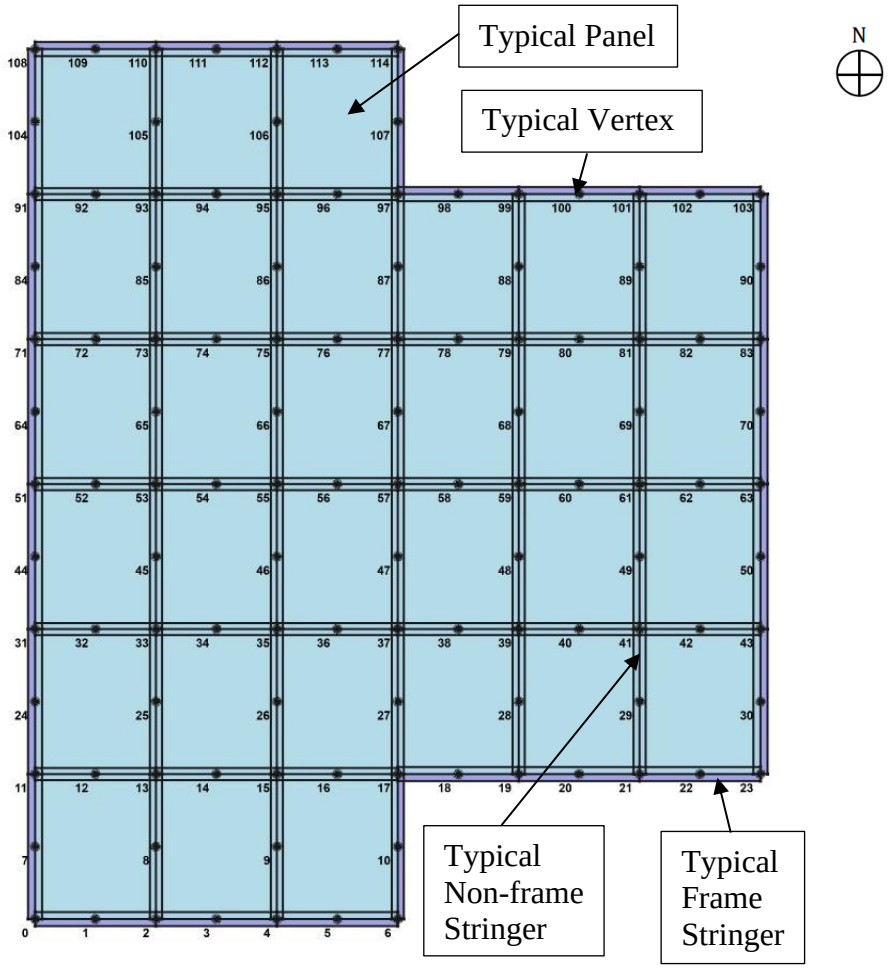

Figure 7-5. SPM for CRSI Design Guide Example 10.2.

7.2.2 Spring Stiffnesses

The perimeter moment frames indicated by dashed lines in Figure 7-1 have stiffnesses calculated using Eq. (30). For use in the SPM, it was necessary to distribute the moment frame stiffness along several DOFs. The moment frame stiffness was divided by the moment frame length to yield a unit stiffness per length. The stiffness was then distributed to the moment frame columns based on tributary length. Spring stiffnesses were only applied in the direction of analysis, as the moment frame is allowed to translate freely out of plane. Example spring

stiffness calculations for the moment frame along column line A (the southernmost column line) are shown in Table 7-1.

Table 7-1. Example Column Stiffness Calculation for Moment Frame Along Line A.

Moment Frame Column ID	Moment Frame Total Stiffness, Eq. (30), k_i (k/in.)	Moment Frame Unit Stiffness, k_i / L_{frame} (k/in./ft)	Column Tributary Length in Direction of Moment Frame (ft)	Column Stiffness (k/in.)
1A	2575.8	42.9	10	429.3
2A			20	858.6
3A			20	858.6
4A			10	429.3

7.2.3 Loading

As opposed to applying the seismic force as a linearly varying distributed load in the EBM, the seismic force is distributed to the stringers based on tributary area. The total seismic load, 127.5 kips, is divided by the total roof area, 14400 ft^2, to determine the unit seismic load per square foot. The tributary area of each stringer (half of the panel area on each side of the stringer) is then multiplied by the unit seismic load per square foot to determine the seismic force applied to each stringer. The seismic force is applied at the middle DOF on the stringer, which represents applying the seismic force as a constant linear force along the entire stringer length. Because the middle DOF on the stringer corresponds with the corresponding panel edge DOF, the seismic force is immediately distributed into both the stringer and the panels on both sides of the stringer. Seismic force calculations are conducted for loads in the North-South direction and for loads in the East-West direction, but loads are only applied in one cardinal direction per SPM analysis.

7.2.4 Output

Outputs for the linear SPM analysis conducted in Boring Square are shown in Figure 7-6 and Figure 7-7. Although SPM analyses are conducted for loads in all four cardinal directions, only outputs for applied seismic loads in the West and South directions are shown here because panel forces, stringer forces, and reaction forces are equal and opposite for East and North loads, respectively. Red denotes compression, and blue denotes tension.

(a)

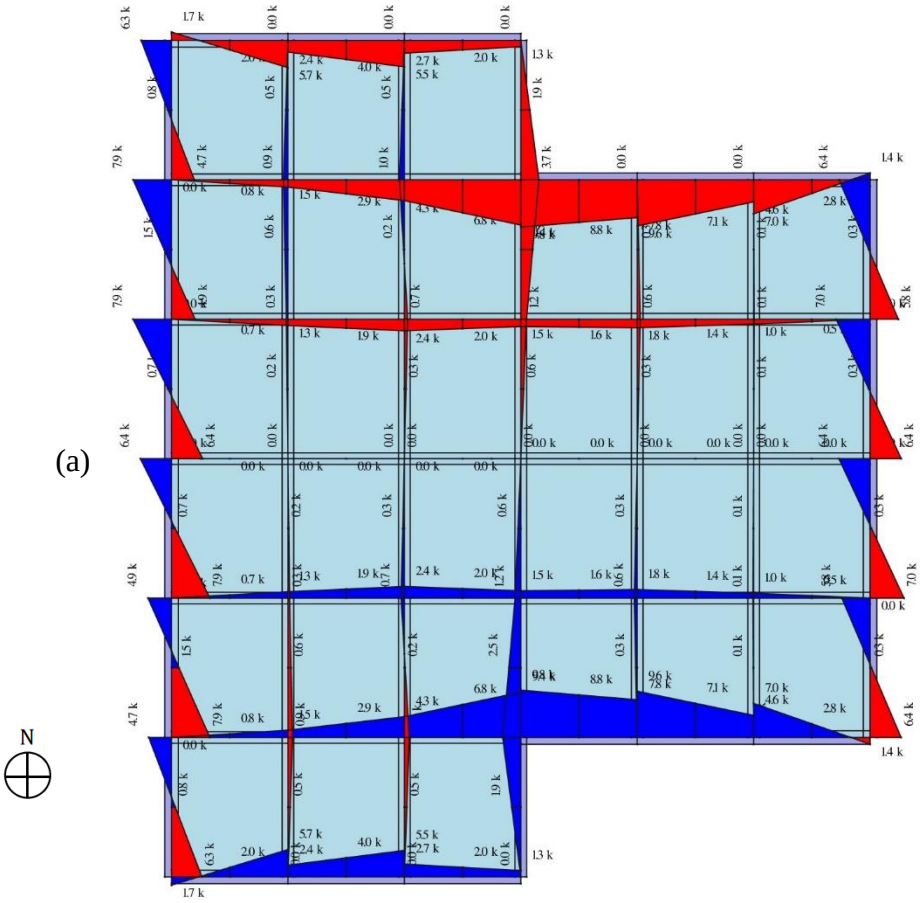

(b)

-3.8	-1.6	0.7			
-4.6	-3.0	-1.9	1.0	2.6	4.4
-5.3	-3.6	-1.5	0.9	3.0	4.9
-5.3	-3.6	-1.5	0.9	3.0	4.9
-4.6	-3.0	-1.9	1.0	2.6	4.4
-3.8	-1.6	0.7			

Figure 7-6. SPM Output for Seismic Load in the South Direction: a) Stringer Axial Forces (kip); b) Panel Shear Stresses (psi).

(a)

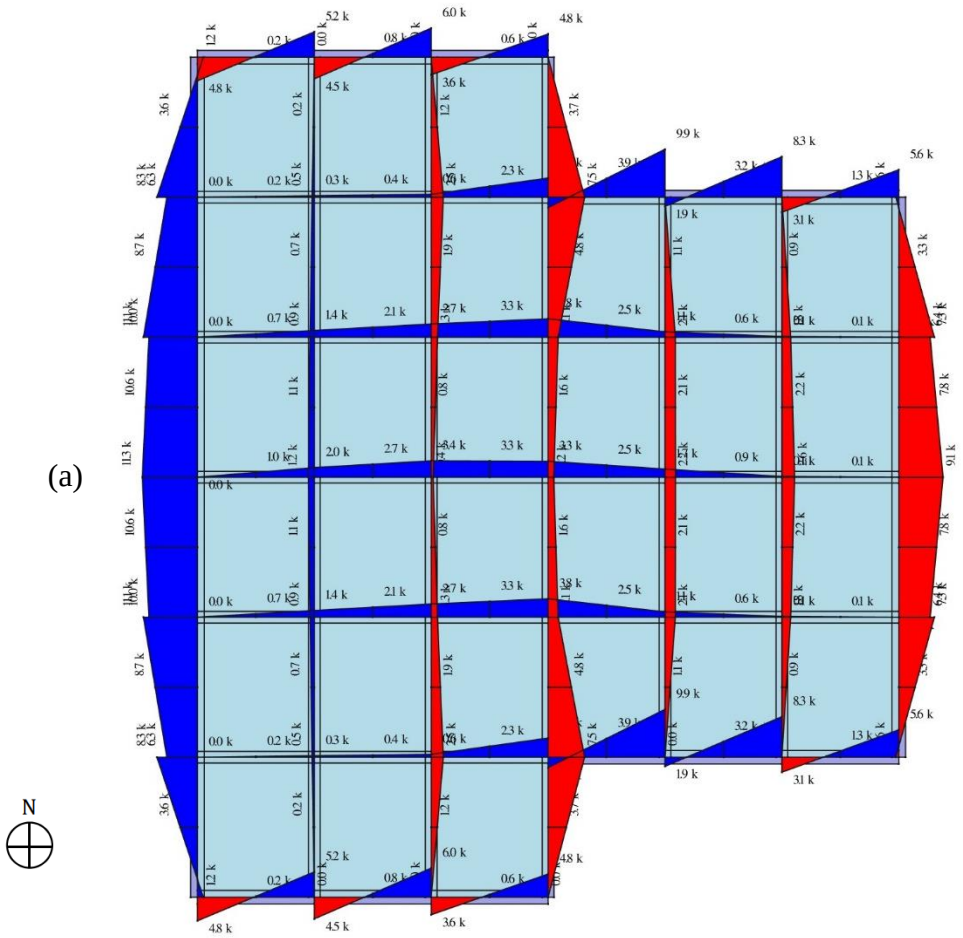

(b)

4.1	4.3	3.3			
2.1	2.3	2.8	5.1	4.2	3.4
0.6	0.7	1.1	1.5	1.5	1.1
-0.6	-0.7	-1.1	-1.5	-1.5	-1.1
-2.1	-2.3	-2.8	-5.1	-4.2	-3.4
-4.1	-4.3	-3.3			

Figure 7-7. SPM Output for Seismic Load in the West Direction: a) Stringer Axial Forces (kip); b) Panel Shear Stresses (psi).

7.3. Comparison of SPM and Beam Model

This section includes direct side-by-side comparisons of chord, collector, and diaphragm shear demands between the EBM and SPM. Additionally, stress concentrations identified by the SPM are also compared against their relative EBM demands. This section focuses on specific differences between demands determined using the two analytical methods, as a broader comparison of the analytical methods is discussed in Section 7.4. Tension and compression are considered positive and negative, respectively.

A comparison of axial demands between the EBM and SPM for seismic load in the south direction is shown in Figure 7-8. South direction panel demands are compared in Figure 7-9. West direction axial demands are compared in Figure 7-10, and west direction panel demands are compared in Figure 7-11.

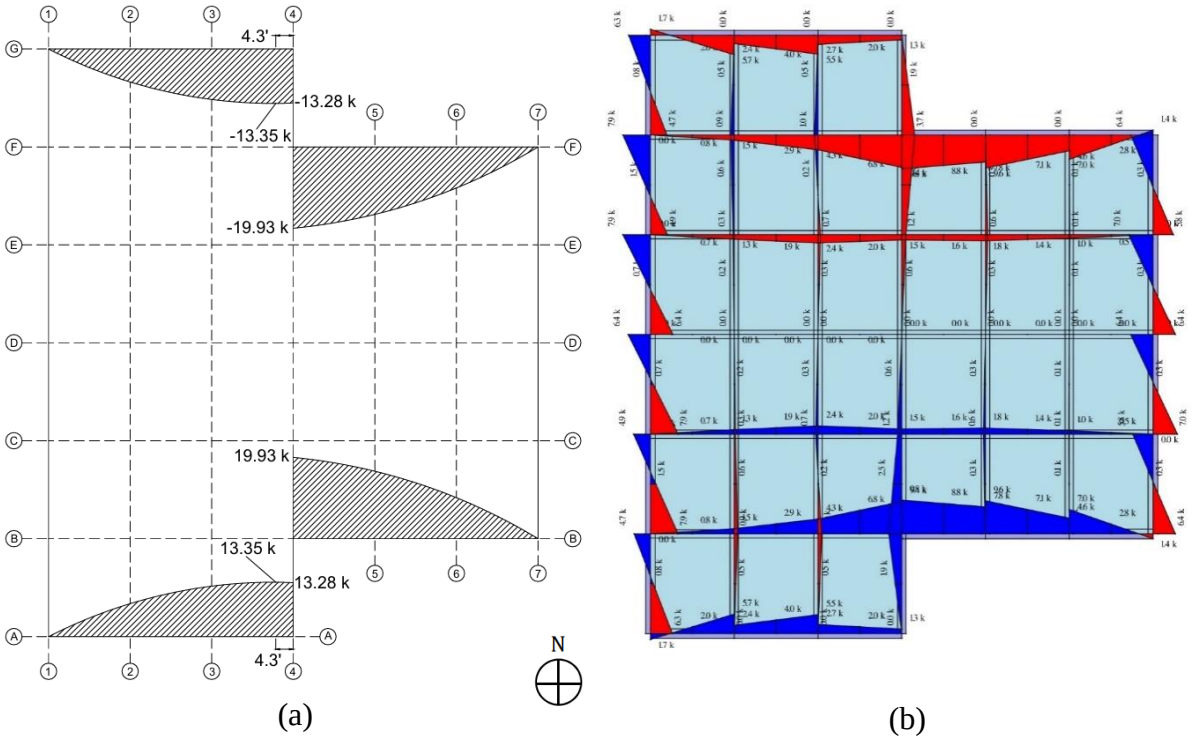

Figure 7-8. Axial Demands for Seismic Load in the South Direction: a) EBM; b) SPM.

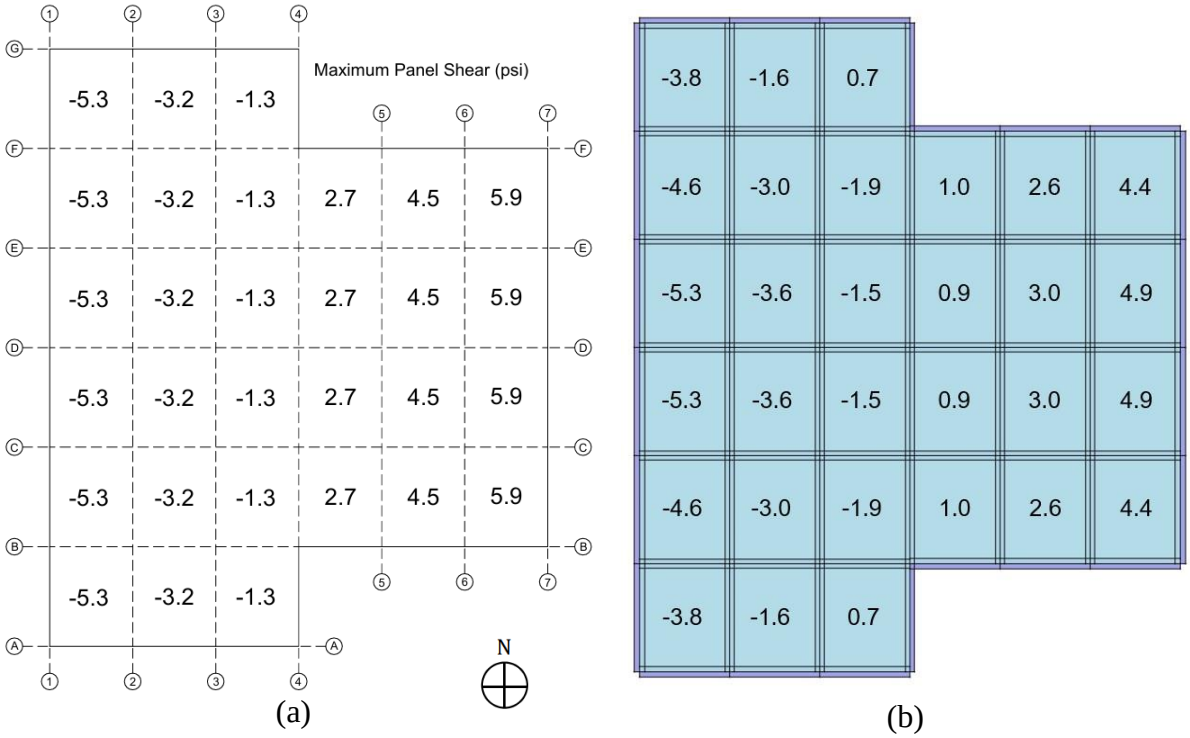

Figure 7-9. Panel Demands (psi) for Seismic Load in the South Direction: a) EBM; b) SPM.

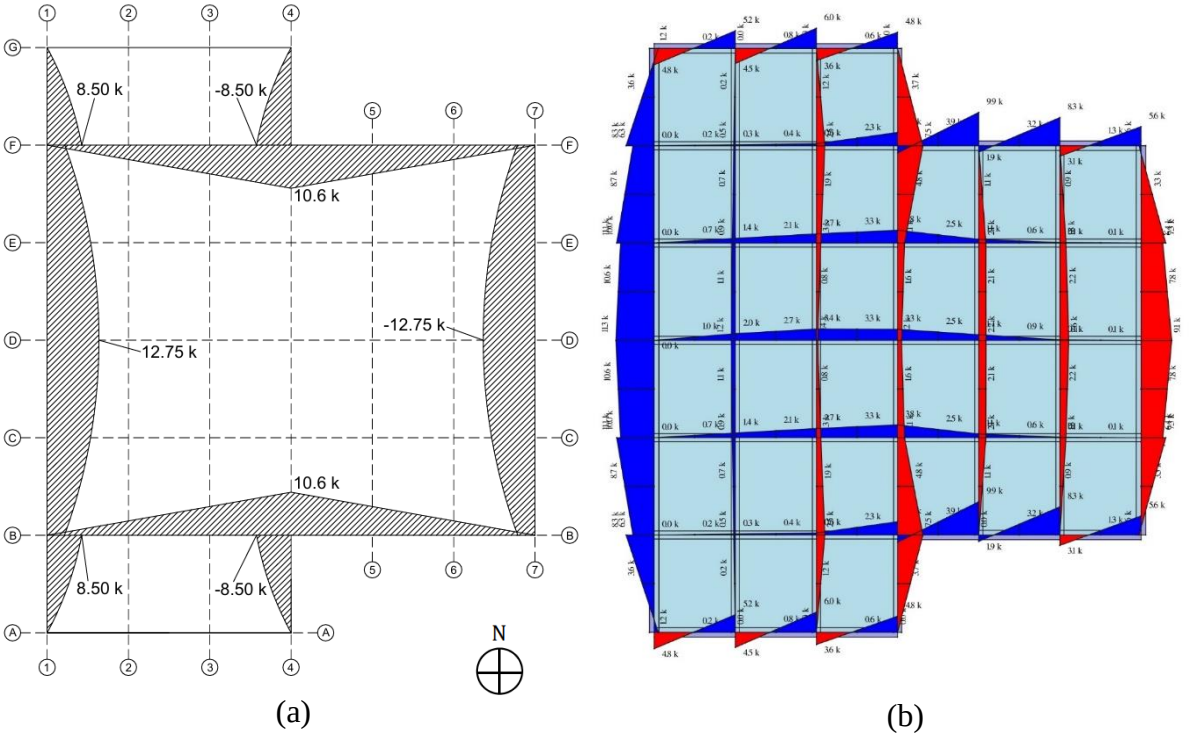

Figure 7-10. Axial Demands for Seismic Load in the West Direction: a) EBM; b) SPM.

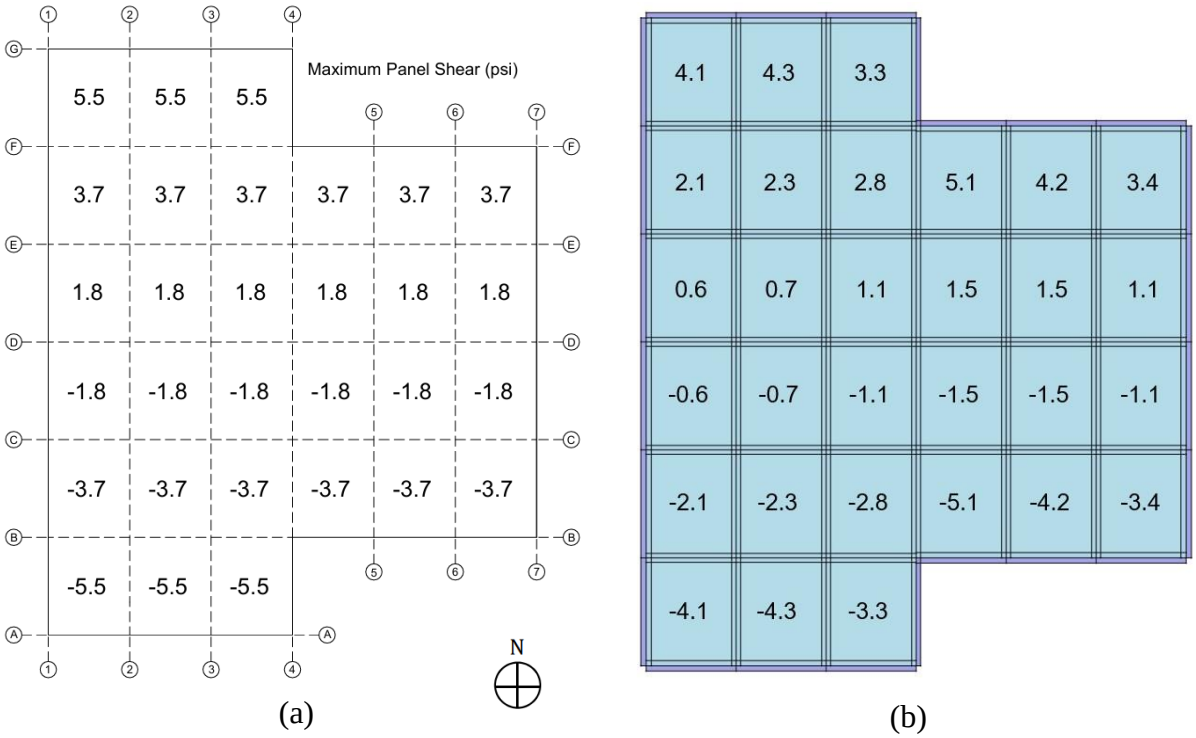

Figure 7-11. Panel Demands (psi) for Seismic Load in the West Direction: a) EBM; b) SPM.

7.3.1 Chord Demands

Chord demands from both analyses are shown in Figure 7-12. In most locations, the axial demands along each column line are less in the SPM. This demonstrates a key difference between the SPM and EBM; the presence of stringers along every column line introduces chords at multiple locations as opposed to a single tensile and compressive chord. The sole tensile and compressive chords in the EBM concentrate chord demand to the exterior stringers, while the diaphragm moment demand is distributed across multiple stringer lines in the SPM. As an effect, the SPM captures the axial demand on line B between lines 1 and 4 and line 4 between lines B and F for South and West loads, respectively. This axial demand is not explicitly captured by the EBM, although a design engineer may detail reinforcement at these locations by inspection.

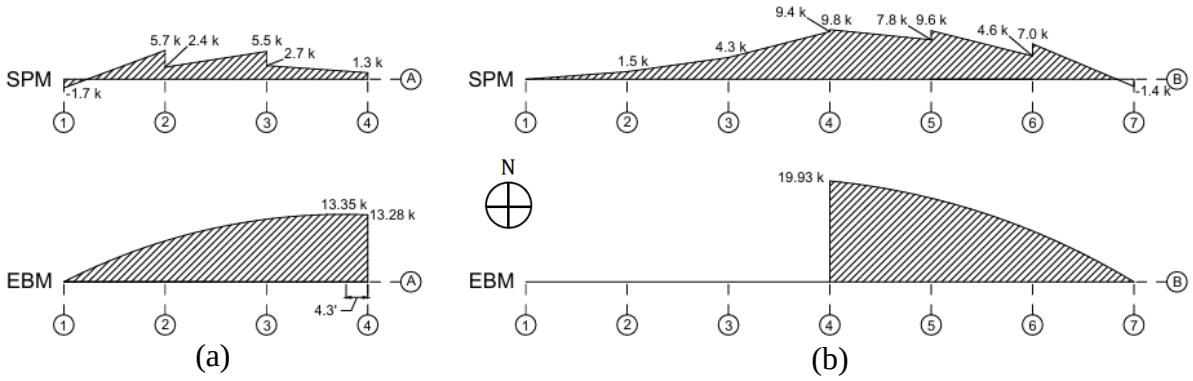

(a) (b)

Figure 7-12. Chord Demands for Seismic Force in the South Direction: a) Along Line B; b) Along Line A.

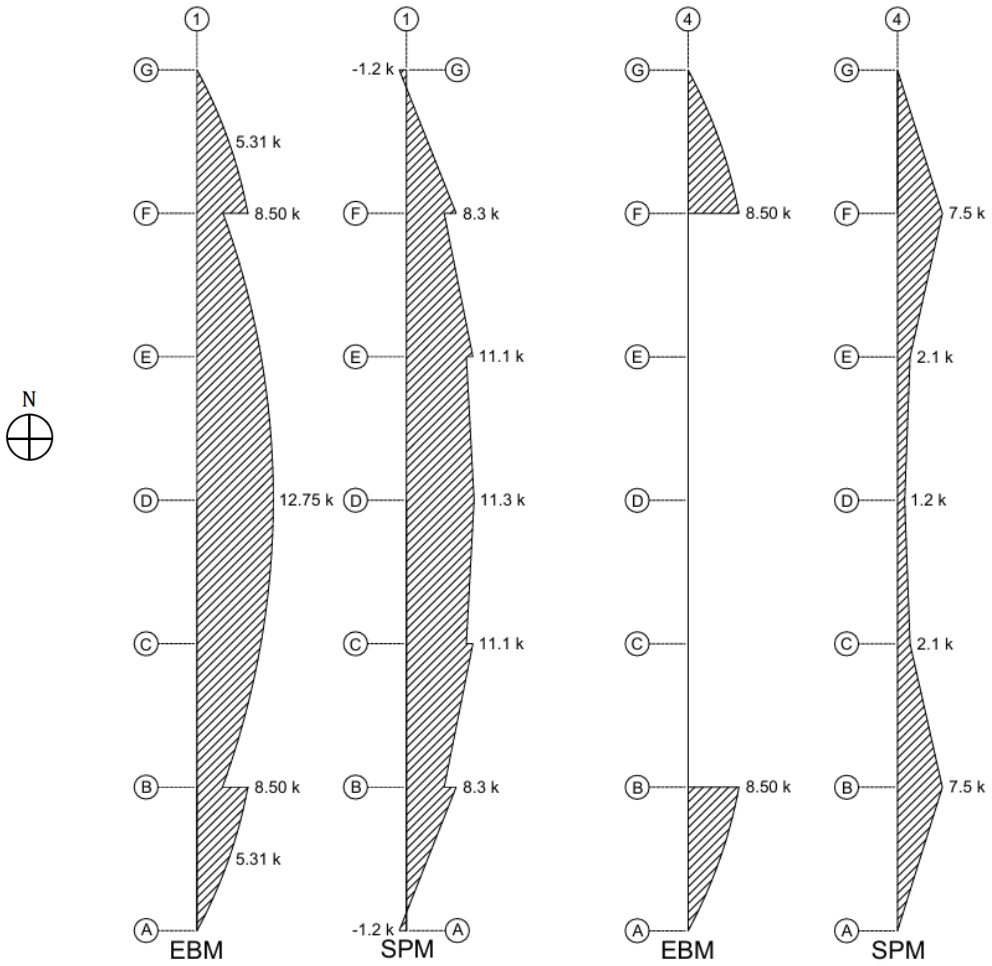

(a) (b)

Figure 7-13. Chord Demands: a) Along Line 1 for Seismic Force in the West Direction; b) Along Line 4 for Seismic Force in the East Direction.

7.3.2 Collector Demands

A comparison of SPM and EBM collector demands along line B (identical for line F) is shown in Figure 7-14. The EBM only requires collectors for loads in the East-West direction, as the vLFRS elements in the N-S direction extend the entire diaphragm depth. The collector force along line B between lines 1 and 4 is over two times greater in the EBM. As visualized in Figure 7-7(a), the reduced collector demand in the SPM along line B is attributed to the variance in load path between the two analytical methods. The presence of collectors solely along lines B and F is challenged by the SPM, which indicates more distributed axial demands along lines B, C, D, E, and F. The SPM indicates that diaphragm shear is also collected along lines C, D, and E, and then transferred laterally through the panels into the exterior stringers. Consequently, the collector demand along line B between lines 4 and 7 is greater in the SPM. The large steps in the SPM collector demand are due to the variance in load distribution to the vLFRS between the two methods. The EBM assumes a linearly varying distribution of load, while the SPM distributes load only at the columns.

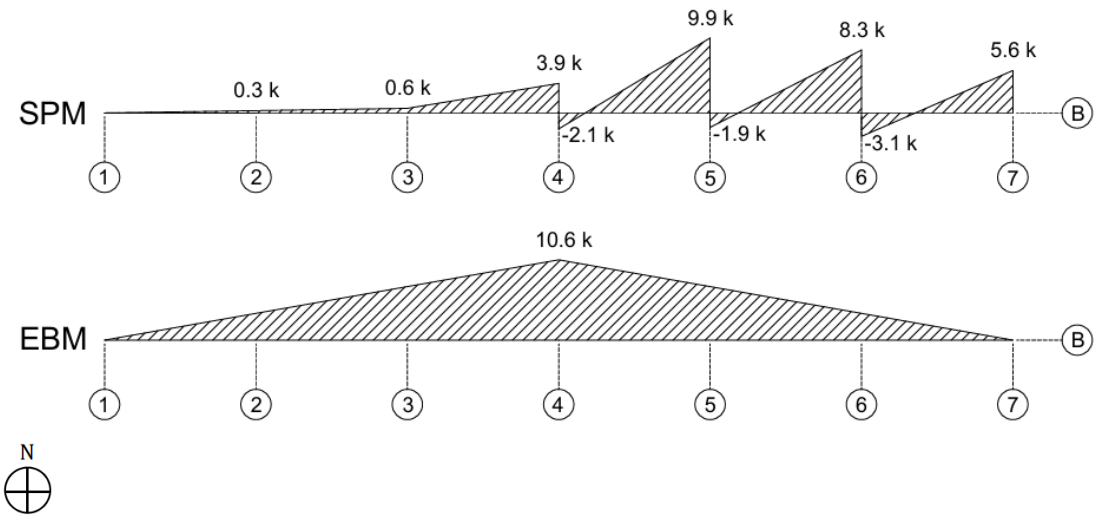

Figure 7-14. Collector Demands for Seismic Force in the West Direction Along Line B/F.

7.3.3 Diaphragm Shear Demands

Comparisons of diaphragm shear demands from the EBM and SPM are shown in Figure 7-15 and Figure 7-16. The key difference between diaphragm shear demands between the analytical methods is that diaphragm shear is more distributed in the SPM. The EBM assumes a constant shear demand along the diaphragm depth, while the shear distribution is more

concentrated at the center and at reentrant corners in the SPM. Additionally, the maximum shear demand in the SPM is occasionally less than the constant shear demand in the EBM, likely due to the portion of the seismic load that is tributary to the exterior stringers. In the EBM, the entire seismic force travels through the diaphragm, while only the portion of the seismic force tributary to the interior stringers (80% in all directions) travels through the panels.

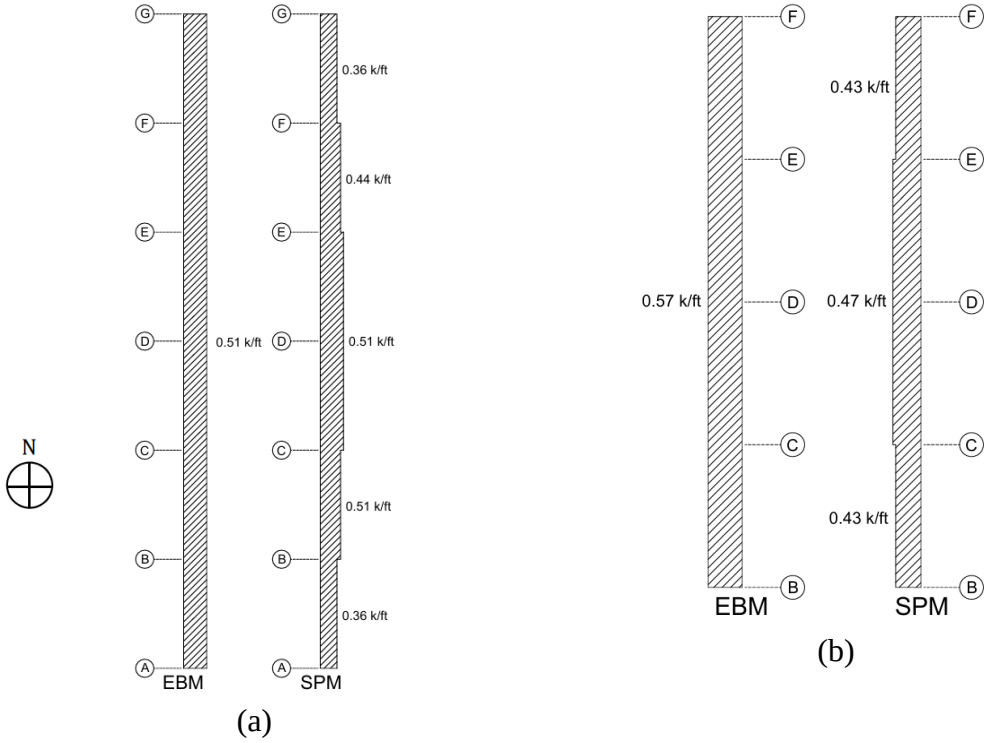

Figure 7-15. Diaphragm Shear Demands for Seismic Force in the South Direction: a) Immediately East of Line 1; b) Immediately West of Line 7.

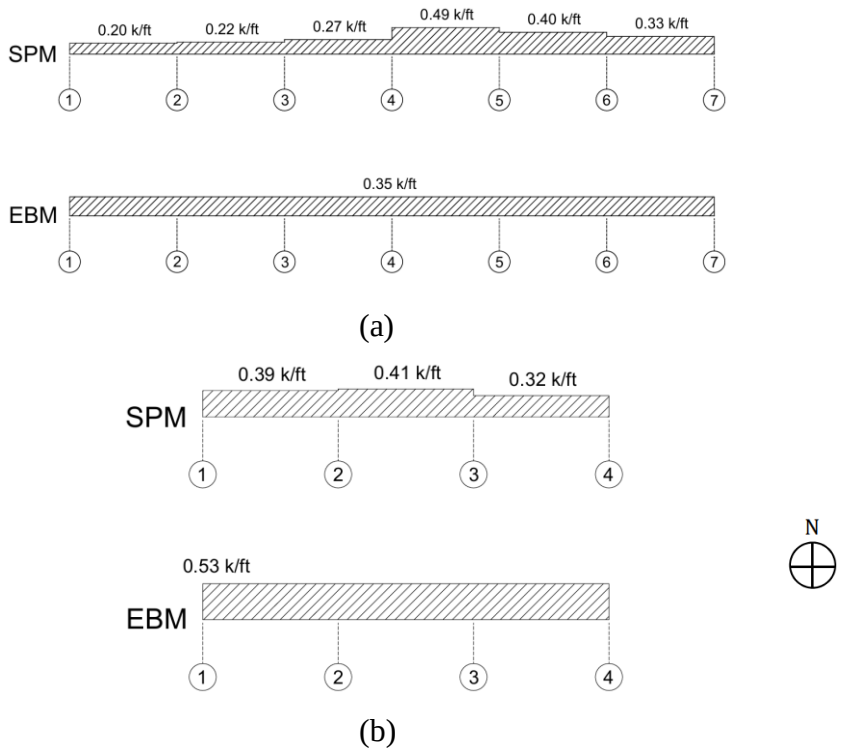

Figure 7-16. Diaphragm Shear Demands for Seismic Force in the West Direction: a) Immediately North of Line B; b) Immediately North of Line A.

7.3.4 Stress Concentrations

The SPM is able to explicitly capture stress concentrations in the model, while stress concentrations must be considered independently from the analytical model when using the EBM. This effect is best visualized through the stringer and panel demands around the reentrant corners in Figure 7-6 and Figure 7-7. For seismic load in the North or South direction, the EBM does not explicitly provide any axial demands along column line 4, while the SPM explicitly captures stringer demands along this column line. Additionally, the SPM captures increased diaphragm shear demands in the panels around the reentrant corner, while the EBM assumes constant shear demand along the diaphragm depth.

7.4. Discussion

A linear SPM was constructed and analyzed to determine design demands for a reinforced concrete diaphragm. The SPM captures variances in chord, collector, and diaphragm shear demands where the EBM oversimplifies diaphragm behavior. Additionally, stress

concentrations around reentrant corners are explicitly identified and quantified in the SPM. The use of the SPM simplifies the design procedure, as one model is sufficient for determining demands for all load combinations, while rigid or flexible diaphragm analysis must first be conducted to determine relevant inputs for the EBM.

While the total seismic load applied to the diaphragm is lower in the SPM due to the portion of load that is tributary to the perimeter moment frames, localized demands in the SPM are in some cases higher than those predicted by the EBM. This is best demonstrated by the presence of collector demands in the SPM along lines C, D, and E for seismic load in the West direction. Where the EBM assumes diaphragm shear collects along lines B and F, the SPM reveals that lines C, D, and E collect diaphragm shear and transfer it into the vLFRS through the panels in the East portion of the diaphragm. The SPM is able to capture variances in load path due to diaphragm geometry, while the EBM always assumes the flow of internal stresses to be analogous to a beam.

Although this example features relatively low seismic demands and a diaphragm with regular geometry and well-distributed vertical elements, the key takeaway is the difference in the flow of internal stresses between the models. The SPM provides a more accurate representation of load redistribution, capturing localized effects that are not captured in the EBM. This difference is particularly valuable in more complex diaphragm configurations where irregular geometry and vertical elements affect the load path.

Furthermore, the SPM output is clearly interpretable design demands due to the simple stress states in the panels and the stringers. The design engineer does not need to make section cuts such as those necessary in a finite element model. The stringers can be designed using provisions from ACI 318 (2019) for elements subject to pure tension or compression, and the panels can be analyzed as simple rectangular diaphragms using Chapter 12 of ACI 318 (2019), where the gross concrete area is simply the panel edge dimension in the direction of analysis times the panel thickness. In the case of designing an externally bonded FRP retrofit for shear strengthening of a reinforced concrete diaphragm, Eq. (28) can be used to determine the FRP contribution to shear strength, where the effective depth is the panel edge dimension in the direction of seismic load.

To investigate the ability of the SPM to quantify demands for more complex diaphragm layouts, the perimeter moment frames in the CRSI example are replaced with shear walls that do not extend the entire diaphragm depth. The locations of the shear walls are shown in Figure 7-17. Loading, discretization, and the total stiffness of the vertical elements are consistent with the SPM discussed earlier in this chapter. Instead of applying the vLFRS stiffnesses along multiple adjacent bays, stiffness is applied at the middle stringer DOF at the shear wall locations, representing a distributed stiffness along the entire one-bay shear wall. The outputs for loading in the South and West direction are shown in Figure 7-18 and Figure 7-19, respectively.

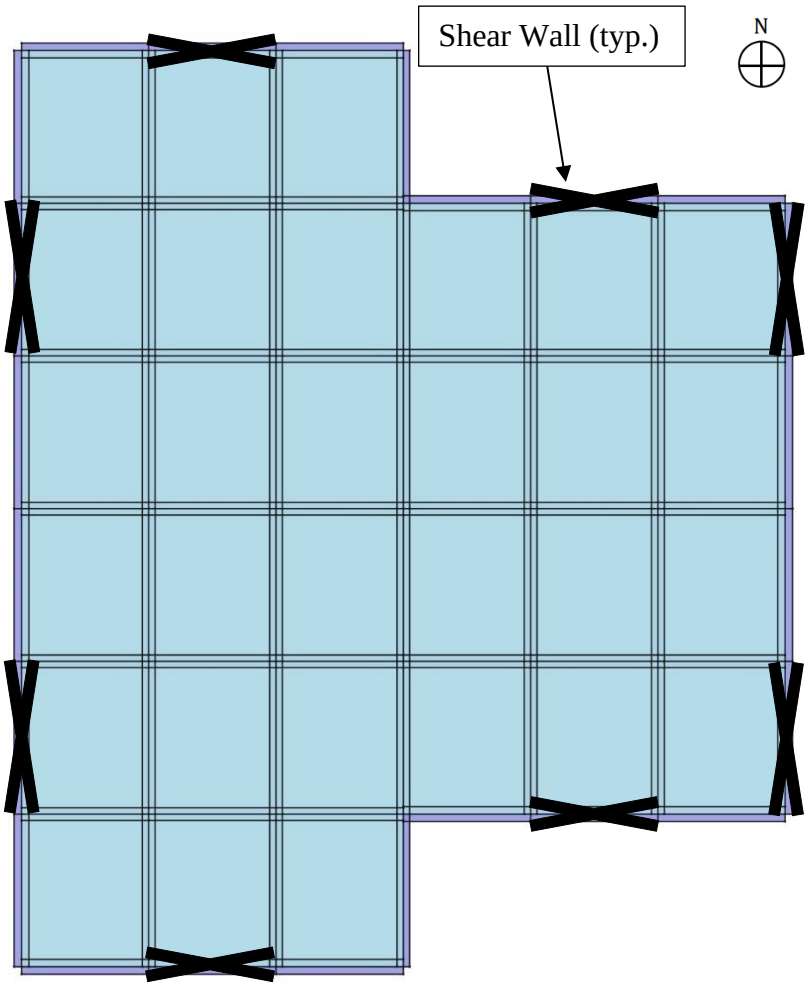

Figure 7-17. Shear Wall Locations in Adjusted SPM.

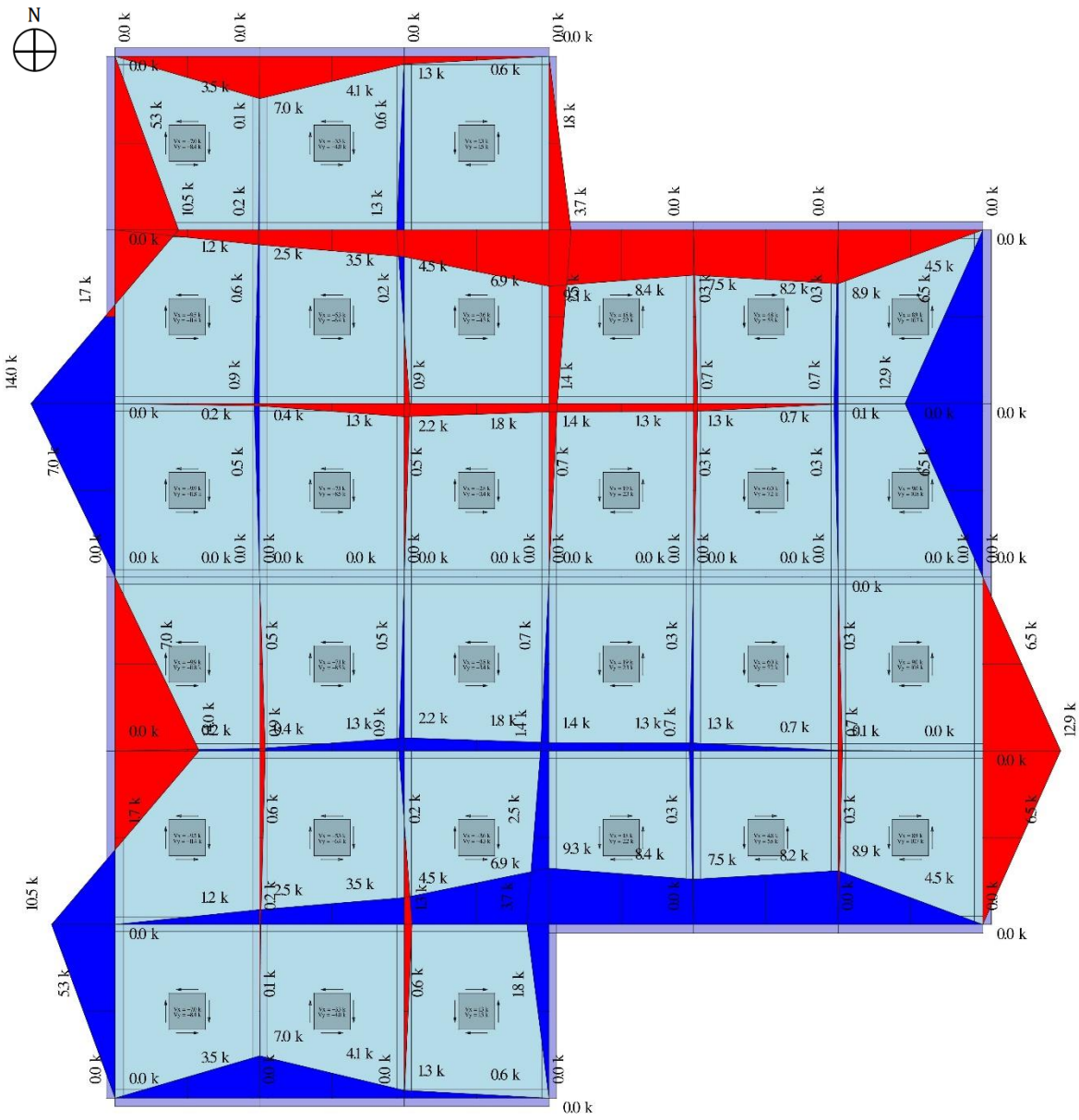

Figure 7-18. SPM with Shear Walls Output for Seismic Load in the South Direction.

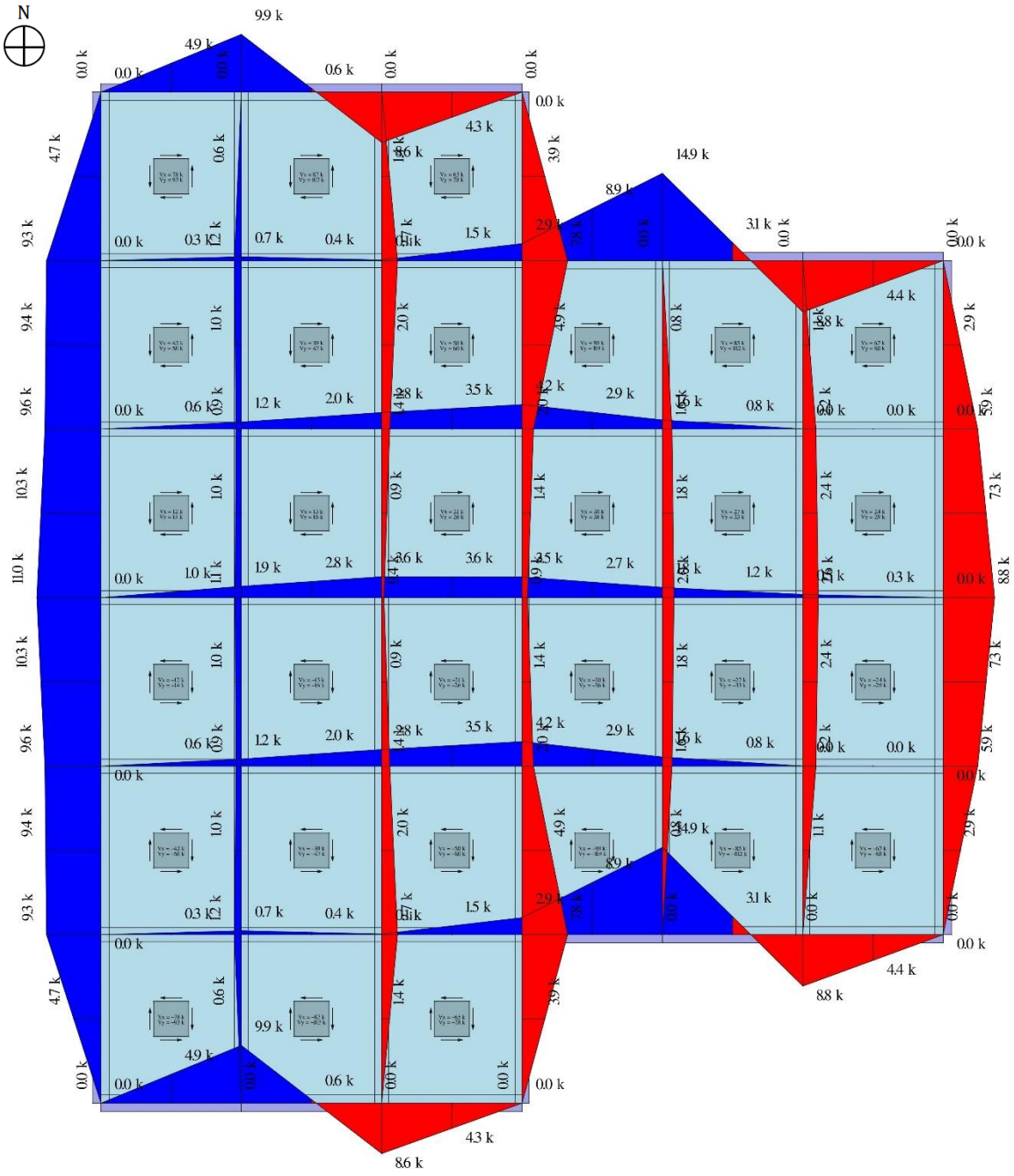

Figure 7-19. SPM with Shear Walls Output for Seismic Load in the West Direction.

Although the overall magnitude of maximum collector demands is similar to those calculated by the EBM for this vLFRS configuration, the SPM captures the influence of the internal load path on the collector force distribution. This is demonstrated by the effect of the reentrant corner on collector demands along lines B and F for West direction loading, and the influence of chord demands along lines B and F on collector demands along lines 1 and 7 for

South direction loading. While the load path through the diaphragm remains consistent – with internal axial and panel demands nearly identical to those in the original SPM – the primary difference between the two SPM analyses is how the axial forces are distributed around the perimeter. In the original model, these forces are transferred to the vLFRS at discrete column locations, whereas in the adjusted model, they are collected and distributed linearly along the diaphragm perimeter.

Chapter 8. Conclusions

8.1. Summary of Research

This research aimed to improve the design and analysis of FRP-strengthened reinforced concrete diaphragms by evaluating the performance of diaphragm specimens and investigating methods for determining diaphragm demands. This was accomplished through experimental investigation, database development, and analytical modeling using the SPM. The experimental results of eight reinforced concrete diaphragm specimens were presented to broaden the breadth of experimental data available on the performance of reinforced concrete diaphragms strengthened with externally bonded FRP. A database of 19 diaphragm specimens was assembled, including the eight specimens described in this thesis, six specimens from Hutton et al. (2023), and five specimens from Aryan et al. (2022) to better inform key findings and design recommendations. FRP shear strengthening was effective in increasing strength and post-cracking stiffness of all strengthened specimens. FRP ply orientation, ply configuration, and mechanical anchorage were all found to influence the behavior of the strengthened diaphragm specimens. Additionally, the SPM was investigated for use in determining diaphragm demands based on a more rational and realistic understanding of load path. In the CRSI design guide example, the SPM was found to have many advantages over the EBM, including the identification of stress concentrations, load paths, and more distributed chord, collector, and diaphragm shear demands. A summary of key findings and design recommendations is included in this chapter.

8.2. Key Findings

Experimental results from this thesis indicate:

1. Externally bonded FRP is effective in increasing in-plane shear strength of the reinforced concrete diaphragm specimens. The superposition of transverse steel, concrete, and FRP contributions to shear strength provides a conservative estimate of in-plane shear capacity.

2. Diaphragm specimens without FRP typically experience crushing of the diagonal compression strut, potentially followed by rupture of internal steel reinforcement.

3. Diaphragm specimens strengthened with FRP typically experience global debonding of the FRP from the concrete substrate at peak load followed by crushing of the diagonal compression strut. However, strut crushing or direct shear failures can govern in heavily strengthened specimens. Specimens utilizing anchorage may also experience anchor rupture, anchor pullout, or rupture of the FRP due to anchorage-induced stress concentrations.

4. Reinforcing steel strain data indicate that transverse and longitudinal reinforcement in the diaphragm field begins to yield prior to global debonding of the FRP. Steel reinforcement in the diaphragm field and in the chords do not carry high compressive stress.

5. An inverse relationship between FRP surface coverage and diaphragm ductility was found for FRP strengthening schemes that were either unanchored or anchored with fiber splay anchors. Ductility ratios for 0% and 100% surface coverage were approximately 3.0 and 2.0, respectively. Reduced ductility was attributed to the less gradual strength decay in specimens with high surface coverage.

6. Providing mechanical anchorage at the ends of FRP sheets was found to not have an influence on diaphragm shear capacity.

Key findings pertaining to the in-plane shear capacity of reinforced concrete diaphragms strengthened with externally bonded FRP include:

1. Unidirectional FRP sheets oriented in an orthogonal grid were more effective in increasing shear strength than an equivalent configuration all oriented parallel to applied shear, likely due to the reduced stiffness of the independent orthogonal layers.

2. FRP sheets oriented perpendicular to applied shear can be considered 50% as effective in contributing to shear strength relative to parallel sheets and still lead to conservative estimations of in-plane shear capacity.

3. Specimens that were retrofitted above the $8A_{cv}\sqrt{f_c'}$ limit, intended to guard against crushing of the concrete compressive strut, achieved $12.6A_{cv}\sqrt{f_c'}$ on average.

4. The design effective strain of FRP, calculated per ACI PRC-440.2R-23 (2023), appears to be a reasonable lower bound. In most diaphragm specimens, the design strain was conservative relative to both measured and estimated strains. For specimens governed or partially governed by FRP debonding, the estimated strain exceeded the design strain by an average of 44%, with a COV of 48%.

Key findings for establishing diaphragm design forces include:

1. The SPM may be an attractive alternative to the EBM as it outputs clearly interpretable design demands and one model is valid for all load combinations regardless of diaphragm flexibility.

2. The SPM identifies a more rational and realistic load path based on diaphragm geometry, SPM discretization, and vLFRS stiffnesses where the EBM always assumes the flow of internal stresses to be analogous to a beam.

3. The SPM identifies more distributed chord, collector, and diaphragm shear demands relative to the EBM, in addition to identifying chords and collectors at locations they are not present in the EBM.

8.3. Design Recommendations

Design recommendations were informed from the diaphragm specimen database analyzed in Chapter 5 and discussed in Chapter 6. The design recommendations address gaps in existing provisions in ACI PRC-440.2R-23 (2023) that have been adopted for diaphragm shear strengthening, in addition to validating and building upon the design recommendations proposed in Hutton et al. (2023). The following design considerations are recommended for externally bonded FRP shear strengthening of reinforced concrete diaphragms:

1. Diaphragm shear capacity can be represented as the superposition of steel, concrete, and FRP contributions, as shown in Eq. (29), where the FRP strength reduction factor ψ_f is 0.75 for one-sided strengthening per Hutton et al. (2023).

2. The concrete and steel contribution to diaphragm shear capacity can be calculated per ACI 318-19 (2019), as shown in Eq. (2) and Eq. (3), where the gross concrete area $A_{cv} = b_w d$.

3. The design effective strain can be calculated using equations in Section 11.4.1.2 of ACI PRC-440.2R-23 (2023) considering the recommendation that $k_2 = 1.0$ from Hutton et al. (2023).

4. The design effective strain of an orthogonal grid of unidirectional FRP should be calculated per layer and the orthogonal layers should be considered to not contribute to each other's stiffness.

5. The shear strength contribution of orthogonal layers of FRP should be calculated per layer and superimposed, as shown in Eq. (28).

6. The directionality factor should be considered to account for the effect of ply orientation on the shear strength contribution of FRP. The directionality factor is 1.0 for strengthening parallel to applied shear, 1.414 for strengthening in the assumed principal tensile direction, 0 for strengthening in the assumed principal compressive direction, and 0.5 for strengthening parallel to applied shear.

7. The nominal shear capacity should be less than $8A_{cv}\sqrt{f_c'}$ to guard against crushing of the diagonal compression strut.

8. As recommended in Hutton et al. (2023), end anchorage should be designed to 1.5 times the tensile force developed in the anchored FRP sheet.

9. For strengthening only parallel to applied shear, intermediate anchorage should be spaced in an alternating configuration between adjacent sheets to reduce the impact of anchorage forces on the stress distribution in the diaphragm field.

10. To provide end anchorage to an orthogonal grid of FRP, it is recommended to provide a perimeter of anchorage between the two layers.

8.4. Limitations and Future Work

While the findings of this thesis provide valuable insights into the performance of FRP-strengthened reinforced concrete diaphragms, several limitations should be acknowledged. The experimental database analyzed and discussed in this thesis is limited in scope, particularly in terms of reinforcement ratios, anchorage types, FRP ply orientation, and governing failure modes for heavily strengthened specimens. In the database, transverse reinforcement ratios ranged between 0.0015 and 0.0023, all near the ACI 318 (2019) minimum of 0.0018. Future work should be conducted to investigate the performance of FRP-strengthened diaphragms with a broader range of transverse reinforcement ratios.

Although Specimen CD7 and CD8 support conclusions on strengthening with and without fiber splay anchors, limited comparisons between anchorage systems can be made, as no two specimens were identical except for their anchor system. Future work should be conducted to investigate the performance of different anchorage systems using specimens that are otherwise identical. Furthermore, four specimens in the database featured FRP oriented in any direction other than parallel to the applied shear, and all of these specimens were strengthened with CFRP and contained fiber splay anchors. Future work should be conducted to investigate the performance of non-parallel FRP orientations of lower modulus FRP with varying anchorage types.

The three specimens in the database that feature an orthogonal grid of FRP did not solely experience FRP debonding at peak load, as their peak strength was affected by the strength of the underlying concrete diaphragm. Although the experimental results from these specimens were crucial in investigating the ACI 318 (2019) limit to guard against crushing of the compression strut, future work should be conducted including specimens strengthened with an orthogonal grid of FRP that are designed to fail in global FRP debonding. The proposed methodology for quantifying the shear strength contribution of FRP oriented in any direction should be revisited once more experimental data is available.

Additionally, the estimated FRP contributions to shear strength and estimated effective FRP strains were calculated using steel and concrete contributions estimated by a beam-based approach. As shown in Section 5.2, specimen capacity is difficult to predict using beam-based approaches, especially for specimens containing perimeter beams. In particular, assuming the concrete contribution to shear strength is $2A_{cv}\lambda\sqrt{f_c'}$ regardless of diaphragm geometry, steel reinforcement layout, and FRP strengthening scheme results in a stark oversimplification of diaphragm behavior. As such, there is a need to fundamentally reconsider how diaphragms are analyzed, from the conventional deep beam analogy to a localized approach that traces load paths, recognizes diagonal tension and compression behavior, and accounts for the non-uniform flow of internal stresses through the diaphragm.

Furthermore, the comparisons made between the EBM and SPM in Chapter 7 are based on a design example of one reinforced concrete diaphragm with regular geometry, no openings, and well-distributed vLFRS elements. Future work should be conducted to investigate the efficacy of the SPM in determining demands of more complex reinforced concrete diaphragms.

Finally, the specimens included in the database were all designed to represent a critical portion of a reinforced concrete building diaphragm. Their geometry, boundary conditions, and loading may not fully represent their behavior as part of a larger, continuous diaphragm. While the design methodology proposed in this thesis was validated on an element level, the role of orthogonal FRP and in-plane reinforcing steel in diaphragm response remains unclear. The directionality factor and effective depths in the proposed methodology for quantifying the FRP contribution to shear strength are difficult to justify mechanically, especially in a system with multi-directional reinforcement, irregular geometry, and complex crack paths. Future work involving large multi-bay or even full-scale reinforced concrete diaphragm specimens should be conducted to ensure that the specimens analyzed and discussed in this thesis accurately represent their behavior as part of a full-scale diaphragm. Prior to validation through full-scale experimental or analytical studies, caution should be exercised when extrapolating the results of this thesis to full-scale design.

References

ACI Committee 318 (2019) *Building code requirements for structural concrete (ACI 318-19) and commentary (ACI 318R-19)*, Published by the American Concrete Institute.

ACI Committee 440 (2023) *Guide for the design and construction of externally bonded FRP systems for strengthening concrete structures (ACI PRC-440.2R-23)*, Published by the American Concrete Institute.

Aryan, H., Gencturk, B., and Alkhrdaji, T.. (2022) "In-plane shear strengthening of reinforced concrete diaphragms using fiber reinforced polymer composites." *Advances in Structural Engineering*, 0(0), 1-17.

ASTM (2017) *Standard Test Method for Splitting Tensile Strength of Cylindrical Concrete Specimens (C496-17)*, Published by ASTM International.

ASTM (2021) *Standard Test Method for Compressive Strength of Cylindrical Concrete Specimens (C39-22)*, Published by ASTM International.

ASTM (2022) *Standard Practice for Making and Curing Concrete Test Specimens in the Field (C31-22)*, Published by ASTM International.

ASTM (2022) *Standard Test Methods and Definitions for Mechanical Testing of Steel Products (A370-22)*, Published by ASTM International.

Avellaneda-Ramirez, R., (2021) "Experimental Behavior of Concrete Filled Steel Deck Diaphragms" Personal Communication, Virginia Tech, Blacksburg, VA.

Bentz, E. (2001) *Response-2000, Shell-2000, Triax-2000, Membrane-2000 User Manual.*

Blauuwendraad, J. (2018). *Stringer-Panel Models in Structural Concrete*. Springer.

Design guide for reinforced concrete diaphragms: A guide to assist design professionals in efficiently designing and detailing reinforced concrete diaphragms. (2019). . Concrete Reinforcing Steel Institute.

Dhakal, P., Hutton, H., Eatherton, M.R., and Jacques, E. (2022) "Workshop Report: Development of FRP Retrofit Guidelines for Deficient Reinforced Concrete Horizontal Lateral Force Resisting Systems." VTechWorks, 0(0), 1-33.

Dhakal, P. (2025). *ANALYSIS AND DESIGN OF FRP RETROFIT OF REINFORCED CONCRETE DIAPHRAGMS* [Doctoral Dissertation]. Virginia Polytechnic Institute and State University.

Fanella, D., & Mota, M. (2018). Design of Reinforced Concrete Diaphragms for Wind. *STRUCTURE Magazine*.

FEMA (2006) *Techniques for the seismic rehabilitation of existing buildings (FEMA 547)*, Published by the Federal Emergency Management Agency.

FEMA (2007) *Interim testing protocols for determining the seismic performance characteristics of structural and nonstructural components (FEMA 461),* Published by the Federal Emergency Management Agency.

Fyfe (2022a) *Tyfo SCH-41,* Published by FyfeFRP.

Gardiner, D. R. (2011). *Design Recommendations and Methods for Reinforced Concrete Floor Diaphragms Subjected to Seismic Forces*. https://doi.org/10.26021/1231

Godínez, S. E., & Restrepo, J. I. (2023). Stringer-panel model to support the seismic design and response verification of building diaphragms. *Resilient Cities and Structures*, 2(1), 46–67. https://doi.org/10.1016/j.rcns.2023.02.003

Godínez, S. E., Restrepo, J. I., & Rodríguez, M. E. (2024). Modeling of building diaphragms for Nonlinear Response-History Analysis. ACI Structural Journal. https://doi.org/10.14359/51742155

Hoogenboom, P. C. J. (1998). *Discrete elements and nonlinearity in design of structural concrete walls*. http://ci.nii.ac.jp/ncid/BB05880332

Hutton, H. (2023). *EXPERIMENTAL PROGRAM FOR FIBER REINFORCED POLYMER RETROFIT OF REINFORCED CONCRETE DIAPHRAGMS* [MS Thesis]. Virginia Polytechnic Institute and State University.

Jacques, E. (2025). Boring Square v4.1: Stringer-Panel Method FEA Solver [Computer software]. Virginia Tech, Blacksburg, VA.

Khalifa, A., Gold, W. J., Nanni, A., & MI, A. A. (1998). Contribution of externally bonded FRP to shear capacity of RC Flexural members. *Journal of Composites for Construction*, *2*(4), 195–202. https://doi.org/10.1061/(asce)1090-0268(1998)2:4(195

Nakashima, M., Huang, T., and Lu, L.-W. (1981) "Seismic Resistance Characteristics of Reinforced Concrete Beam-Supported Floor Slabs in Building Structures." *Fritz Laboratory Reports*, Bethlehem, Pennsylvania.

Maeda, T., Asano, Y., Sato, Y., Ueda, T., & Kakuta, Y. (1999). A Study on Bond Mechanism of Carbon Fiber Sheet. In Proceedings of the Third International Symposium on Non-Metallic (FRP) *Reinforcement for Concrete Structures (Vol. 1, pp. 279–286)*. Japan Concrete Institute, Japan.

Moehle, J. (2015). *Seismic Design of Reinforced Concrete Buildings*. McGraw-Hill Education.

Ormeno, M., Jing, J., Rogers, R., and del Rey Castillo, E. (2019) "Capacity of diaphragm strengthened with FRP: comparison between ACI 440.2R and in-situ tests," *Proceedings,*

2019 Pacific Conference on Earthquake Engineering, New Zealand Society for Earthquake Engineering, Auckland, NZ, 4–6 April 2019.

Scarry, J. M. (2014). "Floor diaphragms – Seismic bulwark or Achilles' heel," *Proceedings, 2014 Pacific Conference on Earthquake Engineering, New Zealand Society for Earthquake Engineering*, Auckland, NZ, 21–23 March 2014.

Simpson Strong-Tie (2022a) CSS V-Wrap C100HM, Published by Simpson Strong-Tie Company.

Simpson Strong-Tie (2022b) CSS V-Wrap C220HM, Published by Simpson Strong-Tie Company.

Triantafillou, T. C. (1998). Shear strengthening of reinforced concrete beams using Epoxy-Bonded FRP composites. *ACI Structural Journal*, 95(2). https://doi.org/10.14359/531

Appendix A: Specimen Details for CD7 and CD8

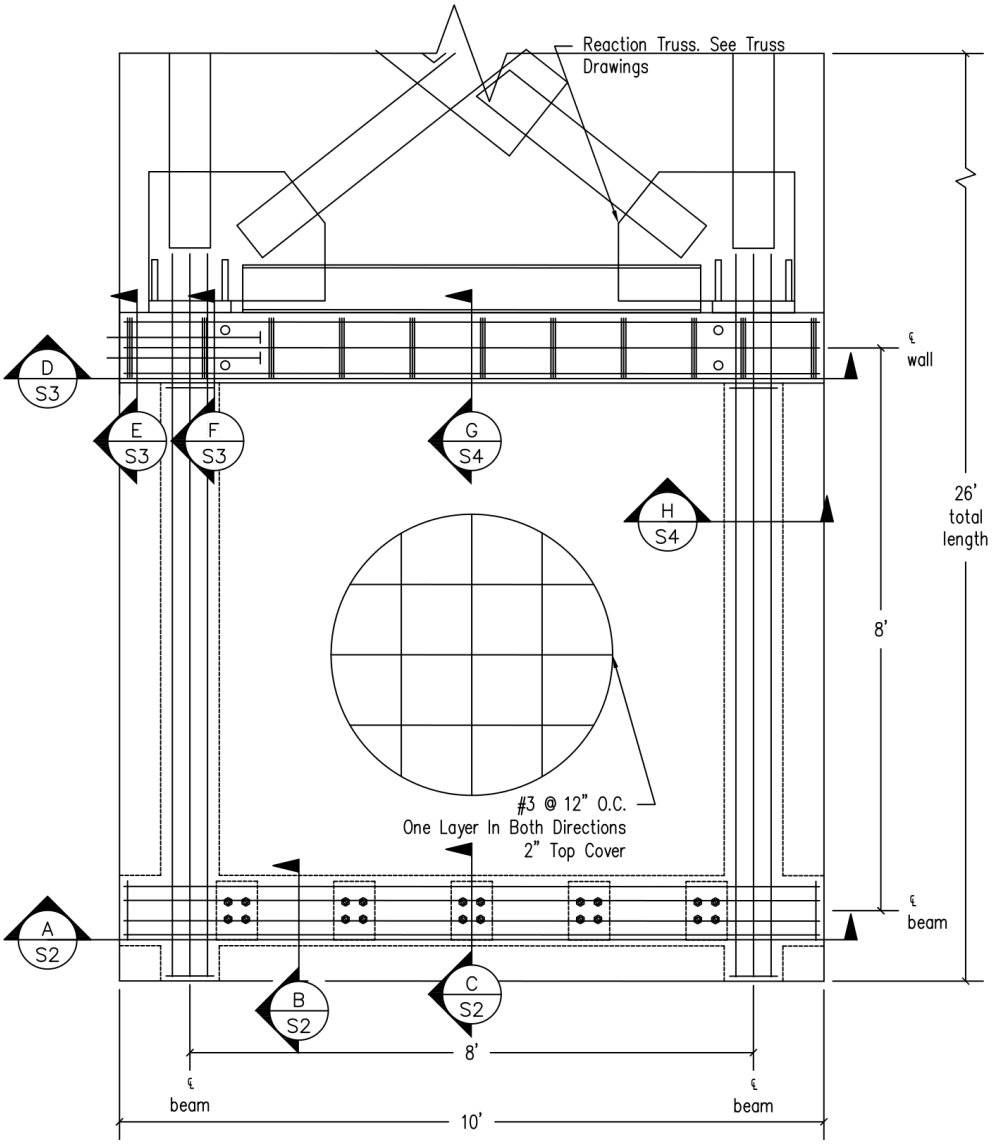

.\Masters\Auto Cad VT Logo.jpg

VIRGINIA TECH
CHARLES E. VIA JR. DEPARTMENT OF CIVIL & ENVIRONMENTAL ENGINEERING
200 PATTON HALL
BLACKSBURG, VA 24061
P: 540-231-6635

PROJECT:
Concrete Diaphragm Test Setup

SHEET NOTES:
1. Not all stirrups are shown for clarity

REVISIONS:

NO.	DATE	BY
1	7/12/2021	RTS

DESIGNED BY:
DRAWN BY: R. Stevens
CHECKED BY:
DATE: 7/2/2021
PROJECT NO.:

SHEET TITLE:
REBAR AND EMBEDMENT LAYOUT

SHEET NO.: 1 of 12

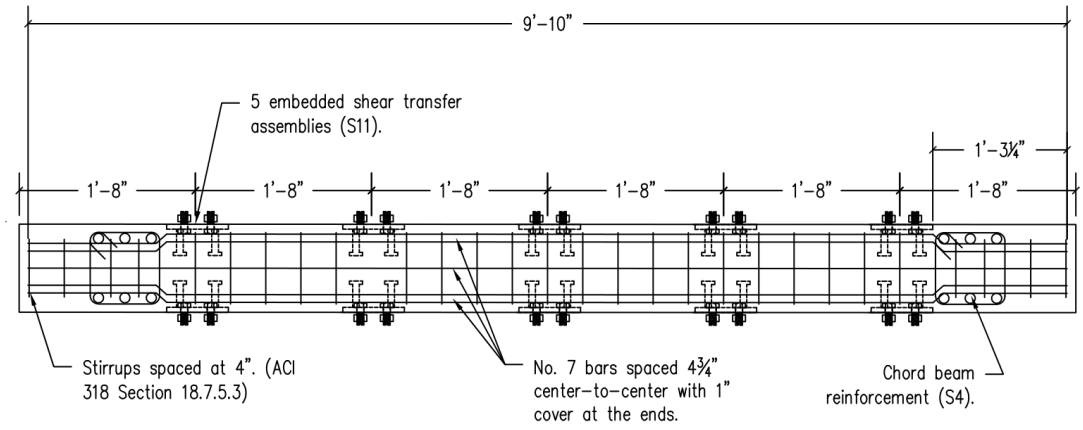

A/S2 EDGE BEAM REBAR
Scale:3/4"=1'

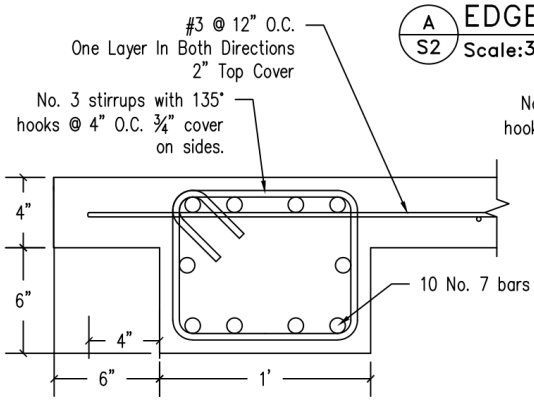

B/S2 EDGE BEAM REBAR
Scale: 3"=2'

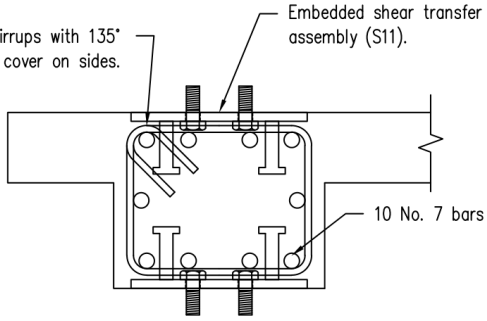

C/S2 EDGE BEAM REBAR
Scale: 3"=2'

.\Masters\Auto Cad VT Logo.jpg

VIRGINIA TECH
CHARLES E. VIA JR. DEPARTMENT OF CIVIL & ENVIRONMENTAL ENGINEERING
200 PATTON HALL
BLACKSBURG, VA 24061
P: 540-231-6635

PROJECT:
Concrete Diaphragm Test Setup

SHEET NOTES:

REVISIONS:

NO.	DATE	BY
1	7/12/2021	RTS
2	7/14/2021	RTS

DESIGNED BY:
DRAWN BY: R. Stevens
CHECKED BY:
DATE: 7/1/2021
PROJECT NO.:

SHEET TITLE:
SECTION VIEWS

SHEET NO.: 2 of 12

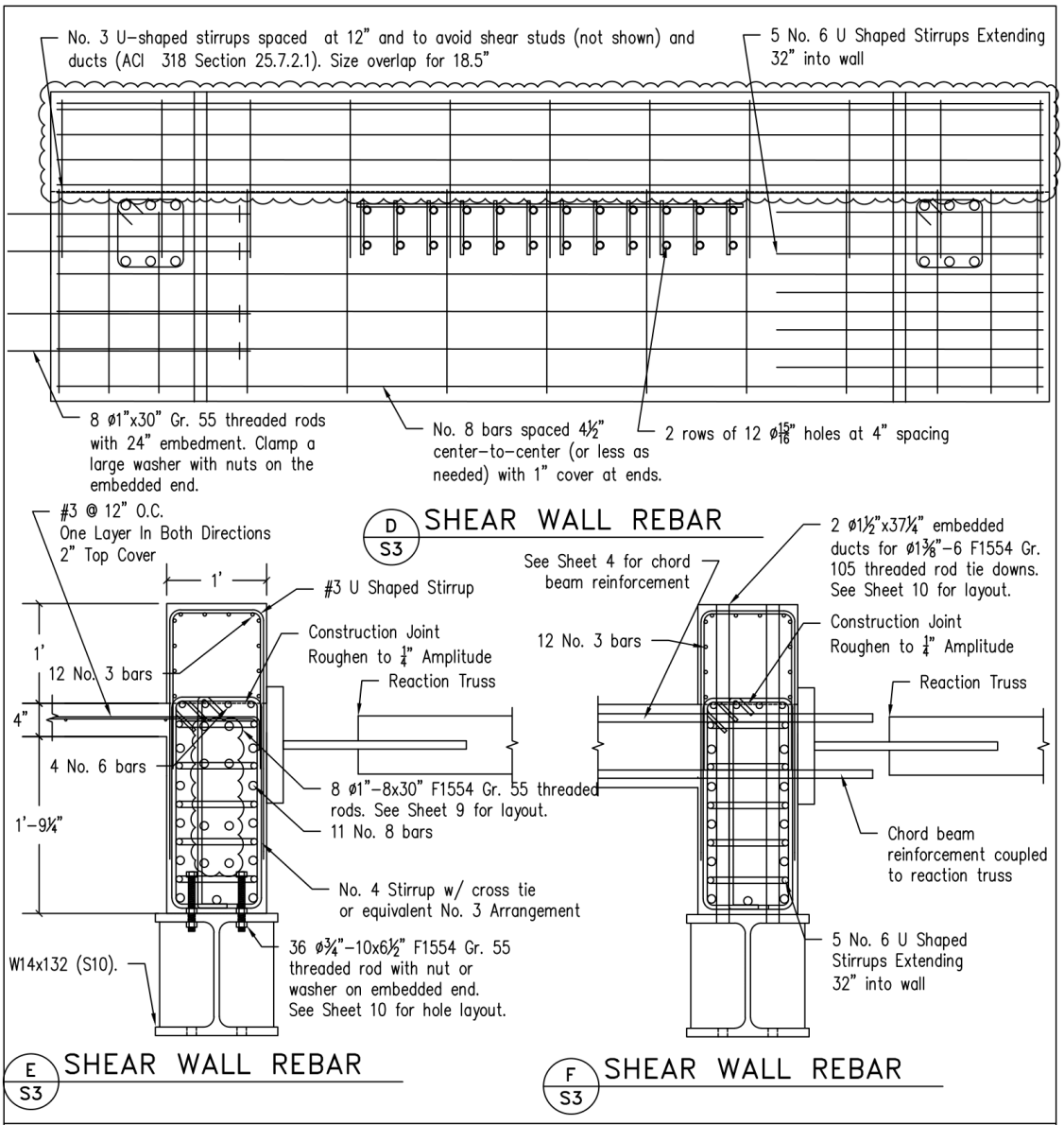

D S3 SHEAR WALL REBAR

E S3 SHEAR WALL REBAR

F S3 SHEAR WALL REBAR

.\Masters\Auto Cad VT Logo.jpg

VIRGINIA TECH
CHARLES E. VIA JR. DEPARTMENT OF CIVIL & ENVIRONMENTAL ENGINEERING
200 PATTON HALL
BLACKSBURG, VA 24061
P: 540-231-6635

PROJECT:
Concrete Diaphragm Test Setup

SHEET NOTES:
1. Scale is 3/4"=1'

REVISIONS:

NO.	DATE	BY
1	7/8/2021	RTS
2	7/14/2021	RTS

DESIGNED BY:
DRAWN BY: R. Stevens
CHECKED BY:
DATE: 7/1/2021
PROJECT NO.:

SHEET TITLE:
SECTION VIEWS

SHEET NO.: 3 of 12

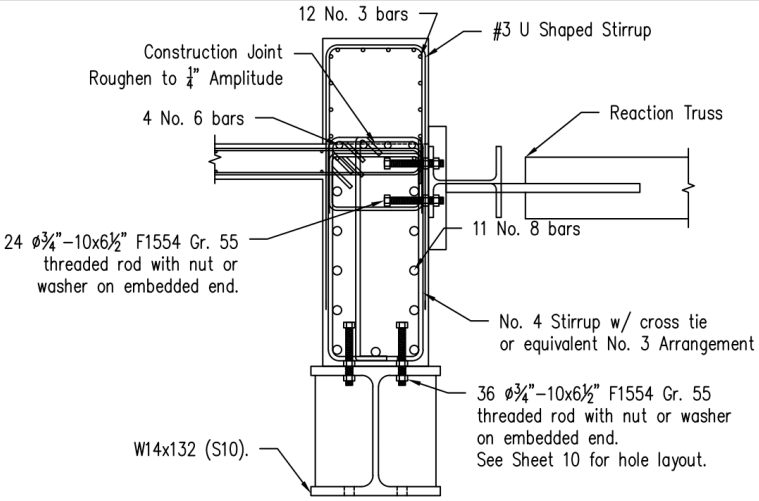

G / S4 SHEAR WALL REBAR
Scale:3/4"=1'

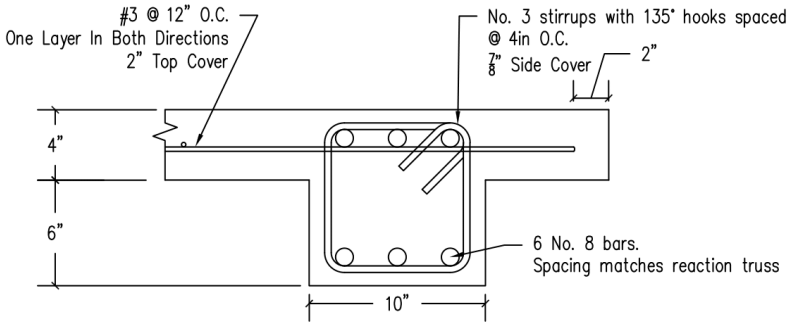

H / S4 CHORD BEAM REBAR
Scale: 3"=2'

.\Masters\Auto Cad VT Logo.jpg

VIRGINIA TECH
CHARLES E. VIA JR. DEPARTMENT OF CIVIL & ENVIRONMENTAL ENGINEERING
200 PATTON HALL
BLACKSBURG, VA 24061
P: 540-231-6635

PROJECT:
Concrete Diaphragm Test Setup

SHEET NOTES:

REVISIONS:

NO.	DATE	BY
1	7/8/2021	RTS
2	7/14/2021	RTS

DESIGNED BY:
DRAWN BY: R. Stevens
CHECKED BY:
DATE: 7/2/2021
PROJECT NO.:

SHEET TITLE:
SECTION VIEWS

SHEET NO.: 4 of 12

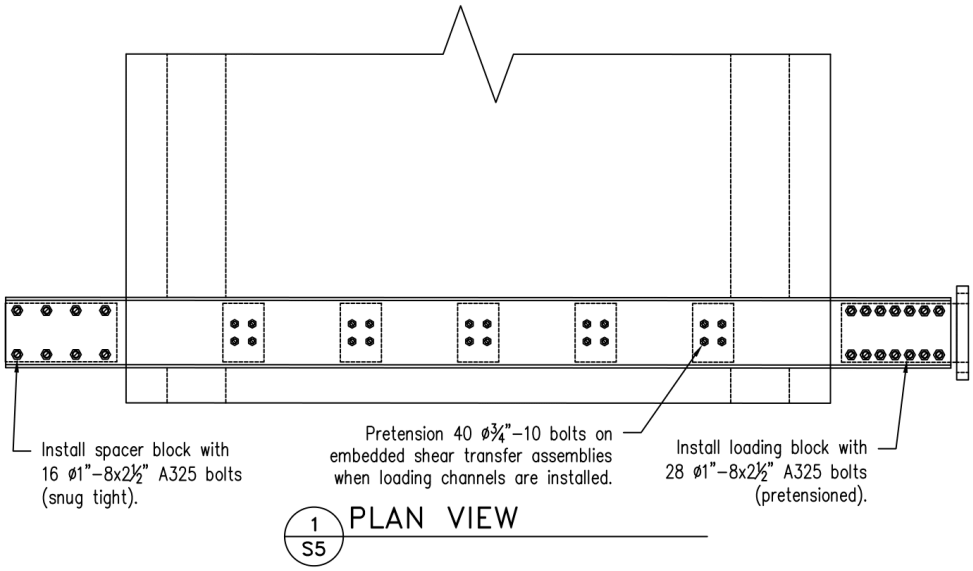

1/S5 PLAN VIEW

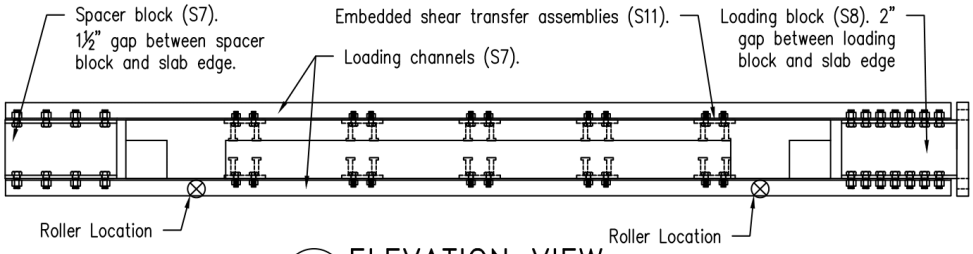

2/S5 ELEVATION VIEW

.\Masters\Auto Cad VT Logo.jpg

VIRGINIA TECH
CHARLES E. VIA JR. DEPARTMENT OF
CIVIL & ENVIRONMENTAL
ENGINEERING
200 PATTON HALL
BLACKSBURG, VA 24061
P: 540-231-6635

PROJECT:
Concrete Diaphragm Test Setup

SHEET NOTES:
1. Scale is 1/2"=1'

REVISIONS:

NO.	DATE	BY
1	7/12/2021	RTS
2	7/14/2021	RTS

DESIGNED BY:
DRAWN BY: R. Stevens
CHECKED BY:
DATE: 7/2/2021
PROJECT NO.:

SHEET TITLE:
LOADING CHANNEL INSTALLATION

SHEET NO.: 5 of 12

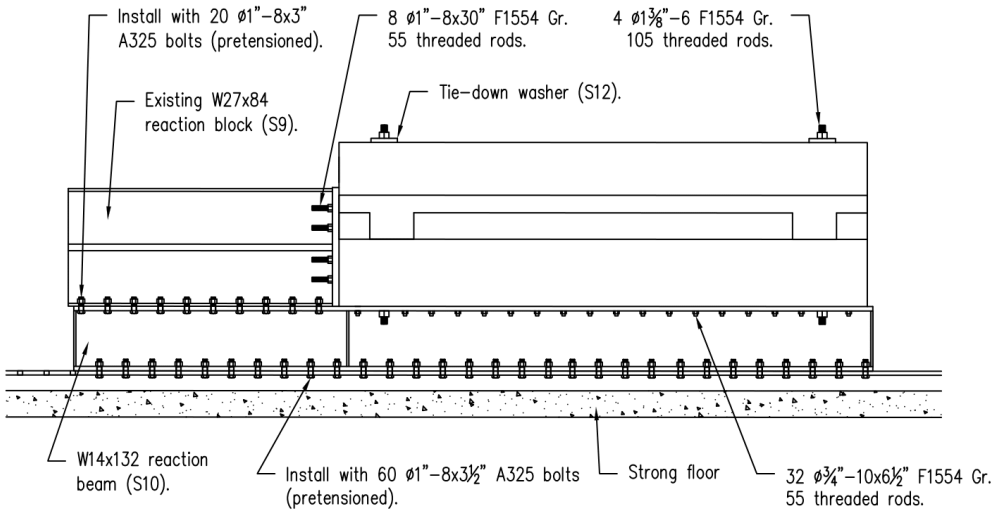

.\Masters\Auto Cad VT Logo.jpg

VIRGINIA TECH
CHARLES E. VIA JR. DEPARTMENT OF CIVIL & ENVIRONMENTAL ENGINEERING
200 PATTON HALL
BLACKSBURG, VA 24061
P: 540-231-6635

PROJECT:
Concrete Diaphragm Test Setup

SHEET NOTES:
1. Scale is 3/8"=1'

REVISIONS:

NO.	DATE	BY
1	7/8/2021	RTS
2	7/14/2021	RTS

DESIGNED BY:
DRAWN BY: R. Stevens
CHECKED BY:
DATE: 7/2/2021
PROJECT NO.:

SHEET TITLE:
REACTION ASSEMBLY

SHEET NO.: 6 of 12

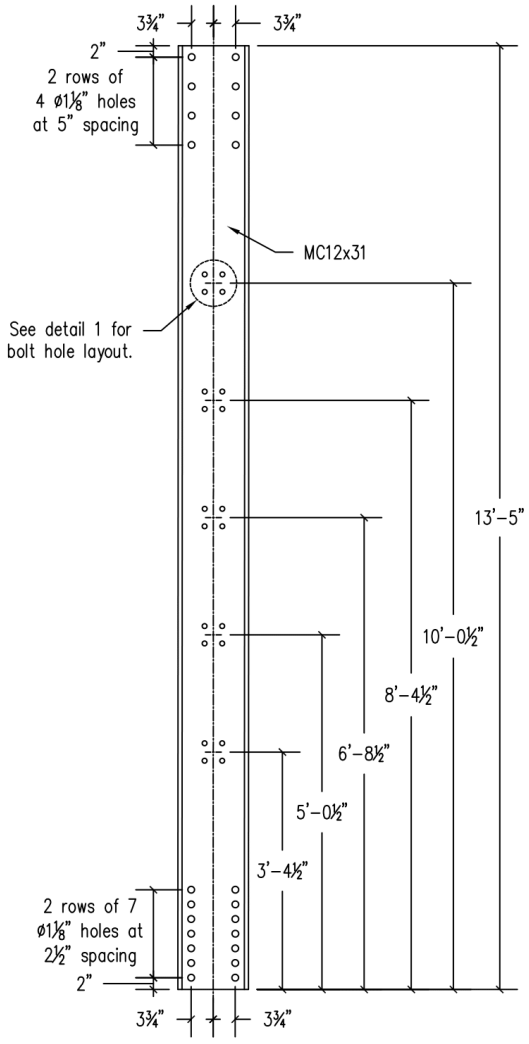

3 S7 LOADING CHANNEL (QTY: 2)
Scale:1/2"=1'

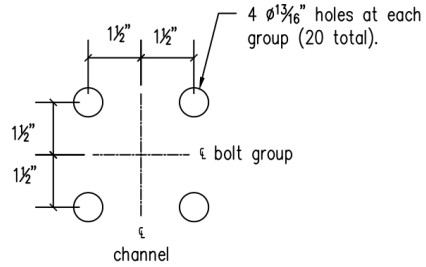

1 S7 HOLE LAYOUT
Scale: 3"=1'

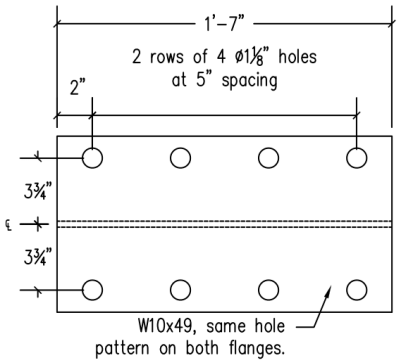

2 S7 SPACER BLOCK (QTY: 1)
Scale: 3"=2'

.\Masters\Auto Cad VT Logo.jpg

VIRGINIA TECH
CHARLES E. VIA JR. DEPARTMENT OF
CIVIL & ENVIRONMENTAL
ENGINEERING
200 PATTON HALL
BLACKSBURG, VA 24061
P: 540-231-6635

PROJECT:
Concrete Diaphragm Test Setup

SHEET NOTES:

REVISIONS:		
NO.	DATE	BY
1	7/14/2021	RTS

DESIGNED BY:
DRAWN BY: R. Stevens
CHECKED BY:
DATE: 7/1/2021
PROJECT NO.:

SHEET TITLE:
LOADING CHANNEL
AND SPACER BLOCK

SHEET NO.: 7 of 12

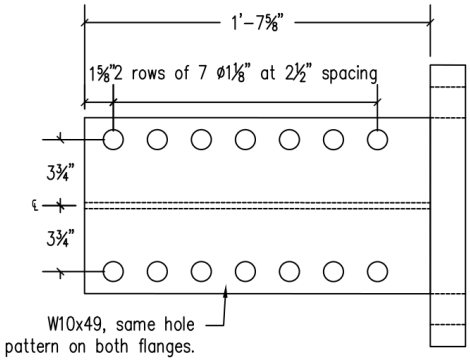

1 S8 LOADING BLOCK

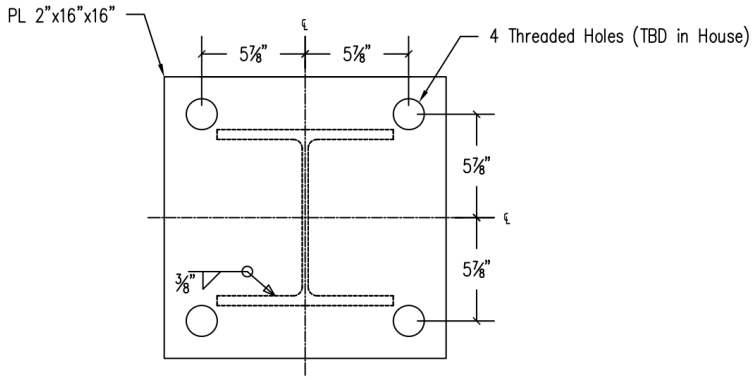

2 S8 END–PLATE

.\Masters\Auto Cad VT Logo.jpg

VIRGINIA TECH
CHARLES E. VIA JR. DEPARTMENT OF CIVIL & ENVIRONMENTAL ENGINEERING
200 PATTON HALL
BLACKSBURG, VA 24061
P: 540-231-6635

PROJECT:
Concrete Diaphragm Test Setup

SHEET NOTES:
1. Scale is 1 1/2"=1'
2. W10x49 is centered on the end-plate

REVISIONS:

NO.	DATE	BY
1	7/8/2021	RTS

DESIGNED BY:
DRAWN BY: R. Stevens
CHECKED BY:
DATE: 7/1/2021
PROJECT NO.:

SHEET TITLE:
LOADING BLOCK (QTY: 1)

SHEET NO.: 8 of 12

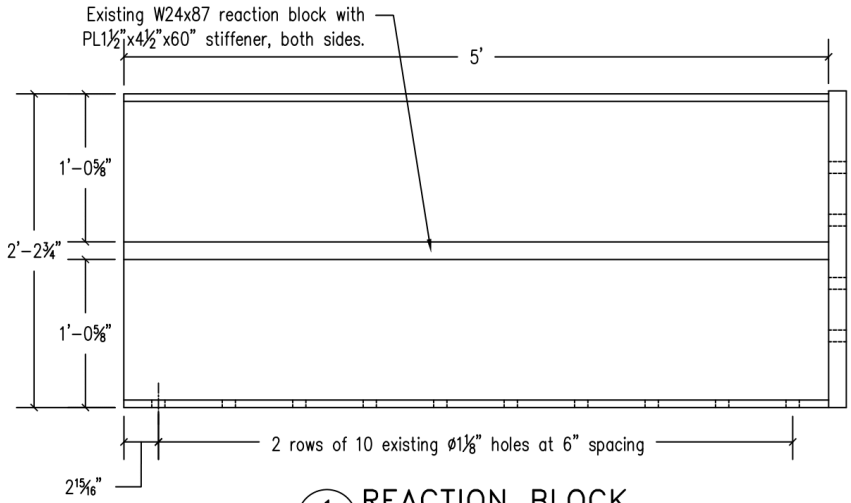

1 S9 REACTION BLOCK

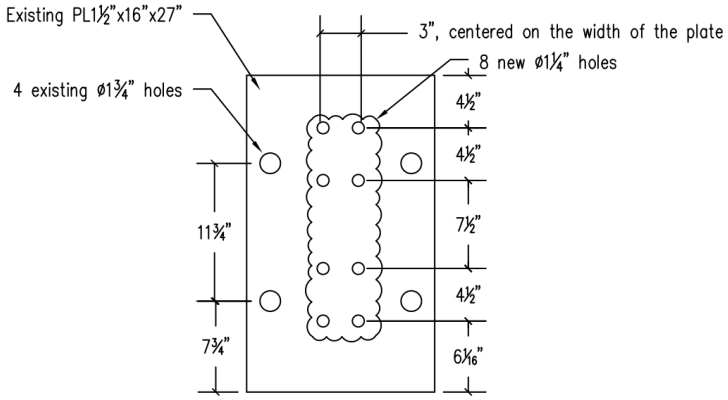

2 S9 NEW HOLE LAYOUT

.\Masters\Auto Cad VT Logo.jpg

VIRGINIA TECH
CHARLES E. VIA JR. DEPARTMENT OF CIVIL & ENVIRONMENTAL ENGINEERING
200 PATTON HALL
BLACKSBURG, VA 24061
P: 540-231-6635

PROJECT:
Concrete Diaphragm Test Setup

SHEET NOTES:
1. Scale is 1"=1'
2. Work to be done by VT

REVISIONS:		
NO.	DATE	BY
1	7/8/2021	RTS

DESIGNED BY:
DRAWN BY: R. Stevens
CHECKED BY:
DATE: 6/28/2021
PROJECT NO.:

SHEET TITLE:
END REACTION BLOCK (QTY: 2)

SHEET NO.: 9 of 12

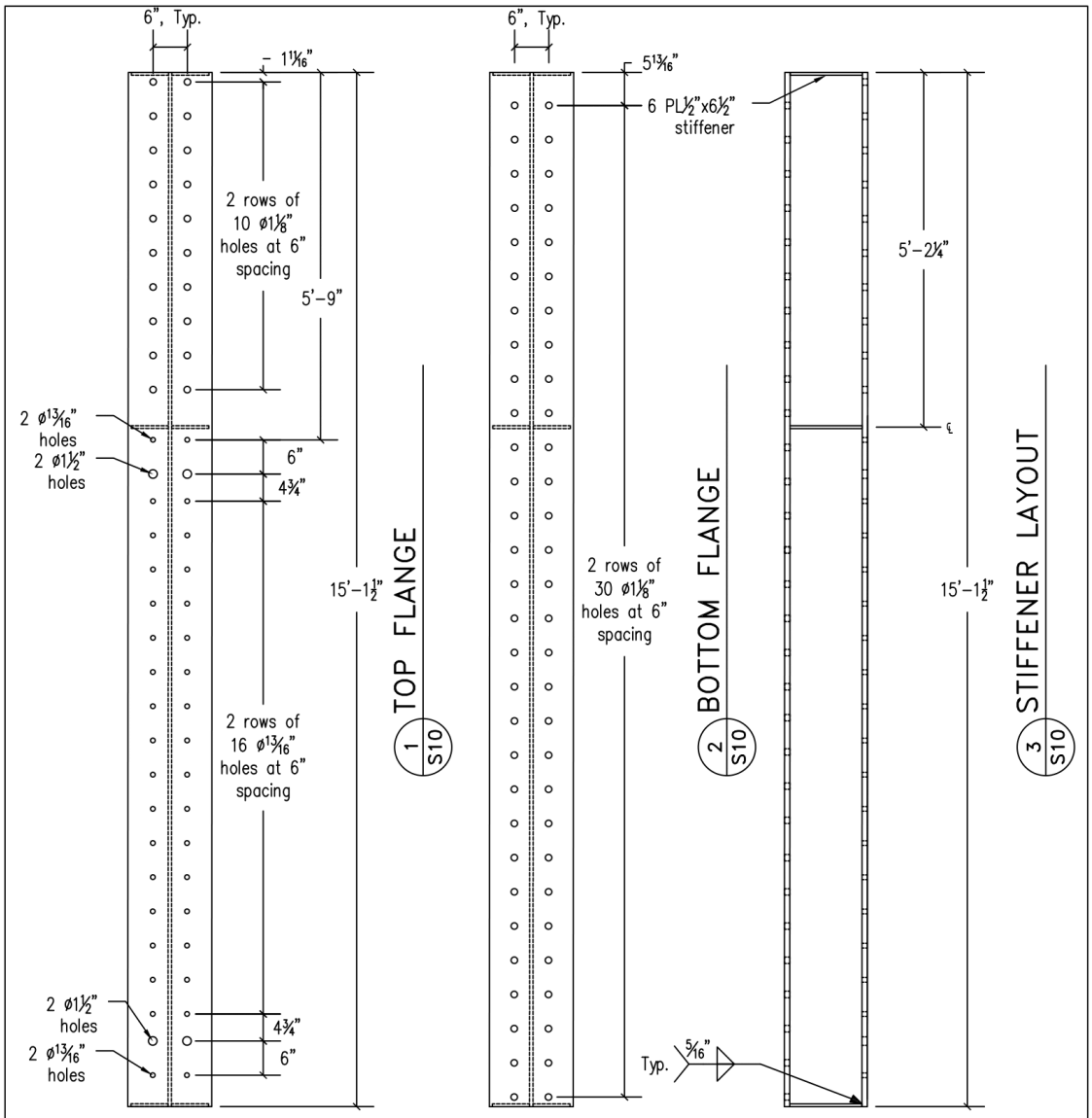

.\Masters\Auto Cad VT Logo.jpg

VIRGINIA TECH
CHARLES E. VIA JR. DEPARTMENT OF
CIVIL & ENVIRONMENTAL
ENGINEERING
200 PATTON HALL
BLACKSBURG, VA 24061
P: 540-231-6635

PROJECT:

Concrete Diaphragm Test Setup

SHEET NOTES:

1. Scale is 1/2"=1'
2. The two lines of bolts are centered across the flange width.

REVISIONS:

NO.	DATE	BY
1	7/8/2021	RTS

DESIGNED BY:
DRAWN BY: R. Stevens
CHECKED BY:
DATE: 7/1/2021
PROJECT NO.:

SHEET TITLE:

BEARING BEAM
(QTY: 2)

SHEET NO.: 10 of 12

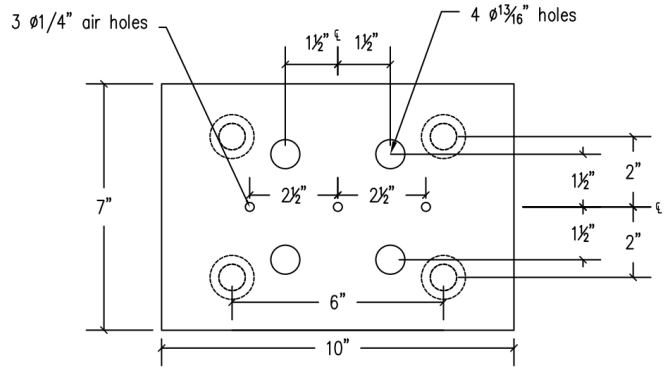

1 S11 BOLT HOLE LAYOUT

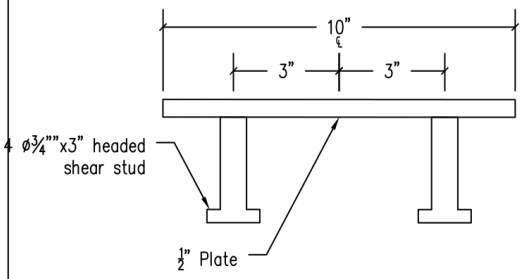

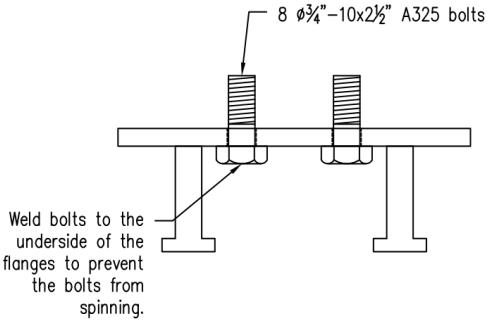

2 S11 SHEAR STUD LAYOUT

3 S11 BOLT INSTALLATION

.\Masters\Auto Cad VT Logo.jpg

VIRGINIA TECH
CHARLES E. VIA JR. DEPARTMENT OF CIVIL & ENVIRONMENTAL ENGINEERING
200 PATTON HALL
BLACKSBURG, VA 24061
P: 540-231-6635

PROJECT:
Concrete Diaphragm Test Setup

SHEET NOTES:
1. Scale is 3"=1'

REVISIONS:

NO.	DATE	BY
1	7/12/2021	RTS
2	7/14/2021	RTS

DESIGNED BY:
DRAWN BY: R. Stevens
CHECKED BY:
DATE: 7/2/2021
PROJECT NO.:

SHEET TITLE:
SHEAR TRANSFER ASSEMBLY
(QTY: 10 PER SPECIMEN)

SHEET NO.: 11 of 12

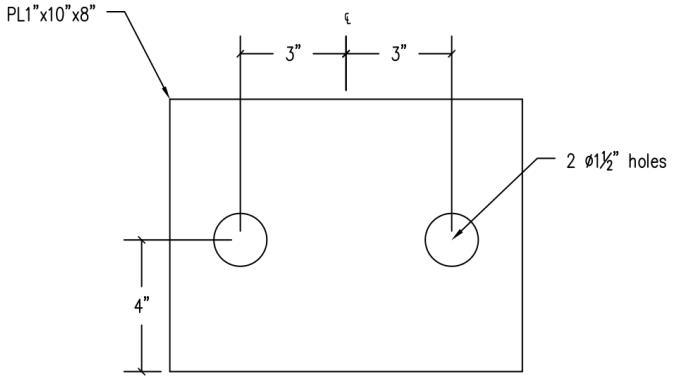

1/S12 HOLE LAYOUT

.\Masters\Auto Cad VT Logo.jpg

VIRGINIA TECH
CHARLES E. VIA JR. DEPARTMENT OF CIVIL & ENVIRONMENTAL ENGINEERING
200 PATTON HALL
BLACKSBURG, VA 24061
P: 540-231-6635

PROJECT:
Concrete Diaphragm Test Setup

SHEET NOTES:
1. Scale is 3"=1'

REVISIONS:

NO.	DATE	BY

DESIGNED BY:
DRAWN BY: R. Stevens
CHECKED BY:
DATE: 7/12/2021
PROJECT NO.:

SHEET TITLE:
TIE-DOWN WASHER (QTY: 2)

SHEET NO.: 12 of 12

Appendix B: Specimen Details for CD9 through CD14

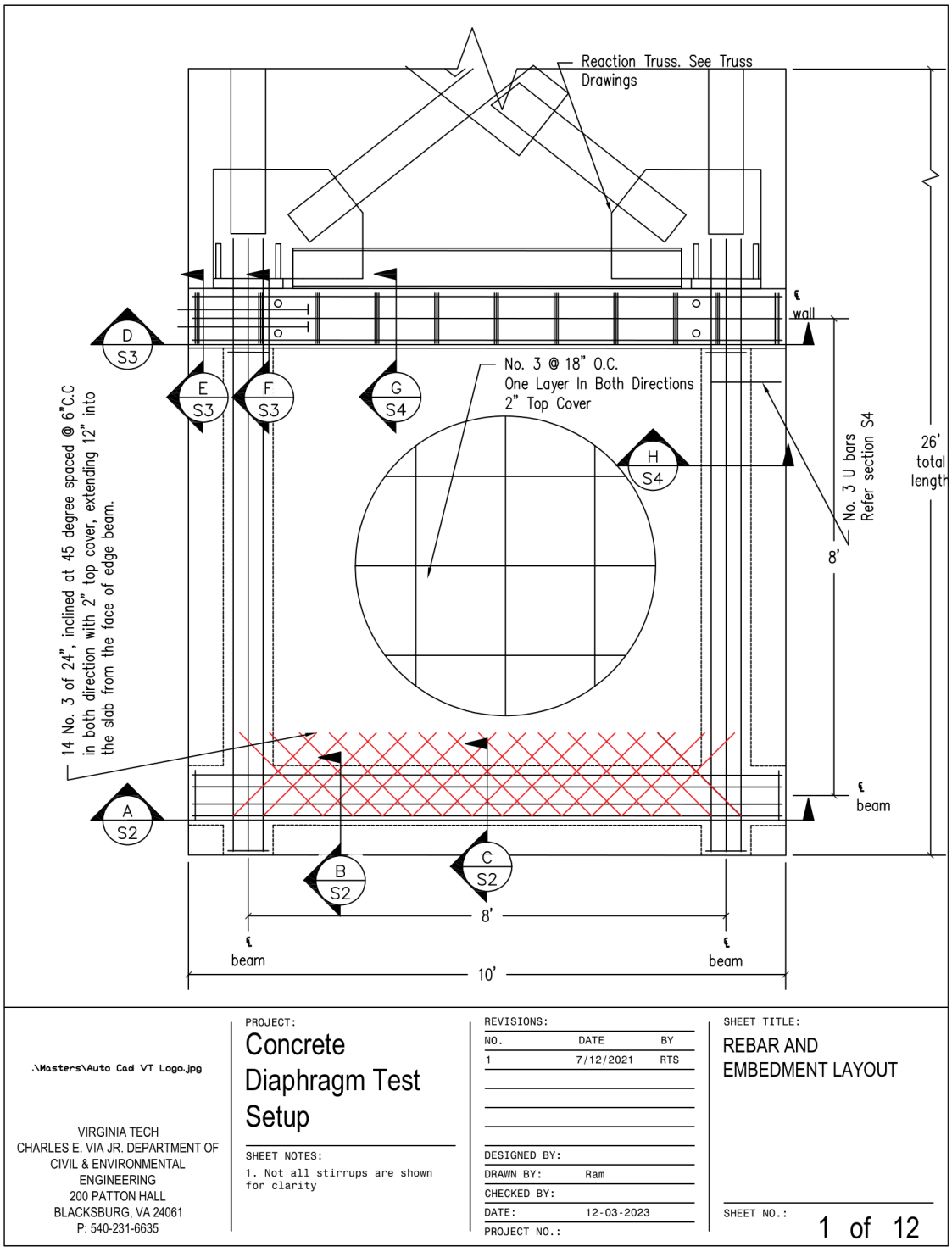

.\Masters\Auto Cad VT Logo.jpg

VIRGINIA TECH
CHARLES E. VIA JR. DEPARTMENT OF CIVIL & ENVIRONMENTAL ENGINEERING
200 PATTON HALL
BLACKSBURG, VA 24061
P: 540-231-6635

PROJECT:
Concrete Diaphragm Test Setup

SHEET NOTES:
1. Not all stirrups are shown for clarity

REVISIONS:

NO.	DATE	BY
1	7/12/2021	RTS

DESIGNED BY:
DRAWN BY: Ram
CHECKED BY:
DATE: 12-03-2023
PROJECT NO.:

SHEET TITLE:
REBAR AND EMBEDMENT LAYOUT

SHEET NO.: 1 of 12

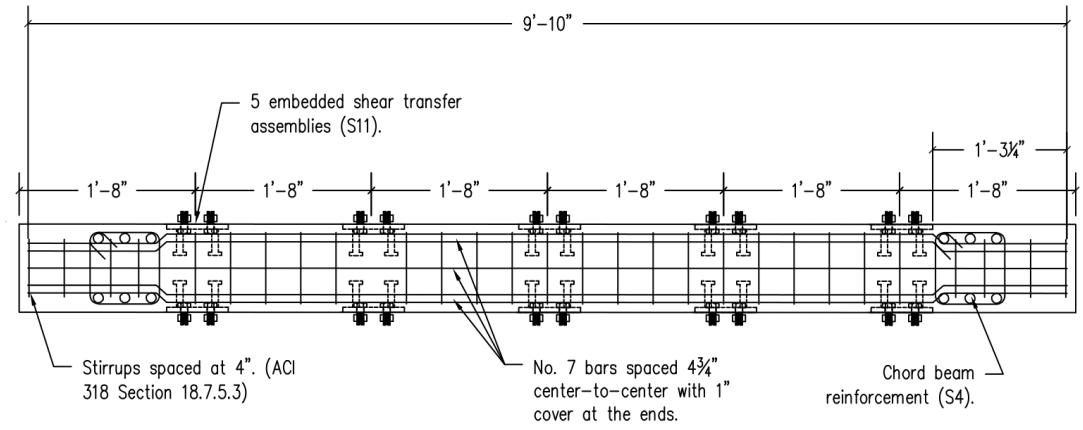

A S2 EDGE BEAM REBAR
Scale:3/4"=1'

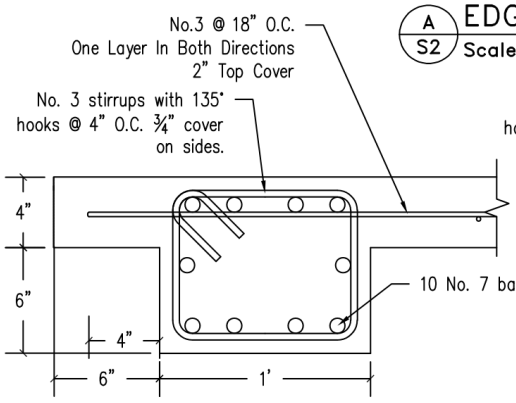

B S2 EDGE BEAM REBAR
Scale: 3"=2'

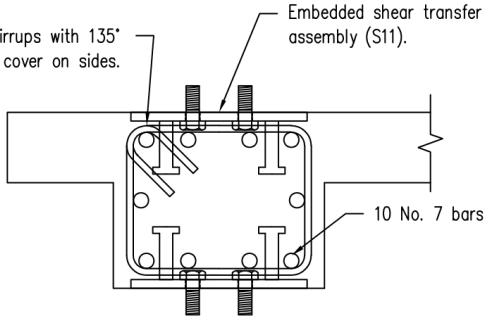

C S2 EDGE BEAM REBAR
Scale: 3"=2'

.\Masters\Auto Cad VT Logo.jpg

VIRGINIA TECH
CHARLES E. VIA JR. DEPARTMENT OF CIVIL & ENVIRONMENTAL ENGINEERING
200 PATTON HALL
BLACKSBURG, VA 24061
P: 540-231-6635

PROJECT:
Concrete Diaphragm Test Setup

SHEET NOTES:

REVISIONS:

NO.	DATE	BY
1	7/12/2021	RTS
2	7/14/2021	RTS

DESIGNED BY:
DRAWN BY: R. Stevens
CHECKED BY:
DATE: 7/1/2021
PROJECT NO.:

SHEET TITLE:
SECTION VIEWS

SHEET NO.: 2 of 12

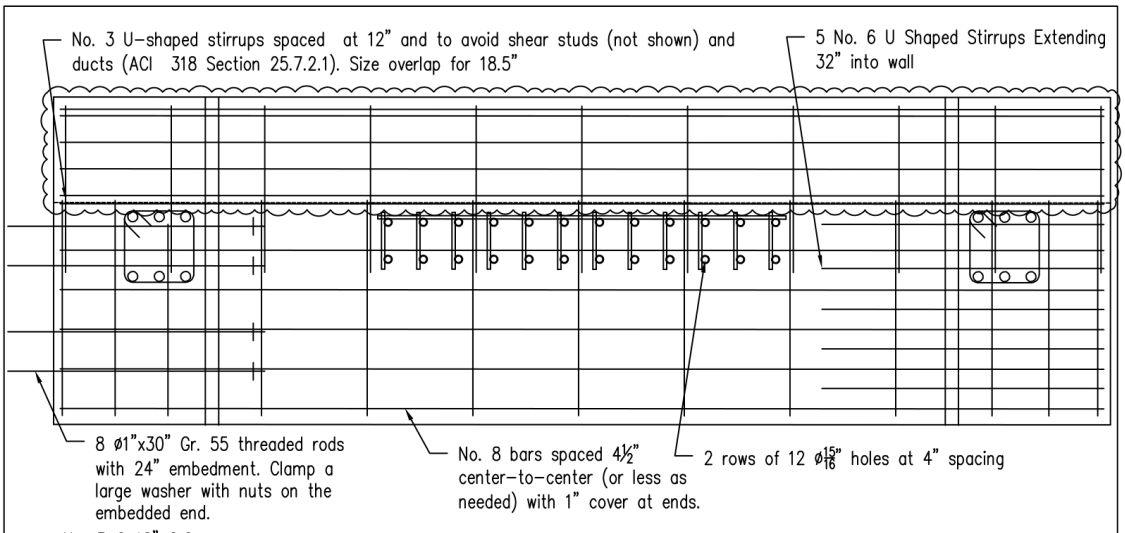

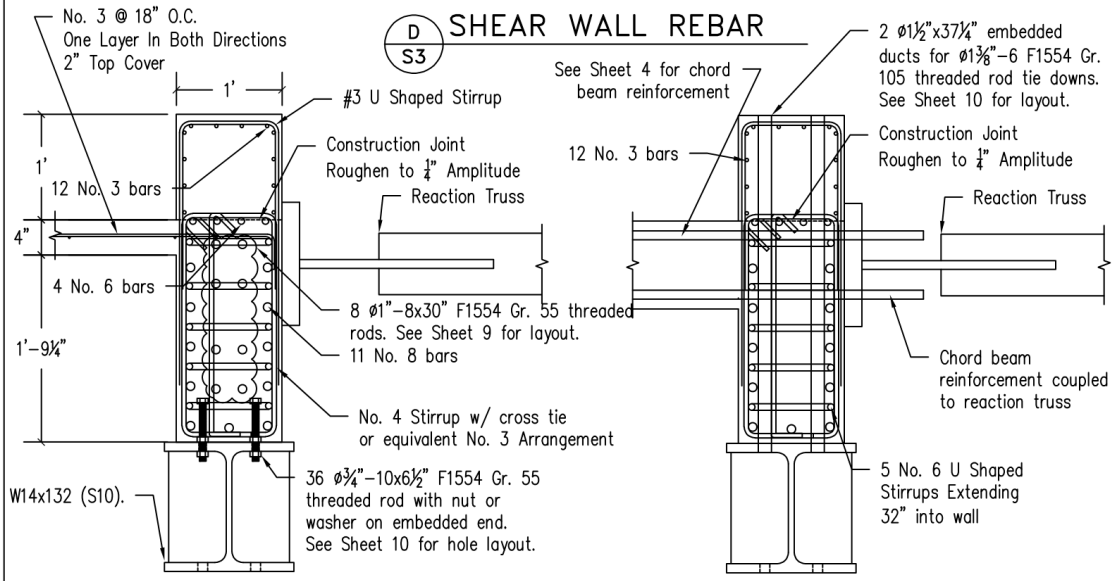

D S3 SHEAR WALL REBAR

E S3 SHEAR WALL REBAR

F S3 SHEAR WALL REBAR

.\Masters\Auto Cad VT Logo.jpg

VIRGINIA TECH
CHARLES E. VIA JR. DEPARTMENT OF CIVIL & ENVIRONMENTAL ENGINEERING
200 PATTON HALL
BLACKSBURG, VA 24061
P: 540-231-6635

PROJECT:
Concrete Diaphragm Test Setup

SHEET NOTES:
1. Scale is 3/4"=1'

REVISIONS:

NO.	DATE	BY
1	7/8/2021	RTS
2	7/14/2021	RTS

DESIGNED BY:
DRAWN BY: R. Stevens
CHECKED BY:
DATE: 7/1/2021
PROJECT NO.:

SHEET TITLE:
SECTION VIEWS

SHEET NO.: 3 of 12

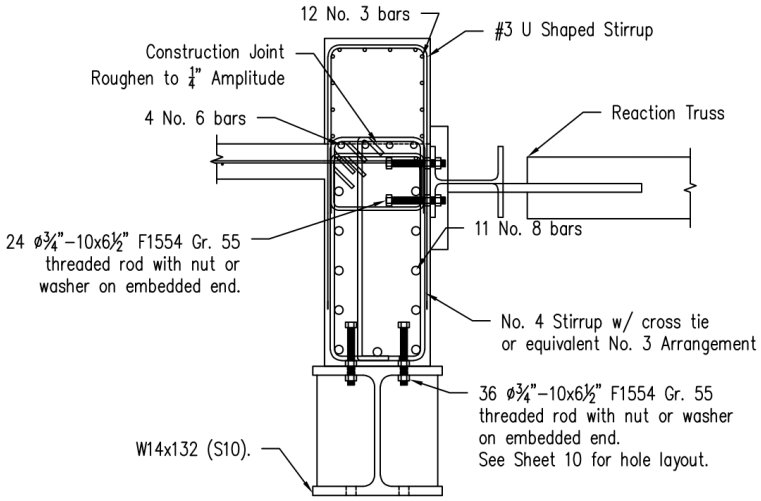

G/S4 SHEAR WALL REBAR
Scale:3/4"=1'

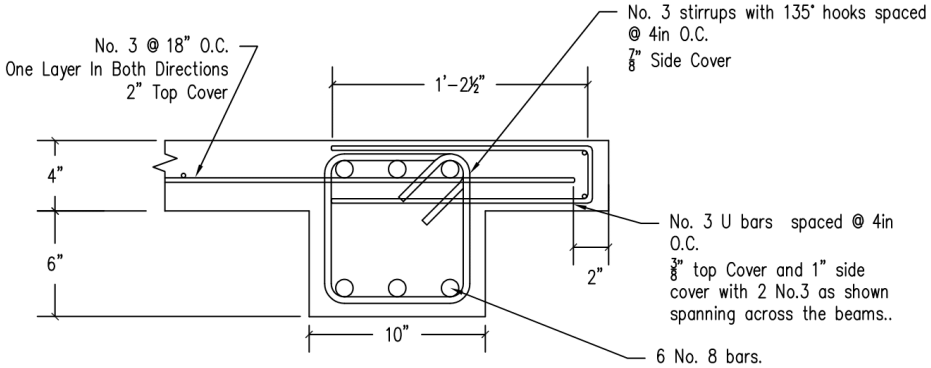

H/S4 CHORD BEAM REBAR
Scale: 3"=2'

.\Masters\Auto Cad VT Logo.jpg

VIRGINIA TECH
CHARLES E. VIA JR. DEPARTMENT OF
CIVIL & ENVIRONMENTAL
ENGINEERING
200 PATTON HALL
BLACKSBURG, VA 24061
P: 540-231-6635

PROJECT:
Concrete Diaphragm Test Setup

SHEET NOTES:

REVISIONS:

NO.	DATE	BY
1	7/8/2021	RTS
2	7/14/2021	RTS

DESIGNED BY:
DRAWN BY: R. Stevens
CHECKED BY:
DATE: 7/2/2021
PROJECT NO.:

SHEET TITLE:
SECTION VIEWS

SHEET NO.: 4 of 12

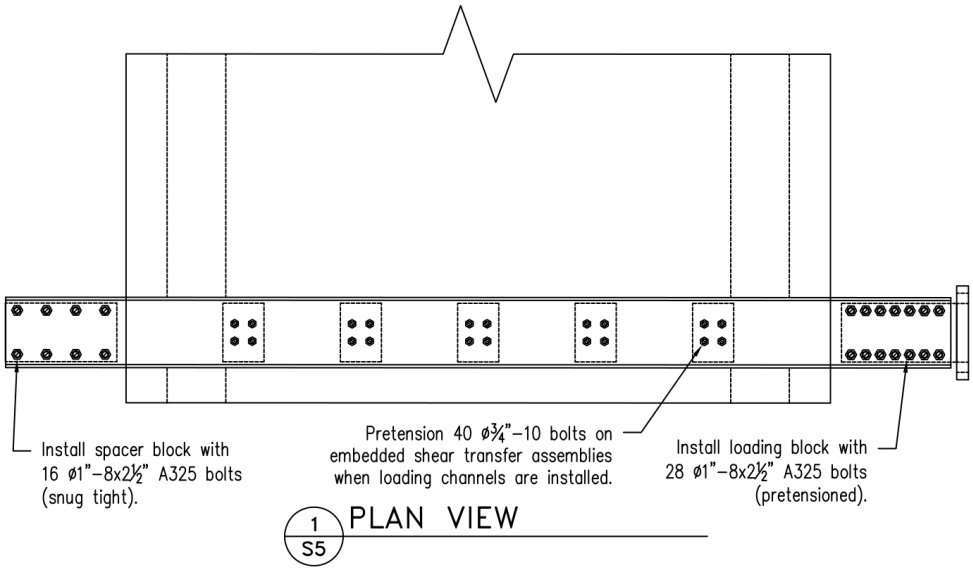

1/S5 PLAN VIEW

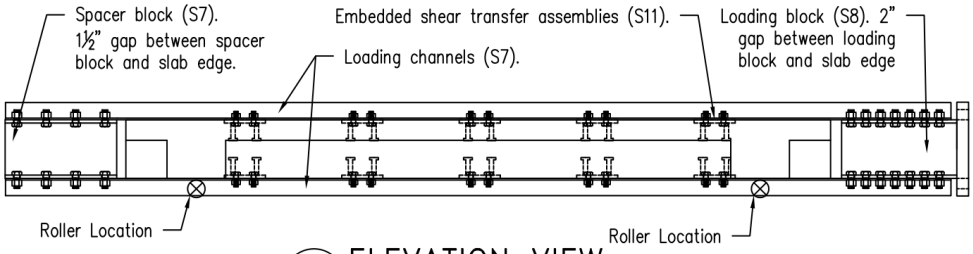

2/S5 ELEVATION VIEW

VIRGINIA TECH

VIRGINIA TECH
CHARLES E. VIA JR. DEPARTMENT OF
CIVIL & ENVIRONMENTAL
ENGINEERING
200 PATTON HALL
BLACKSBURG, VA 24061
P: 540-231-6635

PROJECT:
Concrete Diaphragm Test Setup

SHEET NOTES:
1. Scale is 1/2"=1'

REVISIONS:

NO.	DATE	BY
1	7/12/2021	RTS
2	7/14/2021	RTS

DESIGNED BY:
DRAWN BY: R. Stevens
CHECKED BY:
DATE: 7/2/2021
PROJECT NO.:

SHEET TITLE:
LOADING CHANNEL INSTALLATION

SHEET NO.: 5 of 12

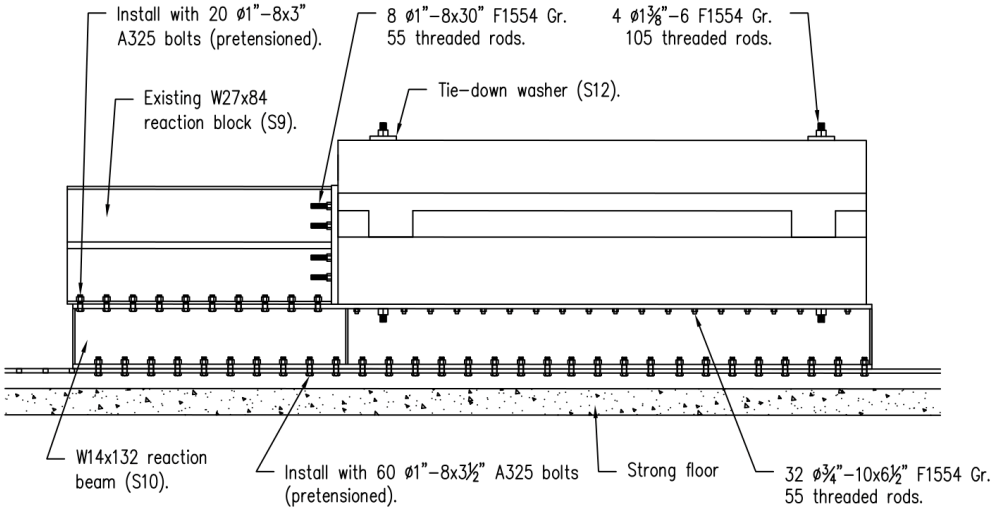

VIRGINIA TECH

VIRGINIA TECH
CHARLES E. VIA JR. DEPARTMENT OF CIVIL & ENVIRONMENTAL ENGINEERING
200 PATTON HALL
BLACKSBURG, VA 24061
P: 540-231-6635

PROJECT:
Concrete Diaphragm Test Setup

SHEET NOTES:
1. Scale is 3/8"=1'

REVISIONS:

NO.	DATE	BY
1	7/8/2021	RTS
2	7/14/2021	RTS

DESIGNED BY:
DRAWN BY: R. Stevens
CHECKED BY:
DATE: 7/2/2021
PROJECT NO.:

SHEET TITLE:
REACTION ASSEMBLY

SHEET NO.: 6 of 12

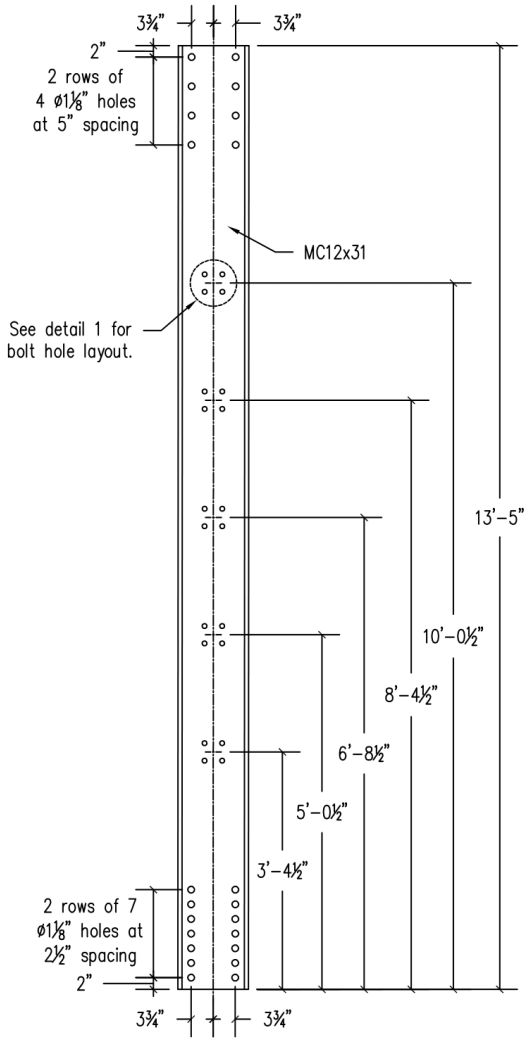

3 S7 LOADING CHANNEL (QTY: 2)
Scale:1/2"=1'

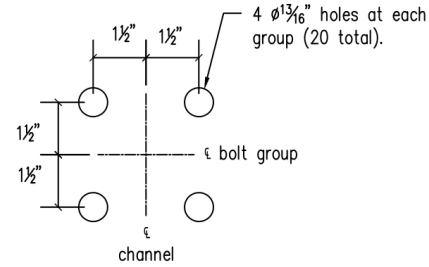

1 S7 HOLE LAYOUT
Scale: 3"=1'

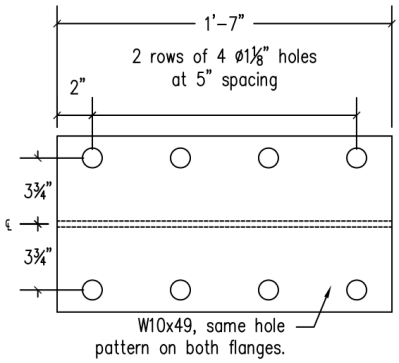

2 S7 SPACER BLOCK (QTY: 1)
Scale: 3"=2'

VIRGINIA TECH

VIRGINIA TECH
CHARLES E. VIA JR. DEPARTMENT OF CIVIL & ENVIRONMENTAL ENGINEERING
200 PATTON HALL
BLACKSBURG, VA 24061
P: 540-231-6635

PROJECT:
Concrete Diaphragm Test Setup

SHEET NOTES:

REVISIONS:

NO.	DATE	BY
1	7/14/2021	RTS

DESIGNED BY:
DRAWN BY: R. Stevens
CHECKED BY:
DATE: 7/1/2021
PROJECT NO.:

SHEET TITLE:
LOADING CHANNEL AND SPACER BLOCK

SHEET NO.: 7 of 12

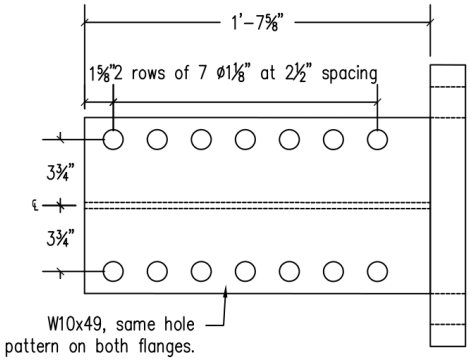

1 S8 LOADING BLOCK

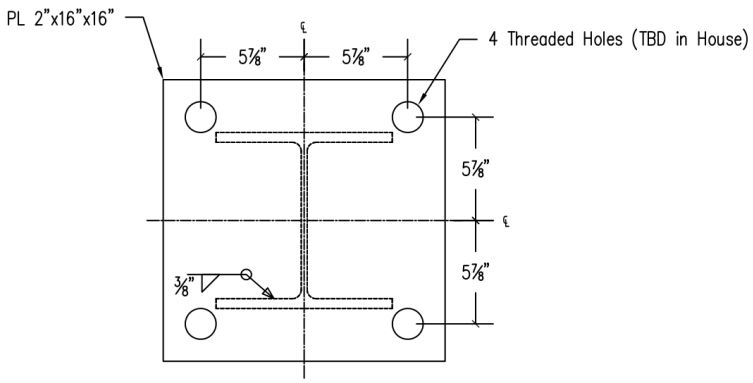

2 S8 END–PLATE

VIRGINIA TECH

VIRGINIA TECH
CHARLES E. VIA JR. DEPARTMENT OF CIVIL & ENVIRONMENTAL ENGINEERING
200 PATTON HALL
BLACKSBURG, VA 24061
P: 540-231-6635

PROJECT:
Concrete Diaphragm Test Setup

SHEET NOTES:
1. Scale is 1 1/2"=1'
2. W10x49 is centered on the end-plate

REVISIONS:

NO.	DATE	BY
1	7/8/2021	RTS

DESIGNED BY:
DRAWN BY: R. Stevens
CHECKED BY:
DATE: 7/1/2021
PROJECT NO.:

SHEET TITLE:
LOADING BLOCK (QTY: 1)

SHEET NO.: 8 of 12

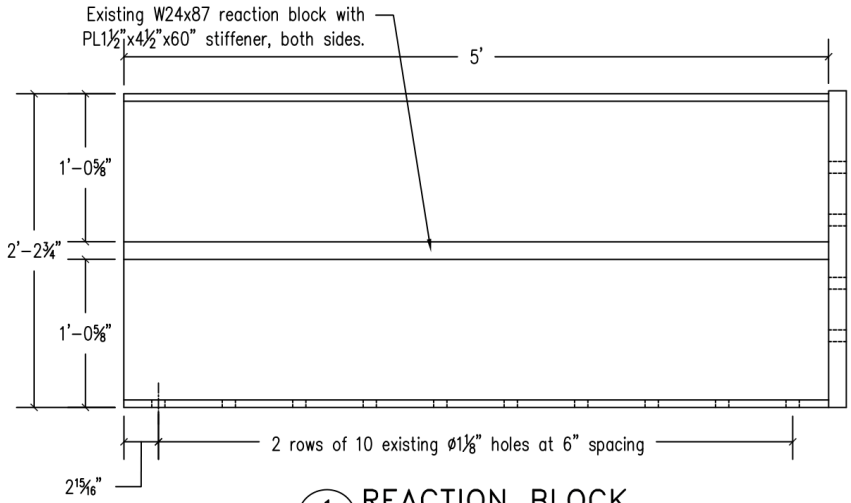

1 S9 REACTION BLOCK

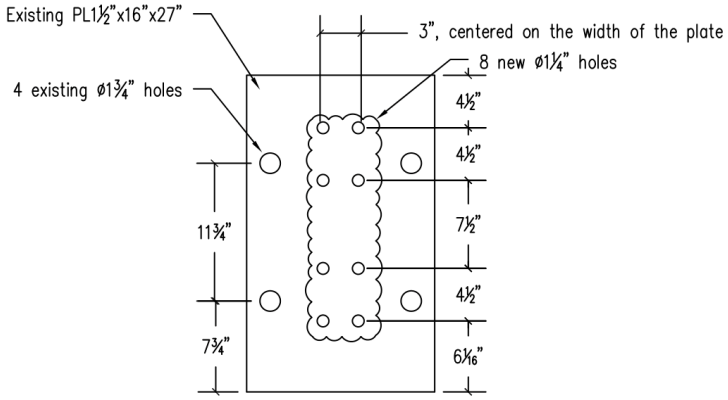

2 S9 NEW HOLE LAYOUT

VIRGINIA TECH

VIRGINIA TECH
CHARLES E. VIA JR. DEPARTMENT OF CIVIL & ENVIRONMENTAL ENGINEERING
200 PATTON HALL
BLACKSBURG, VA 24061
P: 540-231-6635

PROJECT:
Concrete Diaphragm Test Setup

SHEET NOTES:
1. Scale is 1"=1'
2. Work to be done by VT

REVISIONS:		
NO.	DATE	BY
1	7/8/2021	RTS

DESIGNED BY:
DRAWN BY: R. Stevens
CHECKED BY:
DATE: 6/28/2021
PROJECT NO.:

SHEET TITLE:
END REACTION BLOCK (QTY: 2)

SHEET NO.: 9 of 12

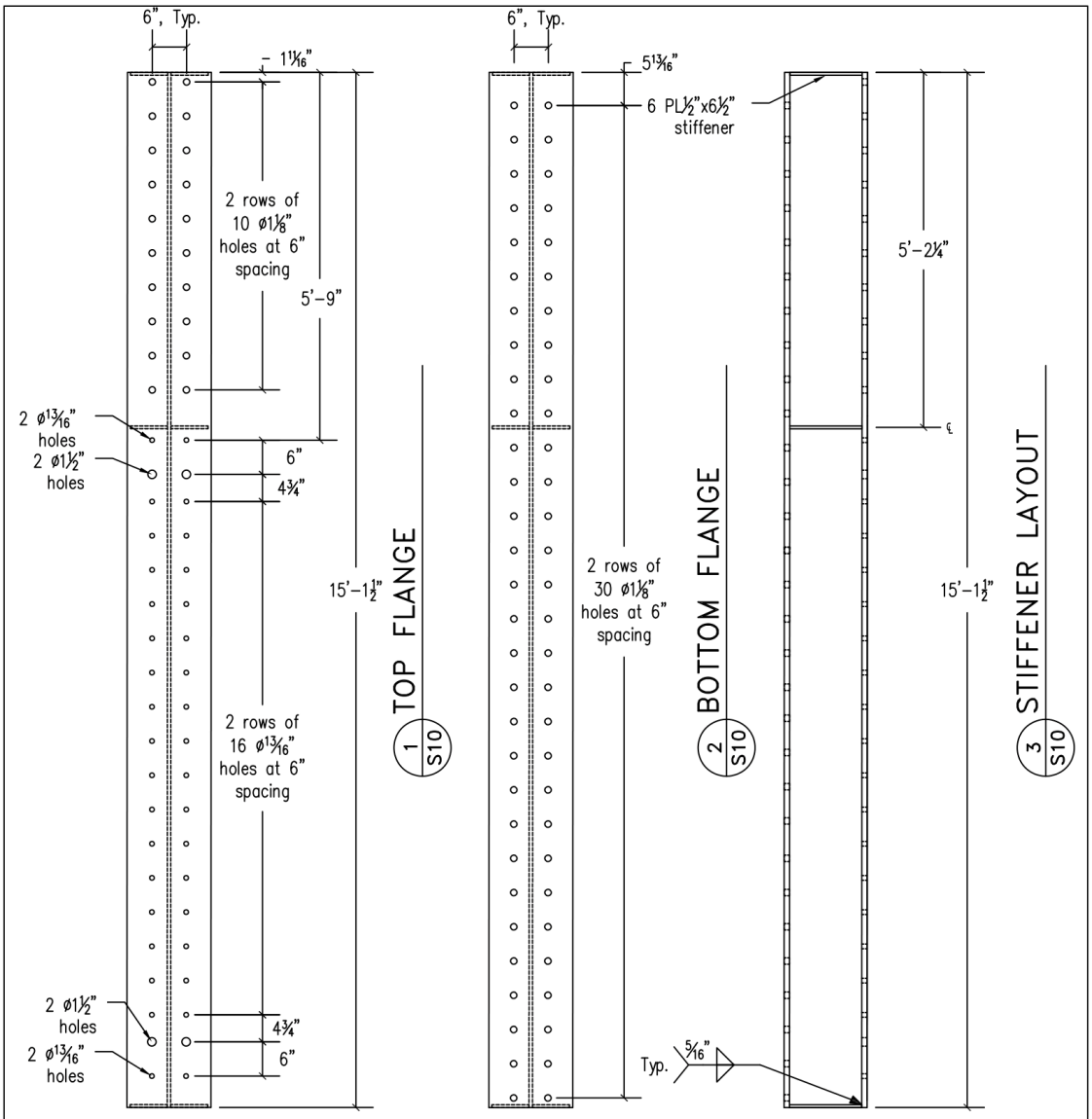

VIRGINIA TECH

VIRGINIA TECH
CHARLES E. VIA JR. DEPARTMENT OF
CIVIL & ENVIRONMENTAL
ENGINEERING
200 PATTON HALL
BLACKSBURG, VA 24061
P: 540-231-6635

PROJECT:

Concrete Diaphragm Test Setup

SHEET NOTES:

1. Scale is 1/2"=1'
2. The two lines of bolts are centered across the flange width.

REVISIONS:

NO.	DATE	BY
1	7/8/2021	RTS

DESIGNED BY:
DRAWN BY: R. Stevens
CHECKED BY:
DATE: 7/1/2021
PROJECT NO.:

SHEET TITLE:

BEARING BEAM
(QTY: 2)

SHEET NO.: 10 of 12

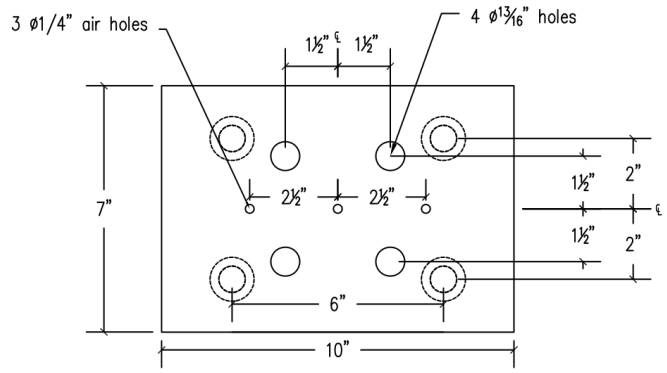

1 S11 BOLT HOLE LAYOUT

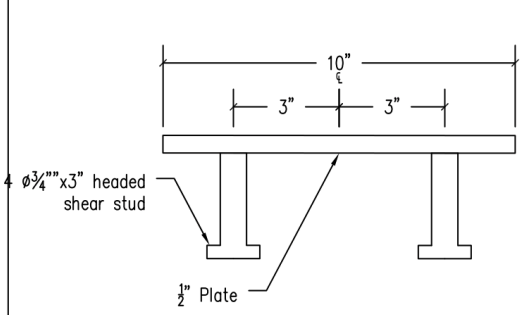

2 S11 SHEAR STUD LAYOUT

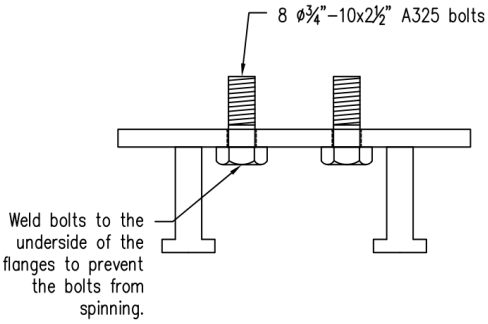

3 S11 BOLT INSTALLATION

VIRGINIA TECH
CHARLES E. VIA JR. DEPARTMENT OF CIVIL & ENVIRONMENTAL ENGINEERING
200 PATTON HALL
BLACKSBURG, VA 24061
P: 540-231-6635

PROJECT:
Concrete Diaphragm Test Setup

SHEET NOTES:
1. Scale is 3"=1'

REVISIONS:

NO.	DATE	BY
1	7/12/2021	RTS
2	7/14/2021	RTS

DESIGNED BY:
DRAWN BY: R. Stevens
CHECKED BY:
DATE: 7/2/2021
PROJECT NO.:

SHEET TITLE:
SHEAR TRANSFER ASSEMBLY (QTY: 10 PER SPECIMEN)

SHEET NO.: 11 of 12

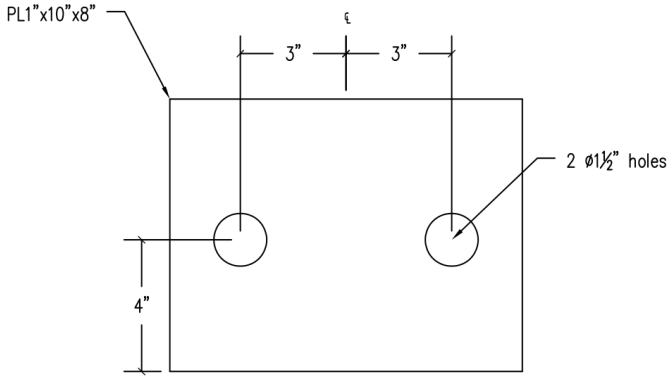

1/S12 HOLE LAYOUT

VIRGINIA TECH
CHARLES E. VIA JR. DEPARTMENT OF CIVIL & ENVIRONMENTAL ENGINEERING
200 PATTON HALL
BLACKSBURG, VA 24061
P: 540-231-6635

PROJECT:
Concrete Diaphragm Test Setup

SHEET NOTES:
1. Scale is 3"=1'

REVISIONS:

NO.	DATE	BY

DESIGNED BY:
DRAWN BY: R. Stevens
CHECKED BY:
DATE: 7/12/2021
PROJECT NO.:

SHEET TITLE:
TIE-DOWN WASHER (QTY: 2)

SHEET NO.: 12 of 12

Appendix C: FRP Technical Data Sheets

Smarter Strengthening Solutions™

CSS V-Wrap™ C100HM

High-Modulus Code-Listed Unidirectional Carbon Fabric

SIMPSON Strong-Tie | structural TECHNOLOGIES

DESCRIPTION

CSS V-Wrap C100HM is a high-modulus unidirectional carbon fiber fabric with fibers oriented in the 0° direction. The CSS V-Wrap C100HM system is field laminated using a two-part 100% solids and high-strength CSS V-Wrap-approved structural adhesives to form a carbon fiber reinforced polymer (CFRP) system used to reinforce and strengthen structural elements.

CODE REPORTS AND COMPLIANCE

ICC ES **ICC-ES ESR-4930**

MATERIAL PROPERTIES

Typical Data

Storage Conditions	Store dry at 40°F – 90°F (4°C – 32°C)
Color	Black
Primary Fiber Direction	0° (unidirectional)
Weight	9.7 oz./yd.² (330 g/m²)
Shelf Life	10 years

Dry Fiber Properties	
Tensile Strength	790,000 psi (5,440 MPa)
Tensile Modulus	42 x 10^6 psi (289,550 MPa)
Elongation at Break	1.9%

Cured Laminate Properties	Average Values	Design Values*
Tensile Strength	216,000 psi (1,490 MPa)	165,000 psi (1,138 MPa)
Modulus of Elasticity	16.7 x 10^6 psi (115,100 MPa)	15 x 10^6 psi (103,400 MPa)
Elongation at Break	1.3%	1.1%
Thickness	0.02 in. (0.51 mm)	0.02 in. (0.51 mm)
Strength per Unit Width	4,320 lb./in. (0.76 kN/mm)	3,300 lb./in. (0.58 kN/mm)

*Design properties are based on ACI 440.2R using average minus three standard deviations.

MADE IN USA with GLOBAL MATERIALS

PERFORMANCE FEATURES

- ICC-ES ESR-4930 listed product
- UL Listed (ul.com/database)
- NSF/ANSI Standard 61 listed product for drinking water systems
- 0% VOC
- 100% solvent-free
- Non-corrosive reinforcement system
- Lightweight flexible fabric can be wrapped around complex shapes
- Used for shear, confinement or flexural strengthening
- High strength and high modulus
- Lightweight
- Reduces crack width
- Low aesthetic impact

APPLICATIONS

CSS V-Wrap fabrics can be used to resolve strength deficiencies and increase the load-carrying capacity of buildings, bridges, silos, chimneys and other structures.

- Load increases
- Seismic strengthening
- Repair structural elements
- Change in structural system
- Design or construction defects

PACKAGING

Roll Size (Width x Length)	Model No.
24 in. x 150 ft. / 50 yd. (610 mm x 45.7 m)	CV-C100HM24-50

HOW TO USE

Design
Design should comply with ACI 440.2R or another recognized design/specification entity and is typically based on CFRP contribution determined by detailed analysis. Design values will vary based on project requirements and applicable environmental and strength reduction factors. Contact STRUCTURAL TECHNOLOGIES at (410) 859-6502 to determine applicable design factors.

Surface Preparation
Surfaces to receive CSS V-Wrap C100HM must be clean and sound. They must be dry and free of frost. All dust, laitance, grease, curing compounds, waxes, deteriorated materials and other bond-inhibiting materials must be removed from the surface prior to application. Existing uneven surfaces must be filled with appropriate epoxy putty or repair mortar. Use abrasive blasting, pressure washing, shotblasting, grinding or other approved mechanical means to achieve an open-pore texture with a concrete surface profile of not less than CSP-3 (ICRI). In certain applications and at the engineer's discretion, the bond between the substrate and the fabric may be determined to be non-critical (such as in column confinement applications). All corners must be rounded to ½" radius minimum. The adhesive bond strength of the concrete may be verified after surface preparation by random pull-off testing (ASTM C1583) at the discretion of the engineer. Minimum tensile strength of 200 psi must be achieved for concrete.

Handling
Approved personal protection equipment should be worn at all times. Particle mask is recommended for possible airborne particles. Gloves are recommended when handling fabrics and resins to avoid skin irritation. Safety glasses are recommended to prevent eye irritation. Wear chemical-resistant clothing/gloves/goggles. Ventilate area. In absence of adequate ventilation, use a properly fitted NIOSH respirator.

Cutting
Fabric can be cut to appropriate length by using commercial quality heavy-duty scissors.

Application
Installation of the CSS V-Wrap strengthening system should be performed only by a specially trained, approved contractor. The CSS V-Wrap strengthening system shall consist of CSS V-Wrap carbon fabric and CSS V-Wrap 770 epoxy.

Note the specified number of plies, ply widths and fiber orientation. Mix resin components using recommended procedures on product datasheet. Apply one coat of CSS V-Wrap 770 epoxyy as a primer to the surface using a nap roller. Fill minor concrete defects such as bug holes and other imperfections using CSS V-Wrap 770 epoxy mixed with fumed silica (thickened epoxy) or CSS V-Wrap PF putty filler. Apply thickened epoxy or putty using a trowel. Adjust the gap between saturator rollers to approximately 42 mils. Using a saturator machine, pre-saturate the appropriate length of CSS V-Wrap fabric with CSS V-Wrap 770 epoxy as a saturant. Install the saturated CSS V-Wrap fabric. Use a rib roller to remove all air pockets and ensure intimate contact with the surface. If a splice is needed, a minimum 6" overlap is required to achieve continuity. On multiple plies with splices, stagger the splice locations. If required, apply topcoat material.

Limitations
- Design calculations must be approved by a licensed professional engineer.
- System is a vapor barrier.
- Concrete deterioration and steel corrosion must be resolved prior to application.
- Minimum application temperature is 40°F.

Storage
Store material in a cool, dark space. Low humidity is recommended.

CAUTION

Protective Measures: The use of safety glasses and chemically-resistant gloves is recommended. Use appropriate clothing to minimize skin contact. The use of a NIOSH-approved respirator is required to protect respiratory tract when ventilation is not adequate to limit exposure below the PEL. Refer to Safety Data Sheets (SDS) available at **strongtie.com/sds** for detailed information.

FIRST AID

Skin: Wash fibers off skin with water and soap. If fibers are embedded in the skin, remove with tweezers. Discard clothing that may contain embedded fibers. Seek medical advice if exposure results in adverse effects.

Eyes: Immediately flush with a continuous water stream for at least 20 minutes. Washing immediately after exposure is expected to be effective in preventing damage to the eyes. Seek medical advice.

Inhalation: If there is inhalation exposure to the fibers of this product, remove source of exposure and move affected person to fresh air. If not breathing, give artificial respiration. If there is breathing difficulty, give oxygen. Seek medical advice for any respiratory problems.

Ingestion: Not expected to occur since ingestion is not a likely route of exposure for this product. If ingestion does occur, DO NOT INDUCE VOMITING. Nothing by mouth if unconscious. Seek medical advice.

CLEAN-UP

Environmental Precautions

Spill/Release and Cleanup Procedures: In case of spill, collect (e.g., sweep up, vacuum, etc.) spilled material and either reuse or dispose of properly. Chopped or milled carbon fibers may be slippery if spilled, posing an accident risk. Wear personal protective equipment as described in the SDS during cleanup activities.

LIMITED WARRANTY

This product is covered by the Simpson Strong-Tie RPS Product Limited Warranty, which is available at **strongtie.com/limited-warranties** or by calling Simpson Strong-Tie at (800) 999-5099.

Smarter Strengthening Solutions™

CSS V-Wrap™ C220HM

High-Modulus, Code-Listed Unidirectional Carbon Fabric

DESCRIPTION

CSS V-Wrap C220HM is a high-modulus, unidirectional carbon-fiber fabric with fibers oriented in the 0° direction. The CSS V-Wrap C220HM system is field laminated using a two-part, 100%-solids high-strength CSS V-Wrap-approved structural adhesive to form a carbon-fiber-reinforced polymer (CFRP) system for the reinforcement and strengthening of structural elements..

CODE REPORTS AND COMPLIANCE

ICC-ES ESR-4930

MATERIAL PROPERTIES

Typical Data

Storage Conditions	Store dry at 40°F–90°F (4°C–32°C)
Color	Black
Primary Fiber Direction	0° (unidirectional)
Weight	22 oz./yd.^{2} (740 g/m^2)
Shelf Life	10 years

Dry Fiber Properties	
Tensile Strength	670,000 psi (4,600 MPa)
Tensile Modulus	37 x 10^6 psi (260,000 MPa)
Elongation at Break	1.65%

Cured Laminate Properties	Average Values	Design Values*
Tensile Strength	152,000 psi (1,050 MPa)	128,000 psi (880 MPa)
Modulus of Elasticity	14.7 x 10^6 psi (101,300 MPa)	14.2 x 10^6 psi (98,000 MPa)
Elongation at Break	1.05%	0.9%
Thickness	0.04 in. (1.0 mm)	0.04 in. (1.0 mm)
Strength per Unit Width	6,080 lb./in. (1.06 kN/mm)	5,120 lb./in. (0.9 kN/mm)

*Design properties are based on ACI 440.2R using average minus three standard deviations.

MADE IN USA with GLOBAL MATERIALS

PERFORMANCE FEATURES

- ICC-ES ESR-4930 listed product
- 0% VOC
- 100% solvent free
- Noncorrosive reinforcement system
- Lightweight flexible fabric can be wrapped around complex shapes
- Used for shear, confinement or flexural strengthening
- High strength and high modulus
- Lightweight
- Reduces crack width
- Low aesthetic impact

APPLICATIONS

CSS V-Wrap fabrics can be used to resolve strength deficiencies and increase the load-carrying capacity of buildings, bridges, silos, chimneys and other structures.

- Load increases
- Seismic strengthening
- Repair structural elements
- Change in structural system
- Design or construction defects

PACKAGING

Roll Size (Width x Length)	Model No.
12 in. x 100 yd.	CV-C220HM12-100
(305 mm x 91.4 m)	CV-C220HMA12-100
24 in. x 50 yd.	CV-C220HM24-50
(610 mm x 45.7 m)	CV-C220HMA24-50

HOW TO USE

Design
Design should comply with ACI 440.2R or another recognized design/specification entity and is typically based on CFRP contribution determined by detailed analysis. Design values will vary based on project requirements and applicable environmental and strength reduction factors.

Surface Preparation
Surfaces to receive CSS V-Wrap C220HM must be clean and sound. They must be dry and free of frost. All dust, laitance, grease, curing compounds, waxes, deteriorated materials and other bond-inhibiting materials must be removed from the surface prior to application. Existing uneven surfaces must be filled with appropriate epoxy putty or repair mortar. Use abrasive blasting, pressure washing, shotblasting, grinding or other approved mechanical means to achieve an open-pore texture with a concrete surface profile of not less than CSP-3 (ICRI). In certain applications and at the engineer's discretion, the bond between the substrate and the fabric may be determined to be noncritical (such as in column confinement applications). All corners must be rounded to ½" (12.7 mm) radius minimum. The adhesive bond strength of the concrete may be verified after surface preparation by random pull-off testing (ASTM C1583) at the discretion of the engineer. Minimum tensile strength of 200 psi must be achieved for concrete.

Handling
Approved personal protection equipment should be worn at all times. Particle mask is recommended for possible airborne particles. Gloves are recommended when handling fabrics and resins to avoid skin irritation. Safety glasses are recommended to prevent eye irritation. Wear chemical-resistant clothing/gloves/goggles. Ventilate area. In absence of adequate ventilation, use a properly fitted NIOSH respirator.

Cutting
Fabric can be cut to appropriate length by using commercial-quality heavy-duty scissors.

Application
Installation of the CSS V-Wrap strengthening system should be performed only by a specially trained, approved contractor. The CSS V-Wrap strengthening system shall consist of CSS V-Wrap carbon fabric and CSS V-Wrap 770 epoxy.

Note the specified number of plies, ply widths and fiber orientation. Mix resin components using recommended procedures on product datasheet. Apply one coat of CSS V-Wrap 770 epoxy as a primer to the surface using a nap roller. Fill minor concrete defects such as bug holes and other imperfections using CSS V-Wrap 770 epoxy mixed with fumed silica (thickened epoxy) or CSS V-Wrap PF putty filler. Apply thickened epoxy or putty using a trowel. Adjust the gap between saturator rollers to approximately 42 mils. Using a saturator machine, presaturate the appropriate length of CSS V-Wrap fabric with CSS V-Wrap 770 epoxy as a saturant. Install the saturated CSS V-Wrap fabric. Use a rib roller to remove all air pockets and ensure intimate contact with the surface. If a splice is needed, a minimum 6" (152 mm) overlap is required to achieve continuity. On multiple plies with splices, stagger the splice locations. If required, apply topcoat material.

Limitations
- Design calculations must be approved by a licensed professional engineer.
- System is a vapor barrier.
- Concrete deterioration and steel corrosion must be resolved prior to application.
- Minimum application temperature is 40°F. (4°C)

Storage
Store material in a cool, dark space. Low humidity is recommended.

CAUTION

Protective Measures: The use of safety glasses and chemically-resistant gloves is recommended. Use appropriate clothing to minimize skin contact. The use of a NIOSH-approved respirator is required to protect respiratory tract when ventilation is not adequate to limit exposure below the PEL. Refer to Safety Data Sheets (SDS) available at **strongtie.com/sds** for detailed information.

FIRST AID

Skin: Wash fibers off skin with water and soap. If fibers are embedded in the skin, remove with tweezers. Discard clothing that may contain embedded fibers. Seek medical advice if exposure results in adverse effects.

Eyes: Immediately flush with a continuous water stream for at least 20 minutes. Washing immediately after exposure is expected to be effective in preventing damage to the eyes. Seek medical advice.

Inhalation: If there is inhalation exposure to the fibers of this product, remove source of exposure and move affected person to fresh air. If not breathing, give artificial respiration. If there is breathing difficulty, give oxygen. Seek medical advice for any respiratory problems.

Ingestion: Not expected to occur since ingestion is not a likely route of exposure for this product. If ingestion does occur, DO NOT INDUCE VOMITING. Nothing by mouth if unconscious. Seek medical advice.

CLEAN-UP

Environmental Precautions

Spill/Release and Cleanup Procedures: In case of spill, collect (e.g., sweep up, vacuum, etc.) spilled material and either reuse or dispose of properly. Chopped or milled carbon fibers may be slippery if spilled, posing an accident risk. Wear personal protective equipment as described in the SDS during cleanup activities.

LIMITED WARRANTY

This product is covered by the Simpson Strong-Tie RPS Product Limited Warranty, which is available at **strongtie.com/limited-warranties** or by calling Simpson Strong-Tie at (800) 999-5099.

TYFO® SCH-41 Composite

using Tyfo® S Epoxy

DESCRIPTION
The Tyfo® SCH-41 Composite is comprised of the Tyfo® S Epoxy and Tyfo® SCH-41 reinforcing fabric. Tyfo® SCH-41 is a custom, uni-directional carbon fabric orientated in the 0° direction. The Tyfo® S Epoxy is a two-component epoxy matrix.

USE
The Tyfo® SCH-41 fabric is combined with Tyfo® S Epoxy to provide an ambient-cure, wet-layup, composite system for strengthening bridges, buildings and other structures.

ADVANTAGES
- ICC-ES ESR-2103 listed product
- IAPMO UES ER-595 listed product
- UL listed, fire-rated assembly component
- Tyfo® Systems are NSF/ANSI Standard 61-G certified
- Proven long-term performance and durability
- Excellent wet-out and handling properties
- 100% solids, solvent-free epoxy matrix
- Low viscosity, long working time
- Ambient cure application

PACKAGING
Tyfo® SCH-41: 24" x 300 lineal ft. (600 sq. ft.) Typically ships in 12" x 13" x 27" boxes.
Tyfo® S Epoxy: Pre-measured 5-gallon units with a combined material volume of 4 gallons or in 55-gallon drums.

COVERAGE
Approximately 3 to 4 units of Tyfo® S Epoxy per roll of the Tyfo® SCH-41 fabric.

CONSUMPTION RATE
Fabric-to-epoxy ratio by weight:
For Tyfo® SCH Fabrics: 1 : 1
For Tyfo® SEH Fabrics: 1 : 0.8

SHELF LIFE
Epoxy - two years in original, unopened and properly stored containers.
Fabric - 10 years in proper storage conditions.

STORAGE CONDITIONS
Store epoxy at 60°F to 100°F (15°C to 38°C). Resin is susceptible to crystallization at temperatures below 50°F. If crystallized, epoxy must be reheated until clear. Store fabric rolls flat, not on ends, and at temperatures below 100°F (38°C). Avoid moisture and water contamination.

Typical Dry Fiber Properties

Material properties are based on standard laboratory conditions (23°C, 50 percent relative humidity.)

Property	Typical Test Value
Tensile Strength	620,000 psi (4.3 GPa)
Tensile Modulus	36.0 x 10^6 psi (250 GPa)
Ultimate Elongation	1.7%
Density	0.064 lbs./in.^{3} (1.77g/cm^3)
Minimum weight per sq. yd.	19 oz (644 g/m^2)

Composite Gross Laminate Properties

Property[3]	ASTM Method	ACI 440.2R Properties[1]	Design Properties[2]
Ultimate Tensile Strength in Primary Fiber Direction	D3039	131,000 psi (903 MPa)	131,000 psi (903 MPa)
Elongation at Break		0.90%	0.90%
Tensile Modulus		14.6 x 10^6 psi (100 GPa)	12.6 x 10^6 psi (87 GPa)
Tensile Strength per inch width	D7565	5,240 lbf/in width (918 N/mm)	5,240 lbf/in width (918 N/mm)
Tensile Stiffness per inch width		584 x 10^3 lbf/in width (102 kN/mm)	504 x 10^3 lbf/in width (88 kN/mm)
Nominal Laminate Thickness	D1777	0.04 in.	0.04 in.

[1] Strength is defined as the mean strength (171 ksi) minus 3 standard deviations. Modulus is defined as the reported mean modulus, and elongation is defined as the calculated strain from the design strength and modulus.
[2] Tensile modulus is defined as the 5th percentile value representing the 80% lower confidence bound of a 2 parameter Weibull distribution (ASTM D7290).
[3] Design values may require additional reduction factors based on expected exposure conditions, type of application, and design life assumptions.

Additional Composite Properties

Property[4]	ASTM Method	Typical Test Values	Design Values
Flexural Strength	D790	110,000 psi (758.4 MPa)	82,500 psi (568.8 MPa)
Flexural Modulus		8.5 x 10^6 psi (58.6 GPa)	7.0 x 10^6 psi (48.3 GPa)
Longitudinal Compressive Strength	G8	50,000 psi (344.8 MPa)	42,500 psi (293 MPa)
Longitudinal Compressive Modulus	D149	11.2 x 10^6 psi (77.2 GPa)	9.5 x 10^6 psi (65.5 GPa)
Longitudinal Coefficient of Thermal Expansion		3.6 ppm/°F	
Transverse Coefficient of Thermal Expansion	D570	20.3 ppm/°F	

[4] Contact FyfeFRP LLC engineers to confirm project specification values and design methodology.

INSTALLATION OF THE TYFO® SCH-41 SYSTEM

DESIGN
The Tyfo® SCH-41 system is designed to meet specific project criteria dictated by the engineer of record and any relevant building codes and/or guidelines. The design shall be based on the allowable strain for each type of application and the design modulus of the material. FyfeFRP LLC engineering staff may provide preliminary design, specification wording and application details based on the project requirements.

INSTALLATION
The Tyfo® system is to be installed by FyfeFRP LLC trained and certified applicators in accordance with the FyfeFRP LLC quality control manual, project specifications, and design requirements.

SURFACE PREPARATION
The required surface preparation is dependent on the type of element being strengthened. In general, the surface must be clean, dry and free of protrusions or cavities to prevent voids behind the Tyfo® system. Column surfaces that will receive continuous wraps typically only require a clean, sound substrate. Discontinuous wrapping surfaces (walls, beams, slabs, etc.) require a minimum CSP-2 profile to prepare for bonding, achieved by light sandblast, grinding or other approved methods per ICRI 310.2R. Tyfo® Composite Anchors may be incorporated in the designs. FyfeFRP LLC engineering staff will provide the proper specifications and details based on project requirements.

MIXING TYFO® S EPOXY
For pre-measured units in 5-gallon containers, pour the contents of component B into the component A container. Mix thoroughly with a low speed mixer at 400 to 600 RPM until uniformly blended. Ensure epoxy is transferred between the A and B buckets. For 55-gallon drums, mix component A and component B per the appropriate weight or volumetric mix ratio. Resin may be heated to achieve desired viscosity (i.e. radiant heating, drum heaters, water bath). Mixed Tyfo® S Epoxy may be thickened by adding up to 7 percent by weight of fumed silica (such as Cab-o-sil TS-720) or approved filler such as HDPE fibers. DO NOT THIN. Solvents will prevent proper cure.

PROTECTIVE COATINGS
Apply a final coat of thickened Tyfo® S Epoxy to all fabric edges, including butt splice, termination points and jacket edges. Paint between 24 and 72 hours after final application of epoxy. If more than 72 hours after application, prepare the surface by light sandblast or hand sanding to lightly etch the surface. Please refer to FyfeFRP LLC's NSF Listing for the NSF-61G listed application method (www.NSF.org).

LIMITATIONS
Recommended substrate temperature range is 50°F to 100°F (10°C to 38°C). All coating applications to be performed at a minimum of 5.4°F above the dew point. Maintain conditions for the first 48 hours of cure. Temperatures below 50°F will significantly increase the viscosity of the mixed product. Higher viscosity will reduce fabric penetration, introduce additional air into the system, and extend the cure times beyond 48 hours. DO NOT THIN. Solvents will prevent proper cure.

Epoxy Material Properties		
Cure schedule: 72 hour post-cure at 140°F (60°C)[1]		
Property	**ASTM Method**	**Typical Test Value**
Glass Transition Temperature, T_g	D4065/E1356	180°F (82°C)
Tensile Strength	D638 Type 1	10,500 psi (72.4 MPa)
Tensile Modulus		461,000 psi (3.18 GPa)
Elongation		5.0%
Compressive Strength	D695	12,500 psi (86.2 MPa)
Compressive Modulus		465,000 psi (3.2 GPa)
Flexural Strength	D790	17,900 psi (123.4 MPa)
Flexural Modulus		452,000 psi (3.12 GPa)
Shore D Hardness	D2240	87±3
Water Absorption (24 hours) Water Absorption (13 weeks)	D570	0.33% 1.98%
Adhesion Strength[2] Concrete (ASTM D7522) Steel Epoxy	D4541	>400 psi (concrete failure typ.) >1200 psi >1200 psi

[1] Testing temperature: 73°F (23°C).
[2] Adhesion strength dependent on surface preparation and substrate thickness. Concrete adhesion strength is dependent on the concrete strength and is based on a minimum CSP-2 profile. Steel adhesion strength is based on SSPC-SP10 and SSPC-SP11 surface preparation methods. Cure schedule: 7 days at 73°F (23°C).

CAUTION!

CLEANUP
Collect with absorbent material. Dispose in accordance with local disposal regulations. Uncured material can be removed with approved solvent. Cured materials must be mechanically removed.

HAZARDS
Consult the Safety Data Sheets (SDS) for associated hazards. SDS will be supplied upon request.

Consult safety data sheet (SDS) for more information. For industrial use only.

FyfeCo.com | FyfeInfo@cs-nri.com | +1.855.708.3617

V: 03.06.2022

Smarter Strengthening Solutions™

CSS V-Wrap™ HMCA

Carbon Fiber Anchor

DESCRIPTION

CSS V-Wrap HMCA is a high-strength, high-modulus unidirectional carbon fiber anchor designed to be field laminated with CSS V-Wrap 770 epoxy to create a carbon-fiber-reinforced polymer (CFRP) composite anchor for improving force transfer.

MATERIAL PROPERTIES

Typical Data

Storage Conditions	Store dry at 40°F – 90°F (4°C – 32°C)
Color	Black
Shelf Life	10 years

Dry Fiber Properties	
Tensile Strength	790,000 psi (5,440 MPa)
Tensile Modulus	42 x 10^6 psi (289,550 MPa)
Elongation at Break	1.9%

Cured Laminate Properties	Design Values
Tensile Strength	165,000 psi (1,138 MPa)
Modulus of Elasticity	15.0 x 10^6 psi (103,400 MPa)
Elongation at Break	1.1%

MADE IN USA with GLOBAL MATERIALS

PERFORMANCE FEATURES

- Manufactured using ICC-approved raw materials
- High tensile modulus and strength
- Lightweight
- Noncorrosive
- Flexible
- Various finish options

APPLICATIONS

The CSS V-Wrap HMCA carbon fiber anchor is combined with CSS V-Wrap epoxies and can be used as a standalone reinforcement or to improve end details and anchorage of various CSS V-Wrap designs.

- Load increases
- Seismic strengthening
- Repair of structural elements
- Change in structural system
- Design or construction defects

PACKAGING

Custom anchor lengths and diameters are available in diameters ranging from 0.375" to 1.5" (9 mm to 37 mm) in ⅛" increments.

HOW TO USE

Design
The CSS V-Wrap HMCA carbon fiber anchors shall be designed to meet specific design criteria. The criteria for each project is dictated by the Engineer of Record and any relevant building codes and/or guidelines. Contact Structural Technologies at (410) 859-6502 for engineering support with anchor design.

Surface Preparation
Surfaces to receive CSS V-Wrap HMCA must be clean and sound. They must be dry and free of frost. All dust, laitance, grease, curing compounds, waxes, deteriorated materials and other bond-inhibiting materials must be removed from the surface prior to application. Existing uneven surfaces must be filled with appropriate epoxy putty or repair mortar. Use abrasive blasting, pressure washing, shotblasting, grinding or other approved mechanical means to achieve an open-pore texture with a concrete surface profile of not less than CSP-3 (ICRI). In certain applications and at the engineer's discretion, the bond between the substrate and the fabric may be determined to be non-critical (such as in column confinement applications). The adhesive bond strength of the concrete may be verified after surface preparation by random pull-off testing (ASTM C1583) at the discretion of the engineer. Minimum tensile strength of 200 psi must be achieved for concrete.

Drilled Hole Preparation
Drill holes to specified diameter, depth and angle according to approved drawings using a rotary hammer drill, a carbide-tipped drill bit conforming to ANSI B212.15-1994, router bits, and a Simpson Strong-Tie® ETB brush.

Drilled hole diameter shall be anchor diameter plus ⅛" (3.18 mm). Round the top edge of the drilled hole using router bits to specified radius. Using clean, compressed air, blow out any remaining debris for four seconds, then clean with the appropriate sized Simpson Strong-Tie ETB brush for a minimum of four cycles, and again blowing out any remaining debris for another four seconds with compressed air.

Application
Manually saturate the anchor and ensure full fiber saturation is achieved. Install the saturated anchor in accordance with the approved project drawings and specifications. Refer to the CSS V-Wrap 770 Epoxy Saturant Technical Data Sheet for all information on the approved epoxy.

Limitations
Minimum application temperature is 40°F.

Storage
Store material in a cool, dark space. Low humidity is recommended. Store at 40°F to 90°F (4°C to 32°C). Avoid freezing. Avoid moisture and water contamination.

CAUTION

Protective Measures: The use of safety glasses, chemical-resistant gloves and appropriate clothing to minimize skin contact is recommended. The use of a NIOSH-approved respirator is required to protect respiratory tract when ventilation is not adequate to limit exposure below the PEL. Refer to Safety Data Sheets (SDS) available at **strongtie.com/sds** for detailed information.

FIRST AID

Skin: Wash fibers off skin with water and soap. If fibers are embedded in the skin, remove with tweezers. Discard clothing that may contain embedded fibers. Seek medical advice if exposure results in adverse effects.

Eyes: Immediately flush with a continuous water stream for at least 20 minutes. Washing immediately after exposure is expected to be effective in preventing damage to the eyes. Seek medical advice.

Inhalation: If there is inhalation exposure to the fibers of this product, remove source of exposure and move affected person to fresh air. If not breathing, give artificial respiration. If there is breathing difficulty, give oxygen. Seek medical advice for any respiratory problems.

Ingestion: Not expected to occur since ingestion is not a likely route of exposure for this product. If ingestion does occur, DO NOT INDUCE VOMITING. Nothing by mouth if unconscious. Seek medical advice.

CLEAN-UP

Spill/Release and Cleanup Procedures: In case of spill, collect (e.g., sweep up, vacuum, etc.) spilled material and either reuse or dispose of properly. Chopped or milled carbon fibers may be slippery if spilled, posing an accident risk. Wear personal protective equipment as described in the SDS during cleanup activities.

LIMITED WARRANTY

This product is covered by the Simpson Strong-Tie RPS Product Limited Warranty, which is available at **strongtie.com/limited-warranties** or by calling Simpson Strong-Tie at (800) 999-5099.

Smarter Strengthening Solutions™

CSS V-Wrap™ 770

Epoxy Saturant

SIMPSON Strong-Tie | structural TECHNOLOGIES

DESCRIPTION

CSS V-Wrap 770 is a two-part, 100% solids epoxy for high-strength composite bonding applications. CSS V-Wrap 770 matrix material is combined with CSS V-Wrap carbon and glass fabrics to provide a wet-layup composite for strengthening of structural members. It is formulated to provide high elongation to optimize properties of the CSS V-Wrap composite systems. It provides a long working time for application, with no offensive odor. CSS V-Wrap 770 may be thickened with fumed silica to produce a tack coat/putty or a finishing coat, depending upon the project requirements. CSS V-Wrap 770 contains no Volatile Organic Compounds (VOC) or solvents.

CODE REPORTS AND COMPLIANCE

ICC-ES ESR-4930

MATERIAL PROPERTIES*

Part A & B Properties

Approximate Pot Life	3 to 6 hours at 68°F (20°C)
Color	**Part A:** Clear **Part B:** Clear **Mixed:** Clear
Density	**Part A:** 9.7 lb./gal (1.16 kg/L) **Part B:** 7.9 lb./gal (0.95 kg/L) **Mixed:** 9.17 lb./gal (1.11 kg/L)
Mixing Ratio	100A:41B by volume 100A:33B by weight
Shelf Life	24 months stored in unopened containers at 70°F (21°C)
Storage	Store material in a dry area between 40°F (4°C) and 100°F (38°C) with no exposure to moisture.

Cured Epoxy Properties	Average Values
Tensile Strength (ASTM D638)	8,800 psi (60.7 MPa)
Tensile Modulus (ASTM D638)	400,000 psi (2,760 MPa)
Elongation at Break (ASTM D638)	4.4%
Flexural Strength (ASTM D790)	16,000 psi (110.3 MPa)
Flexural Modulus (ASTM D790)	420,000 psi (2,896 MPa)
Compressive Strength (ASTM D695)	12,200 psi (84.1 MPa)
Compressive Modulus (ASTM D695)	440,000 psi (3,304 MPa)
T_g (ASTM E1640)	187°F (86°C)
VOC Content (ASTM D2369)	0% VOC

* Curing schedule: 72 hours post cure at 140°F (60°C)

MADE IN USA with GLOBAL MATERIALS

PERFORMANCE FEATURES

- ICC-ES ESR-4930 listed product
- UL listed (ul.com/database)
- 100% solvent-free
- Good high / low temperature properties
- High elongation
- NSF/ANSI Standard 61 listed product for drinking water systems

APPLICATIONS

CSS V-Wrap 770 is a multi-use epoxy that performs as a primer, tack coat/putty, and saturating resin for the CSS V-Wrap carbon and glass fiber systems. Fumed silica may be added to thicken the resin. The maximum ratio by volume is 1.5 of fumed silica to 1 part of resin.

PACKAGING

Kit Size	Model No.
4 US gallon (15.1 L)	CV-ES7704KT

HOW TO USE

Surface Preparation
CSS V-Wrap 770 should be applied to substrates that are free of protrusions, dust, oils, and other surface contaminates or bond-inhibiting materials. Substrates should be dry and exhibit an open pore structure.

Application
Apply primer to repair surfaces with a medium nap roller or non-shedding brush. Ensure full saturation of fabric sheets is achieved before installation. Heavier fabrics typically require mechanical saturation. Apply thickened CSS V-Wrap epoxy using trowels.

Basic Application Equipment
Application processes for CSS V-Wrap 770 will require mixing drill, mixing paddle, ¼" nap rollers, steel rollers, paint brushes, trowels and saturator.

Mixing
Combine the contents of CSS V-Wrap 770-A pail and CSS V-Wrap 770-B pail together making sure to scrape all material from the sides of the pail and mix for 3 minutes using a mixer at a speed of 400–600 RPM until uniformly blended. Transfer the mixed epoxy into the other pail and mix for an additional 2 minutes. Mix ratio: by volume 100A:41B, by weight 100A:33B.

Observe Working Time Limitations
Mix no more material than can be applied within the working time. Available work time, temperature and complexity of the application will determine how much material should be mixed at one time. Keep material cool and in shaded area, away from direct sunlight in warm weather. During hot weather, work time can be extended by keeping the material cool before and after mixing or by immersing the pot in ice water.

Maintenance
Periodically inspect the applied material and repair localized areas as needed.

Coverage Rates
As a Primer:

Concrete:	225 ft.²/gal (5.5 m²/L)
Masonry (Concrete):	125 ft.²/gal (3.0 m²/L)
Masonry (Clay):	200 ft.²/gal (4.9 m²/L)

As a Putty/Tack Coat:

Filler:	60 ft.²/gal (1.5 m²/L)

(Depending on surface roughness)

As Saturant:

CSS V-Wrap C100H / C100HM	80 ft.²/gal (1.9 m²/L)
CSS V-Wrap C200H / C200HM	60 ft.²/gal (1.5 m²/L)
CSS V-Wrap C400H / C400HM	40 ft.²/gal (1 m²/L)
CSS V-Wrap C220B	60 ft.²/gal (1.5 m²/L)
CSS V-Wrap EG50 / EG50B	60 ft.²/gal (1.5 m²/L)

Coverage rates may vary based on installation procedure and fabric type. Contact STRUCTURAL TECHNOLOGIES at (410) 859-6502 for coverage rates.

Limitations
Only apply CSS V-Wrap 770 when the ambient temperature is between 40°F and 100°F (4°C to 38°C). Topcoat selection should be based upon requirements for protection from environmental exposures, aesthetics and fire protection/burn characteristics.

Storage
Store in a cool, dry area (40°F and 100°F [4°C to 38°C]) away from direct sunlight, flame or other hazards.

CAUTION

Component "A": Causes skin and serious eye irritation. May cause an allergic skin reaction.

Component "B": CORROSIVE! Harmful if swallowed. Causes severe skin burns and eye damage. May cause an allergic skin reaction.

Protective Measures: The use of safety glasses and chemically-resistant gloves is recommended. Use appropriate clothing to minimize skin contact. The use of NIOSH-approved respirator is required to protect respiratory tract when ventilation is not adequate to limit exposure below the PEL. Refer to Safety Data Sheets (SDS) available at **strongtie.com/sds** for detailed information.

These products are for professional and industrial use only and are to be installed by trained and qualified applicators. Trained applicators must follow installation instructions.

FIRST AID

Eye Contact: Immediately flush eyes with plenty of cool water for at least 15 minutes while holding the eyes open. If redness, burning, blurred vision, or swelling persists, seek medical advice.

Skin Contact: In case of contact, remove product and immediately wash affected area with plenty of soap and water for at least 5 minutes. Do not apply greases or ointments. Remove contaminated clothing. Clean contaminated clothing with soap and water before re-use. If redness, burning or swelling persists, seek medical advice.

Ingestion: DO NOT INDUCE VOMITING. Never administer anything by mouth to an unconscious person. Rinse out mouth with water, then drink sips of water to remove taste from mouth. Seek medical advice. Do not leave victim unattended. If vomiting occurs spontaneously, lay victim on side and keep head lower than waist to prevent aspiration.

Inhalation: If respiratory irritation or distress occurs, remove victim to fresh air. If breathing is difficult, give oxygen. If breathing stops, apply artificial respiration. Seek medical advice.

CLEAN-UP

Environmental Precautions: Construct a dike to prevent spreading. Keep out of sewers, storm drains, surface waters and soils.

Equipment: Use methyl ethyl ketone or acetone. Observe fire and health precautions when using solvents. Dispose of in accordance with local regulations.

Small Spills: Soak up with an absorbent material, such as clay, sand or other suitable non-reactive material. Place in leak-proof containers. Seal tightly for proper disposal.

Large Spills: Approach suspected leaks with caution. Construct a dike or trench to contain material. Soak up with an absorbent material, such as clay, sand or other suitable non-reactive material. Place in leak-proof containers. Seal tightly for proper disposal.

Disposal: Dispose of container and unused portions in accordance with local, state and federal regulations. Emptied container may contain product residue and should not be reused.

LIMITED WARRANTY

This product is covered by the Simpson Strong-Tie RPS Product Limited Warranty, which is available at **strongtie.com/limited-warranties** or by calling Simpson Strong-Tie at (800) 999-5099.

TYFO® S
Saturant Epoxy

DESCRIPTION
The Tyfo® S Epoxy is a two-component epoxy matrix material for bonding applications. The Tyfo® S Epoxy combined with the Tyfo® fabrics make up the Tyfo® Systems which are NSF/ANSI Standard 61-G certified for drinking water systems. It is a high elongation material which gives optimum properties as a matrix for the Tyfo® system. It provides a long working time for application, with no offensive odor.

USE
The Tyfo® S Epoxy matrix material is combined with the Tyfo® fabrics to provide an ambient-cure wet-layup composite system for strengthening structural members. Tyfo® S Epoxy may be thickened with fumed silica (such as Cab-O-Sil TS-720) to be used as a primer, tack coat or finish depending on project requirements.

ADVANTAGES
- ICC-ES ESR-2103 listed product
- IAPMO UES ER-595 listed product
- Tyfo® Systems are NSF/ANSI Standard 61-G certified
- Good high and low temperature properties
- 100% solids, solvent-free
- Long working time
- High elongation
- Ambient cure

PACKAGING
Pre-measured 5-gallon units with a combined material volume of 4 gallons or in 55-gallon drums.

EPOXY MIX RATIO
100A : 34.5B by weight
100A : 42.0B by volume

CONSUMPTION RATE
Fabric-to-epoxy ratio by weight:
For Tyfo® SCH Fabrics: 1 : 1
For Tyfo® SEH Fabrics: 1 : 0.8

SHELF LIFE
Epoxy - two years in original, unopened and properly stored containers.
Fabric - 10 years in proper storage conditions.

STORAGE CONDITIONS
Store epoxy at 60°F to 100°F (15°C to 38°C). Resin is susceptible to crystallization at temperatures below 50°F. If crystallized, epoxy must be reheated until clear. Store fabric rolls flat, not on ends, and at temperatures below 100°F (38°C). Avoid moisture and water contamination.

Epoxy Material Properties

Material properties are based on standard laboratory conditions (23°C, 50 percent relative humidity.)

Property	Typical Test Value	
Net Weight	Component A Component B Mixed	27.4 lbs. (2.8 gal) 9.60 lbs. (1.2 gal) 37.0 lbs. (4.0 gal)
Color	Component A Component B Mixed	Clear to amber Clear to yellow Clear to amber
Viscosity	Component A Component B Mixed	11,000-13,000 cps 11 cps 600-700 cps
Density (D792) Pounds/Gallon	Component A Component B Mixed	9.7 (1.16 kg/L) 7.9 (0.95 kg/L) 9.2 (1.11 kg/L)
Pot Life (Working Time)	Mixed	3 to 4 hours
Gel Time (Time to Gelation)	Mixed	10 hours

Epoxy Material Properties

Cure schedule: 72 hour post-cure at 140°F (60°C)[1]

Property	ASTM Method	Typical Test Values
Glass Transition Temperature, T_g	D4065 E1356	180°F (82 C)
Tensile Strength	D638 Type 1	10,500 psi (72.4 MPa)
Tensile Modulus		461,000 psi (3.18 GPa)
Elongation		5.0%
Compressive Strength	D695	12,500 psi (86.2 MPa)
Compressive Modulus		465,000 psi (3.2 GPa)
Flexural Strength	D790	17,900 psi (123.4 MPa)
Flexural Modulus		452,000 psi (3.12 GPa)
Shore D Hardness	D2240	87±3
Water Absorption (24 hours) Water Absorption (13 weeks)	D570	0.33% 1.98%
Adhesion Strength[2] Concrete (ASTM D7522) Steel Epoxy	D4541	 >400 psi (concrete failure typ.) >1200 psi >1200 psi

[1] Testing temperature: 73°F (23°C).
[2] Adhesion strength dependent on surface preparation and substrate thickness. Concrete adhesion strength is dependent on the concrete strength and is based on a minimum CSP-2 profile. Steel adhesion strength is based on SSPC-SP10 and SSPC-SP11 surface preparation methods. Cure schedule: 7 days at 73°F (23°C).

HOW TO USE THE TYFO® S SATURANT EPOXY

INSTALLATION
The Tyfo® system is to be installed by FyfeFRP LLC trained and certified applicators in accordance with the FyfeFRP LLC quality control manual, project specifications, and design requirements.

SURFACE PREPARATION
The required surface preparation is dependent on the type of element being strengthened. In general, the surface must be clean, dry and free of protrusions or cavities to prevent voids behind the Tyfo® system. Column surfaces that will receive continuous wraps typically only require a clean, sound substrate. Discontinuous wrapping surfaces (walls, beams, slabs, etc.) require a minimum CSP-2 profile to prepare for bonding, achieved by light sandblast, grinding or other approved methods per ICRI 310.2R. Tyfo® Composite Anchors may be incorporated in the designs. FyfeFRP LLC engineering staff will provide the proper specifications and details based on project requirements.

MIXING TYFO® S EPOXY
For pre-measured units in 5-gallon containers, pour the contents of component B into the component A container. Mix thoroughly with a low speed mixer at 400 to 600 RPM until uniformly blended. Ensure epoxy is transferred between the A and B buckets. For 55-gallon drums, mix component A and component B per the appropriate weight or volumetric mix ratio. Resin may be heated to achieve desired viscosity (i.e. radiant heating, drum heaters, water bath). Mixed Tyfo® S Epoxy may be thickened by adding up to 7 percent by weight of fumed silica (such as Cab-o-sil TS-720) or approved filler such as HDPE fibers. DO NOT THIN. Solvents will prevent proper cure.

THICKENED TYFO® S EPOXY
Use Cab-o-sil TS-720 by Cabot Corp. or similar. For horizontal and vertical surfaces, use up to 2.0 lbs. fumed silica per kit or 5.4 percent by weight. For overhead surfaces use up to 2.5 lbs. per kit or 6.7 percent by weight. Site conditions may affect the amount of fumed silica required to achieve desired thickness. Do not exceed 7 percent by weight.

APPLICATION
Tyfo® S Epoxy is applied to the Tyfo® fabric using a saturator machine or by approved manual saturation methods (trowel, roller, or similar). Hand saturation is allowable, provided the epoxy is applied uniformly and meets the required fiber-to-epoxy ratio. Tyfo® S Epoxy is applied as a prime coat by brush or roller. Please refer to FyfeFRP LLC's NSF Listing for the NSF 61-G listed application method (www.NSF.org).

LIMITATIONS
Recommended substrate temperature range is 50°F to 100°F (10°C to 38°C). All coating applications to be performed at a minimum of 5.4°F above the dew point. Maintain conditions for the first 48 hours of cure. Temperatures below 50°F will significantly increase the viscosity of the mixed product. Higher viscosity will reduce fabric penetration, introduce additional air into the system, and extend the cure times beyond 48 hours. DO NOT THIN. Solvents will prevent proper cure.

CAUTION!

CLEANUP
Collect with absorbent material. Dispose in accordance with local disposal regulations. Uncured material can be removed with approved solvent. Cured materials must be mechanically removed.

HAZARDS
Consult the Safety Data Sheets (SDS) for associated hazards. SDS will be supplied upon request.

Consult safety data sheet (SDS) for more information.
For industrial use only.

FyfeCo.com | FyfeInfo@cs-nri.com | +1.855.708.3617

V: 03.06.2022

Appendix D: Shear Angle Corrections

Corrections to the global shear angle measurements were necessary for all specimens. These corrections were typically necessary due to spalling of concrete at the mounting point for string potentiometer SP-SE. Specimen CD8 required additional correction due to concrete also spalling at the mounting point for SP-TS. The correction process for Specimen CD8 is shown in Figure D1, where linear trendlines are established for the reliable portion of the data. The slopes of the trendlines are presented in Table D1. To correct the data, Eq. (34) was applied after the data point indicated in Table D1.

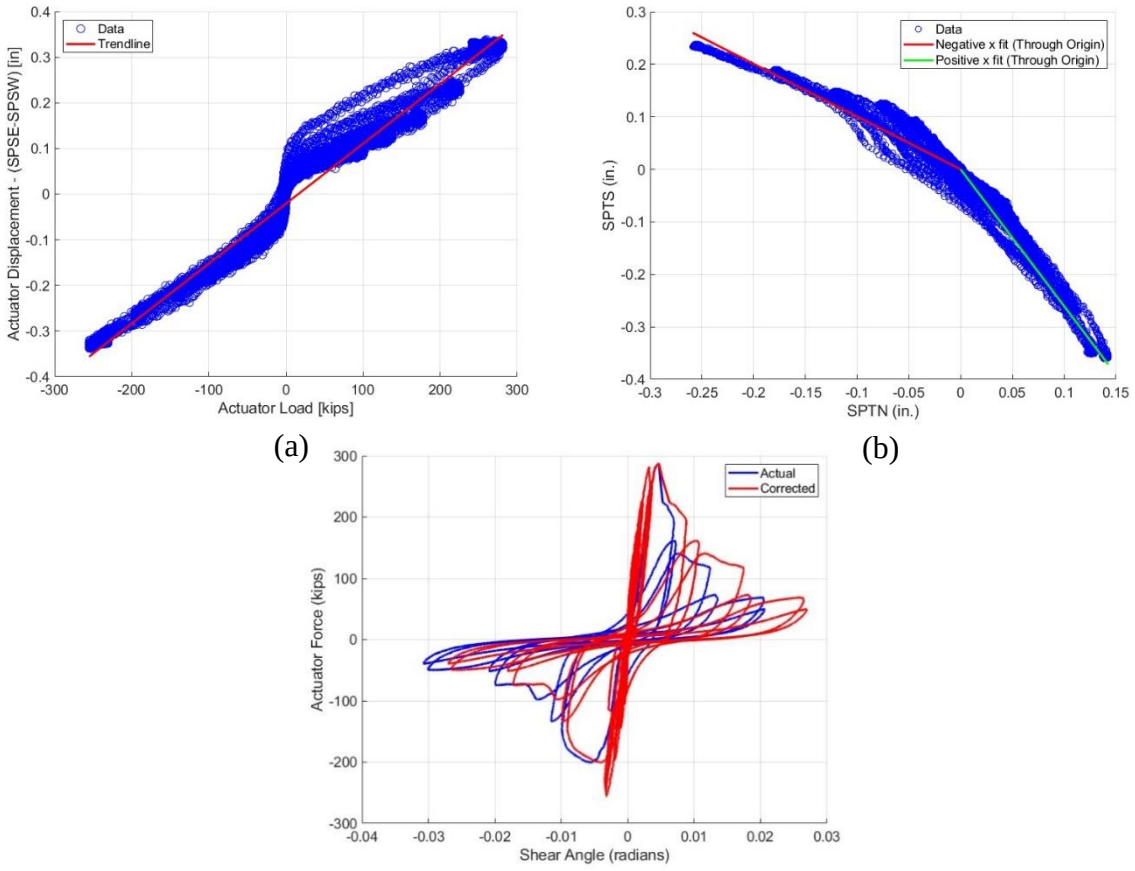

Figure D1. Global Shear Angle Correction for Specimen CD8: a) Linear Trendline for SP-SE Correction; b) Bilinear Trendline for SP-TS Correction; c) Corrected and Actual Global Shear Angle.

Table D1. Slopes of Trendlines Used in Specimen CD8 Correction.

ID	Slope (k/in.)	Data point after which correction was applied
$k_{CD8,TS}$	-1.0047 for SP-TS > 0	41800
	-2.6049 for SP-TS < 0	
$k_{CD8,SE}$	0.0013134	41800

$$\gamma_{CD8\_Corrected} = \frac{\Delta MTS - k_{CD8,SE} * V_{MTS}}{A} - \frac{\Delta TN - k_{CD8,TS}\Delta TN}{B} \qquad (34)$$

where: $\gamma_{CD8\_Corrected}$ is the corrected global shear angle for Specimen CD8 (rad); Δ_{MTS} is the recorded actuator displacement (in.); $k_{CD8,SE}$ is the slope of the trendline in Figure D1(a) (k/in.); $k_{CD8,TS}$ are the slopes of the trendline in Figure D1(b); V_{MTS} is the actuator's recorded load (kip); ΔTN is the displacement recorded by sensor SP-TN (in.); ΔTS is the displacement recorded by sensor SP-TS (in.); A is the center-to-center distance between sensors SP-SE and SP-SW (in.); and B is the center-to-center distance between sensors SP-TN and SP-TS (in.).

Specimen CD9 through CD14 all required global shear angle correction due to spalling of concrete at the mounting point for string potentiometer SP-SE. The correction procedure involved established a linear best fit correlation between the actuator load and the difference between actuator displacement Δ_{MTS} and ($\Delta \boldsymbol{SE} - \Delta \boldsymbol{SW}$) and applying the correction to data after the sensor mounting point spalled. A comparison between the actual and corrected hysteretic global shear angle responses for Specimen CD9 through CD14 is shown in Figure D2. The linear trendlines used in data correction are shown in Figure D3, and their slopes are reported in Table D2. To correct the data, Eq. (35) was applied after the data point indicated in Table D2.

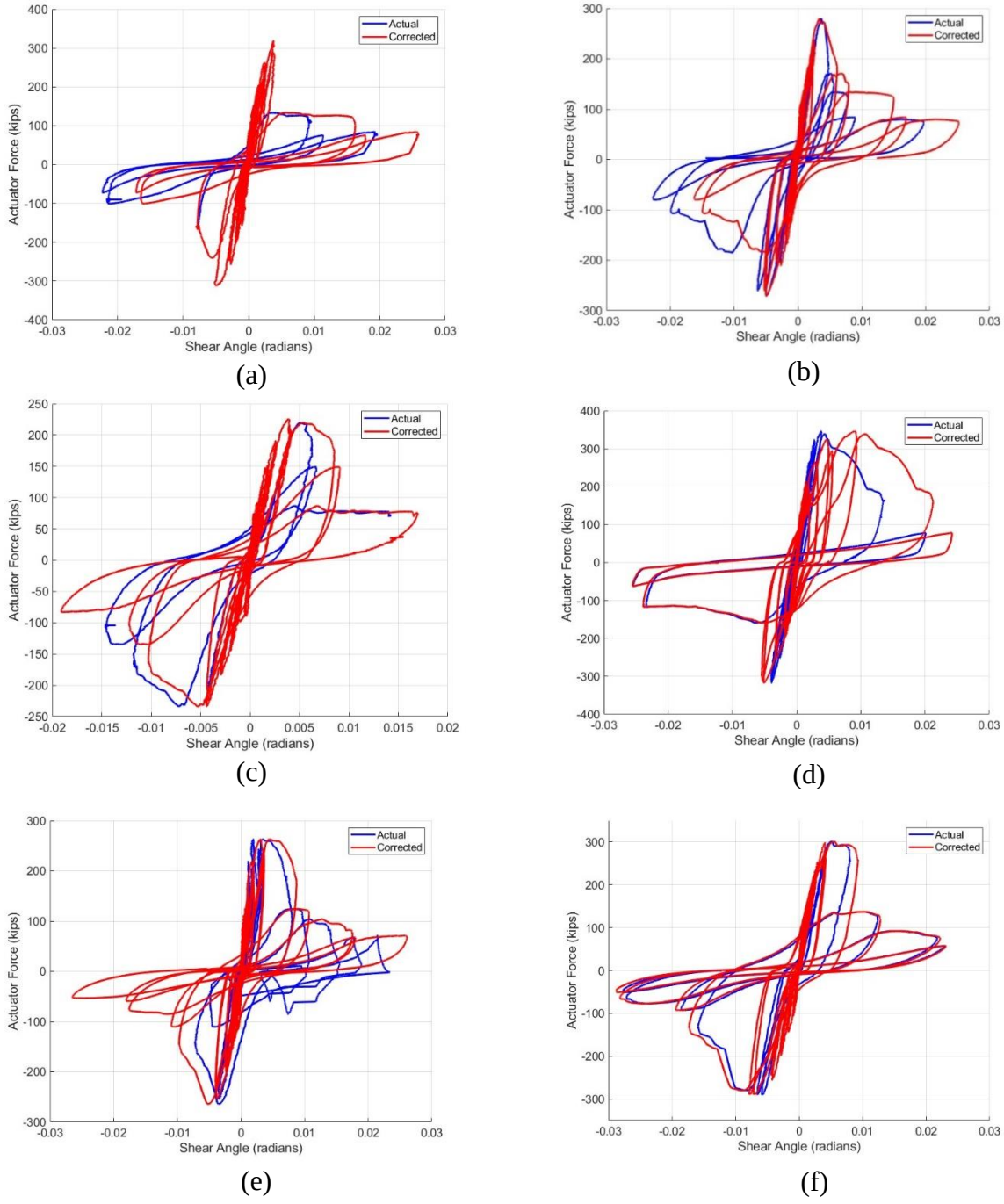

Figure D2. Actual and Corrected Global Shear Angle for Specimen: a) CD9; b) CD10; c) CD11; d) CD12; e) CD13; f) CD14.

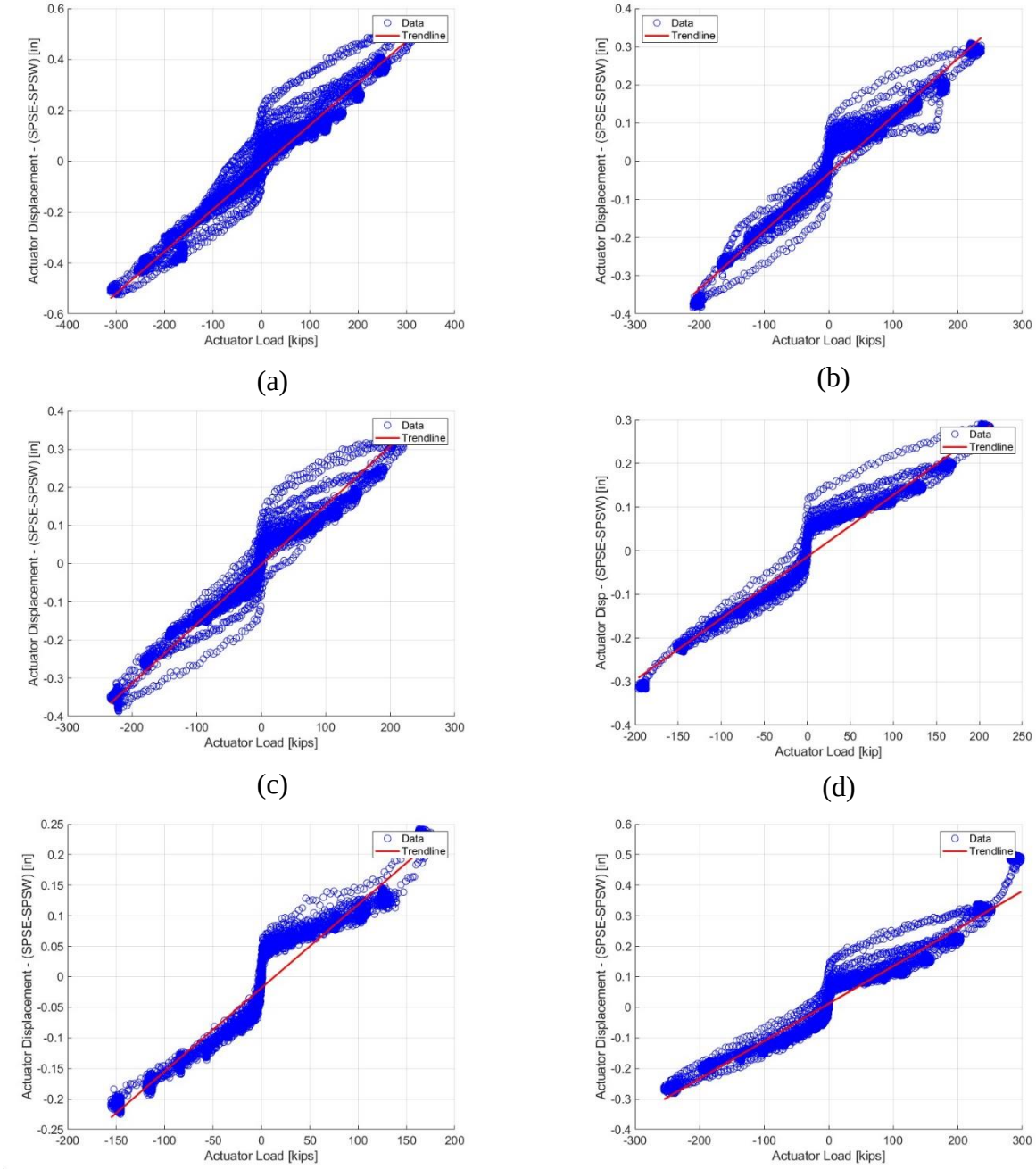

Figure D3. Linear Trendline for SP-SE Correction for Specimen: a) CD9; b) CD10; c) CD11; d) CD12; e) CD13; f) CD14.

$$\gamma_{CD\_Corrected} = \frac{\Delta MTS - k_{CD} * V_{MTS}}{A} - \frac{\Delta TN - \Delta TS}{B} + x \qquad (35)$$

where: $\gamma_{CD\_Corrected}$ is the corrected global shear angle (rad); Δ_{MTS} is the recorded actuator displacement (in.); k_{CD} is the slope of the trendline in Figure D3 (k/in.); V_{MTS} is the actuator's

recorded load (kip); ΔTN is the displacement recorded by sensor SP-TN (in.); ΔTS is the displacement recorded by sensor SP-TS (in.); A is the center-to-center distance between sensors SP-SE and SP-SW (in.); B is the center-to-center distance between sensors SP-TN and SP-TS (in.); and x is a constant used to facilitate smooth transition at the correction point (rad).

Table D2. Parameters for Specimen CD9-14 Global Shear Angle Correction.

Specimen ID	**Slope of trendline in Figure D3, k_{CD} (k/in.)**	**Constant to facilitate smooth transition, x (rad)**	**Data point after which correction was applied**
CD9	0.0016529	0.00085943	17100
CD10	0.0015062	0	17000
CD11	0.0015536	0	17300
CD12	0.0014141	0.00042079	16887
CD13	0.0013656	0	13000
CD14	0.0012282	-0.00146471	32000

The global shear angle correction process for Specimen CD7 was necessary due to exceeding the range of sensor SP-SW. The correction process is not depicted here graphically. It involved establishing a linear correlation between actuator displacement and the SP-SW reading and simply replacing the portion of the data limited by sensor range with the product of the trendline slope and the actuator displacement.

Appendix E: Distances Between String Potentiometers

Before each test, the center-to-center distances between the mounting points of each string potentiometer were measured and documented. These measurements were essential for determining the global shear angle. The labeling convention used for organizing and referencing these measurements is shown in Figure E1. Detailed values for each test are presented in Table E1.

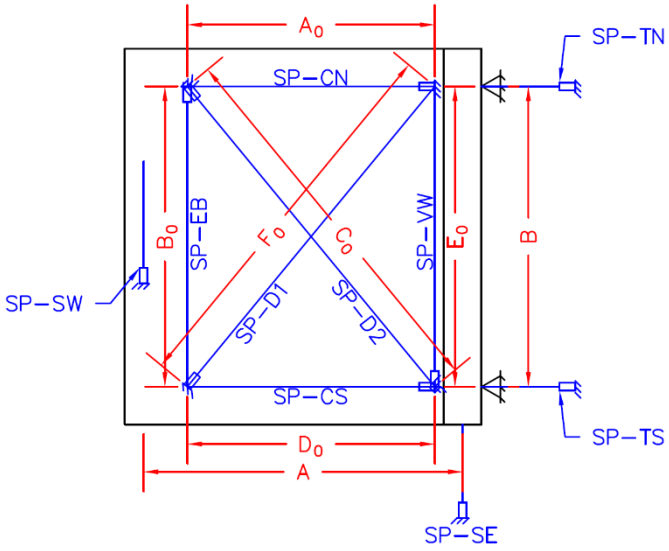

Figure E1. Labeling Convention for String Potentiometers [From (Hutton et al. 2023)].

Table E1. String Potentiometer Center-to-center Distances.

Specimen	A_0 (in.)	B_0 (in.)	C_0 (in.)	D_0 (in.)	E_0 (in.)	F_0 (in.)	A (in.)	B (in.)
CD7	76.50	96.00	123.00	76.50	96.00	122.50	102.875	115.50
CD8	77.50	93.50	121.00	77.00	95.00	123.50	105.00	117.50
CD9	75.75	97.00	123.50	75.75	97.00	122.00	105.00	114.50
CD10	76.75	94.5625	119.3125	73.375	94.5625	121.375	106.875	116.125
CD11	72.25	108.25	130.50	71.625	108.50	129.75	104.375	115.75
CD12	71.50	108.50	130.25	71.125	108.625	129.50	106.375	114.375
CD13	74.00	94.125	121.75	75.75	94.375	119.125	105.875	115.375
CD14	69.75	95.3125	118.875	72.0625	94.25	117.875	106.125	115.3125